

Study of dislocations from continuous flattening anneal and its effect on magnetic properties of grain oriented electrical steel

Sreevathsan Ramanathan

A thesis submitted to the Cardiff University in candidature for the degree of

Doctor of Philosophy

Wolfson Centre for Magnetism
Cardiff School of Engineering
Cardiff University
Wales, United Kingdom

2013



Academic Supervisors
Dr Jeremy P Hall
Prof Sam L Evans



Industrial Supervisors
Mr. Keith Jenkins
Dr. Darran Richards

Acknowledgements

I would like to thank my academic supervisors Dr. Jeremy P Hall and Prof. Sam L Evans, for their support and guidance during this work. The freedom they provided to work on new ideas is highly appreciated.

Industrial expertise and suggestions to improve this work from my industrial supervisors Mr. Keith Jenkins and Dr. Darran Richards are highly appreciated. My gratitude also goes to Mr. Andy Green from Cogent Power Ltd., who worked with me during the initial phase of this project.

Many thanks to my mentor and friend Dr. Ikenna Nlebedim for guiding me at the crucial starting phase of my PhD. I would like to thank Dr. Phil Anderson for all his guidance with magnetic measurements. My gratitude goes to Ms. Pam Cummings for her help with metallography and discussions on the metallurgy of electrical steels. Special thanks to Mr. Frank Xu and Dr. Nkwachukwu Chukuchekwa for their help in magnetic measurements.

A major part of this work could not have been completed without the support of technicians at the school of engineering. My special thanks to Mr. Paul Farrugia, Mr. Michael Baynton, Mr. Andrew Rankmore and Mr. Steven Mead who lend me their technical expertise while building my experimental setup. My sincere gratitude also extends to staff in research and finance offices.

Endless support in a personal and professional way from my friends at Wolfson without which this project wouldn't have been possible is highly appreciated. Special thanks to Dr. Y Melikhov, Lukasz, Piotr and Shervin for making Wolfson centre for magnetics an enjoyable place to work. Thanks to my friends Madhav and Thaya for their unconditional support and belief.

I am indebted to the unwavering support of my fiancée/best friend Ragini and my friend Mahesh without which the completion of this work would have been impossible. Last but not the least I am forever indebted to my amma and appa (parents) for their guidance and motivation all through my life. Motivation and support from Geetha mom and dad are highly appreciated.

The funding for this work provided by Cogent Power Ltd., (Tata Steel Europe) is acknowledged. Thanks to the UK magnetism society for the students bursary support and Dennis Hadfield Award for the best student article.

DECLARATION

This work has not previously been accepted in substance for any degree and is not concurrently submitted in candidature for any degree.

Signed (candidate) Date

STATEMENT 1

This thesis is being submitted in partial fulfillment of the requirements for the degree of PhD.

Signed (candidate) Date

STATEMENT 2

This thesis is the result of my own independent work/investigation, except where otherwise stated. Other sources are acknowledged by explicit references.

Signed (candidate) Date

STATEMENT 3

I hereby give consent for my thesis, if accepted, to be available for photocopying and for inter-library loan, and for the title and summary to be made available to outside organisations.

Signed (candidate) Date

Summary of the thesis

Deformation mechanism and dislocation dynamics in grain oriented electrical steel (GOES) is not well established during the continuous flattening anneal process. This work deals with the study of deformation mechanisms during the process and the effect of lattice defects created during the process on the final magnetic properties of GOES.

A heat transfer model of the continuous flattening anneal furnace was developed to calculate the temperature profile of the strip throughout the process. The heat transfer model showed the stability of peak strip temperature at 850°C when the line speed was varied from 60-90m/min. A deformation mechanism map was constructed for two varieties of GOES. The main implication of this model is the knowledge of the effect of process parameters like stress, temperature and strain rate on the formation of dislocation structure in GOES during continuous flattening anneal process.

LAFFAS (Lab Annealing Furnace for Flattening Anneal Simulation) was constructed to simulate the continuous flattening anneal process and produce samples for dislocation study and magnetic testing. The high temperature mechanical behaviour of Conventional Grain Oriented+[®] (CGO+ - new GOES product) and its effect on magnetic properties were also analysed.

Polygonization in GOES and the factors affecting polygonization were studied in detail. Initial orientation of the grains was determined to be a rate controlling factor for degree of polygonization along with temperature and annealing time. The degree of polygonization was shown to be an important parameter affecting the change in domain width. A localised decrease in specific total loss was observed at 1.5T and 50Hz in grains where polygonization was complete. An increase in specific total loss of about 10-35% at 1.5T and 50Hz in bulk polycrystalline material was observed due to the sensitivity of polygonization to initial texture resulting in incomplete polygonization in a high percentage of grains.

Table of contents

S.No	Title	Page
	Declaration statements	II
	Acknowledgements	III
	Summary of the thesis	IV
	Table of contents	V
	Glossary of terms	IX
Chapter 1	Introduction	1
1.1	Introduction and overview of the project	2
1.2	Overview of the material	2
1.3	Source of lattice defects	3
1.4	Power loss components and effect of lattice defects on magnetic properties	4
1.5	Aim of this investigation	5
1.6	Research methodology	5
1.7	References	7
Chapter 2	Ferromagnetism and Domain theory	8
2.1	Ferromagnetism and Domain theory	9
2.2	Magnetic domains	9
2.3	Magnetostatic energy	11
2.4	Magnetocrystalline anisotropy energy	12
2.5	Domain wall energy	13
2.6	Magnetoelastic energy	14
2.7	External applied field	15
2.8	Losses in magnetic materials	17
2.9	Dislocations and their effects on magnetic properties	19
2.10	References	22
Chapter 3	Literature review – Production and evolution of GOES	24
3.1	History of electrical steel production and improvements	25
3.2	Manufacturing process of GOES	27
3.3	Evolution and advancements in the manufacturing process	34
3.3.1	Mechanisms of Goss texture evolution	34
3.3.2	Eddy current loss reduction in electrical steel	39
3.3.3	Dependence of anomalous component on magnetic domains	39
3.3.4	Electrical steel coatings	43
3.4	Continuous thermal flattening anneal line	44
3.5	References – Chapter 3	48
Chapter 4	Heat transfer model of continuous flattening anneal (M-line) line using finite element analysis (COMSOL)	55
4.1	Introduction to the furnace model	56
4.2	Purpose of the flattening anneal heat transfer model	56
4.3	Background study of furnace models	57
4.4	Furnace design	58
4.5	Modelling strategy	59

4.6	Heat transfer physics	64
4.6.1	Heat balance calculation in the furnace	65
4.6.2	Heat transfer used in the model	66
4.7	Physical properties of the materials used in the model	68
4.8	Effect of mesh size	70
4.9	Results	71
4.9.1	Radiant tube model	71
4.9.2	Full furnace model	75
4.9.3	Radiant cooling zone	77
4.9.4	Compressed open air cooling zone	78
4.10	Discussion	79
4.11	Conclusion	84
4.12	References	86
Chapter 5	Deformation mechanism maps – Modelling of the deformation mechanism in Fe-3% Si alloys	88
5.1	Introduction	89
5.2	Background study on deformation mechanism maps	89
5.3	Materials – Chemical composition and grain structure	91
5.4	Model and Program	92
5.4.1	Deformation modes in the model	92
5.4.2	Rate equations	93
5.4.3	Flowchart of the program	95
5.4.4	Input data	96
5.4.5	Material parameters and kinetic analysis	96
5.5	Results	98
5.6	Discussion	103
5.6.1	Diffusional creep	104
5.6.2	Dislocation creep	105
5.6.3	Effect of strip thickness and line speed on deformation mechanism	106
5.6.4	Combining the heat transfer model with deformation mechanism	106
5.7	Conclusions	110
5.8	References	112
Chapter 6	Novel system to simulate continuous flattening anneal Construction and Calibration	114
6.1	Introduction	115
6.2	CASIM2 – Review and Drawbacks	115
6.3	LAFFAS – Design and construction	117
6.4	Sample dimensions	118
6.5	Tension setup	119
6.6	Strain uniformity test	120
6.7	Load cell and indicator – Calibration	122
6.8	Experiment atmosphere	123
6.9	Heating and temperature measurement	124
6.9.1	Power source and input current calculation	125
6.9.2	Electrode design for supplying power	126
6.9.3	Temperature measurement – Infrared thermocouple calibration	127

6.9.3	Control circuit	130
6.10	Summary	130
6.11	References	132
Chapter 7	Experiments in LAFFAS and Magnetism-Microstructure correlation	133
7.1	Introduction	134
7.2	Purpose of the LAFFAS simulator experiments	134
7.3	Experimental procedure	135
7.3.1	Sample preparation for annealing	135
7.3.2	Annealing in LAFFAS	136
7.3.3	Measurement of elongation	137
7.3.4	Calculation of dislocation density	138
7.4	Design of experiments	140
7.5	Material data	140
7.6	Results	141
7.6.1	Chemical testing	141
7.6.2	Effect of increase in stress on dislocation structures at 850°C	142
7.6.3	Load-elongation study for CGO+	145
7.6.4	Effect of stress relief anneal on specific total loss above threshold dislocation density	150
7.7	Discussion	151
7.7.1	Effect of applied stress on dislocation density and power losses at 850°C in CGO+	151
7.7.2	Load – Temperature – Elongation in CGO+	154
7.7.3	Effect of varying temperature and stress on power loss	154
7.7.4	Comparison of B-H characteristics	155
7.7.5	Relationship between the size of pinning sites and pinning effect	157
7.8	Conclusions	158
7.9	References	160
Chapter 8	Factors affecting polygonization of dislocations and their effects on magnetic properties of Fe-3.25% Si steel	161
8.1	Introduction	162
8.2	Polygonization – mechanism	162
8.3	Driving forces for Polygonization	165
8.4	Literature review on polygonization	167
8.4.1	Introduction to polygonization	167
8.4.2	Polygonization in Fe-Si single crystals	168
8.4.3	Effect of microstructure and texture on magnetic properties of Fe-Si steel	168
8.5	Experimental methods to study polygonized dislocations and its effects	170
8.6	Results	175
8.6.1	Effect of temperature on polygonization in CGO	175
8.6.2	Effect of temperature on polygonization in HiB	175
8.6.3	Effect of soaking time on degree of polygonization	176
8.6.4	Dependence of polygonization on relative orientation of grains to direction of curvature	178

8.6.5	Effect of degree of polygonization on magnetic domain structures	179
8.6.6	Effect of polygonized line spacing on magnetic domain width	181
8.6.7	Effect of degree of polygonization on localized power losses	183
8.6.8	Effect of polygonized dislocation on power losses in CGO	188
8.6.9	Effect of polygonized dislocation on power losses in HiB	193
8.6.10	Comparison of domain pinning effect in CGO and HiB	197
8.7	Discussion	198
8.7.1	Phase change and possibility of grain growth after heat treatment	198
8.7.2	Effect of temperature on polygonization	199
8.7.3	Effect of soaking time at heat treatment temperature	200
8.7.4	Polygonization dependence on orientation	202
8.7.5	Effect of polygonization on domain structure	204
8.7.6	Effect of polygonized dislocations on localized power losses	204
8.7.7	Effect of polygonization on specific total loss	205
8.8	Conclusions	207
8.9	References	210
Chapter 9	Conclusions and future work	213
9.1	Conclusions	214
9.2	Future work	216
	Appendix	
A5.1	'C' - Computer program to calculate the predominant deformation mechanism	218
A5.2	Calculation of stress on the strip from thickness and line speed	234
A8.1	Method used in separation of loss components from specific total loss	239

Glossary of terms

a_c - area of the dislocation core

B - Magnetic flux density

b - Burger's vector of the dislocation

CASIM2 - Continuous annealing simulator 2

CGO - Conventional grain oriented electrical steel

CGO+ - Conventional grain oriented electrical steel +

COMSOL - FEM simulation software package

C_p - Specific heat capacity of the material

d - grain size

D_b - boundary diffusion coefficient

D_{eff} - effective diffusion coefficient

D_v - the lattice diffusion coefficient

D_c - core diffusion coefficient

emf - electro motive force

E - Elongation

E_D - Magnetostatic energy

E_k - Magnetocrystalline anisotropy energy

E_λ - Magnetoelastic energy

E_w - Domain boundary energy

E_H - External applied field

GOES - Grain oriented electrical steel

$G_{m,u}$ - Surface irradiation from the domain on the upper side

$G_{ext,u}$ - Surface irradiation from the other domains to the current domain on the upper side

$G_{m,d}$ - Surface irradiation from the domain on the down side

$G_{ext,d}$ - Surface irradiation from the other domains to the current domain on the lower side

G_u - Upside surface irradiation

G_d - Lowerside surface irradiation

HiB - High permeability grain oriented electrical steel

HTCA - High temperature coil anneal

H - Magnetization

h - Convective heat transfer co-efficient

J_u – Surface radiosity at the upper side
 J_d – Surface radiosity at the down side
 $K1, K2$ – Anisotropy constants
 K – Thermal conductivity of material
LAFFAS – Lab Annealing Furnace for Flattening Anneal Simulation
 L_f - final gauge length after annealing
 L_i - initial gauge length before annealing
 n – Stress exponent
 P – Specific total loss
 P_H – Hysteresis loss
 P_e – Eddy current loss
 P_a – Anomalous loss
 Q_{in} - Heat input by fuels into the radiant tubes
 Q_{Load} – Heat input to the steel strip
 Q_w – Heat loss through the walls
 Q_{gas} – Heat absorbed by the furnace gases
 Q_{wrt} – Heat absorbed by walls and the radiant tubes
 Q_{anam} – Heat lost at the ends of the furnace
 Q_{wg} – Heat loss through exit flue gases
 Q – Activation energy
 T – Temperature
 t – Time
 T_{ext} – Furnace atmosphere temperature
 α – Thermal expansion co-efficient
 σ – Stefan Boltzmann constant
 μ - Dynamic viscosity
 ε – Emissivity
 δ - thickness of the grain boundary
 ρ – Density of the material
 ε_u – Emissivity of the surface in upper side
 ε_d - Emissivity of the surface in the down side
 τ – Shear stress
 Ω - atomic volume

Chapter 1

Introduction

1.1 Introduction and overview of the project

As the energy requirements keep increasing with technological advancements, there is an increasing need to reduce power losses during transmission. With the environmentally sustainable engineering goals becoming stricter, it calls for a highly efficient power transmission. The efficiency of power transmission depends on the core material of the transformer. The core material used in transformers is required to have high magnetic permeability and low power losses. Power losses are affected by a variety of factors like the chemical composition, grain size, foreign inclusions, precipitates and lattice defects [1]. The focus of this work is to understand the effect of lattice defects (dislocations) on the magnetic properties of grain oriented electrical steel (GOES). These lattice defects could be the result of either the production process or post-processing of the finished material into transformer cores. The emphasis of this work is on the lattice defects created during the production process of GOES. To understand the effect of these lattice defects on magnetic properties of the steel, it is essential to understand the formation of lattice defects in the material during the production process of GOES.

1.2 Overview of the material

Grain oriented electrical steels (GOES) with a composition of Fe – 3.25% Si with ultra-low carbon (<0.001%) is the most widely used material in the manufacture of power transformer cores owing to its high permeability and low power losses [1]. The name ‘grain oriented’ denotes the special {110}<100> texture also known as Goss orientation[2] imparted to GOES along the rolling direction resulting in the easy magnetization direction <100> in the direction of external applied field in the transformer. The two variants of the GOES are the conventional grain oriented electrical steel (CGO) and high permeability grain oriented electrical steel (HiB). The difference between CGO and HiB is the grain size and

average degree of mis-orientation allowed away from the Goss texture. In the case of CGO, the typical average mis-orientation is 7° whereas for HGO it is 3° . The grain size of CGO is approximately $3\pm 1\mu\text{m}$ whereas in HiB it is $10\pm 3\mu\text{m}$. High permeability of GOES is highly dependent on the sharpness of Goss texture [3]. A third variety of GOES is called CGO+ which has an orientation tolerance of CGO material but the grain size of HiB with an increased manganese content of 0.2% to aid in the formation of Goss texture was introduced half way through this work due to changes in the product portfolio of Cogent Power Ltd.,

1.3 Source of lattice defects

Lattice defects in GOES have two possible sources

- Defects created during the high temperature deformation processes during the production of GOES
- Post-processing of the finished GOES during transformer construction

During the high temperature deformation processes in the production of GOES, dislocations are created and annihilated in the lattice of the material. The resulting dislocation density of the material is dependent on the process parameters - temperature, stress and strain rate of the deformation processes.

Finished GOES is slit and stress relief annealed before being assembled into transformers and hence undergo considerable degree of deformation during the transformer construction. The amount of strain in the material and stress relief annealing parameters determines the dislocation density in the material used in transformers.

In this work, the creation of defects during the production process and their effect on magnetic properties of the GOES was studied in detail. The continuous thermal

flattening anneal process is given emphasis because of the possibility of introduction of lattice defects in a well annealed material from high temperature coil anneal process. These processes are discussed in detail in chapter 3. The changes in dislocation structure and their effect on magnetic properties by post-processing finished GOES are also discussed in chapter 8.

1.4 Power loss components and effect of lattice defects on magnetic properties

Power loss in GOES comprises of three components - hysteresis, eddy currents and anomalous components [3]. The conditions and mechanisms to reduce these losses are different making it a challenge to optimize all the loss components to achieve a material with lower losses.

Hysteresis loss is reduced by improving the alignment of $\{110\} \langle 100 \rangle$ (Goss texture) grains in the material along the magnetization direction and by reducing the dislocation density of the material. The dislocation density of the material increases hysteresis loss by magnetic domain wall pinning [3].

Classical eddy current losses in the core of the transformer have a direct square relationship with the thickness of the core material [4]. Dislocation density does not affect the classical eddy current losses.

The anomalous loss component can be contributed by the factors listed below [7]

- Non-sinusoidal and localized variations in flux density due to domain walls
- Formation and annihilation of lancet domains
- Domain wall bowing through the depth of the magnetic material

Since magnetic domain structures are dependent on the strain in the lattice of the material, lattice defects affect the anomalous loss component [6]. The detailed mechanism of anomalous loss reduction is described in section 2.8.

The combination of hysteresis, eddy currents and anomalous losses constitute the overall power loss of the material and an ideal transformer core material should have as low power loss as possible at operating flux densities of 1.5-1.7T and 50Hz or 60Hz.

1.5 Aim of this investigation

The major objective of this investigation is to understand the formation of dislocations during the final flattening anneal in the production of GOES and its effect on the magnetic properties. The list of objectives for this work are given below

- Develop a finite element model to study the temperature distribution of the strip through the furnace
- Develop a deformation mechanism map for GOES to understand the deformation behaviour in the process
- Design and build an experimental system to simulate the flattening anneal
- Dislocation and magnetic study correlations of the simulated samples
- Study the effect of dislocation rearrangements on the magnetic domains and power losses of GOES
- Understand the effect of thermal flattening anneal system on the final magnetic properties of GOES to assist Cogent Power Ltd.,

1.6 Research methodology

A finite element model of the temperature distribution in the flattening anneal furnace was developed using COMSOL multiphysics commercial software package. The

model was divided into two parts to reduce complexity and computational time by modelling the temperature distribution in the radiant tubes and the heat transfer to the steel strip separately.

The temperature data obtained from the model and stress data from the furnace was used in the modelling of the deformation mechanism map. A computer code was developed to understand the deformation mechanism prevailing in the flattening anneal process. The deformation mechanism map provided a combination of stress-temperature-strain rate zones for different deformation mechanisms and the process data was plotted into them to understand the mechanism.

A lab simulator was designed and built to validate the models and to understand the dislocation structures in the sample at different flattening anneal conditions. The system was capable of applying stresses of up to 15MPa at 850°C. AC power loss and DC magnetization measurements were made to correlate between dislocation structures created and magnetic properties.

The effect of rearrangement of dislocations by polygonization through bending and annealing the samples was investigated. The effect of heat treatment temperature, soaking time and orientation of the grains on this rearrangement of dislocations was studied. Changes in magnetic domain structures and power losses at various frequencies from 10-1000 Hz were studied for magnetic and microstructural correlation.

1.7 References

1. P Beckley, *Electrical Steels - a handbook for producers and users*, European Electrical Steels Publishers, Newport, 2000.
2. N P Goss, Trans Am Soc Metal, 1935; 23:511.
3. D Jiles, *Introduction to Magnetism and Magnetic materials*, Chapman and Hall publishers, London, 1998.
4. Z Xia, Y Kang, Q Wang, *Developments in the production of grain-oriented electrical steel*, J Mag Magn Mater, 2008; 320:3229.
5. S D Washko, T H Shen, W G Morris, *The effects of forsterite film on total loss of grain-oriented 3% silicon iron*, J. Appl. Phys., 1982; 53:8296.
6. J W Shilling, G L Houze, *Magnetic properties and domain structure in grain oriented 3% Si-Fe*, IEEE Trans. Magn., 1974; 10:195.
7. F J G Landgraf, M Emura, J C Teixeira, M F deCampos, *Effect of grain size, deformation, aging and anisotropy on hysteresis loss of electrical steels*, J Mag Magn Mater, 2000; 215-216:97.

Chapter 2

Ferromagnetism and Domain theory

2.1 Ferromagnetism and Domain theory

In the case of Fe and other common ferromagnetic transition metals, electrons in the 3d sub shells are unpaired and hence contribute to the resultant magnetic moment. All the other inner sub shells have paired electrons and their spins cancel each other [1]. This gives rise to the phenomenon of ferromagnetism.

Ferromagnetism is the property of materials with the magnetic spins of their electrons aligned parallel to each other. Electrons orbiting an atom have two components of energy associated with them.

1. Orbital momentum arising from the movement of the electrons around the atom
2. Quantum mechanical spin associated with the electron

The orbital momentum is negligible while the quantum mechanical spins of the electrons without pairs in the sub-orbitals can add up to form a substantial resultant magnetic moment.

2.2 Magnetic domains

A region in a magnetic material in which all the individual magnetic moments are aligned in the same direction and that has a uniform net magnetization is a magnetic domain [2]. The net magnetization of the material can be calculated by the vector sum of all the individual domain magnetizations [3].

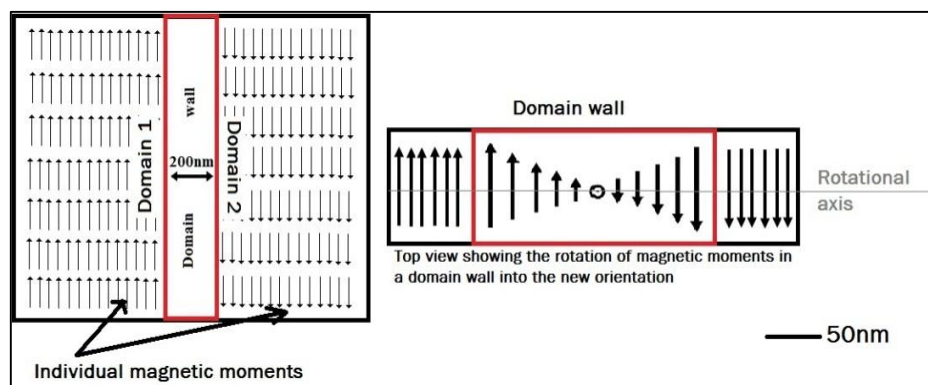


Figure 2.1 Typical magnetic domains and domain wall between two domains

The two types of domain walls are Bloch and Neel walls. These classifications of domain walls arise from the angular transition between areas with two different magnetic moments. In Bloch walls, the angular transition between individual magnetic moments take place in the plane of the moments. In Neel walls, the angular transition takes place outside the plane of the moments [2]. The domains walls of interest to this study are 180° and 90° Bloch domain walls. The 180° domain walls are the walls between parallel magnetic domains, where the magnetic moments in the domain wall have to undergo an 180° angular transition from one domain to align with the adjacent domain. The 90° walls are created to form closure domains at the end of parallel domains. Figure 2.2 below describes 180° and 90° domain walls [4].

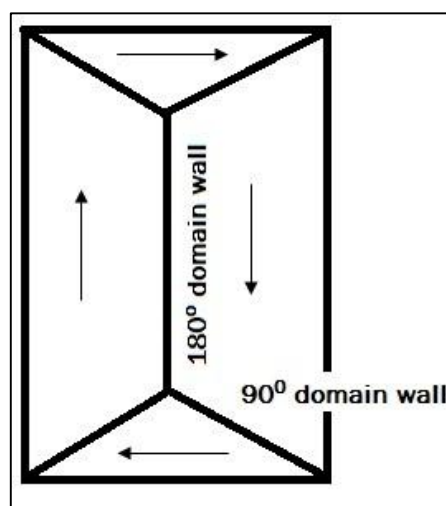


Figure 2.2 Illustration of 180° and 90° domain walls in an isotropic material

Magnetization of a magnetic material takes place by one of the following two mechanisms

- The movement of domain walls between the two domains where the magnetization or a change in orientation of the individual magnetic moments is localized near the mobile domain wall.

- All the individual magnetic moments in domains align themselves to an applied field.

The domain structure in GOES can be understood by considering the magnitude of the terms in the expression of its total energy. The dominant terms of energy in GOES are

- Magnetostatic energy E_D
- Magnetocrystalline anisotropy energy E_k
- Magnetoelastic energy E_λ
- Domain boundary energy E_w
- External applied field E_H

2.3 Magnetostatic energy

Magnetostatic energy is the collection of all the ‘free magnetic pole’ energies in a material. Consider a material with a single large magnetic domain as shown in figure 2.3, the ends of the material have an accumulation of free magnetic poles. The field caused by these poles results in an increase in the potential energy of the system. This can be reduced by forming a multi-domain structure as shown in Figure 2.3(e).

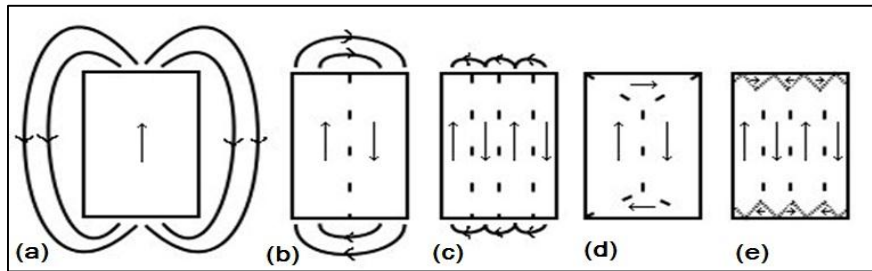


Figure 2.3 Different possible combinations of magnetic domains. Only configuration in (e) exists spontaneously because of the minimization of magneto-static energy [4]

Magnetostatic energy is illustrated in the following equation

$$E_D = \frac{1}{2} N_D \Delta I_n^2 \quad (2.1)$$

Where E_D is the magnetostatic energy, N_D is the demagnetizing coefficient and ΔI_n^2 is the difference in perpendicular component of magnetization between both ends of the

sample. The demagnetizing factor for a thin strip sample in the plane of magnetization can be close to zero and very high (≈ 1) perpendicular to the plane of magnetization.

From Equation 2.1, as the number of domains increases the magnetostatic energy progressively decreases along with the magnetocrystalline energy. The reduction in magnetostatic energy is due to the formation of closure domains thus reducing the large demagnetizing field. A reduction in the magnetocrystalline energy is due to the reduction in the area of closure domains and a subsequent reduction in magnetic moments aligned in a hard magnetization direction. These reductions in domain widths increase the domain boundary energy because of the formation of a large number of domain walls.

2.4 Magnetocrystalline anisotropy energy

Magnetocrystalline anisotropy arises from the different energies associated with different crystallographic directions. The ease of the material to be magnetized in any particular direction is determined by the anisotropy constant K [4]. In the GOES lattice, $\langle 100 \rangle$ is the easy magnetization direction with $\langle 110 \rangle$ and $\langle 111 \rangle$ being progressively harder to magnetize. The difference between the energy spent in magnetizing along the easy and hard axes denotes the Magnetocrystalline anisotropy energy. Magnetocrystalline anisotropy energy in iron is illustrated in the figure 2.4 below.

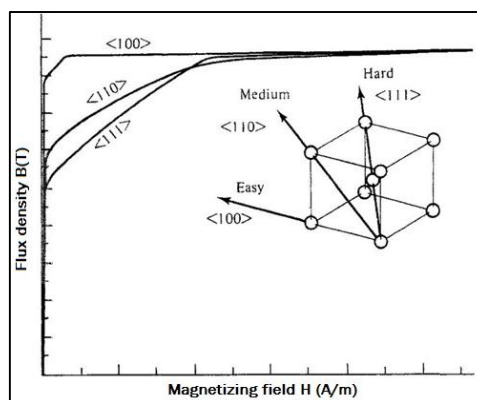


Figure 2.4 Schematic representation of Magnetocrystalline anisotropy energy

adopted from Cullity [5]

The expression for E_k in cubic materials is given by

$$E_k = K_1(\alpha_1^2\alpha_2^2 + \alpha_2^2\alpha_3^2 + \alpha_3^2\alpha_1^2) + K_2(\alpha_1^2\alpha_2^2\alpha_3^2) \quad (2.2)$$

where the $\alpha_1, \alpha_2, \alpha_3$ are the direction cosines of the magnetization within a domain with respect to the cube axes, and K_1 and K_2 are the first and second order anisotropy constants.

Magnetocrystalline energy can be minimized by magnetizing along the easy magnetization direction and hence Goss texture is preferred in grain oriented electrical steel. Minimization of magnetocrystalline energy is accomplished by minimising the magnetic domain width and area of closure domains as explained in section 2.3. As the area of closure domains decrease, the volume of magnetic moments aligned away from the easy magnetization direction decreases thereby minimizing magnetocrystalline anisotropy energy.

2.5 Domain wall energy

Domain boundary or domain wall energy can be defined as the exchange energy between two anti-parallel magnetic spins and the change in magnetocrystalline energy because of the alignment of magnetic moment along hard magnetization directions.

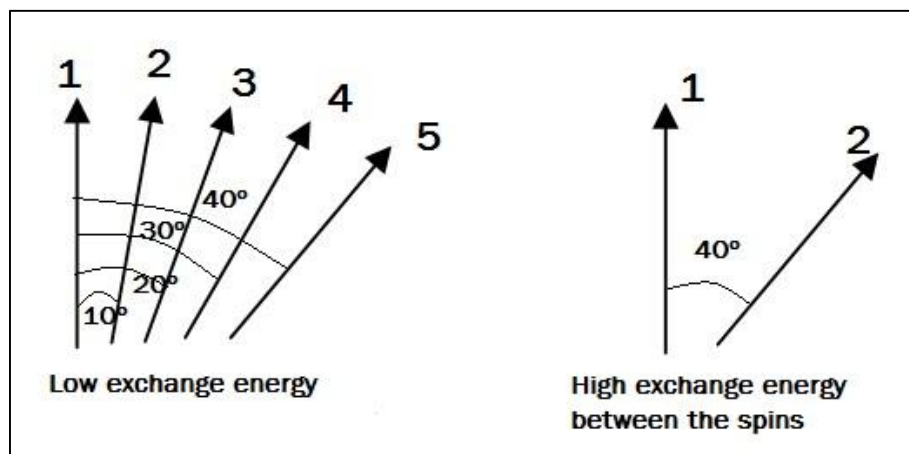


Figure 2.5 Change in exchange energy with the width of magnetic domains – Larger domain wall width leads to low exchange energy

Individual magnetic spin alignment and their effect on overall exchange energy of the system is explained in Figure 2.5. Individual magnetic moments are numbered from 1-5 and the effect of gradual and rapid change in orientation of the individual magnetic moments on the exchange energy is explained.

Alignment of magnetic spins determines the exchange energy between individual moments [4]. The exchange energy between two spins i and j is shown in the equation 2.3 below

$$E_{ex} = -2J\vec{S}_i \cdot \vec{S}_j \quad (2.3)$$

where J is the integration constant and S_i and S_j are the spins. For Iron, J is positive and hence S_i and S_j have to be parallel to minimize exchange energy. Any deviation from being parallel to the adjacent spin increases the exchange energy. Combining figure 2.5 and equation 2.3, a small increase in deviation results in a smaller increase in the exchange energy compared to a rapid change in direction of adjacent spins.

The change in individual orientation of moments is gradual in a wider domain wall whereas it is rapid in a narrow domain wall. Figure 2.5 shows as the domain wall gets thicker, the change in the alignment of magnetic spins is gradual resulting in low exchange energy. However, the presence of a large number of spins away from easy magnetization direction increases the magnetocrystalline energy. A smaller domain thickness corresponds to rapid change in the alignment of spins and hence has higher exchange energy [4]. The magnetocrystalline component in this case is lower because of the presence of lesser number of spins in the hard magnetization direction. GOES has a high anisotropy constant (K) which facilitates the formation of narrow domains without a large increase in exchange energy.

2.6 Magnetoelastic energy

The forces between the magnetic moments explained in the previous sections also result in a force field between the atoms and an elastic strain in the lattice. Magnetoelastic energy decreases linearly with an increase in lattice strain.

For cubic materials, magnetoelastic energy is given by the following equation

$$E_{\lambda} = -B_1 \left[e_{11} \left(\alpha_1^2 - \frac{1}{3} \right) + e_{22} \left(\alpha_2^2 - \frac{1}{3} \right) + e_{33} \left(\alpha_3^2 - \frac{1}{3} \right) \right] - B_2 [e_{12} \alpha_1 \alpha_2 + e_{23} \alpha_2 \alpha_3 + e_{31} \alpha_3 \alpha_1] \quad (2.4)$$

where α_x and e_{xy} are the direction cosines of the magnetization and the lattice strains, with respect to the cube axes, and B_1 and B_2 are constants [3].

But the increase in the force applied by the moments on the lattice leads to an increased strain energy of the lattice. The strain energy of a lattice is illustrated in the following equation

$$E_{el} = \frac{1}{2} C_{11} (e_{11}^2 + e_{22}^2 + e_{33}^2) + \frac{1}{2} C_{44} (e_{12}^2 + e_{23}^2 + e_{31}^2) + \frac{1}{2} C_{12} (e_{22} e_{33} + e_{22} e_{11} + e_{33} e_{11}) \quad (2.5)$$

where C_{11} , C_{44} , and C_{12} are the elastic constants [3].

Minimization of both the magnetoelastic energy and elastic strain energy of the lattice results in an equilibrium lattice strain. This net magnetoelastic energy without any external magnetization is the 'free' magnetostriction energy [3].

2.7 External applied field

An external applied field increases the overall energy of a ferromagnetic system. Widths of the magnetic domains aligned parallel to the external field grow at the expense of oppositely aligned domains. The magnetostatic energy component of the system generates a larger demagnetizing force for the increase in energy of the system. This phenomenon happens by the movement of domain walls. Magnetization by domain wall movement happens in the low induction region of the B-H curve shown in Figure 2.6.

In the high induction region of the B-H curve, the mechanism of magnetization by an external field is by the rotation of magnetic moments away from easy magnetization direction to the direction of the applied field. This mechanism of magnetic moment rotation takes place only at higher fields due to the need to overcome the increase in magnetocrystalline energy component.

Fe-3% Si alloys or GOES have high magnetocrystalline anisotropy constant (K) and thus the magnetization process is mainly by domain wall movement. When GOES is magnetized, only the volumes of domains change with respect to their alignment with the applied field whereas the alignment of magnetic moments inside a domain is unaltered [3].

A typical magnetization curve is shown in the Figure 2.6 below. The domain wall motion during magnetization is irreversible. This phenomenon is called hysteresis and the area enclosed by the curve represents the energy loss.

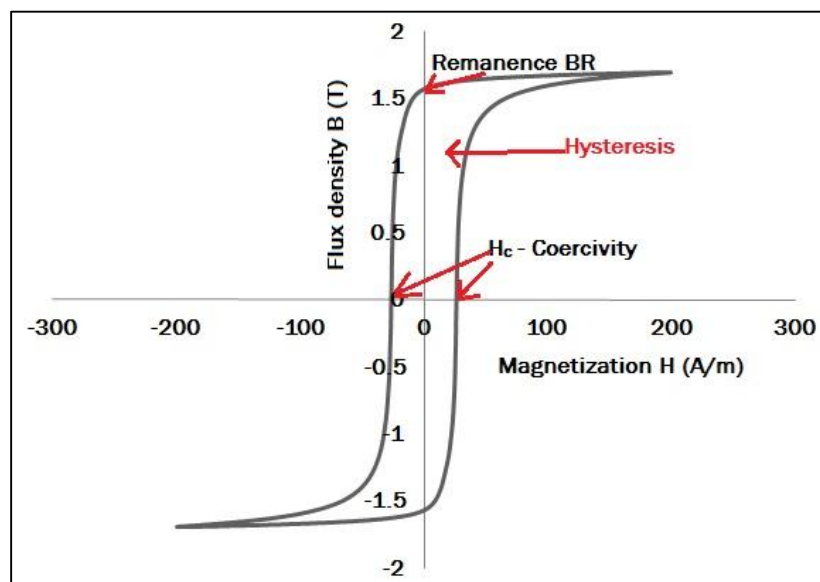


Figure 2.6 A typical hysteresis curve

The magnetization process is irreversible due to several factors that pin the domain wall movement. In GOES, inclusions, precipitates and lattice defects like dislocations acts as pinning sites for domain wall motion. Dislocations increase the local strain energy of

the lattice thus increasing the overall energy of the magnetic material. Various studies were performed on the effect of dislocations on magnetic properties of GOES and are reviewed in the following chapter. Dislocations reduce the magnetic permeability and increase the coercivity of the ferromagnetic material by impeding domain wall motion as shown in Figure 2.7.

Dislocation density, precipitates, inclusions and grain boundaries in the material affects hysteresis losses by pinning magnetic domain walls during magnetization by domain wall motion. The effect of dislocations and other pinning sites are illustrated in a simplified form in Figure 2.7.

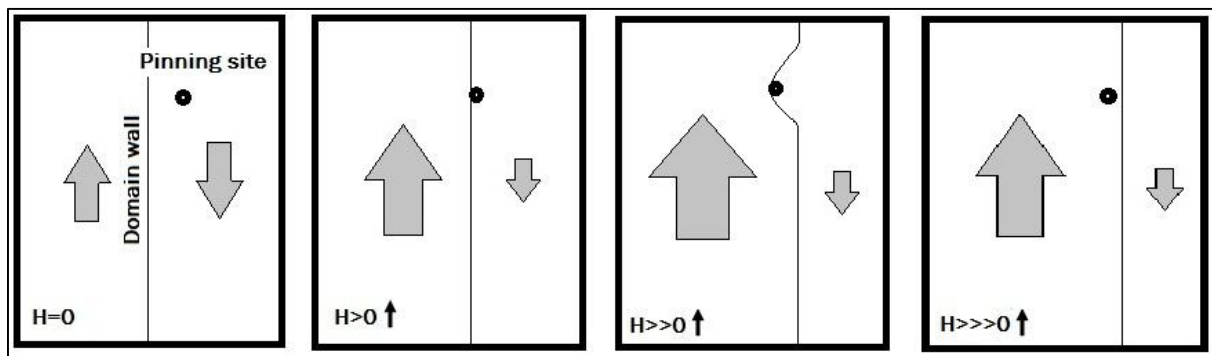


Figure 2.7 Effect of pinning sites on domain wall motion during magnetization

2.8 Losses in magnetic materials

The power losses in a magnetic material can be classified into three components hysteresis, eddy currents and anomalous components as explained in section 1.4.

Hysteresis loss occurs due to the irreversible nature of the magnetization process of a magnetic material when an external field is applied. This phenomenon is shown in figure 2.6 and the energy loss associated is known as hysteresis loss.

When a magnetic material is placed in an alternating magnetic field, eddy currents flow in the direction opposite to the electro motive force (emf) induced in the material due

to the magnetic field. Eddy current loss per excitation cycle and unit mass under sinusoidal excitation in a homogenous material can be calculated by the equation 2.6 [6].

$$\frac{P_e}{f} = \frac{\sigma \pi^2 b^2}{6\rho} f B_p^2 \quad (2.6)$$

Where P_e - Eddy Current, f – Frequency, B_p – Peak flux density, ρ – Density of the material

Experimental measurement of losses shows a discrepancy between the sum of hysteresis and classical eddy current loss when compared to the specific total loss in a material. This difference is due to the anomalous losses. The assumptions described in the calculation of eddy current losses in equation 2.6 are not valid for real materials with inhomogeneities in the material and non-sinusoidal local flux variations due to magnetic domains. Reduction of anomalous losses is important at the operating frequency of transformers (50Hz) as they account to up to 50% of the total losses at 50Hz.

The two mechanisms involved in the reduction of anomalous losses by domain refinement are explained below [7,8].

1. The increase in the number of domain walls when the domain widths are reduced results in reduced domain wall velocity for the same magnetization response. The reduction in domain wall velocity results in a lower anomalous loss component. This mechanism is illustrated in figure 2.8. At any given frequency of magnetization, the velocity of domain walls when the domains are of larger width is higher compared to the velocity of domain walls when the domains are refined as shown in figure 2.8 (b).

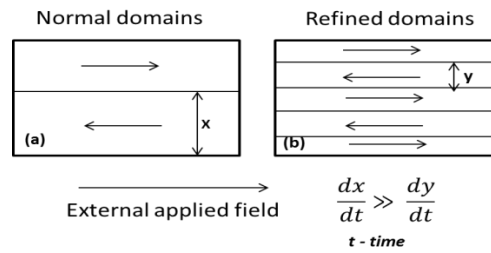


Figure 2.8 Distance of domain wall motion in normal and refined domain structures

2. The distance travelled by the domain walls in a domain refined structure is lower and hence the probability of domain pinning by inclusions or lattice defects is reduced as shown in the figure 2.9.

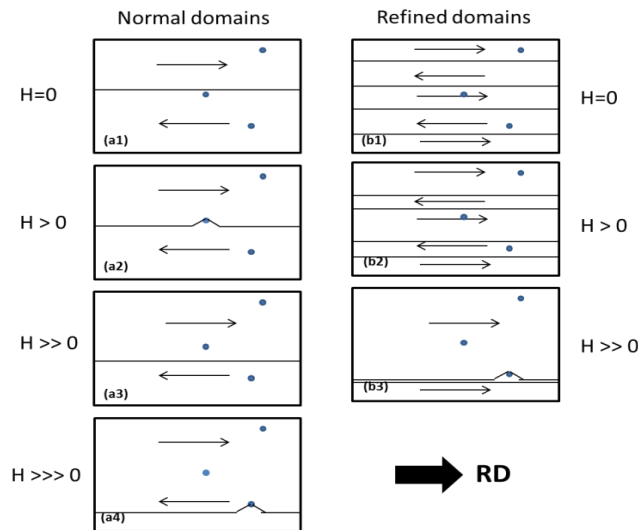


Figure 2.9 Effect on domain refinement on probability of domain pinning during magnetization [8]

2.9 Dislocations and their effects on magnetic properties

During plastic deformation of any polycrystalline material, dislocations are mobile and the mechanism of movement depends on the deformation mechanism involved in the stress, temperature and strain rate conditions involved in the process. In the continuous flattening anneal process the strip undergoes a small plastic strain of less than 0.01. The mechanisms of dislocation movement has been studied extensively [9-13] but the mechanism of deformation in flattening anneal line is not well understood. The effects of

these dislocations on magnetic domains and power losses need to be understood to improve the process.

Hysteresis loss is affected by metallurgical factors in GOES namely,

- Dislocation density, ξ_d
- Grain size, d
- Inclusions and precipitates

A decrease in grain size increases the coercivity H_c that denotes the strength of pinning of domain walls. As the dislocation density increases, H_c increases due to the same reason of domain wall pinning during magnetization [9]. Sablik et.al [9], reported that the increasing dislocation density decreases remanent flux density. The permeability of the material is also lowered by increasing dislocation density.

Coercivity H_c has a linear relationship with both the parameters above. The hysteresis loss (P_H) is related to grain size by

$$P_H = A + Bd \quad (2.7)$$

where A and B are constants and are both directly proportional to ξ_d [10-14].

Sablik et al [15], studied the effect of plastic tensile deformation on hysteresis loops with the same maximum flux density. They found linear relationships between Coercivity H_c , Hysteresis loss P_H and residual plastic strain ϵ_r . As the residual tensile strain increased, coercivity increased and the slope of the hysteresis curve decreased denoting a drop in permeability.

Caroni et al [16], reported a layered magnetic domain structure on GOES with sets of grains both with and without Goss texture after 2% plastic deformation. During deformation, dislocations are arranged in the easy slip systems of BCC Fe-3% Si system - $\{110\}$ and $\{112\}$ in $\langle 111 \rangle$ direction. To minimize strain energy, the dislocations arrange themselves to a layered structure with alternative tension and compression fields in the

lattice. This results in an increase in the magnetoelastic term of energy of the system resulting in layered domain structures. The presence of such structures in both grains with and without Goss structure shows that the domains are a resultant of the alternating stress field by dislocations and not by the actual dislocations themselves.

Sokolov et al [17], reported that the underlying dislocation structure from the manufacturing process is the reason for inhomogeneity in magnetic properties of finished GOES between coils of the same material. They also reported a creep phenomenon in high temperature coil anneals and subsequent flattening anneal. This creates a cell structure of dislocations that leads to a large increase in losses. But this cell structure is different between various locations in the coil depending on the stresses and hence the inhomogeneity in the magnetic properties. They also suggested that individual isolated dislocations do not affect the magnetization process but a higher dislocation density (dislocations grouped together) can reduce the permeability by affecting the magnetization process. They also pointed out that such high dislocation density usually occurs near grain boundaries, foreign phase and inclusion boundaries. There are also reports of individual polygonized boundaries in the middle of the grains that do not affect the magnetization process.

In the current work, the influence of domain width and the effect of lattice defects on domain widths are studied. The variation of domain widths with different dislocation configurations and their effect on anomalous loss of GOES is studied. To understand the effect of dislocations created during the production process on anomalous losses, the mechanism of dislocation rearrangements and its effect on anomalous losses have been studied.

2.10 References

1. F Brailsford, Physical principles of magnetism, Van Nostrand publishers, 1966.
2. A Hubert, R Schafer, Magnetic Domains – Analysis of magnetic microstructures, Springer publications, 1998; 1:3.
3. J W Shilling, G L Houze Jr., *Magnetic properties and domain structure in grain oriented 3% Si-Fe*, IEEE Trans. Magn., 1974; 10:195.
4. D Jiles, Introduction to magnetism and magnetic materials, Chapman and Hall publications, 1991.
5. B D Cullity, C D Abraham, Introduction to magnetic materials, 2 ed., John Wiley and sons, 2008, 199.
6. J G Zhu, S Y R Hui, V S Ramsden, *Discrete modelling of magnetic cores including hysteresis eddy current and anomalous losses*, IEE PROC, 140-4 (1993) 317.
7. J Evetts, *Concise encyclopaedia of magnetic and superconducting materials*, Pergamon press, (1992) 448.
8. J G Benford, *Separation of losses in oriented silicon steels from 0.13 to 0.34 mm thick*, IEEE Trans. Magn., 20-5 (1984) 1545.
9. M J Sablik, *Modeling the effect of grain size and dislocation density on hysteretic magnetic properties in steels*, J Appl Phys., 2001; 89:10.
10. M J Sablik, F J G Landgraf, *Modeling microstructural effects on hysteresis loops with the same maximum flux density*, IEEE Trans. Magn., 2003; 39:2528.
11. J F Bussiere, *On-line measurement of the microstructure and mechanical properties of steel*, Mater Eval., 1986; 44:560.
12. J Sternberk, E Kratochilova, A Gemperle, V Faja, V Walder, *Dependence of characteristics of hysteresis loops on dislocation density for low-alloy Cr-Mo steel*, Czech J Phys B, 1985; 35:1259.

13. C Appino, E Ferrara, F Fiorillo, I Suberbielle, J Degauque, C Lebourg, M Baricco, *Role of Si concentration on the magnetic and mechanical behavior of rapidly solidified Fe-Si laminations*, J Phys, 1998; 8:531.
14. G Ban, P E DiNunzio, S Cicale, T Belgrand, *Identification of microstructure effects in magnetic loss behavior of 3.2% SiFe N.O. electrical steels by means of statistical power: Loss model*, IEEE Trans Magn., 1998; 34:1174.
15. M J Sablik, T Yonamine, F J G Landgraf, *Modeling plastic deformation effects in steel on hysteresis loops with the same maximum flux density*, IEEE Trans. Magn., 2004; 40:5.
16. C A Caroni, E Manghi, N W Dereca, *Influence of dislocation on magnetic domains in plastically deformed 3 % Si-Fe*, IEEE Trans. Magn., 1973; 9:4.
17. B K Sokolov, Y N Dragoshanski, V S Matveeva, M B Tsyrlin, F V Mineev, R B Puzhevich, *Inhomogeneity of magnetic properties of an anisotropic electrical steel and specific features of dislocation structures*, Russ J Nondestruct+, 2004; 40:11.

Chapter 3

Literature review – Production and evolution of GOES

3.1 History of electrical steel production and improvements

The history of electrical steel started with the discovery of reduction in core loss of iron by addition of silicon by Hadfield in early 1900s and anisotropy in magnetic properties of steel was utilized by Honda and Kaya in 1926 [1]. The evolution of the production process of grain oriented electrical steel has proceeded through better Goss orientation, making a thinner gauge of material to reduce eddy current and development of novel surface coatings that help in domain refinement [2].

The development of grain oriented electrical steel started with the discovery of Goss texture that reduced the overall power loss by a great extent. The orientation of planes and directions in Goss grains is shown in Figure 3.1.

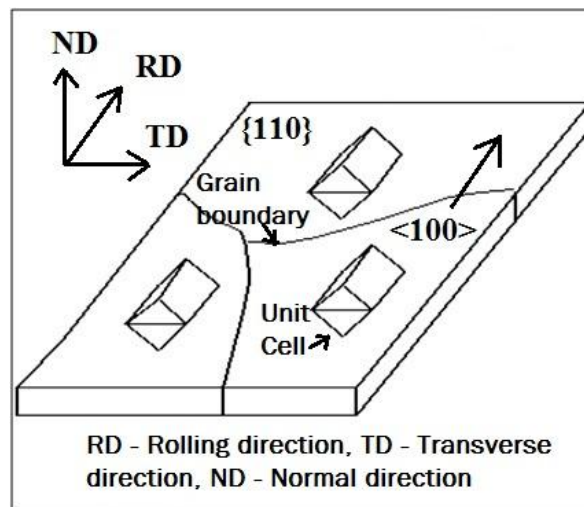


Figure 3.1 Orientation of $\{110\}$ planes and $\langle 100 \rangle$ direction in Goss grains

The hysteresis loss component was shown to be directly related to the relative orientation of the grains to Goss texture [2]. When grains were oriented with their $\{110\}$ $\langle 001 \rangle$ system along the magnetization direction, the hysteresis loss was at a minimum due to easy magnetization along the $\langle 001 \rangle$ direction. Deviation from Goss texture – $\{110\}$ $\langle 100 \rangle$ results in formation of 90° closure domains (Lancet domains) that are created and annihilated during magnetization increasing the hysteresis component of loss [2]. The

driving force for this creation and annihilation of 90° walls is the reduction in magnetostatic energy by forming a path for flux return when the grains are mis-oriented from the surface [2].

Eddy current losses are reduced by a reduction in strip thickness. The development of 0.23mm strip led to a decrease in about 10% of the overall losses compared to the material with same chemistry and 0.3mm thickness [2]. The increase in anomalous loss values were overcome by refining magnetic domain widths by external surface stress application techniques like grooving, laser scribing etc [3-5]. This reduction in domain widths led to a reduction of anomalous loss components by 10% at 50Hz and 1.5T [2].

The possibility of reduction in the anomalous component of losses led to the study of magnetic domain wall motion during the magnetization process. Ideally all the domain walls are 180° walls and move homogeneously during magnetization, but in reality the movement of domain walls is influenced by inclusions and lattice defects that act as pinning sites. Hence a reduction in the distance to which the domain wall moves results in lower change in the velocity of domain wall motion and thus lower losses. Periodic pinning sites or domain refinement structures can be introduced to reduce domain widths in GOES [6-9]. Systematic reduction in domain width by these periodic pinning sites is carried out by processes like grooving, laser irradiation etc [6-9], resulting in reduced anomalous component of losses [10-14]. The resulting domain width will be an optimization of magnetostatic and magnetic domain wall energy components [12].

To optimize hysteresis, eddy current and anomalous loss components it is essential to understand the production process of grain oriented electrical steel and the mechanisms that affect all these components. It is also important to understand the interaction between these mechanisms. The following section reviews the production process and understanding of the following advances in the production of electrical steel.

- Goss texture evolution and secondary recrystallization – to reduce hysteresis loss and improve permeability
- Application of a surface stress by coating for changes in domain structure – to reduce anomalous losses

3.2 Manufacturing process of GOES

The optimum manufacturing process of electrical steel should aim to reduce all the components of loss. The following section introduces the production process of traditional GOES [15] that includes the following steps

1. Continuous casting of Fe-3.25% Si-0.03% C-0.06% Mn slabs
2. Preheating to 1400°C and hot rolling down to 1.9 mm gauge
3. Annealing and pickling
4. Cold rolling – 2 stage reduction in thickness to 0.23-0.35mm
5. Decarburisation anneal
6. High temperature coil anneal – 1200°C – Secondary recrystallisation
7. Phosphate coating and thermal flattening anneal

These process steps are illustrated in the schematic shown in the Figure 3.2.

a) Alloy casting

Alloy of Fe-3.25% Si-0.03%C-0.06% Mn (0.2% Mn in case of CGO+) is continuous cast into slabs. Silicon is added in the melt to reduce the eddy current components of the losses by increasing the resistivity of the steel. The solid solution of Fe-Si system can have a maximum of 6.5% Si in iron. But the technical difficulties (brittleness of the strip) in rolling restrict the percentage of Si in this alloy to 3.25%.

Manganese content in the alloy reacts with sulphur to form MnS precipitate later in the process that inhibits the growth of primary grains and thus favouring the growth of Goss textured $\{110\} \langle 100 \rangle$ grains. The improvement in the sharpness of Goss texture directly aids in reduction of hysteresis loss and hence manganese is a vital alloying element in the manufacture of electrical steels.

(b) Preheating and hot rolling

The slabs are pre-heated to 1400°C to aid the solutionizing of MnS inhibitors before hot rolling. Hot rolling is performed to reduce the thickness of the steel to 1.9mm. It also helps in the dispersion of MnS inhibitors throughout the strip which will help during secondary recrystallisation. The strip is rapidly cooled to 600°C to retain MnS precipitates. The hot rolled coil is then side trimmed to prepare it for the next process stage of acid pickling and anneal.

(c) Annealing and pickling

The hot rolled coil is annealed at 900-950°C before the oxide layer is removed from the surface. In the pickling stage, the strip is acid cleaned by a mixture of sulphuric acid and hydrofluoric acid. At this stage the strip is ready for cold rolling reduction to its final thickness.

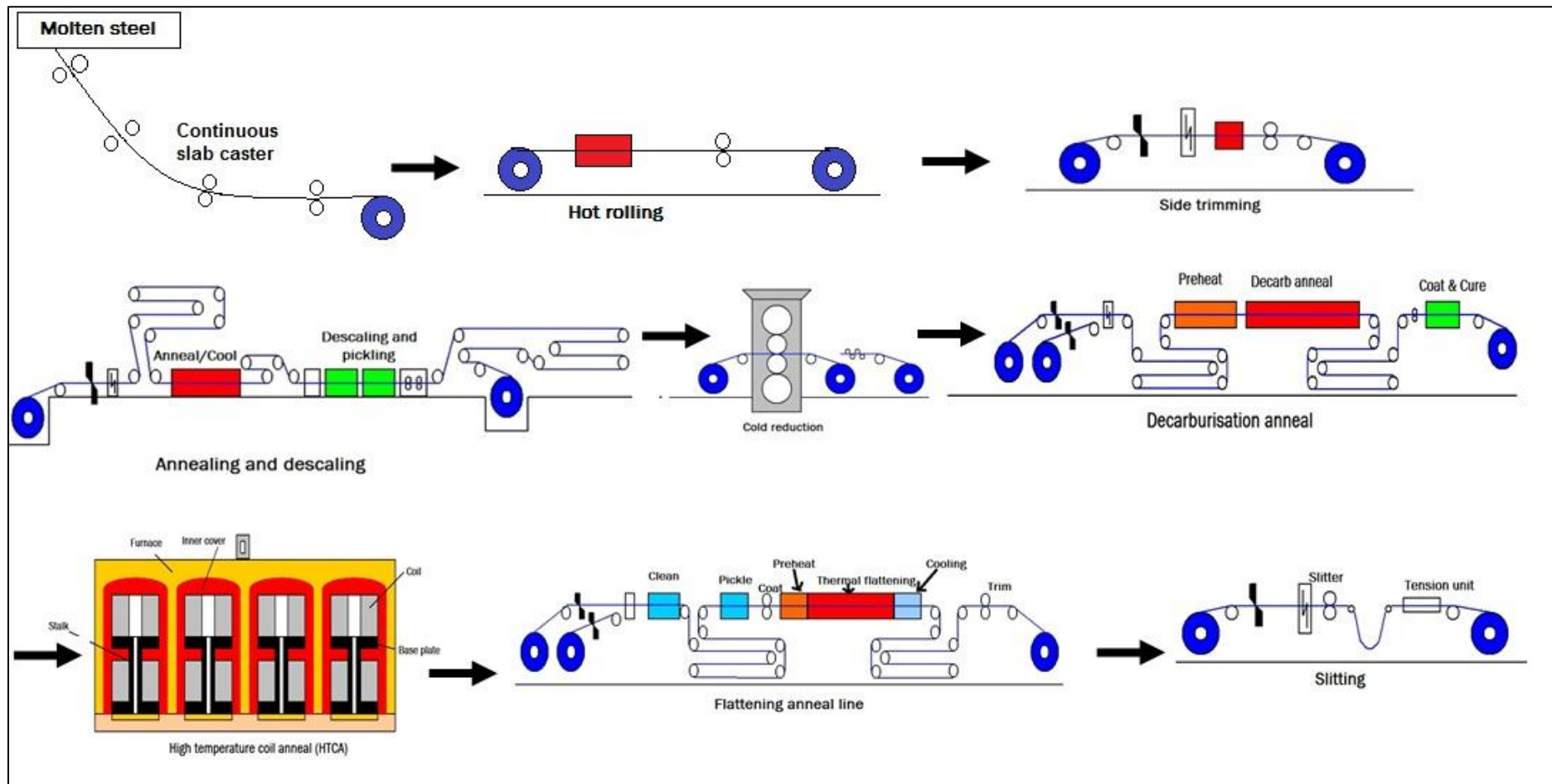


Figure 3.2 Production process of grain oriented electrical steel (Image courtesy : Mr.Keith Jenkins, Cogent Power Ltd., Reproduced with permission from Cogent Power Ltd.,)

(d) Cold rolling and reduction

The annealed and pickled strip is subject to two stages of cold rolling. In the first stage of cold rolling the strip was reduced to an intermediate thickness and in the second step, the strip is reduced to a thickness of 0.23-0.35mm dependent on the final gauge required. Between the two cold reduction steps the strip undergoes an intermediate recrystallization anneal where the dislocations created by plastic deformation during cold working are annealed and primary recrystallisation takes place. The second step of cold rolling increases the strain energy of the system again, which aids in the secondary recrystallisation process.

(e) Decarburisation anneal

The presence of carbon in the steel further than this step is detrimental for its magnetic properties by forming carbide inclusions. Thus in this step, the steel is annealed in a moist nitrogen-hydrogen atmosphere at 850°C. During this process, carbon in the steel combines with the moisture in the atmosphere to exit as carbon monoxide. An oxide layer is formed on the surface of the strip as described in Figure 3.3.

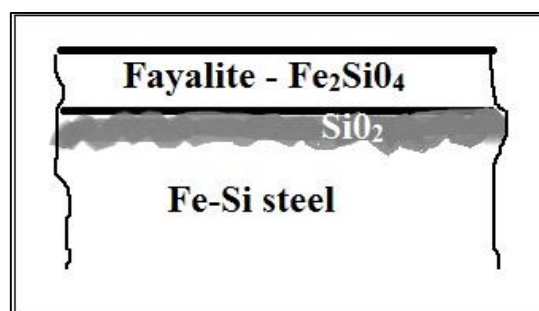


Figure 3.3 Schematic of the edge section along the rolling direction showing oxide layer formation and composition in decarburisation stage

At the end of the decarburisation process the texture components of electrical steel are favourable for preferential growth of Goss grains during secondary recrystallization. A

minor {110}<100> texture and a major {111}<112> texture at this stage is favourable since the Goss grains can undergo abnormal grain growth by consuming {111}<112> texture. At the end of decarburisation stage, MgO slurry is coated over the the steel strip. MgO facilitates the formation of a fosterite referred to as glass film at the end of high temperature coil anneal (HTCA) process. It also prevents the adjacent layers of the coil from sticking together during the HTCA process.

(f) High temperature coil anneal (HTCA)

The steel strip is annealed in coil form in a batch type box furnace as shown in the Figure 3.4 at high temperatures of up to 1200°C in an atmosphere of N₂ with 3% dry H₂ with water seals at the base.



Figure 3.4 Coils stacked in a HTCA furnace (The shell of the furnace is removed during loading and unloading) Image reproduced with permission from Cogent Power Ltd., Newport UK

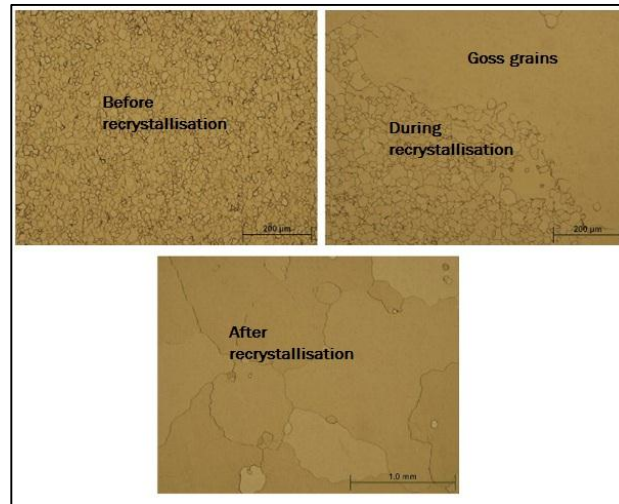


Figure 3.5 Evolution of Goss texture during secondary recrystallization [16]

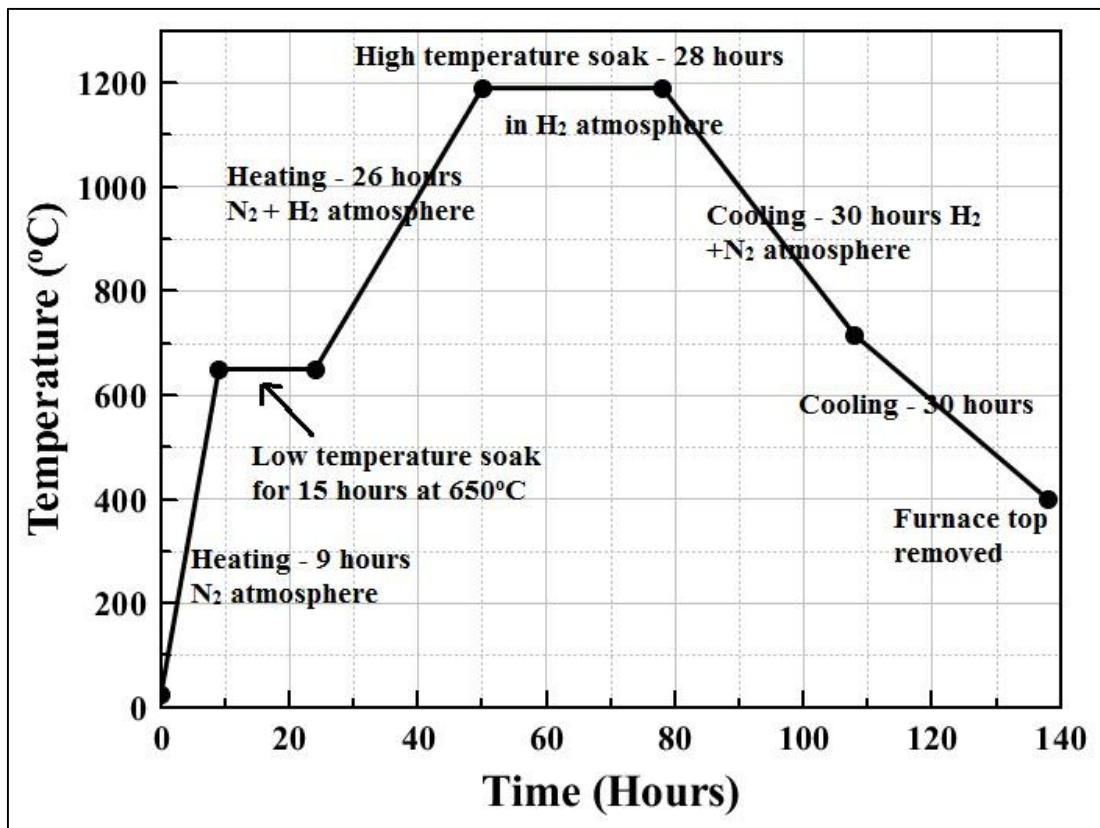


Figure 3.6 Annealing cycle used in HTCA

During HTCA, there is an abnormal growth of Goss grains preferentially over other texture which is illustrated in Figure 3.5. Several mechanisms were attributed to the abnormal grain growth which are discussed in the later sections in this chapter. Primary

grain growth is inhibited by MnS up to 900°C after which the inhibitor solutionizes to allow the secondary recrystallisation process and abnormal grain growth. A fosterite film ($2\text{MgO} \cdot \text{SiO}_2$) is also formed during this process. The fosterite film provides an insulating coating between laminations in a transformer reducing the eddy currents generated.

(g) Phosphate coating and thermal flattening anneal

Electrical steel strip with a fosterite film coating is cleaned to remove any excess MgO on the surface before a phosphate coating is applied on the surface. The purpose of the phosphate coating is to apply an elastic tensile stress on the surface of the steel that helps in magnetic domain refinement resulting in lower anomalous losses. The coating is applied and is cured by open flame heating at a pre-heating furnace up to 600°C.

The strip with cured phosphate coating on it is then moved to the continuous annealing main heating zone of the furnace where it is heated to 850°C by radiant tubes under furnace tension to remove strip distortions from the HTCA process. Four penetration rolls in the heating zones are used to adjust furnace tension and hence to achieve the purpose of distortion removal.

(h) Difference in manufacturing steps between CGO and HiB

The manufacture of HiB is distinct compared to the process described above for conventional grain oriented (CGO) electrical steel in the following ways

- One stage cold working process replaces the two stage cold working in CGO but the overall reduction is increased to about 87% from 60% in CGO. This means a much higher strain energy stored in the system and more driving force for secondary recrystallisation [2].

- Use of AlN inhibitor along with MnS for improved primary grain growth inhibition effect [2].

3.3 Evolution and advancements in the manufacturing process

3.3.1 Mechanisms of Goss texture evolution

The improvement in hysteresis loss component due to the Goss texture is evident from theories of ferromagnetism in chapter 2. Thus the evolution of Goss texture has to be understood before studying its effect on power loss. Several theories have been proposed to explain the Goss texture. The two major theories that try to explain abnormal grain growth were

- primary Goss grain boundaries were Coincidence Site Lattice (CSL) boundaries [17,18]
- primary Goss grains were surrounded by boundaries of high energy thereby increasing their mobility [19]

Shimizu and Harase suggested the CSL boundary mechanism [17]. In this study, the initial texture of the decarburized primary recrystallized steel did not possess large grain of $\{110\}<100>$ orientation. Their mechanism suggested that CSL boundaries [17] are more mobile than normal boundaries and this leads to abnormal grain growth. Several other works suggested the same and emphasised the role of CSL boundaries on abnormal grain growth [18-28].

Hayakawa and Szpunar [29] suggested a different model for the development of Goss texture. The model assumes that Goss grains were surrounded predominantly by high energy boundaries. These high-energy boundaries were associated with high coefficients of diffusion along grain boundaries. Precipitates coarsen along the high energy grain boundaries and increase their mobility. Thus during secondary recrystallisation these

highly mobile grain boundaries move faster than the surrounding grains leading to non-uniform grain growth of Goss grains. This theory was reinforced by several other researchers who suggested the high energy associated with primary Goss grain boundaries leads to abnormal grain growth [29-35].

The high energy boundary theory stated that the grain boundary mobility is aided by tension at the interface and capillary forces [36]. This led to a change in composition of the texture depending on the grain boundary mobility of different orientations.

However Morawiec [37] systematically disproved both the above theories stating the inherent inability of both the theories to provide both quantitative and experimental proof. In the case of the CSL boundary theory, coherent twin boundaries were vaguely compared to Goss grain boundary and thought to be the reason for abnormal grain growth. The theory of high energy boundary was disproved because of the fact that only a small fraction of the high energy boundaries grow into Goss grains during abnormal grain growth. Both these theories in combination could not explain the sharpness of Goss texture in CGO and HGO materials that are 7° and 3° respectively.

Morawiec [37] suggested a new theory that the probability of grain growth is higher when the surface free energy of the primary grain is lower which also explains the sharpness of Goss texture in electrical steels.

The evolution of Goss texture is still not completely understood. The effect of Goss texture on magnetic properties has been studied widely and found beneficial because of the presence of easy magnetization direction $\langle 100 \rangle$ parallel to the rolling direction.

There have been several improvements in the process of manufacture of electrical steels that led to a sharper Goss texture.

(a) Improvements in high temperature coil anneal

Dzubinsky and Kovac [38] studied the effect of heating rate during high temperature coil anneal on Goss texture. Heating rates from 15° to 60° C / hour were

studied. A 25°C/hour heating rate was found to be the optimum for sharpest Goss texture possible. The onset temperature for secondary recrystallization was found to be 900°C. A lower heating rate implies the presence of ingredients of the inhibitor for longer at temperatures below 900°C where their diffusion mobility is high. A lower heating rate also resulted in Ostwald ripening (small inhibitor particles dissolving into the solid solution and re-depositing on to larger particles) of precipitates resulting in reduced inhibition effect. Thus the inhibitor efficiency is weakened during secondary recrystallisation and growth of primary recrystallized grains was not inhibited. At very high heating rates, the driving force required for primary grain growth was high and the effective inhibition of the second phase inhibitor particles was low [38]. They found the effect of heat cycling at the second recrystallisation onset temperature range on improvement in the effect of inhibitors and eventually a sharper Goss texture. A heating rate of 25°C/hour is optimum as the resulting Goss texture was scattered. The scattered nucleation of Goss texture had higher grain boundary energy resulting in a weak inhibition effect.

Dorner et.al., studied the effect of plastic deformation on Fe-3% Si single crystals at 89% cold rolling. Most of the crystals deformed into two orientations that are symmetrical with a weak Goss component. In one of these orientations, shear bands formed by the deformation seem to be aligned with Goss grains. In the other case, new Goss areas were found in between the previously formed Goss micro-bands [39-40].

(b) Improvements in inhibitors and chemical composition

Rosypal [41] studied the effect of decarburization process parameters on the subsequent high temperature coil anneal. Samples from two different experiments with AlN inhibitor were studied with different amounts of nitrogen in the atmosphere. Higher oxidation at the surface of the sample in the decarburisation stage was found to be

beneficial in forming nitrides at the following high temperature coil anneal which results in better inhibition of primary grain growth and a sharper Goss texture[41].

Dzubinsky and Kovac also reported the effect of heating rate on sharpness of Goss texture [42]. Their work describes the weak Goss texture when the heating rate is too low (10°C/hour) or too high (60°C/hour). Application of nitrogen atmosphere that was described in the previous work led to deterioration of Goss texture strength in electrical steels with 1% Cr. Increase in percentage of Cr to 2% and a nitrogen atmosphere improved the final Goss texture. The work also describes the effect of Cu addition on final Goss texture. The value of B_{800} (the value of flux density B in Tesla, at 800 A/m magnetic field) varied from 1.5-1.94T with increasing Cu content which was mainly due to change in grain boundary mobility characteristics during secondary recrystallisation [42].

Takamiya et.al., studied the effect of Sb addition on final Goss texture after secondary recrystallisation[43]. Increase in Sb percentage leads to a segregation along grain boundaries which inhibits grain growth and leads to a strong initial $\{110\}<100>$ intensity. Final annealing at constant temperature leads to further segregation of Sb at grain boundaries and a stronger $\{110\}<100>$ texture [43]. Preferential growth of Goss grains surrounded by inhibited primary grains leads to a higher B_{800} .

Takamiya et.al., studied the effect of hydrogen in the annealing atmosphere on secondary recrystallization and Goss texture sharpness in grain oriented electrical steel with MnS, AlN and Sb inhibitors. In the case of MnS and Sb inhibitors, the sharpness of Goss texture improved with increasing H_2 percentage in the atmosphere. B_{800} improved to 1.95T from 1.94T while the specific total loss fell to 0.82 W/kg from 1.02 W/kg at 1.7T and 50Hz. In electrical steel with AlN inhibitors, increase in H_2 led to easy decomposition of AlN on the surface and reduction in inhibition effect. This led to uninhibited growth of primary grains and a weak Goss texture [44].

(c) Developments in HiB grain oriented electrical steel

The most important improvement in the Goss texture evolution came about by increasing the sharpness of Goss texture from 7° to 3° average mis-orientation. In the development of HiB, Taguchi et.al. [45] found this resulted in approximately 5% increase in B_{800} which reached up to 1.92T from 1.82T in CGO. The hysteresis loss was reduced by approximately 0.2W/Kg at 50Hz and 1.7T [46].

The two major differences that led to the development of HGO were

1. The inhibitor used in HiB was AlN and MnS, whereas it was MnS in CGO. The effect of AlN as described in previous works above can be improved by a N_2 atmosphere in final high temperature coil anneal.
2. The CGO process used a two stage cold rolling and a maximum deformation of up to 60% whereas the HiB process uses one cold rolling stage to a much higher reduction of 87%. This resulted in a primary recrystallisation texture of less $\{110\}<100>$ and more $\{111\}<112>$ textures which during secondary recrystallisation was favourable for the abnormal growth of $\{110\}<100>$ grains and a sharper Goss texture.

Woo et al, reported that AlN precipitation by hot band annealing is not a necessary criterion for improving Goss texture [47]. They studied the effect of 100% N_2 and 5% H_2 - N_2 and the onset temperature of secondary recrystallization on the evolution of Goss texture. The major conclusion was that the sharpness of Goss texture was more dependent on the onset temperature of secondary recrystallization and it was found that at an onset temperature of 1075°C , the requirement of hot band annealing to precipitate AlN is not necessary. This is shown by the change in B_{800} in samples where the onset temperature was varied by adding MgO coating and 5% H_2 - N_2 atmosphere [47].

3.3.2 Eddy current loss reduction in electrical steel

The classical eddy current loss in electrical steel comprises of the eddy currents set up in the electrical steel strips opposing the e.m.f induced by the magnetizing field. Eddy current losses decrease with decreasing thickness and hence any reduction in strip thickness reduces eddy current losses. Shilling and Houze Jr. [48] reported a reduction in eddy current loss of 0.15W/kg at 1.7T and 50Hz when the strip thickness was reduced from 0.3mm to 0.23mm. This reduction in thickness leads to several other disadvantages that place a limit to this reduction in strip thickness. The major disadvantages are

- Unstable secondary recrystallisation
- Increase in hysteresis loss component (due to unstable secondary recrystallisation resulting in a less sharper Goss texture)
- Poor shape and appearance of strip

Increasing the resistivity of the material reduces the eddy current losses according to equation 2.7. Addition of silicon in electrical steel increases the resistivity of the material but deteriorate the rolling ability of the material into thin sheets due to the induced brittleness. Silicon also reduces the saturation magnetization of the steel due to the addition of non-magnetic silicon in a magnetic Iron lattice.

Classical eddy current loss is reduced by reducing the thickness of the steel strip and increasing the resistivity of the material by alloying.

3.3.3 Dependence of anomalous component on magnetic domains

Anomalous losses are components of specific total loss in electrical steel caused by the inhomogeneities in magnetization and material microstructure. Anomalous losses, their sources and the mechanisms of reducing anomalous losses were described in section 2.8.

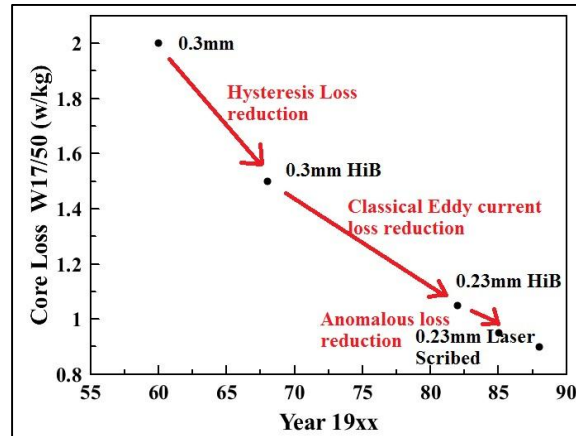


Figure 3.9 Developments in electrical steel production and their effects on loss components [2]

Several improvements in production of the electrical steel sheets were performed to reduce the anomalous component of the losses that depend on magnetic domains. Increase in the number of 180° domain walls or the reduction in domain widths resulted in reduced anomalous losses. Hayes and Wolford [49] reported in 1941 that periodic mechanical scratches in the transverse direction in electrical steel sheets resulted in lowered losses.

Pepperhoff and Fieldler [50] developed a periodic fine grooving mechanism on the steel in the transverse direction. The overall reduction in loss because of the method was found to be about 40% [50].

The change in domain width and structure due to application of surface stress has been widely studied. Domain refinement and its effects on reduction on losses are widely reported [6-9, 51-54]. Various methods of applying localized stresses were developed, the most common one being grooving with steel balls [7].

Plasma irradiation and spark ablation were also studied for the purpose of applying localised stresses [6-9]. The application of surface stress by all the above mentioned methods described has been successful in reducing the core loss. The implementation in

the process line though was extremely difficult because of the slow or expensive nature of the process. Nippon Steel Corporation in 1982 reported a method of producing periodic scribing in the transverse direction over the insulation coating on steel [55]. A typical laser scribed HGO material is shown in the Figure 3.10 and its effect on magnetic domains is shown in Figure 3.11.

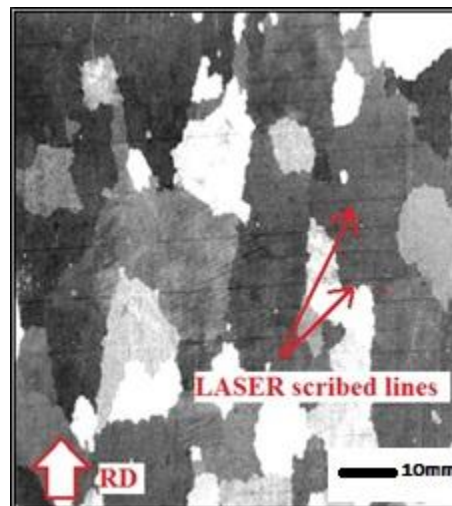


Figure 3.10 Typical HGO grain oriented electrical steel showing laser scribed lines

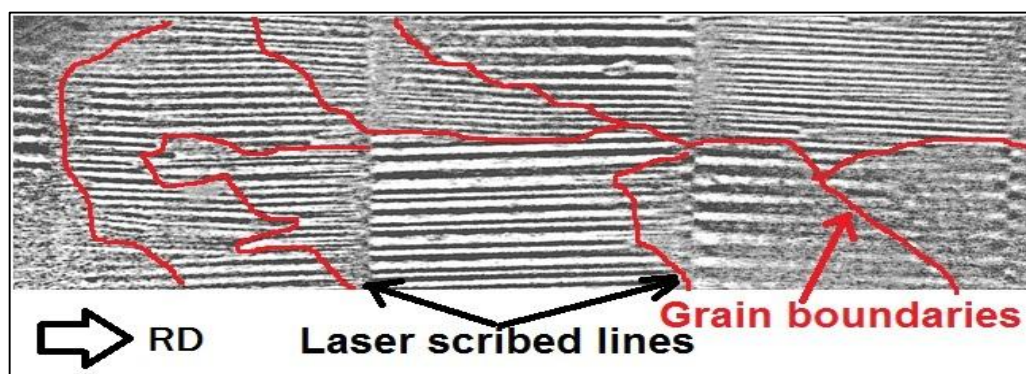


Figure 3.11 Magnetic domain image by Bitter technique showing refinement of domains by laser scribing

The laser scribing method is a non-contact technique to irradiate periodic scribing lines using a Q-switch (giant pulsed laser output with giga-watt scale power) laser. The non-contact nature of the method makes it easy to implement on production lines. Laser irradiation results in localized plastic deformation and an elastic tensile stress area around the scribe. This results in the refinement of magnetic domains and reduced core loss of

electrical steel. Results by Iuchi et.al., showed a 10% reduction in the core loss of electrical steel at higher induction provided the laser irradiation energy is optimum [3].

Imafuku et.al. [56] showed the effect of laser irradiation energy on domain refining and core loss of grain oriented electrical steel. They reported two effects of increase in laser irradiation energy. As the energy increases, the tensile residual stress increases and hence the domains were refined. It also induces a localized plastic deformation that was determined by local hardness measurements. Hence as the energy of laser irradiation increases, the anomalous component drops whereas the hysteresis component increases due to increased localized strain and dislocation density. The optimum laser energy was found to be 3.3 mJ/pulse where the minima of both anomalous and hysteresis components appear [56].

Laser scribing is the most adopted method for industrial applications. The two major disadvantages of laser scribing in spite of its economic advantage are

1. Deterioration of tension coating on the electrical steel strip due to extensive localized plastic deformation.
2. Sensitivity to annealing at temperatures above 550°C. High temperature annealing relieves the elastic tensile stresses and the magnetic properties revert back to un-scribed state.

To overcome these disadvantages several methods of domain refinement were developed [6-9]. Sato et.al, reported a method of grooving periodic lines in the transverse direction of the electrical steel strip resulted in the reduction of overall core loss by 10% [7]. They investigated the effect of grooving on core losses and on the domain structure. A cold rolled sheet of steel is deposited with a resist material in the form of thin grooves of 200µm. This material is electrolytically etched which preferentially forms grooves at the location of the resist material [7]. The final grooves that were formed were 200µm wide

and 20 μ m deep. The new grooving method produced electrical steel strip with a loss of 0.75 W/kg at 1.5 T and 60 Hz [7]. The reduction in core loss in a grooved material was about 10% compared to the material which was not grooved. A reduction in domain width was observed that resulted in reduced anomalous losses. A demagnetising field effect was produced near the grooved areas which resulted in a reduction in domain width [7].

The development of heat resistant domain refinement techniques did not deter the growth of laser irradiation technique from being used widely in industrial processes because of its economic and technical advantages.

Kobayashi et.al [4], suggested the two most important domain features for loss reduction are 1) increase in the number of domain walls that aid in magnetization 2) the decrease in area of closure domains. They utilised an improved high temperature annealing setup to produce a sharper Goss texture and laser scribing to produce a grain oriented silicon steel strip 0.15mm thick with a core loss of 0.42 W/Kg at 1.5T and 50Hz.

3.3.4 Electrical steel coatings

Washko et.al [57], in 1982 reported that the forsterite coating on steel reduced the core loss by 0.04-0.09 W/kg at 1.7T and 60Hz compared to uncoated steel. They observed a domain width refinement of 20-45%. They also showed that the MgO coating applied on the steel strip before HTCA to prevent the strips from sticking to one another forms a rough magnesium silicate glass film thereby increasing the core losses. Swift et al [58] and Foster et al [59] suggested that the increase in core loss is due to the surface roughness caused by the glass film. Shilling et.al [60] and Washko et.al [61] later suggested that the increase in loss is due to domain wall pinning by the forsterite that diffused into the iron layer assisting in the bonding of the coating.

Ushigami et.al [2], suggested a method of replacing the reactive MgO by Al₂O₃ to avoid the formation of rough magnesium silicate film. A surface film of roughness less than 0.3mm is formed. It is also beneficial in a way that the new surface film owing to the

inertness of alumina and smoother surface compared to MgO has much less interaction with the secondary recrystallisation process unlike the magnesium silicate film [2].

The effect of coatings on magnetic properties were widely studied and reported in the literature as shown in the few examples above.

3.4 Continuous thermal flattening anneal line

A gap is perceived in understanding the deformation process in the continuous thermal flattening anneal. The deformation behaviour and the possibility of dislocation formation and rearrangement can have a considerable effect on the magnetic properties of the finished product. Hence there is a necessity to study the flattening anneal line in detail to understand the deformation behaviour and magnetic property correlation. The following section explains the flattening anneal line in detail.

The main purpose of flattening anneal line is to apply the phosphate coating that applies a small tension (2-3 MPa) on the surface of the steel strip and act as an insulating medium. The purpose of this section is to develop the understanding of the flattening anneal process and phosphate coating application. A schematic of the M-line furnace is shown in Figure 3.12 below.

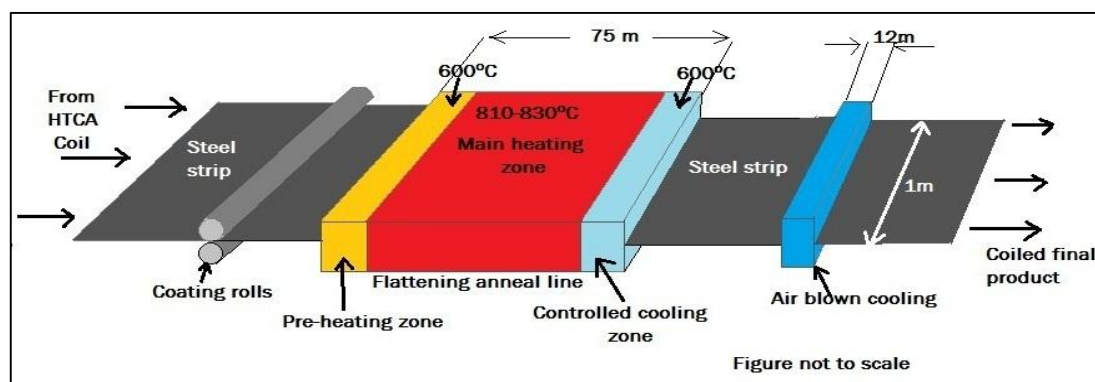


Figure 3.12 Schematic drawing of flattening anneal line showing coating rolls, heating and cooling zones

The continuous annealing line has two sets of rolls – supporting rolls and penetration rolls. As the name suggests the supporting rolls are the rolls on which the strip slides over after the coating is cured throughout the furnace. The four penetrating roles are the movable set of rolls that can move up or down into the path of the strip moving through the furnace. This is illustrated in Figure 3.13.

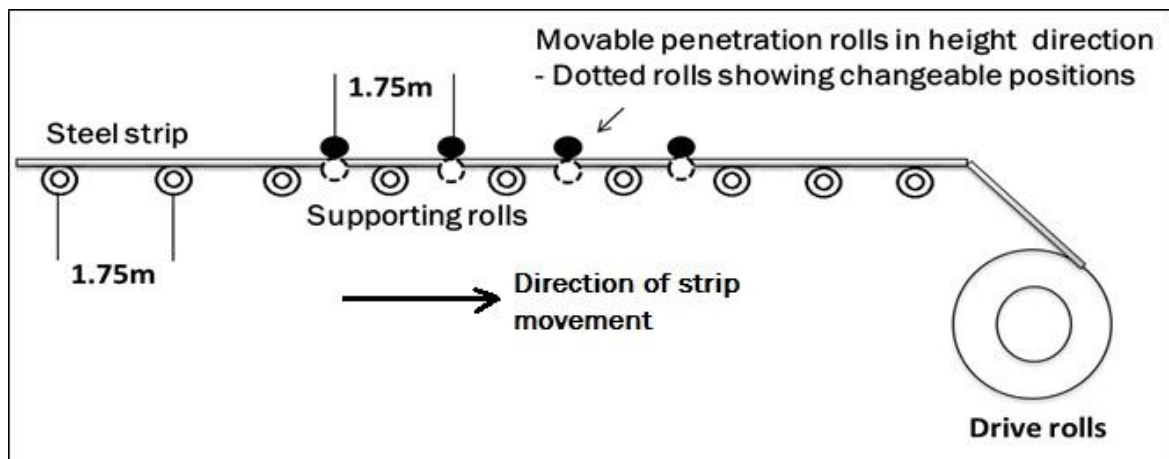


Figure 3.13 Mechanism to apply tension to the steel strip in continuous flattening anneal furnace

The drive rolls at the end of the furnace applies tension of the strip and the penetration rolls can be moved up or down depending on the tension requirements in the furnace. The rolls induces a small bend (approximately 7cms over the length of 175cm strip) to maintain the furnace tension. The tension setup in the furnace is illustrated in Figure 3.13.

The furnace has five major zones

1. Coating section
2. Preheating zone
3. Radiant heating zone
4. Controlled cooling zone

5. Compressed air cooling zone

The process of flattening anneal begins with application of a phosphate insulation coating of few micrometer thickness on the strip. The coating section applies the wet coating on the steel strip by rubber coated rollers and the strip with wet coating passes into the pre-heating zone of the furnace.

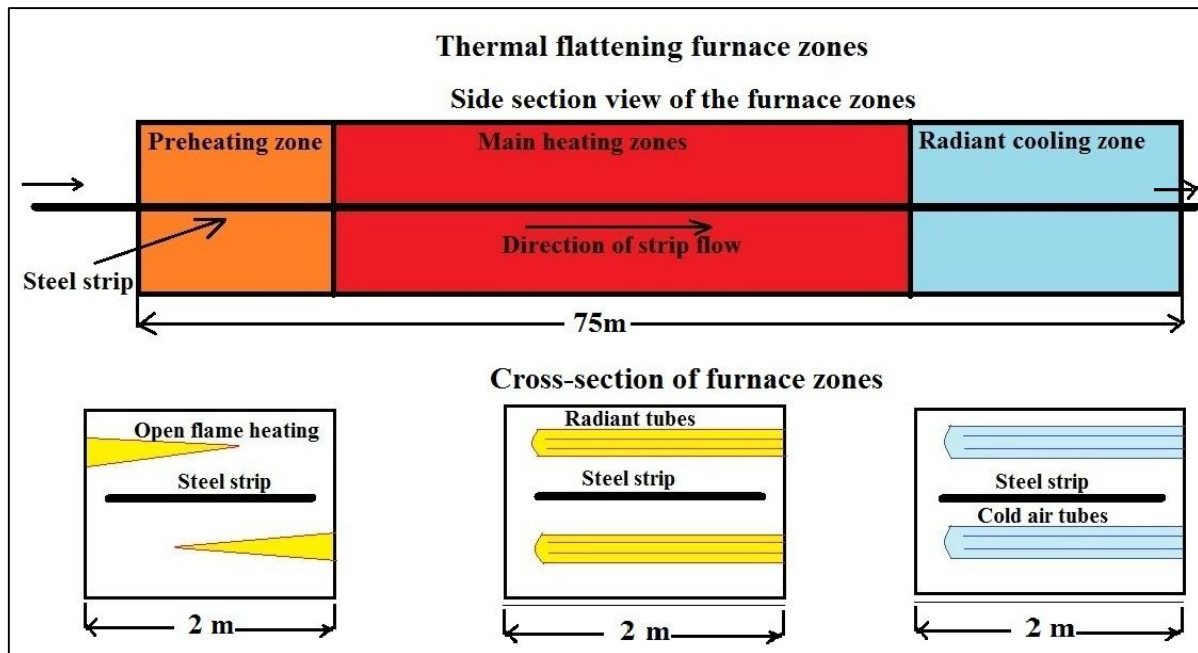


Figure 3.14 Different zones of the M-line furnace and schematic cross-sections of the heating and cooling processes

Schematic longitudinal sections of the furnace are illustrated in the Figure 3.14 above. It shows the heating and controlled cooling sections of the furnace and the respective heating mechanisms. The pre-heating section of the furnace is 14m long and is heated by open flame to cure the coating on the samples before it touches the first supporting roll. The steel strip is heated to 600°C in this zone.

The second zone is the radiant heating zone which is 46m long. Here the steel strip is heated by radiant tubes with high temperature flue gases from natural gas combustion

on the inside. In this zone, the strip is heated to about 810-830°C and soaked at the same temperature until the strip moves to the cooling zone. The zone is maintained at N_2 -3% H_2 atmosphere to prevent any oxidation of the strip and coating. The furnace is maintained at a small positive pressure to prevent atmospheric oxygen from entering the furnace. There are 72 radiant tubes in total in the heating zone.

The first step cooling zone also has tubes with cold air (room temperature) flow to cool down the strip temperature down to 600°C is 13m long after which the cooling is done by blowing compressed air onto the surface of the sample. The flattening anneal line at Cogent Power Ltd., Newport, UK is shown in Figure 3.15.



Figure 3.15 Image of the continuous flattening anneal line (M-line) at Cogent Power Ltd.,
Newport, UK

The purpose of this work is to understand the dislocation dynamics and its effect on power losses. It is important to understand the formation of dislocations in the continuous flattening anneal process and its correlation with magnetic properties. The study of polygonized boundaries and their effect on magnetization process as suggested by Sokolov et al [62], is also addressed in this work.

3.5 References

1. K Honda, S Kaya, *On the magnetisation of single crystals of Iron*, Sci Rep, Tohoku Imp. Univ., 1926; 15:721.
2. Y Ushigami, M Mizokami, M Fujikara, T Kubota, H Fuji, K Murakami, *Recent development of low-loss grain-oriented silicon steel*, J Mag Magn Mater., 2003; 254: 307.
3. T Iuchi, S Yamaguchi, T Ichiyama, M Nakamura, T Ishimoto, K Kuroki, *Laser processing for reducing core loss of grain oriented silicon steel*, J Appl Phys., 1982; 53:2410.
4. H Kobayashi, K Kuroki, E Sasaki, M Iwasaki, N Takahashi, *Heatproof Domain Refining Method Using Combination of Local Strain and Heat Treatment for Grain Oriented 3% Si-Fe*, Phys Scr., 1988; 24:36.
5. Y Ushigami, H Masui, Y Okazaki, Y Suga, N Takahashi, *Development of low-loss grain-oriented silicon steel*, J Mater Eng Per., 1996; 5:310.
6. S Y Cha, C G Kim, S K Chang., *Study of pinning conditions, magnetic domain structure and magnetic properties of laser-scribed 3% Si-steels*, J Mag Magn Mater, 242, 205-207 (2002)
7. H Sato, A Honda, H Nakano, M Ishida, B Fukuda, T Kan, *Development of domain refined grain-oriented silicon steel by grooving*, J Appl Phys., 1993; 73:6609.
8. T Iuchi, S Yamaguchi, T Ichiyama, M Nakamura, T Ishimoto, K Kuroki, *Laser processing for reducing core loss of grain oriented silicon steel*, J Appl Phys., 1982; 53:2410.
9. M Nakamura, K Hirose, T Iuchi, S Yamaguchi, Y Ohya, *Characteristics of laser irradiated grain oriented silicon steel*, IEEE Trans. Magn., 1982; 18: 1508.

10. T Nozawa, M Mizokami, H Mogi, Y Matsuo, *Magnetic properties and dynamic domain behavior in grain-oriented 3 % Si-Fe*, IEEE Trans. Magn., 1996; 32:572.
11. T Nozawa, T Yamamoto, Y Matsuo, Y Ohya, *Relation between total losses under tensile stress in 3 percent Si-Fe single crystals and their orientations near (110) [001]*, IEEE Trans. Magn., 1978; 14:252.
12. J W Shilling, W G Morris, M L Osborn, P Rao, *Orientation Dependence of Domain Wall Spacing and Losses in 3-Percent Si-Fe Single Crystals*, IEEE Trans. Magn., 1978; 14:104.
13. M Yabumoto, S Arai, R Kawamata, M Mizokami, T Kubota, *Recent development in grain-oriented electrical steel with low magnetostriction*, J Mater Eng Per., 1997; 6:713.
14. F J G Landgraf, M Emura, K Ito, P S G Carvalho, *Effect of plastic deformation on the magnetic properties of non-oriented electrical steels*, J Mag Magn Mater., 2000; 215–216:94.
15. P A Anderson, *PhD Thesis – A novel method of measurement and characterization of magnetostriction in electrical steels*, 1999, 11.
16. V Stoyka, F Kovac, O Stupakov, I Petryshynets, *Texture evolution in Fe–3% Si steel treated under unconventional annealing conditions*, Mater Charact, 2010, 61-11, 1066.
17. R Shimizu, J Harase, *Coincidence grain boundary and texture evolution in Fe-3% Si*, Acta Metall., 1989; 37(4):1241.
18. Y Ushigami, Y Suga, N Takahashi, K Kawasaki, Y Chikaura, H Kii, *Dynamic study of secondary recrystallization of 3% Si-Fe by synchrotron x-radiation topography*, J Mater Eng., 1991; 13:113.

19. Y Ushigami, K Murakami, T Kubota, *Analysis of Secondary Recrystallization in Grain Oriented Silicon Steel by Synchrotron X-Ray Topography*, Proceedings of the Grain Growth in Polycrystalline Materials, 1998; 3:491.
20. S Mishra, C Darmann, K Lucke, *On the development of the goss texture in iron-3% silicon*, Acta Metall., 1984; 32(12):2185.
21. J Harase, R Shimizu, D J Dingley, *Texture evolution in the presence of precipitates in Fe-3% Si alloy*, Acta metall., 1991; 39:763.
22. J Harase, R Shimizu, *Texture evolution by grain growth in the presence of MnS and AlN precipitates in Fe-3% Si alloy*, Acta Metall., 1990; 38:1395.
23. Y Yoshitomi, K Iwayama, T Nagashima, J Harase, N Takahashi, *Coincidence grain boundary and role of inhibitor for secondary recrystallization in Fe-3% Si alloy*, Acta Metall., 1993; 41:1577.
24. P Lin, G Palumbo, J Harase, K T Aust, *Coincidence Site Lattice (CSL) grain boundaries and Goss texture development in Fe-3% Si alloy*, Acta Mater., 1996; 44: 4677.
25. J Harase, K Y Kim, Proceedings of the 11th International Conference on Textures of Materials—ICOTOM11, 1996; 423.
26. J Harase, R Shimizu, J Kim, J S Woo, Proceedings of the 12th International Conference on Textures of Materials—ICOTOM12, 1999; 1009.
27. H Afer, N Rouag, R Penelle, *Onset of abnormal growth related to the crystallographic neighbourhood from the texture function - Application to Goss grain growth in magnetic sheets of Fe-3%Si*, Journal of Crystal Growth, 2004; 268:320.
28. N Rouag, G Vigna, R Penelle, *Evolution of local texture and grain boundary characteristics during secondary recrystallisation of Fe-3% Si sheets*, Acta Metall., 1990; 38:1101.

29. Y Hayakawa, J A Szpunar, G Palumbo, P Lin, *The role of grain boundary character distribution in Goss texture development in electrical steels*, J Mag Magn Mater, 1996; 160:143.
30. Y Hayakawa, J. A. Szpunar, Proceedings of the 11th International Conference on Textures of Materials—ICOTOM, 1996; 435.
31. Y Hayakawa, J A Szpunar, *The role of grain boundary character distribution in secondary recrystallization of electrical steels*, Acta Mater., 1997; 45:1285.
32. Y Hayakawa, J A Szpunar, *A new model of Goss texture development during secondary recrystallization of electrical steel*, Acta Mater., 1997; 45:4713.
33. Y Hayakawa, M Kurosawa, M Komatsubara, J A Szpunar, Proceedings of the Third International Conference on Grain Growth, 1998; 615.
34. Y Hayakawa, M Muraki, J A Szpunar, *The changes of grain boundary character distribution during the secondary recrystallization of electrical steel*, Acta Mater., 1998; 46:1063.
35. Y Hayakawa, T Takamiya, M Kurosawa, Proceedings of the 12th International Conference on Textures of Materials—ICOTOM 12, 1999; 1101.
36. T V Philip, R E Lenhart, *Secondary Recrystallization Kinetics in Singly Oriented Silicon Iron*, Trans. Met. Soc. AIME., 1961; 221:439.
37. A Morawiec, *Grain misorientations in theories of abnormal grain growth in silicon steel*, Scripta mater., 2000; 43:275.
38. M Dzubinsky, F Kovac, *Influence of heat cycling on microstructural parameters of Fe–3%Si grain oriented steel*, Scripta Mater., 2001; 45:1205.
39. D Dorner, S Zaefferer, D Raabe, *Retention of the Goss orientation between microbands during cold rolling of an Fe-3%Si single crystal*, Acta Mater., 2007; 55:2519.

40. D Dorner, S Zaefferer, L Lahn, D Raabe, *Overview of Microstructure and Microtexture Development in Grain-oriented Silicon Steel*, J Mag Magn Mater, 2006; 304:183.
41. F Rosypal, *Decarburization annealing of grain-oriented silicon steel with AlN as inhibitor*, J Mag Magn Mater., 1994; 133:220.
42. M Dzubinsky, F Kovac, *Microstructure and texture development of Fe–3%Si GO steel during high temperature annealing*, J Mag Magn Mater., 2003; 254–255: 388.
43. T Takamiya, M Romatubara, Y Hayakawa, T Kan, *Influence of heat treatment before secondary recrystallization on magnetic properties of 3% Si grain-oriented steel containing Sb*, J Mag Magn Mater., 1996; 160:131.
44. T Takamiya, M Kurosawa, M Komatsubara, *Effect of hydrogen content in the final annealing atmosphere on secondary recrystallization of grain-oriented Si steel*, J Mag Magn Mater., 2003; 254–255:334.
45. S Taguchi, A Sakakura, *Process of producing single-oriented silicon steel*, US Patent No. 3,159,511, 1964.
46. Z Xia, Y Kang, Q Wang, *Developments in the production of grain-oriented electrical steel*, J Mag Magn Mater., 2008; 320:3229.
47. J S Woo, C H Ham, B D Hong, J Harase, *The onset temperature of secondary recrystallization and the sharpness of Goss secondary recrystallization texture in the nitrided Fe–3%Si alloy*, Acta Mater., 1998; 46:4905.
48. J W Shilling, G L Houze, *Magnetic properties and domain structure in grain-oriented 3% Si-Fe*, IEEE Trans. Magn., 1974; 10:195.
49. D M Hayes, D S Wolford, *Core loss reduction by mechanical scratching*, US Patent No. 2,234,968, 1941.
50. W Pepperhoff, A Fieldler, *Method for reducing lossiness of sheet metal*, US Patent No. 3,647,575, 1972.

51. D Snell, P Beckley, *Domain refinement of high-permeability grain-oriented electrical steel using low-friction ball units*, J Mag Magn Mater., 1994; 133:167.
52. B Weidenfeller, W Rieheman, *Domain refinement and domain wall activation of surface treated Fe-Si sheets*, J Mag Magn Mater., 1996; 160:136.
53. R Schafer, S Schinnerling., *Bulk domain analysis in FeSi-crystals*, J Mag Magn Mater., 2000; 215:140.
54. K Sato, M Ishida, E Hina, Kawasaki Steel Tech Report, 1998, 39:21.
55. N Takahashi, Y Ushigami, M Yabumoto, Y Suga, H Kobayashi, T Nakayama, T Nozawa, *Production of very low core loss grain-oriented silicon steel*, IEEE Trans. Magn., 1986; 22:490.
56. M Imafuku, H Suzuki, K Akita, K Iwatw, M Fujikura, *Effects of laser irradiation on iron loss reduction for Fe-3%Si grain-oriented silicon steel*, Acta Mater., 2005; 53:939.
57. S D Washko, T H Shen, W G Morris, *The effect of forsterite coatings on magnetic properties and domain structure of grain oriented 3% Si-Fe*, J Appl Phys., 1982; 53:8296.
58. W M Swift, W H Daniels, J W Shilling., *Effect of Surface Morphology on Losses of (110) [001] Oriented Silicon Iron*, IEEE Trans. Magn., 1975;2:1655.
59. K Foster, J H Jackson, *Effect of anneal coatings and surface condition on magnetic properties of grain oriented 3% Si - Fe*, IEEE Trans. Magn., 1980; 16:743.
60. J H Shilling, I G Morris, D R Fecich, P Rao, *Effect of forsterite coatings on the domain structure of grain-oriented 3-percent Si-Fe*, IEEE Trans. Magn., 1978; 14:14.
61. S D Washko, W G Morris, *Effects of coatings on domain wall spacing and core loss in 3% Si-Fe single crystals*, J Mag Magn Mater., 1980; 19:349.

62. B K Sokolov, Y N Dragoshanski, V S Matveeva, M B Tsyrlin, F V Mineev, R B Puzhevich, *Inhomogeneity of magnetic properties of an anisotropic electrical steel and specific features of dislocation structures*, Russ J Nondestruct+, 2004; 40:11.

Chapter 4

Heat transfer model of continuous flattening anneal (M-line) line using finite element analysis (COMSOL)

4.1 Introduction to the furnace model

In the continuous annealing furnace used for thermal flattening, control of strip temperature is strongly influenced by the time taken by the furnace refractory system to respond to changes in set temperature. Thus temperature changes are much slower than the change in control set point. The challenge is the ability of precise measurement by the pyrometers. The accuracy of the pyrometers is strongly influenced by radiation in the furnace atmosphere because of the highly reflective surfaces inside the furnace. This leaves a challenging problem where the furnace conditions are changing during most of its operating time making temperature measurement a difficult task. Because of the difficulty of measurement, a three dimensional furnace model is essential to clearly understand the temperature distribution in the steel strip through the process. Heat transfer in the flattening anneal process in the production of GOES was modelled by finite element analysis and is presented in this chapter. A combination of conduction, convection and surface to surface radiation were incorporated into the model to determine the thermal profile of the strip throughout the process.

4.2 Purpose of the flattening anneal heat transfer model

The deformation mechanism in flattening anneal is of great importance to understand its effect on magnetic properties. To understand the deformation mechanism it is essential to understand the temperature profile of the strip inside the continuous flattening annealing furnace. The flattening anneal furnace at Cogent Power Ltd., has temperature measurement systems (optical pyrometers) that provide temperature data in each sub-zone. It also has infrared pyrometers for strip temperature measurement at three locations in the furnace. This limited temperature data is not sufficient to develop a detailed idea of the process of dislocation creation and annihilation during this process.

Hence it was essential to develop a detailed thermal profile of the strip throughout the furnace in order to gain a better understanding of the flattening anneal process.

4.3 Background study of furnace models

Prieto et al. [1] reported the development of a stepwise thermal model for continuous annealing. In this model, they calculated the temperature distribution of a 250m long steel strip due to difficulties in measurements in the furnace. They divided a continuous annealing furnace into smaller closed sections to simplify the energy balance and heat transfer calculations. All heat transfer mechanisms acting on the steel strip including convection by furnace atmosphere and surface radiation were assumed to be bound by the smaller enclosures introduced by them. A good agreement was attained between the model and the measured data at the thermocouples available in the furnace [1].

Fei et al. [2] reported the effect of strip speed, geometry and radiation properties of the strip, furnace walls and tubes on the temperature distribution in the strip in a vertical continuous annealing furnace. They also analysed the relationship between the temperature of the strip and various other parameters like the total heat transferred, heat transfer coefficient and time. The model used radiative heat transfer and Newton's law of cooling [2].

Depree et al [3] showed that a critical mistake was made by Prieto et al [1] by using a steady state condition on a continuous flattening annealing line. As described in the introduction, a furnace atmosphere is transient during most of the operating time and hence they created a three dimensional COMSOL Multiphysics (software package) model to understand the transient behaviour and temperature distribution on the furnace walls, strip and the atmosphere.

Considering the variation in the process parameters and the system response to these changes the current model was designed in accordance with the idea proposed by Depree et al. [3] for a continuous annealing galvanizing furnace which was similar in several aspects except for the heating mechanism.

4.4 Furnace design

The continuous flattening anneal process line at Cogent Power is a three zone furnace which is 75m long from the start of pre-heat section to the end of controlled cooling section and is used to apply a tension coating on electrical steel strips and to correct edge deformations thereby flattening the strip from the previous high temperature coil annealing process. The three zones in the furnace are

1. Pre-heat zone
2. Main radiant tube heating zone
3. Controlled cooling zone

The layout of the furnace and the location of thermocouples in the furnace are shown below in figure 4.1.

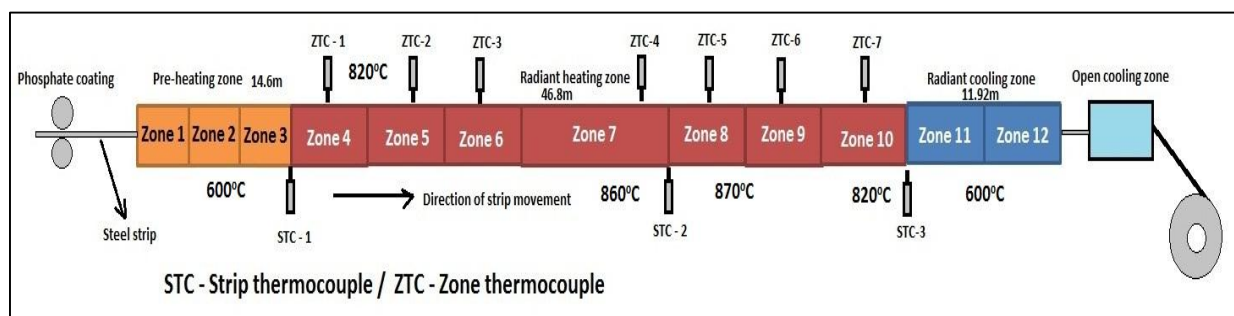


Figure 4.1 Layout of the furnace zones, sub-zones dimensions and the location of strip, zone thermocouples and set zone temperatures

The purpose of the pre-heat zone is to cure the coated strip before it reaches the first supporting roll at the end of sub-zone 2 and to increase the temperature of the strip to aid the main heating zone. This zone is heated by 17 open fired recuperative burners. Recuperative burners can utilize the waste heat downstream from the burner to pre-heat the inlet gases and hence improving thermal efficiency of the burner. The preheating zone can be further subdivided into three sub-zones where sub-zone 1 is heated by five 150 kWh burners, sub-zone 2 with six and sub-zone 3 with seven 180 kWh burners.

The main radiant tube heating zone consists of seven sub-zones (sub-zones 4-10) which are heated by radiant tubes. The radiant tubes are recuperative and the waste hot exit gases after combustion are used to preheat the inlet gas. Sub-zones 4 to 7 are the heating zones whereas sub-zones 8-10 are holding zones where the strip is held at around 850°C.

Sub-zones 11 and 12 are the controlled cooling zones in which cold air at room temperature flows through the cooling tubes. The strip is cooled down to approximately 600°C by the end of these sub-zones and passed through an open cooling zone where compressed air is blown over the strip to reduce the temperature down to approximately 250°C.

4.5 Modelling strategy

The two major components in building the thermal profile of the steel strip throughout the process are

- the heat transfer from the indirect heating radiant tubes
- radiative heat transfer to the furnace walls and the steel strip

The modelling strategy was to model the heat transfer in the furnace by Finite element modelling (FEM) in two steps. The first step was to model the radiant tubes and understand the effect of changes in their efficiency on the zone temperature. This model is shown in Figures 4.2 and 4.3. The mesh strategy used in this first model is shown in Figures 4.4 and 4.5. The meshing scheme was refined in the regions close to the radiant tubes in order to properly represent any small temperature gradients.

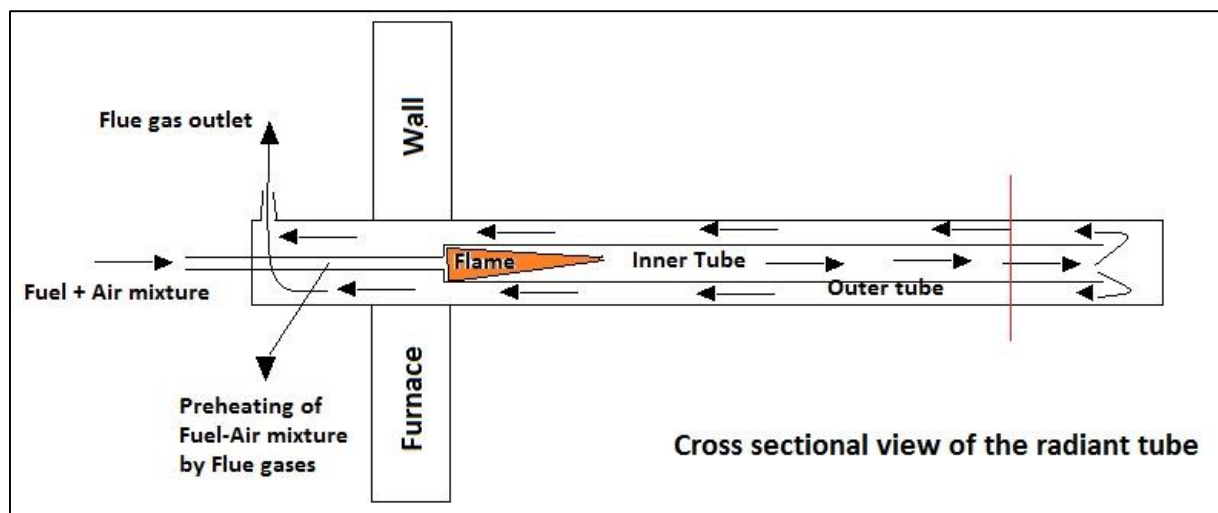


Figure 4.2 Cross-section of the radiant tube showing fuel+air mixture inlet and the path of flue gases

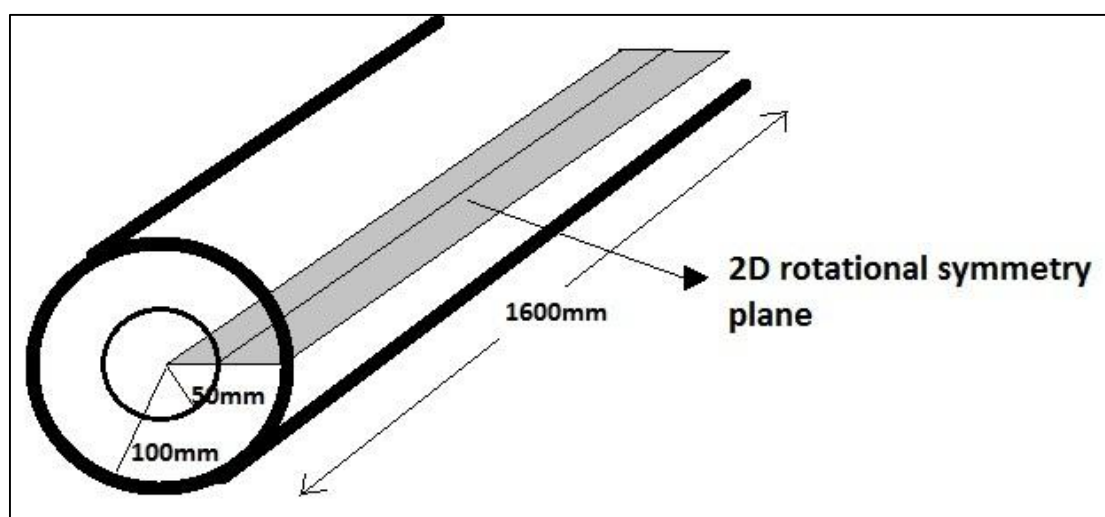


Figure 4.3 Modelling strategy showing two dimensional rotational symmetry in the radiant tube to reduce simplify computation

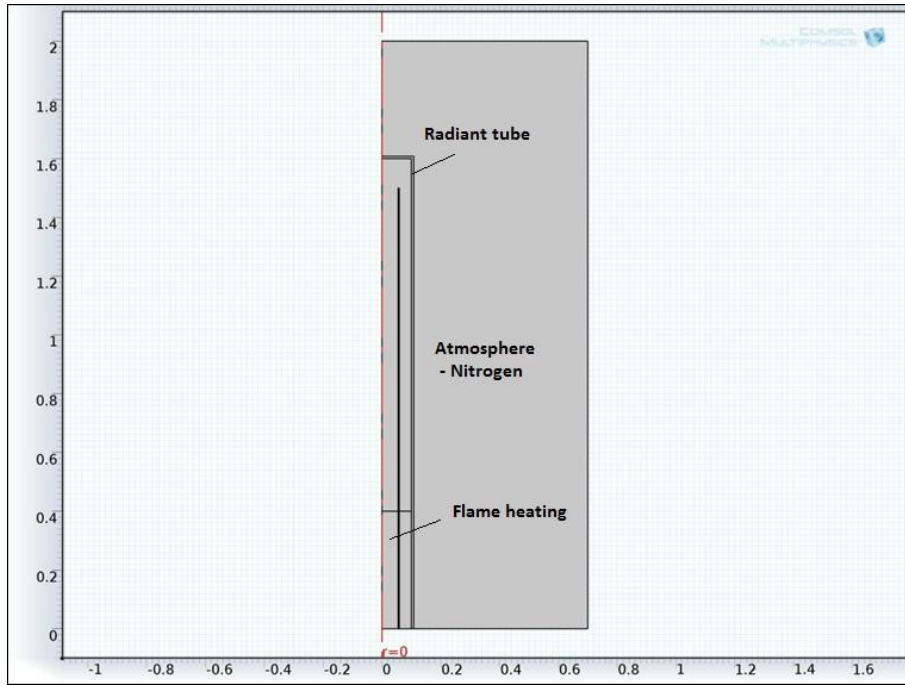


Figure 4.4 Two dimensional model of the radiant tube with surrounding atmosphere

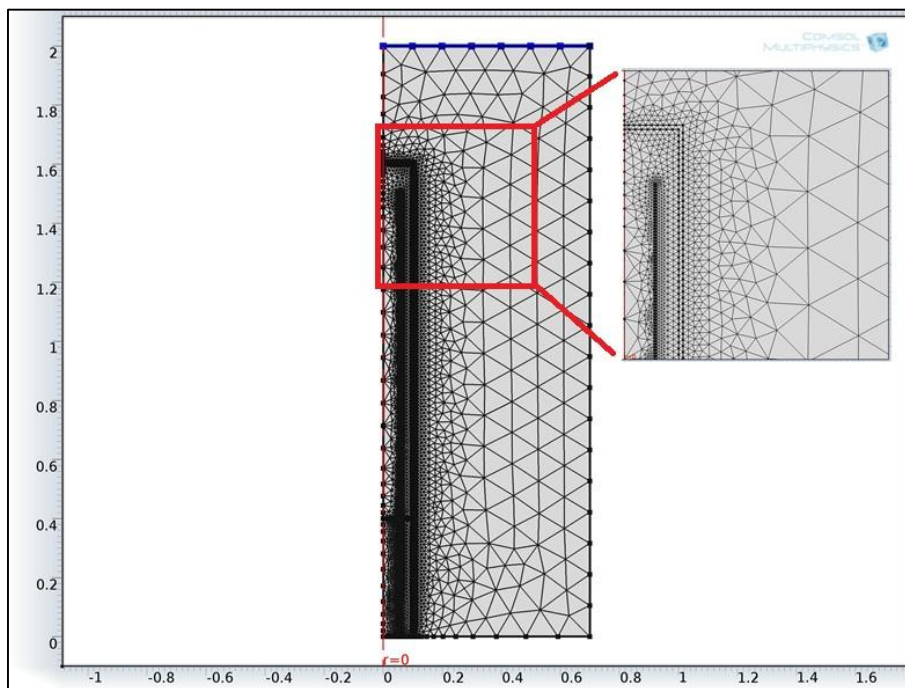


Figure 4.5 Mesh elements concentrated near the radiant tubes

The second step was to use the radiant tubes as steady heat sources in the full furnace three dimensional model in order to determine the heat transfer to the steel strip and hence the strip temperature. A three dimensional model was essential in this case

due to the necessity of taking into account the radiative heat transfer from the furnace walls and tubes to the surface of the strip. Figure 4.6(a) below shows the cross section of the furnace with radiant tubes, steel strip over supporting rolls and the furnace walls. The three dimensional model created to reproduce the furnace cross section and its mesh scheme are shown in the Figure 4.6(b). Simulation was performed in sections of 0.53m long sections of the furnace because of computational limitations of the work station (Intel i7 Quad core processor, 64GB of RAM) used and the geometry of the model is shown in Figure 4.7.

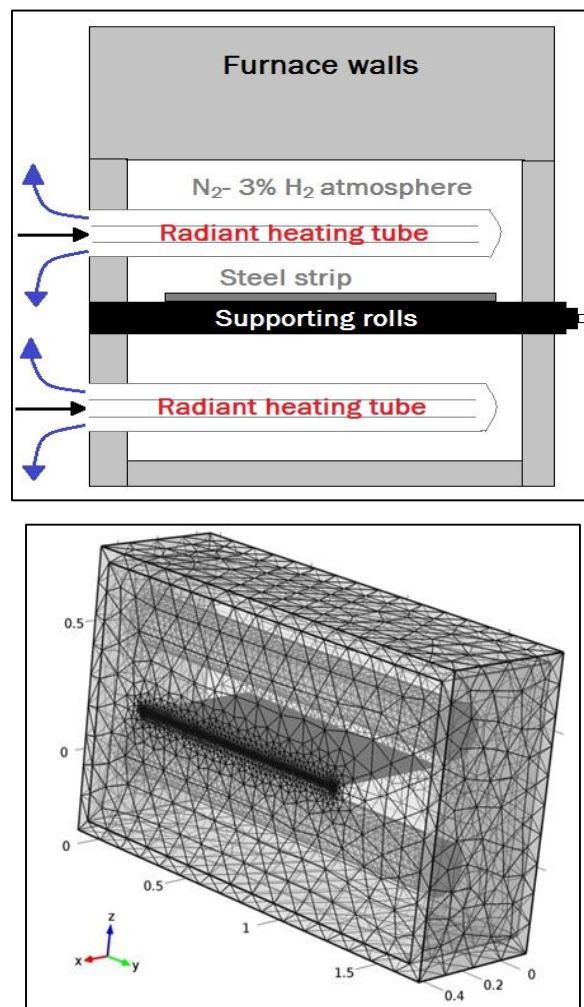


Figure 4.6 (a) Cross section of the furnace at radiant heating and cooling zones (b)

Furnace cross section model and mesh scheme with dimensions in m

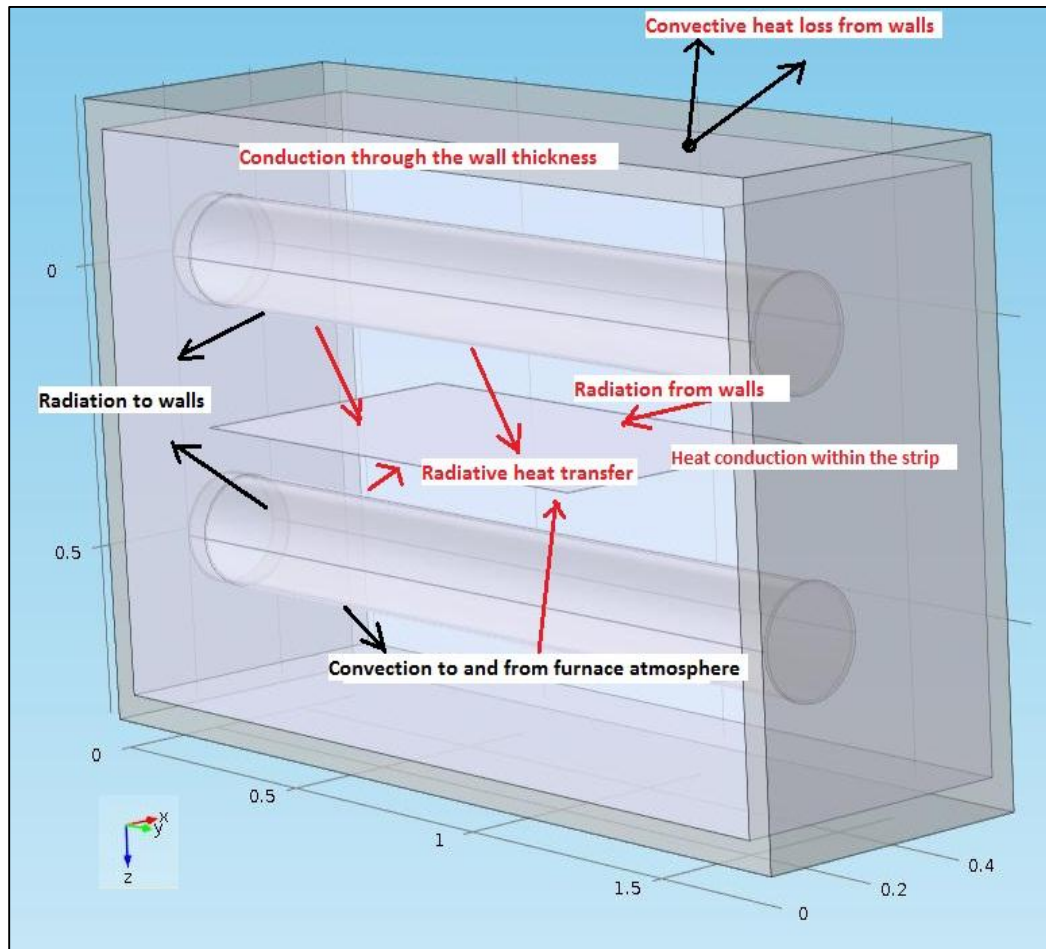


Figure 4.7 Heat transfer physics used in the model (Red arrows showing heat into the steel strip and the black ones showing heat loss)

The heat source for the furnace cross section model was derived from the radiant tube model.

The controlled cooling sections with cold air running through tubes are the same as the radiant heating section except for the cold air flow in the tubes and heat transferred from the strip to the cold air.

The open cooling section by compressed air flow over the strip was modelled by a forced external convection on a strip as shown in Figure 4.8.

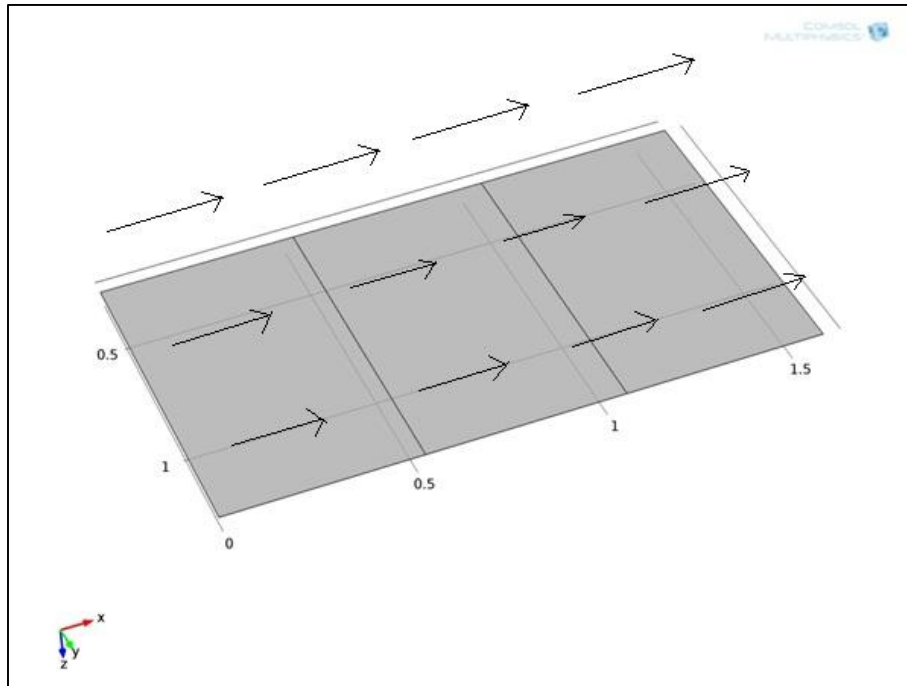


Figure 4.8 Open cooling section modelled with strip and an external forced convection

The starting temperature of the strip section in each sub-zone was the temperature profile calculated in the previous section. To simulate the effect of strip speed on the temperature distribution, time dependent heat transfer was modelled. The temperature profile was calculated for one second in each section at 0.2s time steps. The strip speed effect was simulated by the change in boundary conditions of the strip according to the sub-zone conditions and the time for which the strip is present in the zone.

4.6 Heat transfer physics

The following modes of heat transfer had to be studied in the above model. It included:-

1. Heat transfer in the strip (conduction)
2. Heat transfer from the nitrogen atmosphere to the strip (convection)
3. Heat transfer from radiant tube surface to the strip (Surface-Surface radiation)

4. Heat transfer from the radiant tubes to all other parts of the furnace (Surface-Surface radiation)
5. Reflected heat from other parts of the furnace to the strip (Surface-Surface radiation)
6. Reflected heat from the strip and furnace surface to the surroundings (Surface-Ambient radiation).

This section elaborates the constitutive heat transfer equations used in this study for all the three separate models as explained in the previous section.

4.6.1 Heat balance calculation in the furnace

Heat balance calculation in the continuous annealing furnace was the first step in the model and is schematically explained in the Figure 4.9 below.

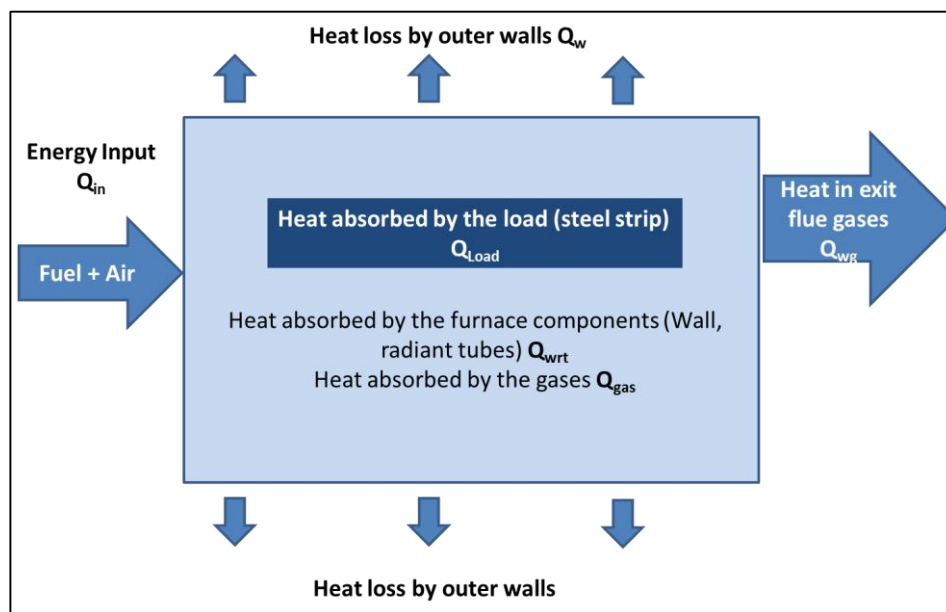


Figure 4.9 Heat balance diagram for the flattening anneal furnace

The heat balance in the flattening anneal furnace can be described by the following equation

$$Q_{in} = Q_{Load} + Q_w + Q_{gas} + Q_{wrt} + Q_{wg} + Q_{anam} \quad (4.1)$$

Where,

Q_{in} - Heat input by fuels into the radiant tubes

Q_{Load} - Heat input to the steel strip

Q_w - Heat loss through the walls

Q_{gas} - Heat absorbed by the furnace gases

Q_{wrt} - Heat absorbed by walls and the radiant tubes

Q_{anam} - Heat lost at the ends of the furnace

Q_{wg} - Heat loss through exit flue gases at 400°C

4.6.2 Heat transfer used in the model

(a) Conduction heat transfer in solids [4]

Heat transfer by conduction takes place within the strip, in the radiant tube and across the furnace walls. This is defined by the equation 4.2

$$\rho C_P \frac{\partial T}{\partial t} + \rho C_P u \cdot \nabla T = \nabla \cdot (K \cdot \nabla T) + Q \quad (4.2)$$

Where,

ρ - Density of the material (kg/m³)

C_P - Specific heat capacity of the material (J/kg.K)

T - Temperature (K)

t - Time (S)

K – Thermal conductivity of material (W/m.K)

Q – heat input to unit volume of the material (W/m³)

(b) Convective heat transfer [4]

Two convective heat transfer mechanisms are in operation in the radiant tube model. The heat transfer from the flue gases to the radiant tubes is the first and the heat transfer from the radiant tubes to the surrounding nitrogen atmosphere is the other. The convective heat transfer is defined by the equation 4.3 given below

$$n.K\nabla T = h.(T_{ext} - T) \quad (4.3)$$

Where T_{ext} – Furnace atmosphere temperature, T – Temperature of the strip, h – Convective heat transfer co-efficient

(c) Surface to surface radiation [4]

Surface to surface radiation is the main mode of heat transfer to the steel strip from the radiant tubes and the furnace walls and is given by the equations 4.4 to 4.8

$$-n.(-K\nabla T) = \varepsilon_u(G_u - \sigma T^4) + \varepsilon_d(G_d - \sigma T^4) \quad (4.4)$$

Where, ε_u – Emissivity of the surface in upper side, ε_d – Emissivity of the surface in the down side, G_u – Upside surface irradiation (W/m²), G_d – Downside surface irradiation (W/m²), T – input temperature (K), σ – Stefan Boltzmann constant $5.6703 \times 10^{-8} \text{ W/m}^2\text{K}^4$

Where,

$$G_u = G_{m,u}(j) + F_{amb,u}\sigma T_{amb,u}^4 + G_{ext,u} \quad (4.5)$$

$G_{m,u}$ – Surface irradiation from the domain on the upper side, $G_{ext,u}$ – Surface irradiation from the other domains to the current domain on the upper side

$$(1 - \varepsilon_u)G_u = J_u - \varepsilon_u \sigma T^4 \quad (4.6)$$

J_u – Surface radiosity at the upper side (W/m²)

$$G_d = G_{m,d}(j) + F_{amb,d} \sigma T_{amb,d}^4 + G_{ext,d} \quad (4.7)$$

$G_{m,d}$ – Surface irradiation from the domain on the down side, $G_{ext,d}$ – Surface irradiation from the other domains to the current domain on the down side

$$(1 - \varepsilon_d)G_d = J_d - \varepsilon_d \sigma T^4 \quad (4.8)$$

J_d – Surface radiosity at the down side (W/m²)

(d) Heat losses [4]

Heat losses by convection and radiation were modelled using equations 4.9 and 4.10 respectively

$$-n.(-K \nabla T) = (T_{ext} - T) \quad (4.9)$$

$$-n.(-K. \nabla T) = \varepsilon. (G - \sigma T^4) \quad (4.10)$$

4.7 Physical properties of the materials used in the model

Thermal and mechanical properties of the materials usually vary with temperatures and this has to be modelled taking into account their temperature dependence. Physical properties of all the materials used in the furnace were used in this model and tabulated in Table 4.1 below. The parameters are given as a function of temperature ‘T’.

Table 4.1 Physical properties of materials used in the model as a function of temperature

Properties	HK 40 alloy[5,6]	Stainless steel[7,8,9]	Alumina[6,10]	Nitrogen + 3% Hydrogen[12]	Fe – 3% Si alloy[8]	Flue gases from combustion[12]
Use	Inner radiant tube	Outer radiant tube	Furnace walls	Furnace atmosphere	Steel strip	Product of combustion (Heat source)
Heat capacity at constant pressure (Cp) J/kg.K	$425.17 + 0.44126 T - 2.517e^{-4} T^2$	$450 + 0.28T - 2.91e^{-4} T^2 + 1.34e^{-7} T^3$	$880 + 0.18T - 1.13e^{-3} T^2$	$1088.22 - 0.3659 T + 7.887 e^{-4} T^2 - 3.7492 e^{-7} T^3 + 3.17599 e^{-11} T^4$	$430 + 0.231 T - 1.9 e^{-2} T^2$	$0.6*(459.91+1.86T-0.0021T^2+1.224e^{-6} T^3)+0.4*(13604.73 - 90.43T+0.277T^2 - 4.21e^{-4} T^3)$
Dynamic viscosity (μ)	-NA-	-NA-	-NA-	$1.772e^{-6} + 6.274e^{-8} T - 3.472e^{-11} T^2 + 1.012e^{-14} T^3$	-NA-	$0.6*(-1.485e^{-6} + 6.467e^{-8} T - 3.66 e^{-11} T^2 + 1.245e^{-14} T^3) + 0.4*(-1.420e^{-6} + 3.83e^{-8} T - 3.85e^{-12} T^2)$
Thermal conductivity (K) W/m.K	$12.31 + 0.01296 T + 4.67e^{-6} T^2$	$14.6 + 1.27e^{-2} T$	$18+1.3 e^{-2} T$	$3.696 e^{-4} + 9.7435 e^{-5} T - 4.0758 e^{-8} T^2 + 7.684 e^{-12} T^3$	$42.1- 0.0127T$	$0.6*(-0.0013 +4.139e^{-5} T+6.708e^{-8} T^2 - 2.110e^{-11} T^3) +0.4*(1.317e^{-4}+5.149e^{-5} T+3.896e^{-8} T^2- 1.368e^{-11} T^3)$
Thermal expansion coefficient (α) 1/K	$1 e^{-5}$	$0.81e^{-5}$	$0.82e^{-5}$	$0.93 e^{-3}$	$1.2e^{-6}$	$1.1e^{-3}$
Density (ρ) kg/m ³	7750	7865	3950	1.165 (NTP)	7650	0.257 (800-1200°C)
Emissivity (ϵ)	0.5	0.3	0.3	-NA-	0.6	-NA-

The physical properties of the materials used in the model are from literature [6-12]. The data has been verified from more than one source for accuracy. But the difference in experimental conditions at which the properties are measured in different sources there is a small variation in the data.

4.8 Effect of mesh size

A study of the effect of mesh size used in the calculations was performed before calculating the actual temperature profile of the strip. This was to optimize the sensitivity of the temperature profile and the computational load and time. The results of this study are tabulated in Table 4.2. A comparison of the temperature profiles is shown in Figure 4.10. The comparison of temperature profiles shows a strong agreement between the temperature calculated with normal and fine meshes. Data calculated with the coarse mesh deviated by approximately 5-10% from the data calculated using the normal and fine meshes. Hence the normal mesh was used in all further calculations to minimize the computational time without compromising the accuracy of the calculation.

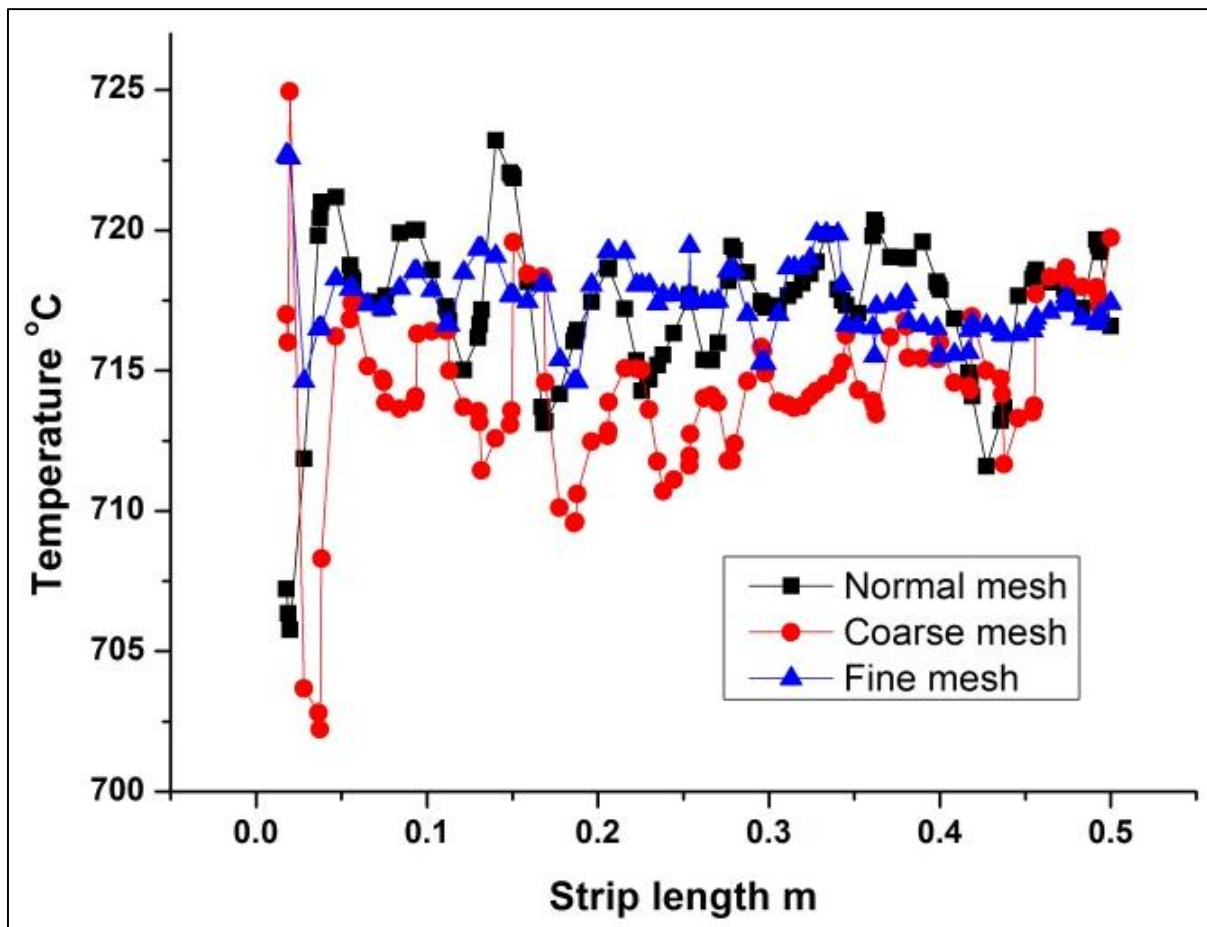


Figure 4.10 Comparison of temperature profile across a steel strip section 0.53m long, along the rolling direction calculated with different mesh sizes

Table 4.2 Comparison of computational time for different mesh sizes in critical areas close to the radiant tube and steel strip

Mesh contents	Number of mesh elements	Computational time
Coarse	48182	2 h 27 m
Normal	102318	4 h 22 m
Fine	341314	18 h 07 m

4.9 Results

4.9.1 Part 1 - Radiant tube model

The radiant heating model was calculated in two parts. This part shows the resultant temperature profile of the surface of the radiant tubes in the different sub-zones in the radiant heating section. The diagram of the thermal profile for a radiant tube in each sub-zone is shown in Figures 4.11-4.15. Figure 4.11(a)-4.15(a) show the cross-section of the temperature profile of the inside of a radiant tube along with the surrounding atmosphere. Figures 4.11(b)-4.15(b) show the temperature profile on the outside of the radiant tube which heats the strip.

(a) Sub-zones 4, 5 and 6

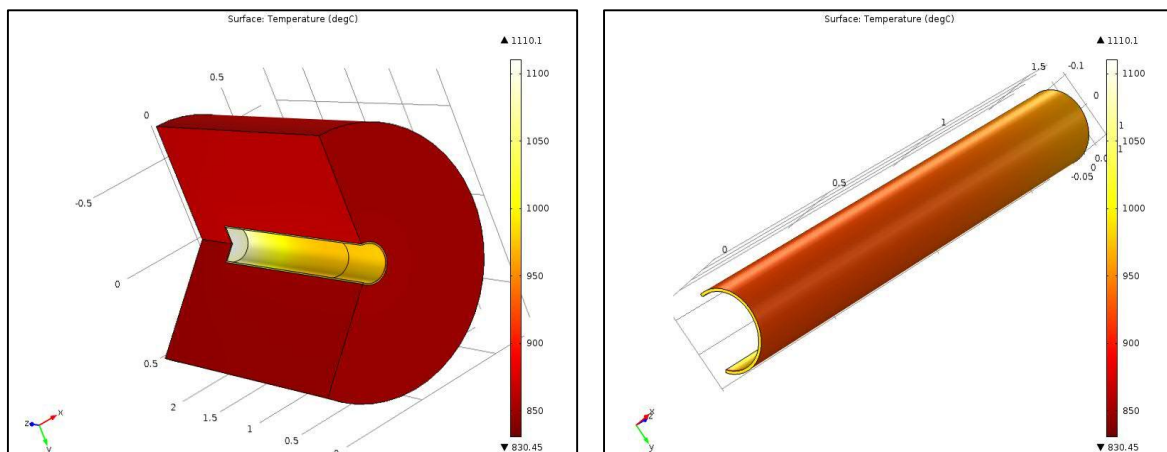
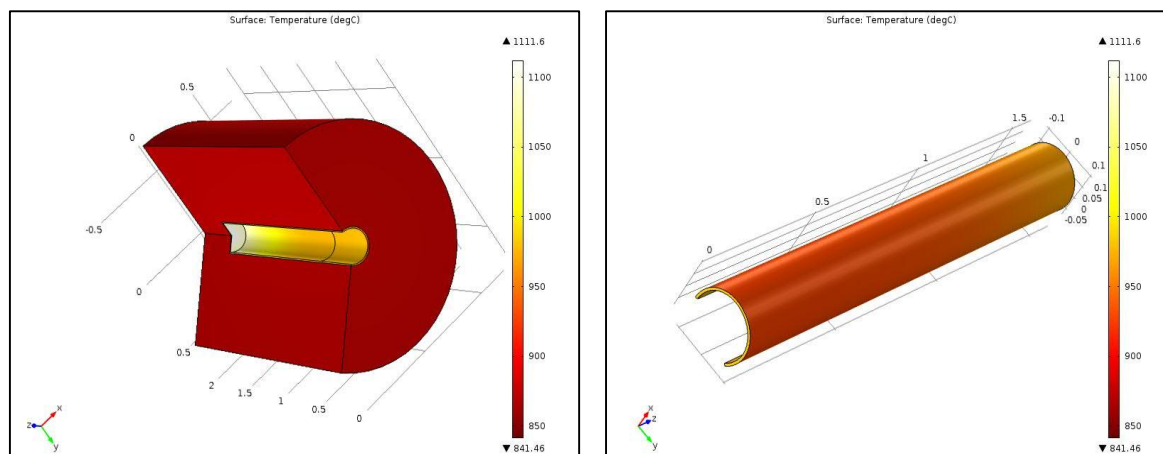
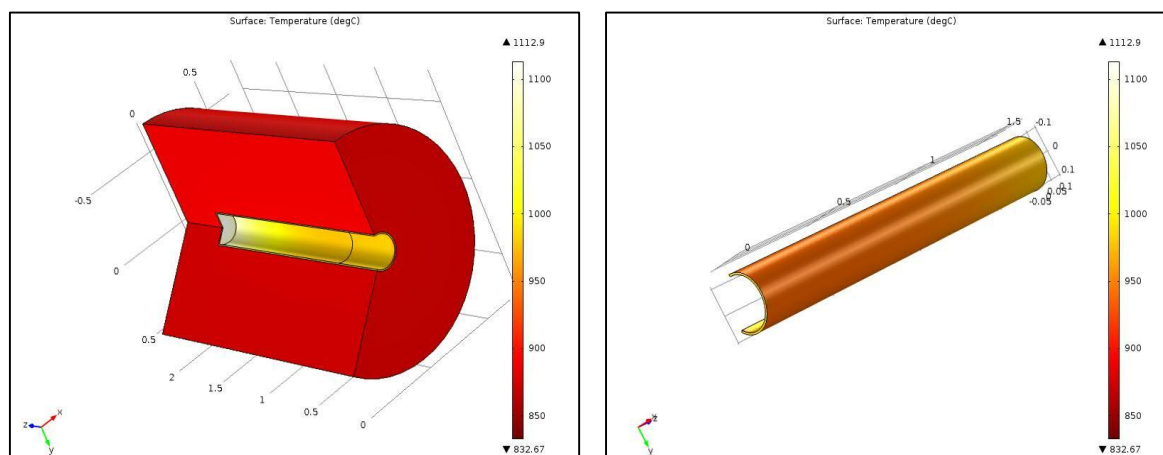


Figure 4.11 (a) Temperature distribution on the inner surface of the radiant tube and the surrounding furnace atmosphere in sub-zones 4, 5 and 6. (b) Temperature profile of the outer radiant tube surface in sub-zones 4, 5 and 6

(b) Sub-zone 7



(c) Sub-zone 8



Sub-zone 9

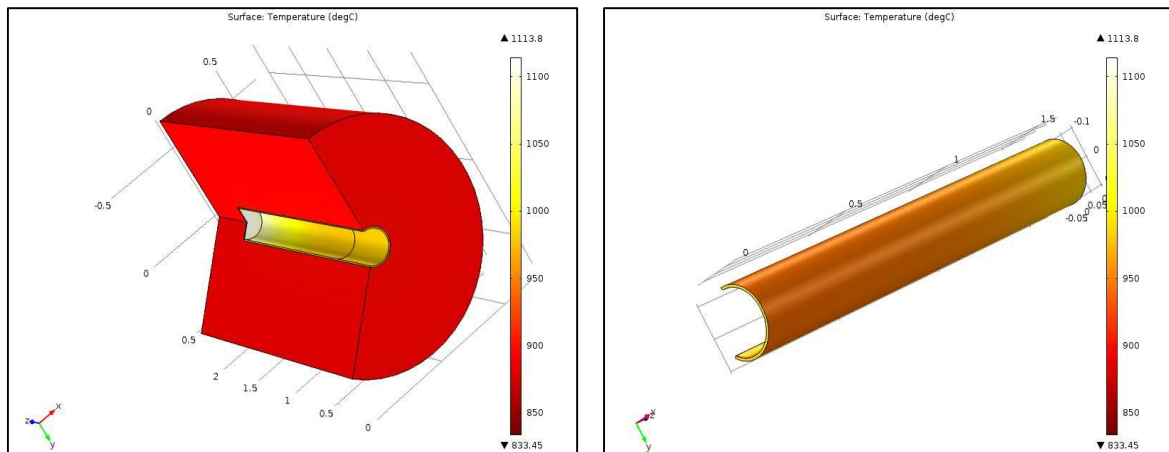


Figure 4.14 (a) Temperature distribution on the inner surface of the radiant tube and the surrounding furnace atmosphere in sub-zone 9 (b) Temperature profile of the outer radiant tube surface in sub-zone 9

(e) Sub-zone 10

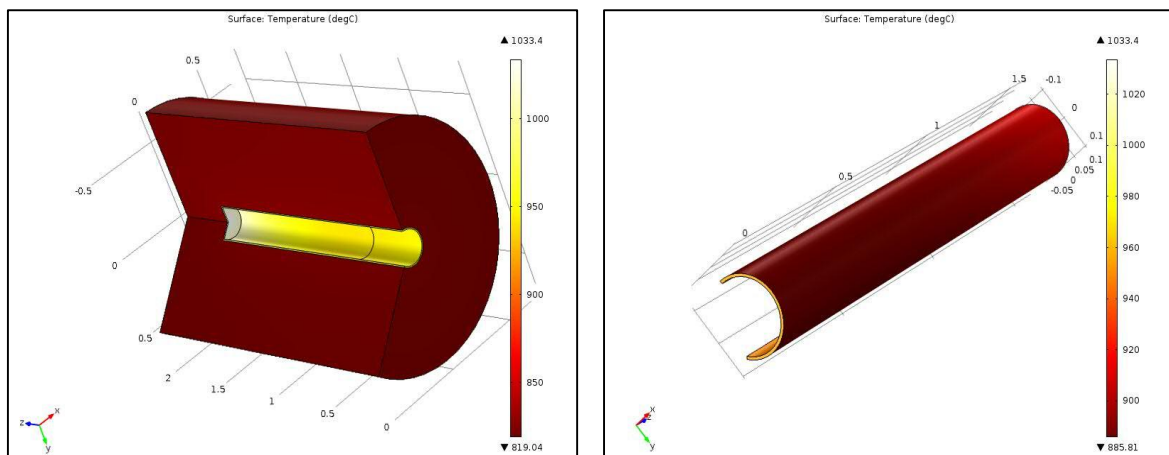


Figure 4.15 (a) Temperature distribution on the inner surface of the radiant tube and the surrounding furnace atmosphere in Sub-zone 10 (b) Temperature profile of the outer radiant tube surface in Sub-zone 10

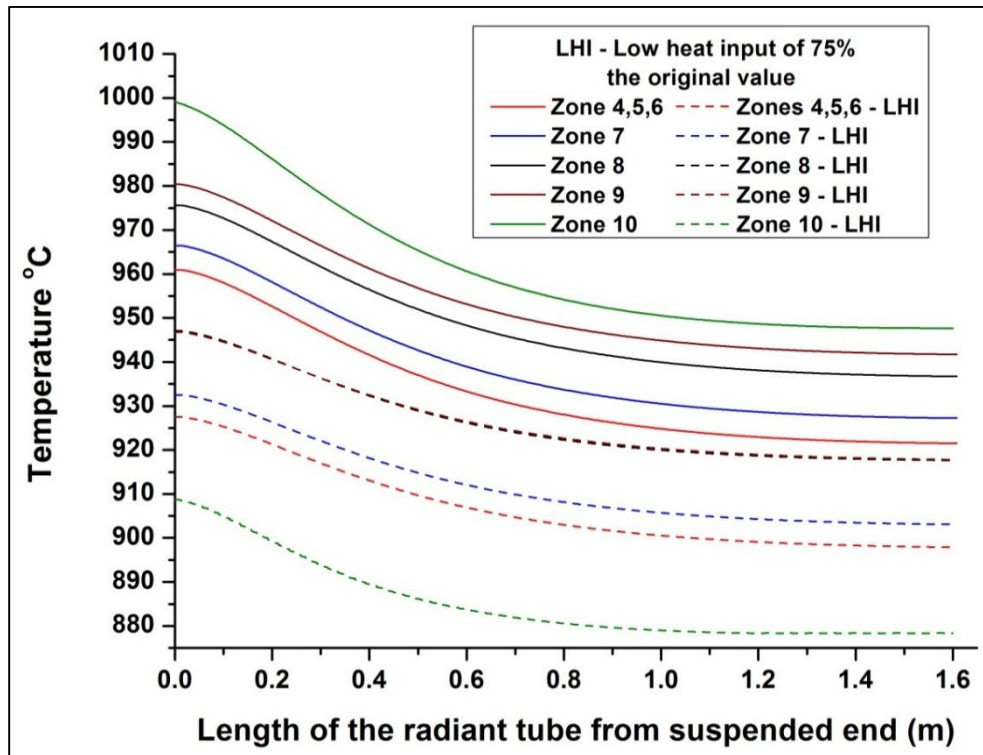


Figure 4.16 Comparison of temperature profiles on the surface of the radiant tubes in different sub-zones with full thermal rating of 37.5 kWh and a reduced heat input of 75% of the original value

A comparison of the change in the surface temperature due to reduction in the efficiency of the radiant tube during operation was also studied by reducing the efficiency of the radiant tubes by 25% (defined as LHI – Low heat input in further discussions) and is shown in figure 4.16. This was done by changing the thermal conductivity and emissivity properties of the radiant tube materials which changes in the course of operation due to deposition of compounds from the flue gases. The temperature loss from reduced heat input is much pronounced in the later heating zones due to the increased spacing in the radiant tubes in these zones and failure of a single radiant tube can cause a larger change in the temperature of the strip.

4.9.2 Part 2 - Full furnace model

The second part of the model was the full radiant tube heating section of the furnace. The results in this section show the temperature profile of the strip in small 0.53m sections. Boundary conditions are changed to simulate the movement of the 0.53m section in the radiant heating sub-zones of the furnace. The temperature distribution in the strip section of 0.53m length along the rolling direction and 1m width the transverse direction to rolling dimension is shown in figure 4.17. The edges are relatively hotter compared to the inside of the strip due to the heat conducted and radiated into the edge boundary.

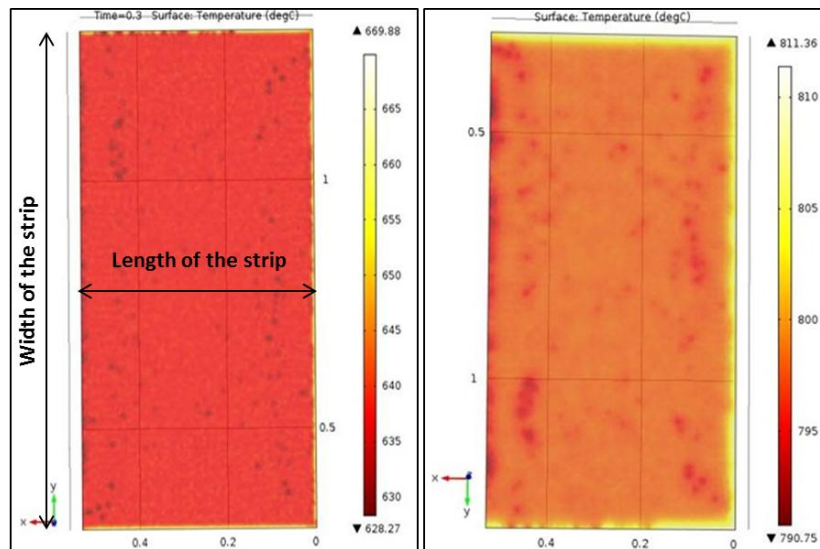


Figure 4.17 a) Temperature distribution of the strip section at the start of radiant heating zone 4 (b) Temperature distribution of the same strip section at the end of sub-zone 4

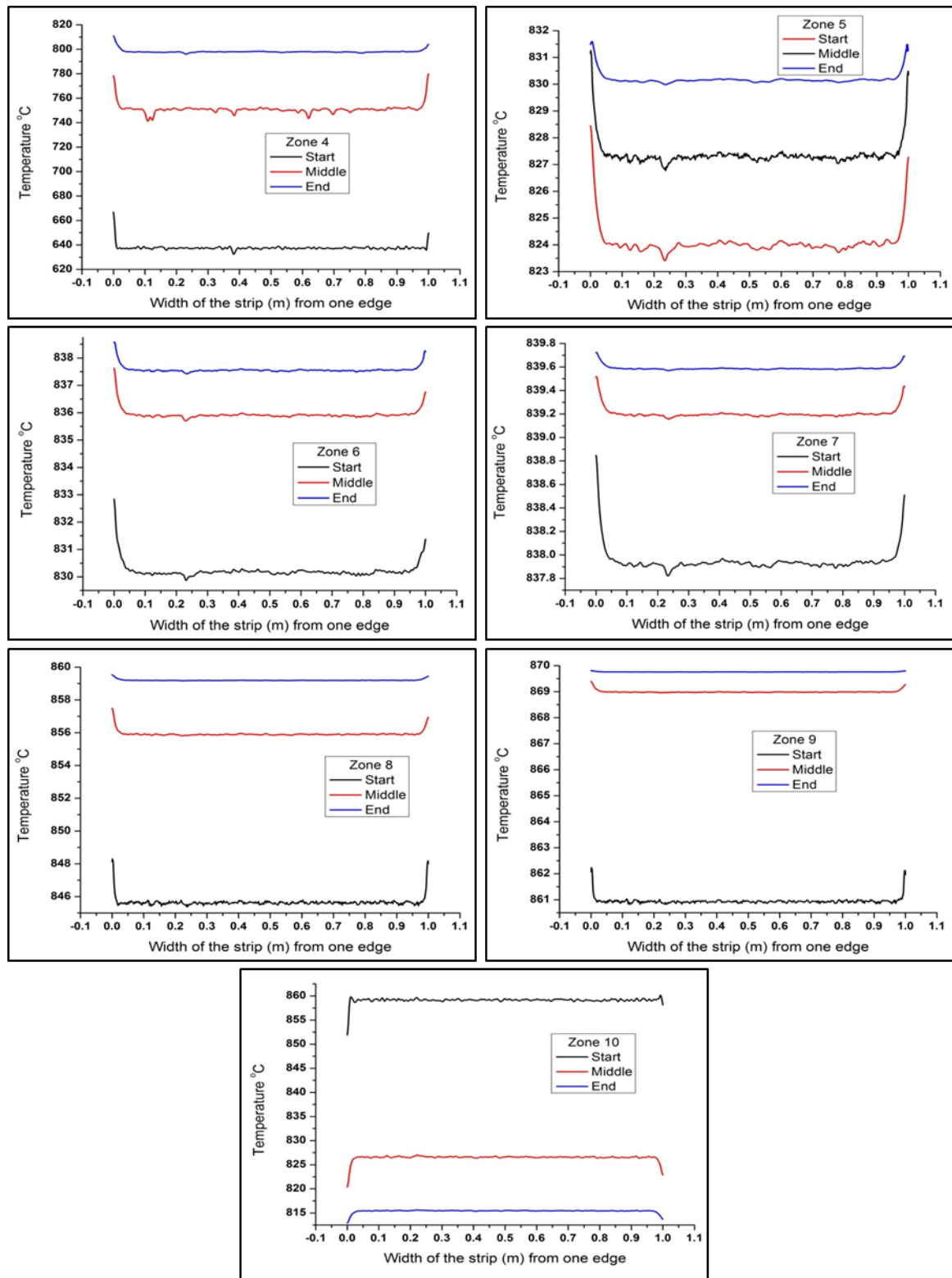


Figure 4.18 Comparison of the temperature across the strip width at the start, middle and end of radiant heating sub-zones 4 – 10 and at 90m/min strip speed

The temperature distributions in figure 4.17 are from the beginning and end of sub-zone 4 and are shown as an example. The temperature distribution at the beginning and end of each sub-zone is shown as a plot of temperature against length of the radiant tube from one step edge in figure 4.18. All sub-zone start and end comparisons are made at 90m/min strip speed.

4.9.3 Radiant cooling zone

The radiant cooling zone is very similar in geometry to the heating zone except that cold air flows through the tubes in this section resulting in controlled cooling of the steel strip down to about 600°C. This is an important zone to study because the cooling rates in this section can cause a profound effect on the final metallurgical and lattice defect structures of the material. Figure 4.19 shows the temperature profile of the small 0.53m section of the strip as it passes through the controlled cooling sub-zones 11 and 12. Figure 4.19 shows the comparison of strip temperatures at the beginning and end of controlled cooling sub-zones 11 and 12. All strip start and end comparisons are made at 90m/min strip speed.

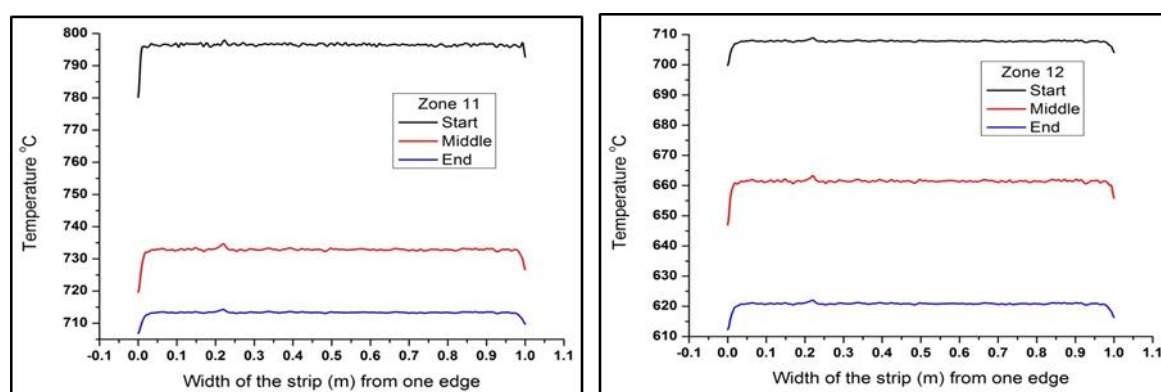


Figure 4.19 Comparison of the temperature across the strip width at the start, middle and end of radiant cooling sub-zones 11 and 12

4.9.4 Compressed air cooling zone

The 7.5m long compressed open air cooling zone was divided into five sections and the results are shown in figures 4.20 and 4.21. This is the final cooling section after which the strip is rolled into coils at about 300°C and allowed to cool in open natural convection.

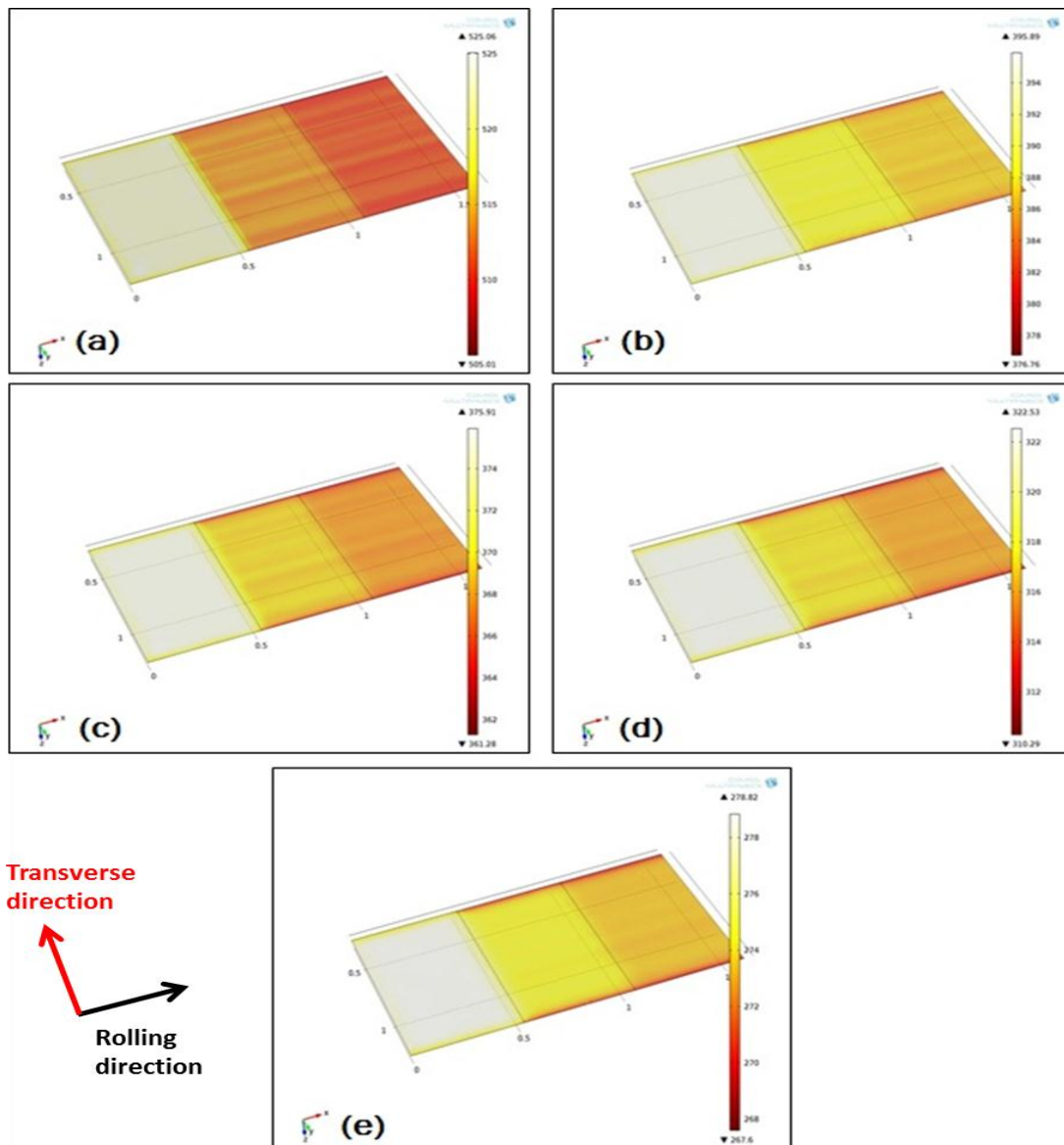


Figure 4.20 Temperature distribution of the strip in the open air cooling zone showing three 0.53m long strip sections combined into one section. Five time steps used to simulate the movement of the strip section in the open cooling zone

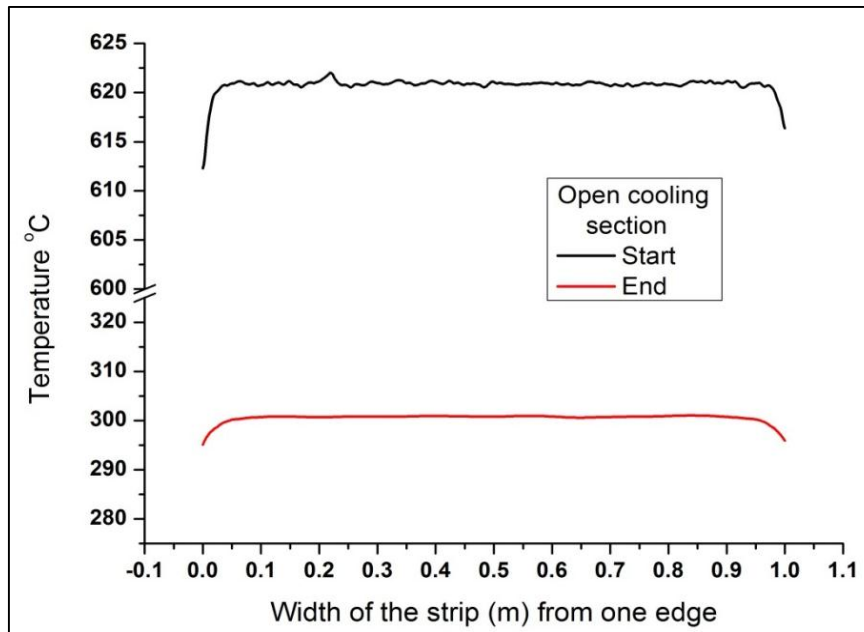


Figure 4.21 Comparison of the temperature across the strip width at the start and end of the open compressed air cooling zone

4.10 Discussion

(a) Radiant tube temperature distribution

The temperature distribution along the length of the radiant tubes is shown in figures 4.11-4.15. A temperature difference of approximately 35°C is observed between the suspended and fixed ends of the radiant tube. This gradient is due to the hot gases losing heat to the surroundings of the radiant tube thereby heating the inside of the furnace. An attempt was made to simulate the failure of a radiant tube that reduces the efficiency of the radiant tube by 25%. The reduction in efficiency in the plant furnace can be due to several reasons like reduction in emissivity of the tube surface as it ages, deposit of phosphoric acid precipitates from combustion waste all of which reduces the thermal conductivity and emissivity of the tube. The change resulted in a drop of 40°C in the radiant tube surface temperature as shown in figure 4.16. The effect of this reduction in surface temperature of one radiant tube in a furnace on the temperature distribution of the steel

strip is difficult to predict because of the uncertainty of failure in all the tubes in the furnace.

(b) Full furnace model

The full furnace model shows the strip is heated to 840°C at the end of sub-zone 6 after which the temperature is maintained at 850°C approximately throughout the heating zone as shown in Figures 4.22 - 4.24.

The temperature profile from the models created were compared with measured strip temperatures at three sub-zones in the flattening anneal furnace. The comparison of temperature profiles of the strip at different strip speed was calculated and compared with the corresponding measured values. Figure 4.22 shows the comparison at 90m/min strip speed and Figure 4.23 shows the comparison at 60m/min strip speeds. These speeds are selected because the actual furnace strip velocity is usually maintained between these two values.

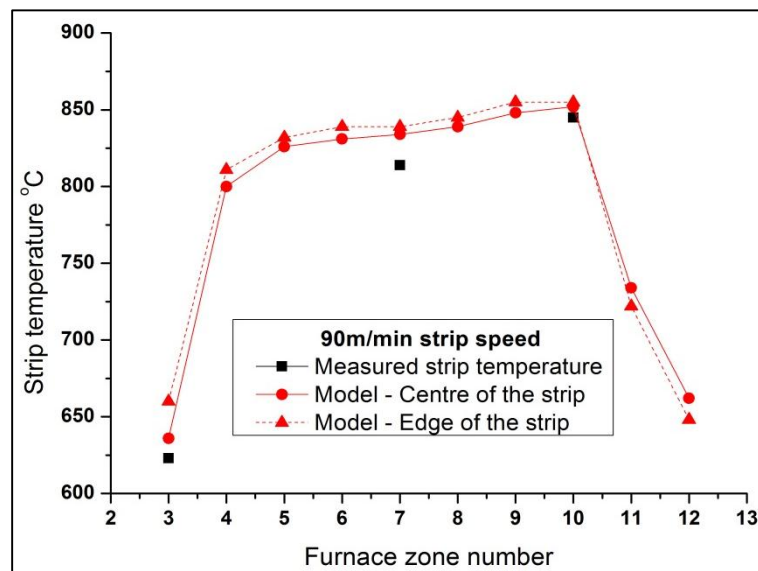


Figure 4.22 Comparison of measured and model temperature profile along the furnace length at a strip speed of 90m/min

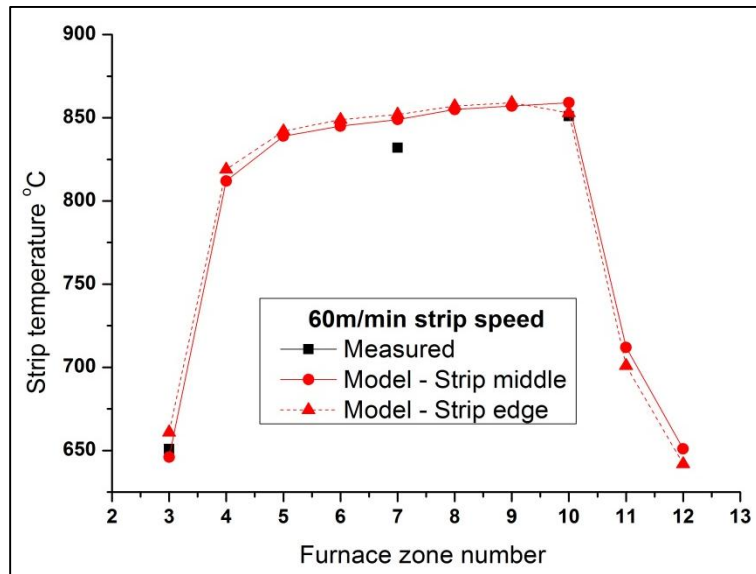


Figure 4.23 Comparison of measured and model temperature profile along the furnace length at a strip speed of 60m/min

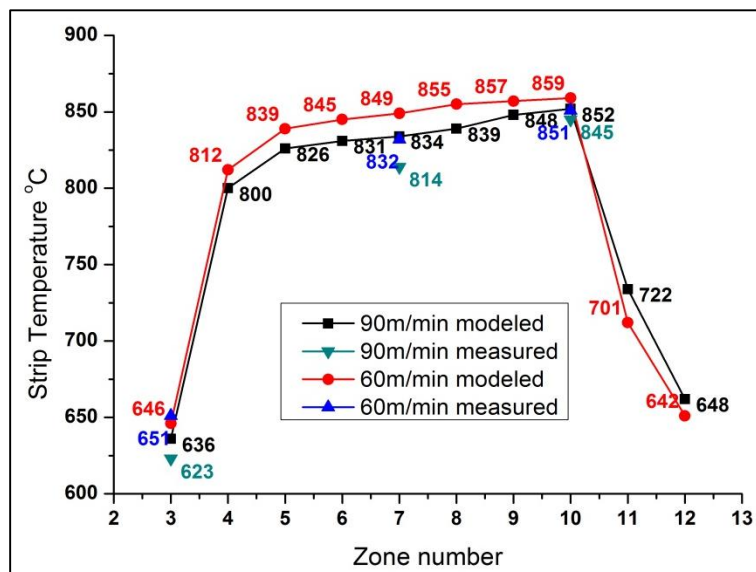


Figure 4.24 Comparison of modelled temperature profiles showing the effect of strip speed on the temperature profile of the strip

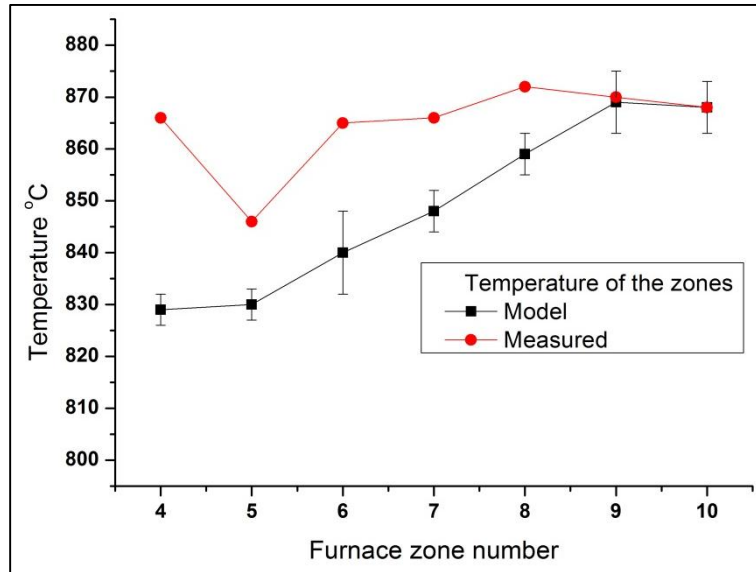


Figure 4.25 Comparison of modelled and measured zone temperatures as a function of different strip speed

The longitudinal strip temperature profile gives a clear insight into the heating rates and increase in temperature of the strip in each sub-zone. The changes in temperature in the controlled cooling zone and the cooling rates are of vital importance in understanding the creation and mobility of lattice defects. Though there is no metallurgical phase change in this material below 900°C, this data throws light on the possible configurations of lattice defects created and retained in the material. The rate of temperature change in radiant heating and controlled cooling zones are analysed and shown in Figure 4.26 below.

The major heat transfer mechanism is by surface-surface radiation and the zones at which the temperature difference between the strip and radiating tubes is the maximum resulting in the highest increase in surface temperature.

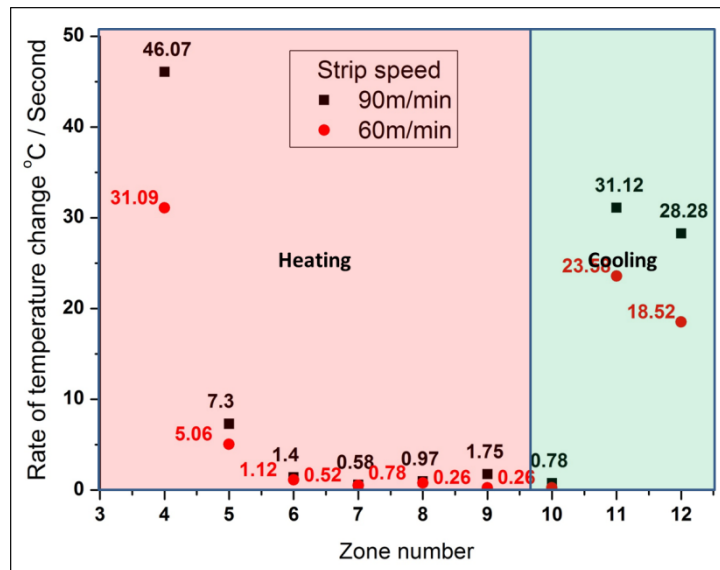


Figure 4.26 Comparison of rate of change in temperature in each sub-zone of the flattening anneal furnace between two strip speeds

The thermal model of the flattening anneal gives important insights into the process as discussed below:-

- The longitudinal and width-wise temperature profile of the strip.
- Heating upto 840°C happens in sub-zones 4-6 as the temperature increase is only 20° after these sub-zones.
- A temperature gradient is observed between the center and edges of the strip. The gradient lowers as the strip progresses through to the homogenization sub-zones.
- The temperature of the strip is homogenized at the later stages of the radiant heating sub-zones (sub-zones 8, 9 and 10).

(c) Error sources in the model

The temperature difference between the center and edges of the sample varied in the sub-zones where the heating rate is rapid as shown in Figure 4.18. The difference in temperature was about 20°C. This is due to the higher heat input by radiation along the

edge faces. This difference disappears as the strip moves into the homogenization sub-zones as shown in Figures 4.22-4.23.

There was always a small difference of about 20-30°C between the modelled and measured values of temperature of the sub-zones and the strip. Depree et.al[3]., reported there was a small difference between modelled and measured values due to slightly reduced temperature reading by the furnace pyrometers. This is due to the radiative loss to the relatively colder strip passing through the furnace. Depree [11] reported that the difference in modelled and measured values can be attributed to the radiative losses from the thermocouple sheaths. These are found to be slightly colder than the actual furnace walls because of the radiative heat losses to the colder strip that passes through and hence a slightly lower temperature. This helps explain the 20°C difference between measured and calculated zone temperature shown in Figure 4.25.

The continuous flattening anneal line model was in close agreement of $\pm 30^\circ\text{C}$ (3.5% difference at 850°C) with the measured pyrometer temperatures from the plant furnace. The data from the thermocouple measurement is sparse but shows the close agreement with the modelled data within 2-3%. In the holding sub-zones (near the end of sub-zone 10) the temperature is in total agreement with the different strip speeds and temperatures. All the temperature comparisons were made from the middle of the strip. Comparison with the edges of the strip show a bigger variation of temperature of up to 5% but there is no plant data available for cross comparison.

4.11 Conclusion

The following conclusions can be made from the heat transfer FEM model of continuous flattening anneal line

1. Temperature profile of the strip throughout the process of continuous flattening anneal is obtained.
2. There is always a temperature difference between the bulk and edges of the strip. This difference can be from 10°C to 30°C depending on the sub-zone at which the strip is present. At sub-zones 4 and 5 where heating rate is higher, the gradient is higher and eventually homogenizes as the strip progresses through the heating zone.
3. Sub-zones 4-6 are the main heating sub-zones after which the strip temperature is shown to be homogenized in sub-zones 7-9.
4. The temperature difference in the strip between the center and edges is negligible in the homogenization sub-zones.
5. The peak temperature of the strip at the end of homogenization sub-zone 9 is the same at 850°C irrespective of the strip speed changing from 60-90m/min.
6. Controlled cooling down to approximately 660°C depending upon the strip speed is attained after the controlled cooling sub-zones 11 and 12.
7. A temperature difference of 20°C exists between the modeled and measured sub-zone temperatures of the furnace.

4.12 References

1. M M Prieto, F J Fernandez, J L Rendueles, *Development of stepwise thermal model for annealing line heating furnace*, Ironmak Steelmak, 32 (2005) 165.
2. W Fei, W Yong Qin, Q Shu Ren, *Modeling of strip heating process in certical continuous heating furnace*, J Iron Steel Res Int, 19-5 (2012) 29.
3. N Depree, M P Taylor, J J J Chen, J Sneyd, S Taylor, S Wang, *Development of a three dimensional heat transfer model for continuous annealing of steel strip*, Ind Eng Chem Res., 51 (2012) 1790.
4. J L Battaglia, *Heat transfer in metal forming processes*, Wiley publishers, 4 (2008).
5. Y J Kim, D G Lee, H K Jeong, Y T Lee, H Jang, *High temperature mechanical properties of HK40 type heat resistant austenitic stainless steels*, J Mater Eng Perform, 19-5(2010)700.
6. J.R. Davis , *ASM Specialty Handbook: Heat-Resistant Materials*, ASM International, (1997) 361.
7. R F Redmond, J Lones, *Enthalpies and heat capacities of stainless steel, zirconium and lithium at elevated temperatures*, Internal document W-7405 Eng.26, Oak Ridge National laboratory, (1952)14.
8. *High temperature characteristics of stainless steels – A designer's handbook*, American Iron and Steel Institute, (1987) 12.
9. R Steiner, *ASM Handbook: Irons, Steels and High-Performance Alloys : Irons, Steels and High-Performance Alloys*, ASM International; 1(1990).
10. K Davis, *Alumina – material review*, EU School of Doctoral Studies Journal, (2010) 109.
11. J L Lytton, J A Hren, K T Kambers, O D Sherby, *Apparatus for the determination of dynamic Young's modulus and internal friction in vacuum at temperatures from 25° C to 1200°C*, Br. J. Appl. Phys., 15 (1964) 1573.
12. C P Kothandaraman, S Subramanyam, *Heat and mass transfer databook*, New Age International Publishers, 2004.

13. N Depree, J Sneyd, S Taylor, M P Taylor, J J Chen, S Wang, M O'Connor, Development and validation of models for annealing furnace control from heat transfer fundamentals, Computers and Chemical Engineering, 34 (2010) 1849.

Chapter 5

Deformation mechanism maps – Modelling of the deformation mechanism in GOES

5.1 Introduction

A deformation mechanism map is a method of representing deformation mechanisms that are predominant in a stress-temperature-strain rate variable space [1]. This chapter describes the method used to calculate a deformation mechanism map by experimental data from the literature into pre-defined model based rate equations that define different modes of creep deformation in a material. The purpose of the model was to study the effect of grain size of GOES on the deformation mechanism in the continuous flattening anneal process. The implications of these findings on the continuous flattening line are the ability to understand the change in deformation mechanism with varying strip thickness and the possibility of refinements in the process parameters to avoid creep by dislocation climb during the continuous flattening anneal process. Since the process is dynamic with wide variations in strip speed and furnace tension, the effect of stress, strain rate and grain size are prioritised in this study. The temperature profile of the strip from the heat transfer model was used to relate the continuous annealing process to the deformation mechanism maps. Two variations of GOES, HiB and CGO with typical average grain sizes of $10\pm 3\mu\text{m}$ and $3\pm 1\mu\text{m}$, were studied and the results compared. Furnace tension and thus stress applied to the strip material were recorded from the flattening anneal line and superimposed onto the deformation mechanism maps.

5.2 Background study on deformation mechanism maps

Ashby [2] in 1972 first reported the idea of deformation mechanism maps. The first deformation mechanism maps are a representation of stress–temperature variable space in which predominant deformation mechanisms by which the material undergoes deformation are plotted. The effect of strain rate is also taken into consideration. The main applications of this map are to study the effect of the crystal lattice on deformation mechanisms, understanding the deformation mechanisms by which a material deforms

and for the selection of suitable metal processing for optimum structural and functional properties [2].

Mohamed and Langdon [3] reported the effect of grain size on deformation mechanisms and subsequently on the deformation mechanism maps. The effect of different grain sizes at various stress-temperature combinations were calculated in pure aluminium. This paper illustrated the effect of small variations in grain size and their effect on deformation mechanisms.

Mohamed and Langdon [4] in 1978 improved their previous model and reported a deformation mechanism map for analysing creep data from high temperatures from $0.4T_m$ to T_m where T_m is the melting point of the material. They also explained a simple procedure to insert strain rate contours into the deformation mechanism maps to make it a three-dimensional process variable space.

Bendersky et al [5] reported the elevated temperature creep behaviour of pure body centred cubic molybdenum with emphasis on creep by dislocation climb. They also explained the relationship between stress-temperature and dislocations, their interaction, stacking fault energy etc., which are the substructural parameters. A wide variety of substructure evolution during high temperature creep was analysed in pure Mo. This helped in understanding the deformation mechanism in Molybdenum during thermo-mechanical processes and resulting functional properties.

Greenwood [6] explained the importance of analysing the microstructure of the material for the determination of the boundary between grain boundary sliding and diffusion controlled creep mechanisms.

Deformation mechanism maps were developed for a wide variety of materials with different crystal lattices to give background knowledge on the effect of various grain sizes, crystal lattice structure etc., on the deformation mechanisms [8-11]. Ashby and Frost defined the method of constructing a deformation mechanism map from experimental

mechanical test data [1]. This mechanical test data is utilized in the model in this study to understand the deformation mechanism in GOES.

5.3 Materials – Chemical composition and grain structure

The chemical composition and the grain structure of the two types of GOES under study are shown below. The samples had equiaxed grains as shown in Figure 5.1 with an nominal grain size of $3\pm 1\text{mm}$ for CGO and $10\pm 3\text{ mm}$ for HiB. The composition of the alloys is shown in Table 5.1 and the subsequent phase diagram of the iron rich side in figure 5.2 shows there is no phase change (red line in figure 5.2) and the material parameters remain unaltered at temperatures in study.

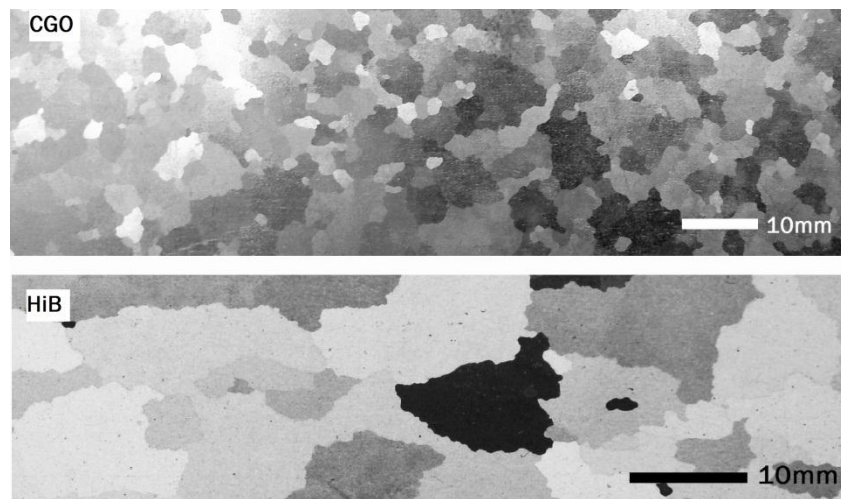


Figure 5.1 Grain structure of CGO (top) and HiB (bottom) in study

Table 5.1 Composition of the two materials – CGO and HiB under study

Material EN 10707 [12]	C	Si	Mn	P	S	Al	N	Cu	Sn	Ti	Fe
M120-27S (CGO)	0.037	3.15	0.06	0.014	0.021	0.03	0.005	0.12	0.03	0.0025	Rest
M103-27P (HiB)	0.06	3.15	0.08	0.02	0.023	0.028	0.008	0.07	0.08	0.0032	Rest

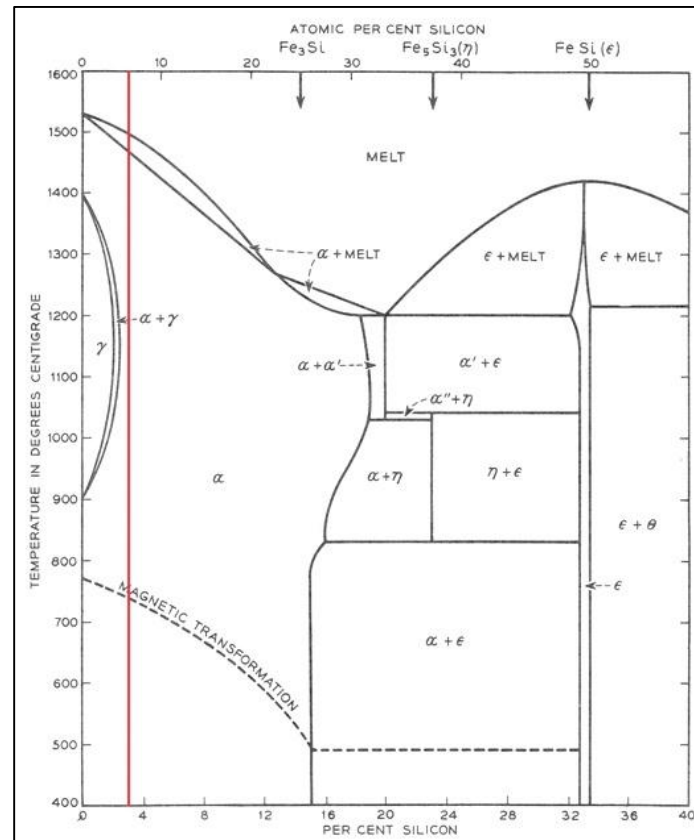


Figure 5.2 Phase diagram of the Iron rich side of Fe-Si binary system [13]

5.4 Model and Program

5.4.1 Deformation modes in the model

The following deformation modes were included in this model. The deformation mechanism space was divided into five major creep mechanisms:

- Coble creep or grain boundary diffusion creep
- Nabarro Herring creep or lattice diffusion creep
- Dislocation core climb
- Lattice climb
- Plasticity region

Grain boundary diffusion and lattice diffusion creep as the name suggests are diffusion controlled mechanisms while the dislocation core climb and lattice climb belong to the power-law creep and are dislocation controlled mechanisms. The diffusion controlled mechanisms depend on the diffusion of atoms (or dislocations) over large areas in the grain or on the grain boundaries and thus have an inverse dependence on the grain size. The power law creep mechanisms are dependent on the ability of dislocations to climb and hence are stress and temperature dependent and are independent of grain size [1]. These mechanisms and their corresponding model based rate equations are discussed below.

5.4.2 Rate equations

Diffusion creep occurs by the diffusion of atoms or vacancies caused by free energy gradient between different parts of the grain. The diffusion co-efficient along both the boundary (Coble creep) and lattice (Nabarro-Herring creep) are added to produce the effective diffusion co-efficient. The following equations [2] were used to calculate the strain rate component by diffusion creep:-

$$\dot{\epsilon}_{df} = \frac{42\tau\Omega D_{eff}}{kTd^2} \quad (1)$$

$$D_{eff} = D_v + D_b \left[\frac{\pi\delta}{d} \right] \quad (2)$$

The rate determining steps of creep by dislocation climb are the ability of dislocations to climb through the lattice at higher temperatures and along the dislocation core at lower temperatures. Climb of dislocations happens by diffusion of vacancies to or from the dislocations. Thus the rate equations [2] have both the core and lattice diffusion co-efficient of vacancies.

$$\varepsilon_{pl}^{\circ} = \frac{A_2 \mu b D_{eff}}{kT} \left(\frac{\tau}{\mu} \right)^n \quad (3)$$

$$D_{eff} = D_v + D_c \left[\frac{10 a_c}{b^2} \left(\frac{\tau}{\mu} \right)^2 \right] \quad (4)$$

where,

D_{eff} - effective diffusion coefficient

a_c - area of the dislocation core

D_v - the lattice diffusion coefficient

D_c - core diffusion coefficient

δ - thickness of the grain boundary - 5 Å

τ - shear stress

μ - shear modulus of the material

k - Boltzmann constant

T - absolute temperature

d - grain size

b - Burger's vector of the dislocation

D_b - boundary diffusion coefficient

Ω - atomic volume

n - stress exponent

5.4.3 Flowchart of the program

The flowchart of the program developed to calculate the strain components from various modes of deformation and compare them to determine the predominant deformation mechanism at a given combination of stress, homologous temperature and strain rate is shown in Figure 5.3. The full program can be found in Appendix 5.1. The method of construction is adopted from the deformation map model developed for Fe-Cr-Al oxide dispersed (PM2000) alloy [14] and the code was developed in 'C'- language for GOES to calculate the deformation mechanisms.

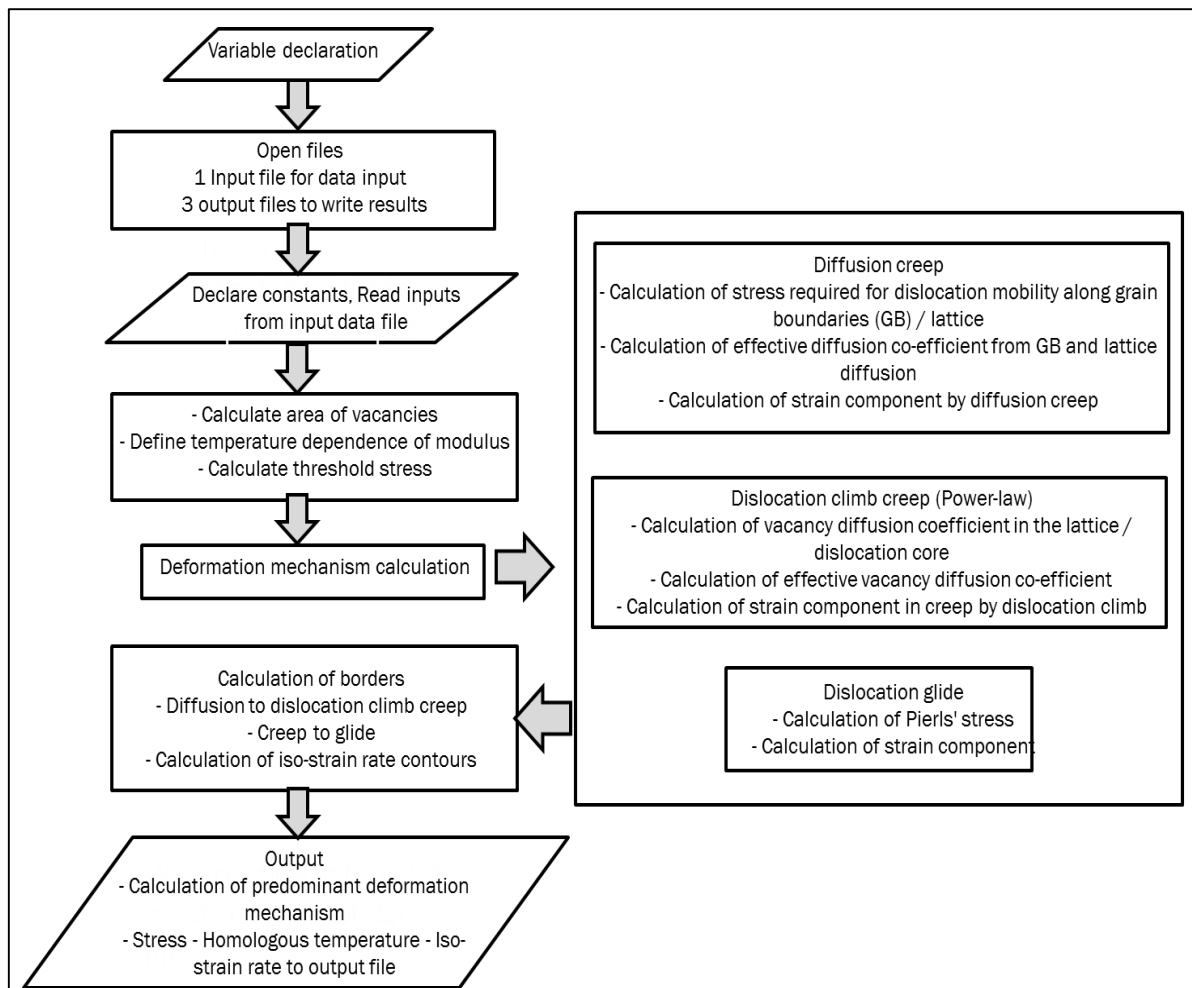


Figure 5.3 Flowchart showing the functions of the program to calculate deformation mechanism maps

5.4.4 Input data

The input data for the calculation of the model were as follows. The input data were fed into the model program as a separate data file. The program is shown in Appendix 5. 1. Table 5.2 elaborates the input data and their units.

Table 5.2 Variables used in the deformation mechanism map code

No.	Variable	Units
1	Grain size of the material (Before recrystallization)	m
2	Grain size of the material (After recrystallization)	m
3	Dislocation density	1/m ²
4	Diffusion co-efficient	m ² /s
5	Activation energy for self-diffusion	J/mol
6	Shear modulus	Pa
7	Burger's vector	M
8	Strain rate	s ⁻¹

5.4.5 Material parameters and kinetic analysis

The flow stress for steady state flow is related to temperature and strain rate through an Arrhenius equation with the strain rate exponent ' n ' and activation energy ' Q '. The calculation of the strain rate exponent and activation energy is important for the determination of deformation mechanisms at different stress-strain rate-temperature combinations. This is shown in figures 5.4 and 5.5 below. The values of the stress exponent and the activation energy were calculated from experimental creep data from the literature [15-20]. The stress exponents calculated for the different temperature ranges are shown in Figure 5.4.

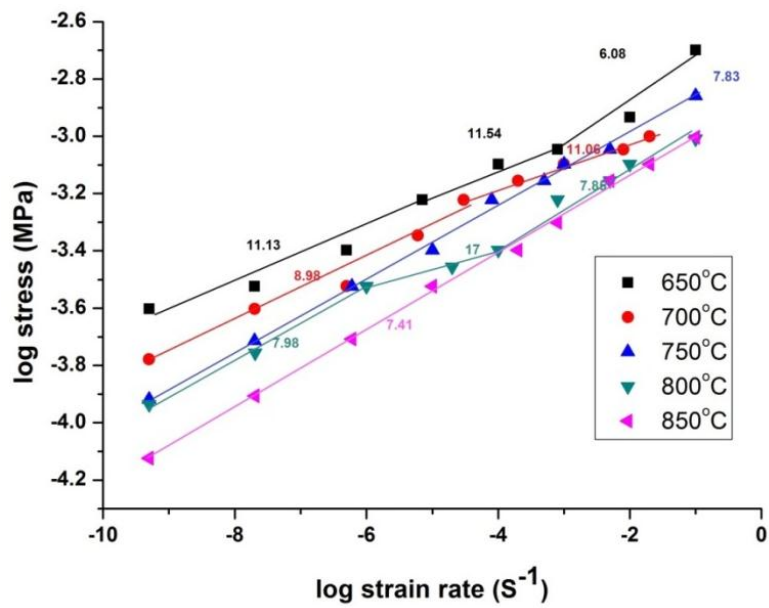


Figure 5.4 Calculation of stress exponent ‘n’ from experimental data obtained from literature [15-20]

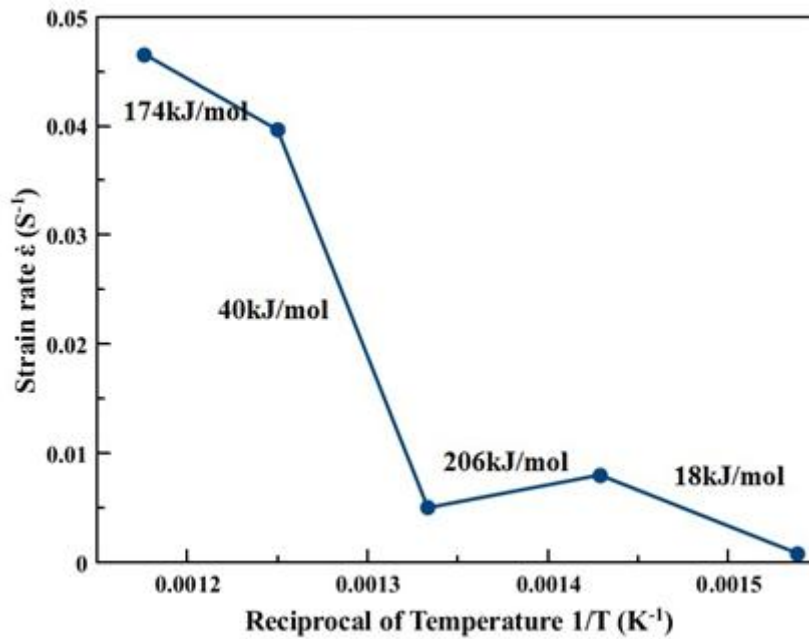


Figure 5.5 Calculation of activation energy ‘Q’ – Figure showing strain rate as a function of reciprocal of temperature at constant normalised stress [15-20]

There is a possibility of experimental variations causing small variations in the data shown in Figure 5.4 and 5.5. However in case of stress exponent, since the calculation is made across a wide range of strain rates, the effect of experimental data variation on the

final deformation mechanism model is minimal. The calculated activation energy was 176 kJ/mol for core diffusion which is consistent with the activation energy calculated for the same mechanism in α -iron to be 174 kJ/mol by Ashby et al [1]. The activation energy for boundary diffusion was found to be 206 kJ/mol and is higher than 174 kJ/mol reported for α -iron by Asbhy et al [1].

5.5 Results

Deformation mechanism maps showing the stress-temperature-deformation mode correlation are shown in the following figures 5.6 and 5.7.

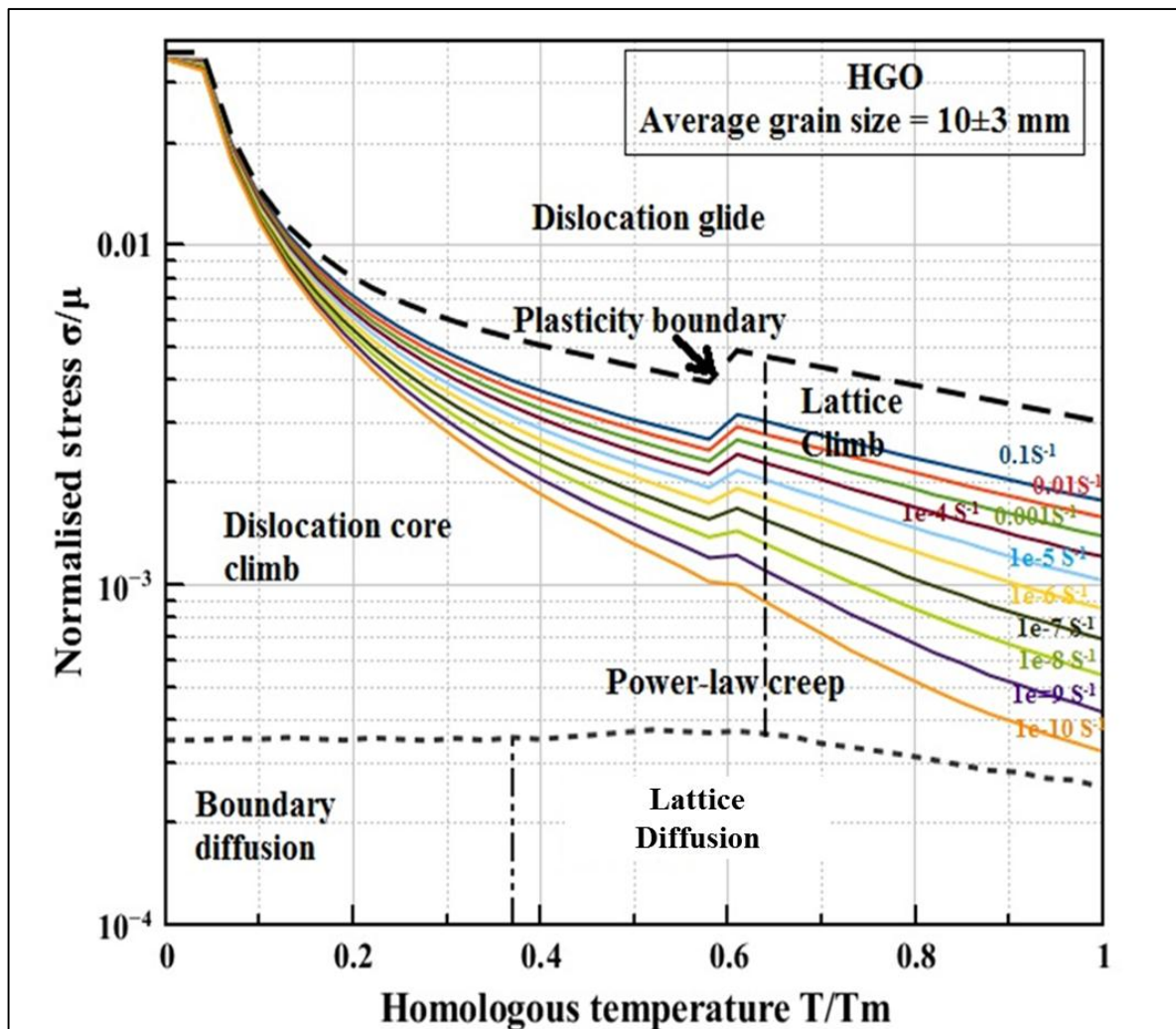


Figure 5.6 Deformation mechanism map for HiB material with an average grain size of 10mm at different strain rates

Iso-strain rate contours are super-imposed on the map to show the effect of strain rate on changes in deformation mechanism.

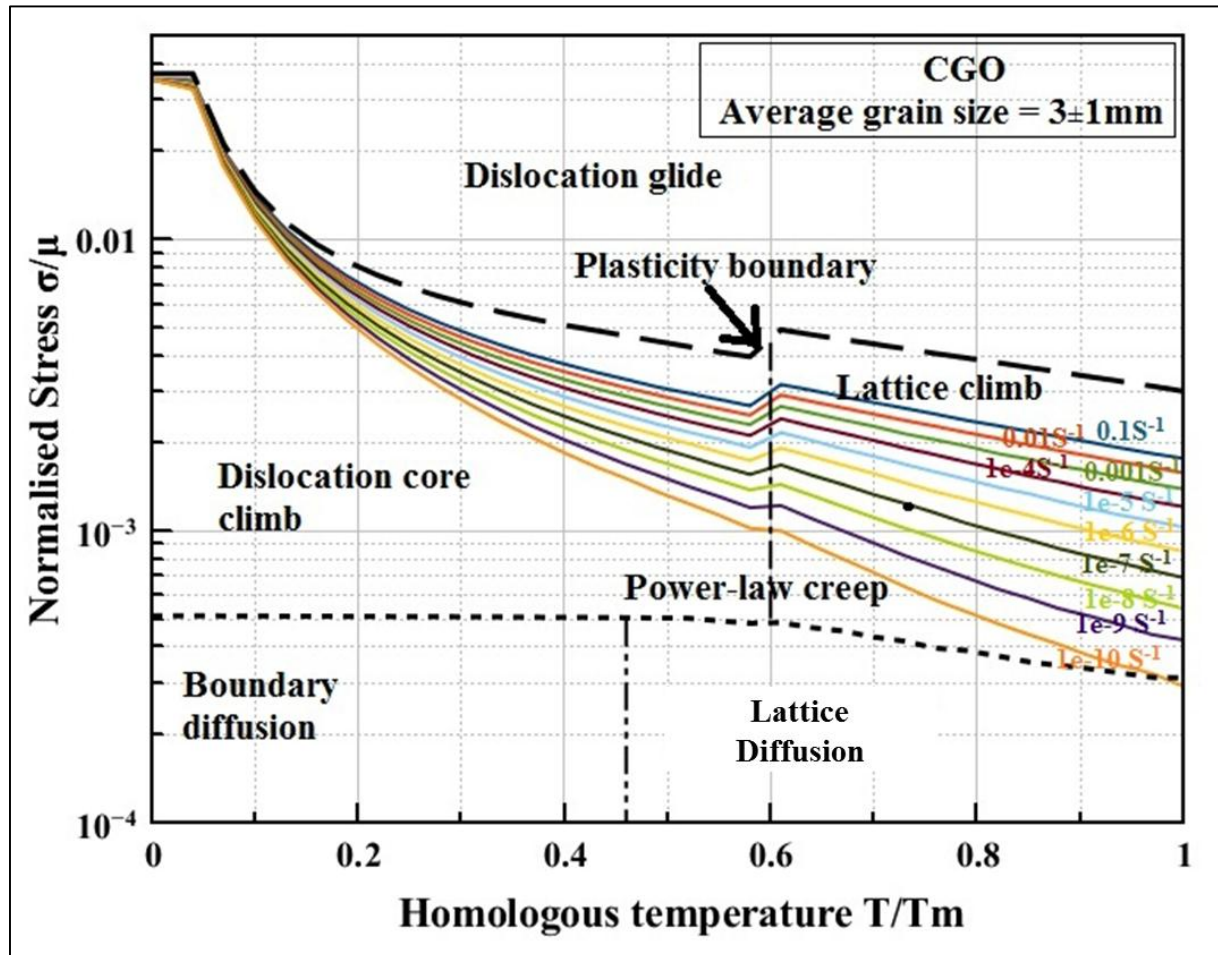


Figure 5.7 Deformation mechanism map for CGO material with an average grain size of 3mm at different strain rates

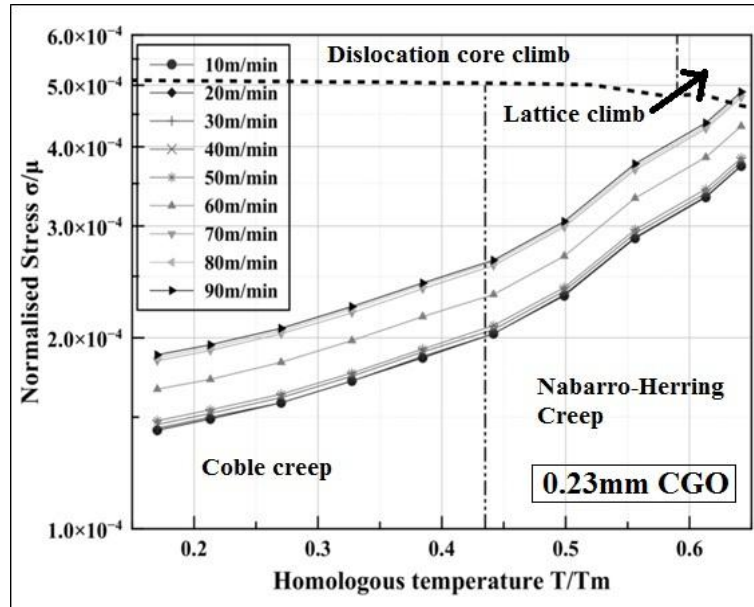


Figure 5.8 Deformation mechanisms at different stress-temperature combinations and line speeds during the continuous annealing of 0.23mm thick CGO strip

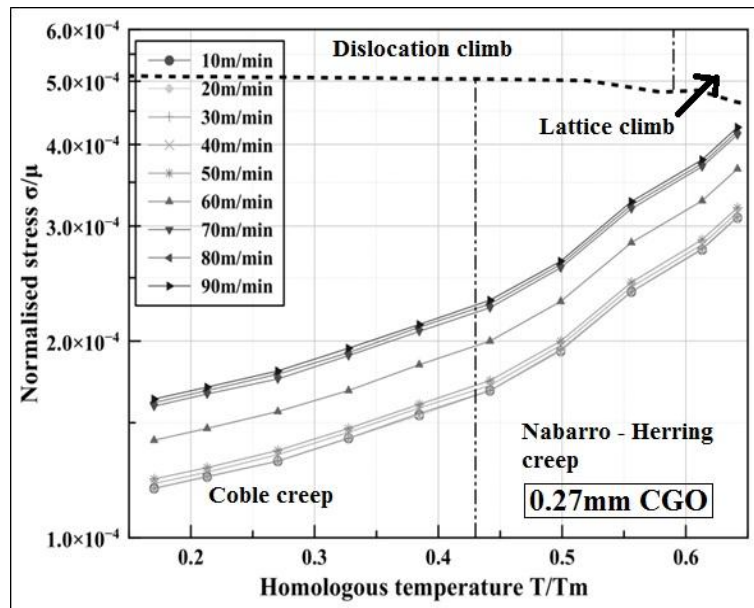


Figure 5.9 Deformation mechanisms at different stress-temperature combinations and line speeds during the continuous annealing of 0.27mm thick CGO strip

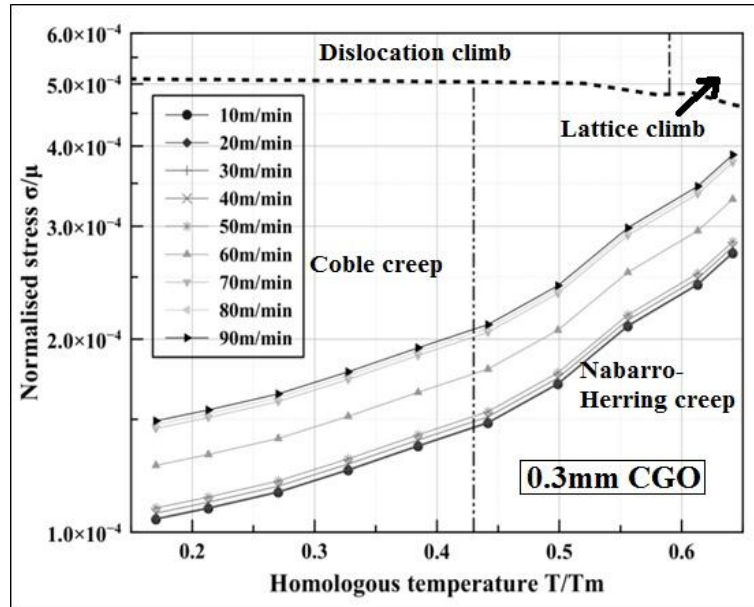


Figure 5.10 Deformation mechanisms at different stress-temperature combinations and line speeds during the continuous annealing of 0.3mm thick CGO strip

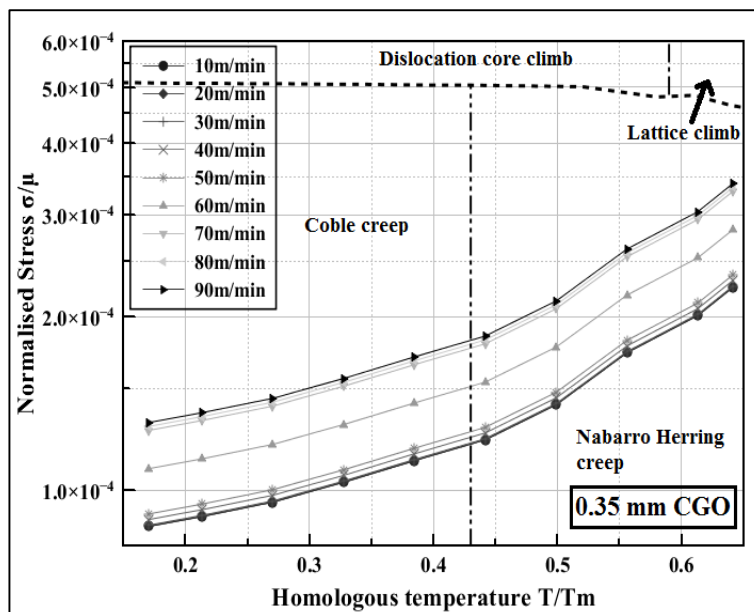


Figure 5.11 Deformation mechanisms at different stress-temperature combinations and line speeds during the continuous annealing of 0.35mm thick CGO strip

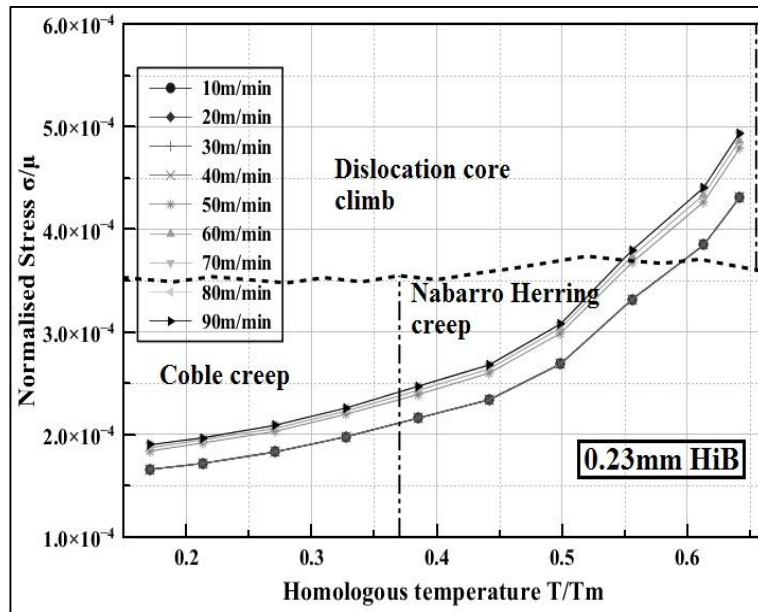


Figure 5.12 Deformation mechanisms at different stress-temperature combinations and line speeds during the continuous annealing of 0.23mm thick HiB strip

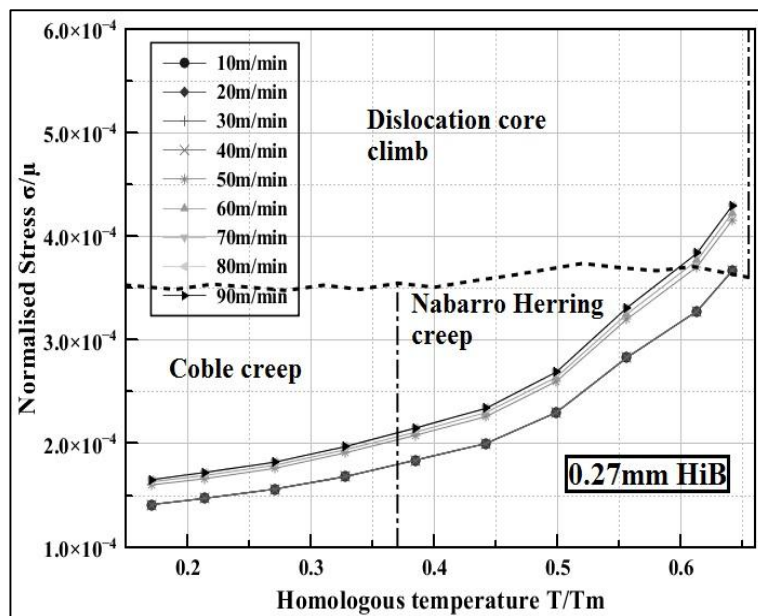


Figure 5.13 Deformation mechanisms at different stress-temperature combinations and line speeds during the continuous annealing of 0.27mm thick HiB strip

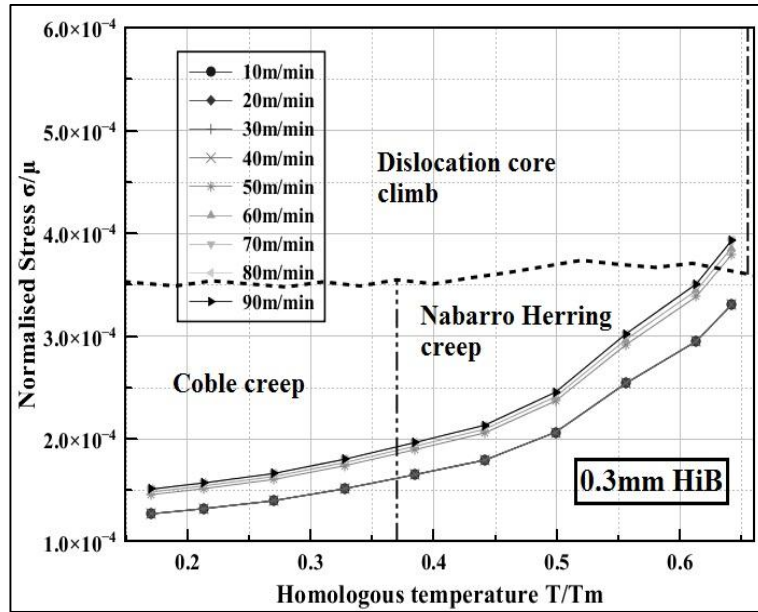


Figure 5.14 Deformation mechanisms at different stress-temperature combinations and line speeds during the continuous annealing of 0.3mm thick HiB strip

5.6 Discussion

The deformation mechanisms in GOES were calculated for two classes of material with different average grain sizes of 10 mm and 3 mm respectively. The deformation mechanism maps for CGO and HiB are shown in Figures 5.6 and 5.7 respectively. Values of stress normalised by shear modulus of the material are plotted against the temperature with different iso-strain rate bars incorporated into the plot. The process stress data is normalised with the shear modulus of the material at various temperatures for two reasons (i) to plot the mechanical tests for the same class of materials (by crystal structure) into a single master curve and (ii) to classify materials into iso-mechanical groups (groups with similar mechanical behaviour) [1].

The deformation mechanism maps in Figures 5.6 and 5.7 are broadly classified into diffusional creep, dislocation creep and glide.

5.6.1 Diffusional creep

Diffusional creep is the predominant deformation mechanism for the most part of the process as shown in Figures 5.6 to 5.7. Two salient features were identified from the deformation mechanism maps for HiB and CGO.

- Coble creep or creep by diffusion along grain boundaries is the predominant deformation mechanism in CGO up to 520°C whereas in HiB it takes place only up to 375°C above which Nabarro-Herring creep or creep by lattice diffusion takes over as the major deformation mechanism. This is because the grain boundary area available for grain boundary diffusion in CGO is higher than that in HiB, since the grain size is approximately one-third of HiB and less grain boundary area. The rate of Coble creep is inversely proportional to the grain size of the material [1]. In the case of HiB, the activation energy of Coble creep is higher compared to that of CGO because of the larger grains and smaller grain boundary area and hence Nabarro-Herring creep takes over as the preferred mechanism at temperatures above 375°C. The mechanisms of Coble and Nabarro-Herring creep are illustrated in Figure 5.15. In both the cases, the diffusion of vacancies is driven by the difference in free energy caused by the variation in hydrostatic stress at different parts of the grain. When tension is applied to the grains, the ends of the grains in the direction of applied force are subjected to high hydrostatic stress compared to the central part of the grains. This results in a gradient of free energy that drives the diffusion of vacancies towards the ends of the grain from the centre of the grains [21].

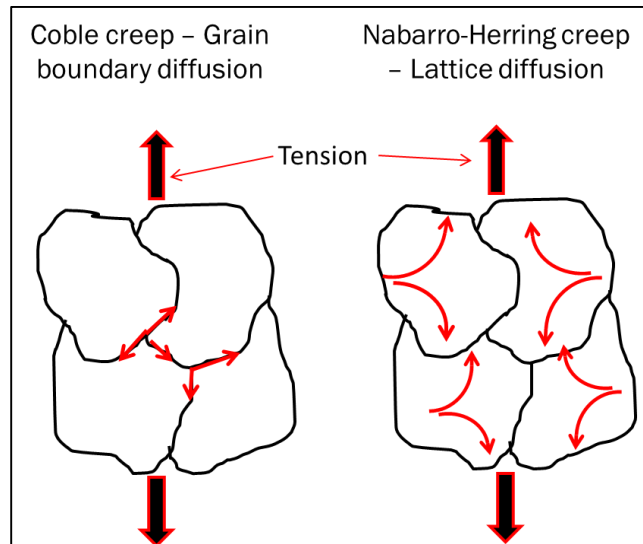


Figure 5.15 Mechanism of Coble and Nabarro-Herring creep [20] Red lines indicating the path of diffusion

- The boundary at which creep by vacancy diffusion changes to creep by dislocation climb is at a higher normalised stress in CGO than in HiB as shown in Figures 5.6 and 5.7. This is again due to the inverse relationship of the diffusion creep phenomenon with grain size. CGO with smaller grain size is more prone to diffusion creep than HiB which is approximately nine times larger than CGO grain size in area.

5.6.2 Dislocation creep

Dislocation creep happens at high stress and temperature conditions. The rate of dislocation creep is higher at higher temperatures. The rate defining mechanism here is the ability of dislocations to climb. The low temperature climb phenomenon takes place by diffusion of vacancies to the dislocations mainly assisted by stress. Here the diffusion of vacancies is localised and happens very close to the core of the dislocations. This is indicated as the dislocation core climb in low temperature region of the deformation mechanism maps shown in figures 5.6 and 5.7. At higher temperatures, atomic diffusion becomes easier since the atoms gain energy to overcome the energy barrier to diffuse into the lattice thereby increasing the mobility of vacancies. This diffusion of vacancies

increases the ease of dislocation climb and hence climb by lattice diffusion of vacancies is the predominant at high temperature regions of the creep by dislocation climb.

5.6.3 Effect of strip thickness and line speed on deformation mechanism

The calculation of stress applied on the samples with varying line speeds and strip thickness is shown in Appendix 5.2 and figures 5.8-5.14. The stresses applied on CGO and HiB strips of various thicknesses and line speeds are plotted against the temperature until 850°C on the deformation mechanism map. Change in deformation mechanism as the strip passes through different zones of the furnace was analysed using the temperature profile obtained from the heat transfer model described in Chapter 4.

The main observations from the superimposition of the stress-temperature relationship from the continuous annealing process on the deformation mechanism maps for GOES are

CGO strip of thickness from 0.23-0.35 mm undergoes diffusional creep at strip speeds upto 90m/min. The only exception is 0.23mm CGO strip at strip speeds above 80m/min where the predominant deformation mechanism changes to climb of dislocations through the lattice.

Deformation mechanisms of HiB strips vary from Nabarro-Herring creep to dislocation core climb with increasing temperature. The shift in dominant deformation mechanism happens between 700-820°C depending on the thickness of the material and line speed.

5.6.4 Combining the heat transfer model with deformation mechanism

This information obtained from the deformation mechanism maps is correlated with the thermal profile of the steel strip inside the continuous annealing furnace from the

heat transfer model explained in Chapter 4. The temperature data for the strip at each zone obtained at different strip speeds from the previous model was compared with Figures 5.6 to 5.7 that show the change in deformation mechanism with strip thickness and drive speed. The results of this comparison are shown in figures 5.16 - 5.20 which explain the change in deformation mechanism for CGO and HiB at different strip thickness and speed as it passes through the various zones of the furnace.

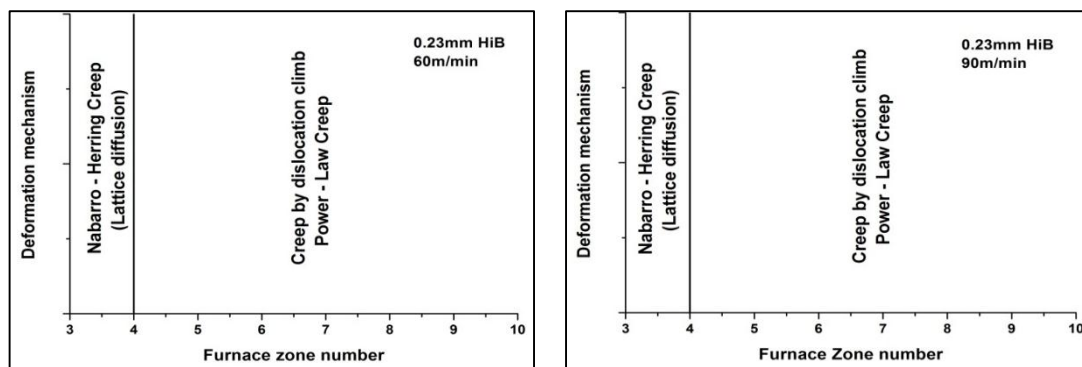


Figure 5.16 Comparison of deformation mechanisms as the strip passes through different zones for 0.23mm thick HiB strip at two different strip speeds

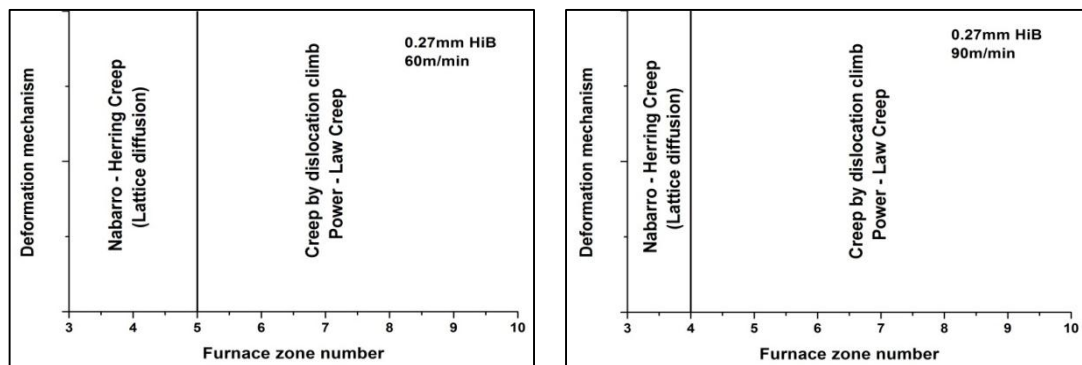


Figure 5.17 Comparison of deformation mechanisms as the strip passes through different zones for 0.27mm thick HiB strip at two different strip speeds

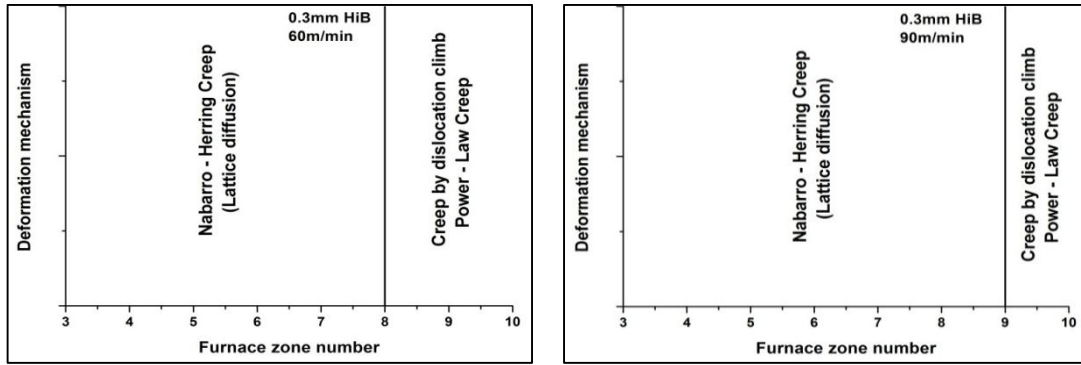


Figure 5.18 Comparison of deformation mechanisms as the strip passes through different zones for 0. 3mm thick HiB strip at two different strip speeds

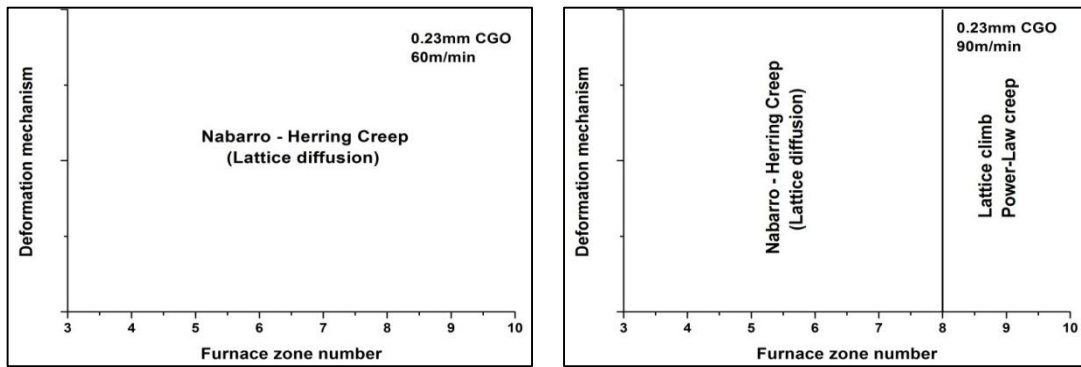
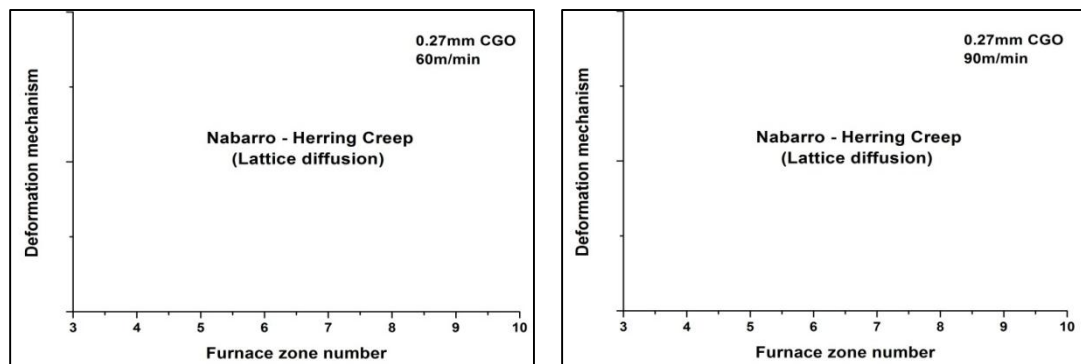


Figure 5.19 Comparison of deformation mechanisms as the strip passes through different zones for 0.23mm thick CGO strip at two different strip speeds



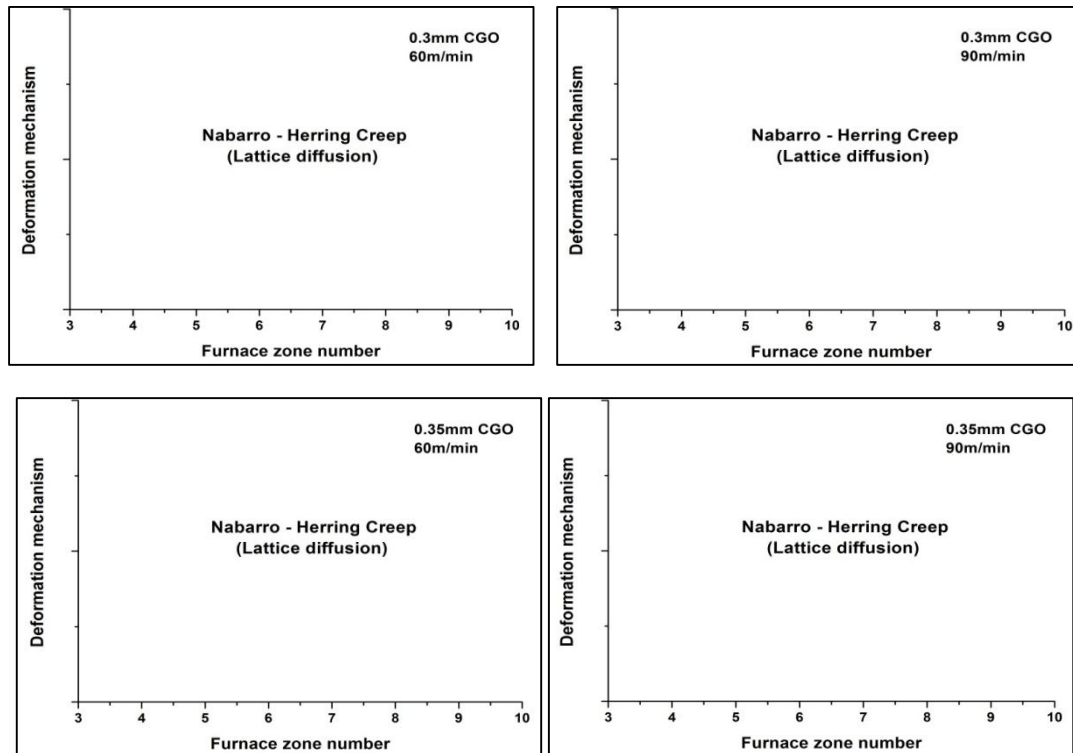


Figure 5.20 Comparison of deformation mechanisms as the strip passes through different zones for 0.27, 0.3, 0.35mm thick CGO strips at two different strip speeds

The line speed at which the strip passes through the continuous annealing line causes some changes in the zone at which the deformation mechanism changes from diffusion to dislocation climb creep. This shift is because of the change in stress. A temperature effect is absent because of the negligible difference in peak temperature depending on the strip speed. Since temperature is not a contributing factor as explained above, the climb assisted creep phenomenon is similar in all line speeds.

The variables that cause the big shift in deformation mechanism are the strip thickness and grain size. Strip thickness results in changing deformation mechanism because of the change in the stress applied to the strip as shown in Appendix 5.2. The dependence of the deformation mechanism on diffusion and applied stress resulted in a large shift in deformation mechanisms.

The model was successful by achieving the following objectives

- creating an understanding of the deformation mechanisms at different process parameter combinations in thermal flattening anneal line

- combination of model and process data provided possible changes to process parameters to maintain the deformation mechanism in diffusion creep range

However the author acknowledges the errors arising out of experimental data from the literature used in the model could influence the model and further experimental work needs to be done before the knowledge from this model can be implemented in the process.

5.7 Conclusions

1. The model shows the predominant deformation mechanism during the continuous flattening anneal process of GOES which is significant in understanding the formation of lattice defects.
2. The use of experimental data from literature to calculate the activation energy was reliable as shown in the agreement in case of core diffusion and a small difference in boundary diffusion. This is an approximation in the model since the calculation of material properties by experiments is outside the scope of this work.
3. CGO strip of gauge thickness 0.23mm undergoes power law creep above 80m/min line speeds. For all other thicknesses in the CGO product portfolio the deformation mechanism is predominantly diffusion.
4. In HiB, the deformation mechanism changes from diffusional creep to dislocation creep between 700-820°C depending on the thickness of the strip, with smaller gauge thickness resulted in dislocation creep at lower temperatures.

5. Comparison of heat transfer model and the deformation mechanism map showed the change in deformation mechanism from diffusion to dislocation creep and the respective zone at which the change occurs according to the line speed.
6. The change in deformation mechanism is attributed to increasing stress at continuous anneal temperatures rather than the line speed because of the absence of significant changes in peak strip temperature according to line speeds.
7. Deformation mechanism of the HiB and CGO materials are determined by the grain size and line speed (variable load being applied).

5.8 References

1. H J Frost, M F Ashby, *Deformation mechanism maps – The plasticity and creep of metals and ceramics*, Pergamon press, 1982.
2. M F Ashby, *A first report on deformation mechanism maps*, Acta Metal., 20-7 (1972) 887.
3. F A Mohamed, T G Langdon, *Deformation mechanism maps based on grain size*, Metall Mater Trans B, 5-11(1974)2339.
4. F A Mohamed, T G Langdon , *A new type of deformation mechanism map for high-temperature creep*, Mater Sci Eng, 32-2 (1978) 103.
5. R Hertzberg, *Deformation and fracture mechanics of engineering materials*, Wiley publishers, 1996.
6. L Bendersky, A Rosen, A K Mukherjee, *Creep and dislocation substructure*, Int Mater Rev, 30-1 (1985) 1.
7. G W Greenwood, *Deformation mechanism maps and microstructural influences*, Mat Sci Eng A, 410–411 (2005) 12.
8. S A Sajjadi, S Nategh, *A high temperature deformation mechanism map for the high performance Ni-base superalloy GTD-111*, Mat Sci Eng A, 307 (2001) 158.
9. S Anbuselvan, S Ramanathan, *Hot deformation and processing maps of extruded ZE41A magnesium alloy*, Mater Design, 31 (2010) 2319.
10. Y C Lin, M S Chen, J Zhong, *Constitutive modeling for elevated temperature flow behaviour of 42CrMo steel*, Comp Mat Sci 42 (2008) 470.
11. Y V R K Prasad, K V Rao, *Processing maps and rate controlling mechanisms of hot deformation of electrolytic tough pitch copper in the temperature range 300–950°C*, Mat Sci Eng A, 391 (2005) 141.
12. *Product technical specifications list*, Cogent Power Ltd., (2010)

13. R Bozorth, *Ferromagnetism*, Wiley publishers, 1993.
14. C Capdevilla, H Bhadeshia, *A code to calculate deformation mechanism map for PM2000 ODS alloy*, Materials algorithms project, Cambridge university, 1999.
15. F S Buffington, K Hirano, M Cohen, *Self-diffusion in iron*, Acta Mater., 1961;9:34.
16. D Graham, D H Tomlin, *Self-diffusion in iron*, Philos Mag., 1963;8:1581.
17. P Guiraldenq, P Lacombe, *Measurement of coefficients of intergranular diffusion of iron in γ phase and comparison with the diffusion with the grain boundaries of α iron*, Acta Mater., 1965;13:51.
18. D W James, G M Leak, *Grain boundary diffusion of iron, cobalt and nickel in alpha-iron and of iron in gamma-iron*, Philos Mag., 1965;12:491.
19. J L Lytton, *Influence of ferromagnetic elastic modulus relaxation on the determination of magnetic specific heat of Fe, Ni, and Co.*, J. Phys. D: Appl. Phys., 1964;35:2397.
20. Y Ishida, C Y Cheng, J E Dorn, *Creep mechanisms in alpha iron*, Trans. AIME, 1966; 236:964.
21. M F Ashby, D R H Jones, *Engineering Materials I*, Butterworth Heinemann publishers, Oxford, 1996.

Chapter 6

Novel system to simulate continuous flattening anneal

Construction and Calibration

6.1 Introduction

The creation and mobility of dislocations under various combinations of stress, temperature and strain rate was studied in detail to understand their effect on magnetic properties of GOES from continuous flattening anneal line. The inability to interrupt and the dynamic nature of the continuous anneal furnace makes it difficult to obtain samples at different deformation conditions. Hence a lab-scale simulator that can take exit-HTCA material and simulate the continuous thermal flattening anneal line (M-line) process at controllable deformation conditions is necessary to produce samples and study their magnetic properties. Cogent Power Ltd., developed a continuous annealing simulator (CASIM2) for the above purpose [1]. The specific total loss of the samples from CASIM2 were on an average 30% higher than the corresponding continuous flattening anneal line samples at 1.2-1.4 W/kg at 1.5T and 50 Hz as opposed to 0.8-0.9 W/kg at similar testing conditions for the plant samples and thus the CASIM2 was considered unsuitable for replication of the M-line process [1]. Hence the new simulator system - LAFFAS (Lab Annealing Furnace for Flattening Anneal Simulation) was developed to overcome the drawbacks of CASIM2 furnace simulator.

6.2 CASIM2 – Review and Drawbacks

Continuous annealing simulator (CASIM2) was built by Cogent Power Ltd., to simulate the continuous flattening anneal line and is shown in Figure 6.1. CASIM2 furnace had a hanging weight system to apply load to the sample and a resistive heating arrangement to heat the sample at rates similar to continuous flattening anneal line. The electrical contact to the samples is made by removing the insulating forsterite and phosphate coating on the sample at two places. The dimensions of the coating removal are approximately 2.5cm through width of the sample. The simulator is controlled by a computer attached with feedback from thermocouple spot welded to the samples. The

annealing cycle is performed in air and the typical heating and cooling cycles are described below [1].

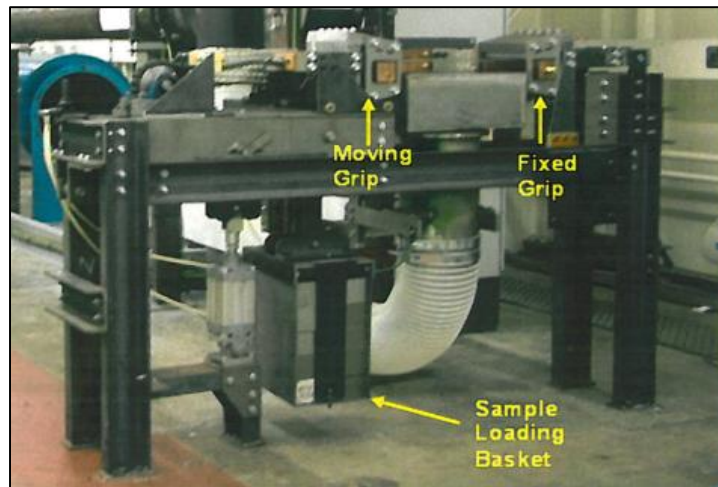


Figure 6.1 CASIM2 furnace showing the loading arrangement marked (Adopted with permission from Cogent development and market research report no 23 by A.Green [1])

The major drawbacks of the CASIM2 system [1] are

- Annealing in air that results in oxidation of the samples at high temperature.
- Electrical connections through spot welded thermocouples which are difficult due to the high silicon content of the sample resulting in detachment of the thermocouples making process control difficult.
- Spot welds also burn through the sample due to the thin gauge (0.23-0.3mm) of GOES samples. The extent of degradation of samples is unknown. The need to spot weld close to the centre of the samples where the coating is to be stripped of is another drawback.
- Annealing produced a concave curvature along the length of the sample that that resulted in the magnetic test results being artificially high due to the elastic stress applied by the weight of the yokes due to sample curvature.

The new system was designed in this work to overcome these drawbacks and to simulate conditions in the flattening anneal line as close as possible in the lab scale. The comparison between the CASIM2 and LAFFAS systems are described in table 6.1.

Table 6.1 Summary – Drawbacks of CASIM2 and remedy in LAFFAS

S.No	Drawback of CASIM2	Remedy in LAFFAS
1	Spot welding of contact thermocouples – Non-reliable because of high silicon content of the sample	Use of non-contact infrared thermocouple
2	Oxidation of the sample surface – experiment in air	Experiment in a sealed enclosure of nitrogen
3	Need to remove coating to attach electrodes for heating	Electrical contact through the jaws. Coating removal only at the ends for about 3 cm.
4	Concave bend along the length that hinders during magnetic testing (Reason unknown)	No concave bend along the length direction observed

6.3 LAFFAS – Design and construction

The mechanical part of LAFFAS (Lab Annealing Furnace for Flattening Anneal Simulation) consists of a tensometer testing machine for loading, load cell to measure the applied load and a load indicator to display the applied load and is connected to the load cell. The jaws to stress the sample are designed and manufactured in-house from a 316 stainless steel block also can be classified into the mechanical part of the system. The design of the new jaws was essential to accommodate a sample up to 120 mm in width compared to the original jaws that are attached to the tensometer which can hold samples only 30mm in width.

The electrical system comprised the power supply for resistance heating, a temperature measurement setup and a feedback circuit that controls the power supply. The high current-low voltage power supply heats the samples by Joule heating. Contact less induction heating was considered first and later eliminated as an option because of the need of a very high frequency power supply (>300kHz) and the unsuitability of the thin steel sheet to be heated by induction. The temperature measurement setup comprises an infrared non-contact thermocouple to avoid spot welding on to the sample. The thermocouple provides input to a digital thermal controller that provides feedback to the power supply according to the temperature of the sample. The design details of the individual components of the electrical system are explained in sections 6.5-6.9 below. The capabilities of LAFFAS system are described in table 6.2.

Table 6.2 Capabilities of the LAFFAS system for annealing GOES samples

No.	Parameter	Value
1	Maximum load	0-170 kg tension
2	Maximum power	26 kW (2000 A x 13 V)
3	Maximum jaw displacement	25 mm
4	Thermocouple calibration	500-1100°C
5	Thermocouple limit	1250°C
6	Maximum width of the sample	120 mm
7	Maximum length of the sample	350 mm

6.4 Sample dimensions

The sample size used in LAFFAS system is 340 x 65 mm (Length x Width). Length of the sample is restricted to 340 mm due to physical constraints of the system. Width is fixed at 65 mm to produce two samples of Epstein width (30mm) from each annealing step. The sample width in this case was limited by the dimensions of the tensometer setup

used for applying stress. A schematic of the sample and holes for loading is shown in Figure 6.2 below.

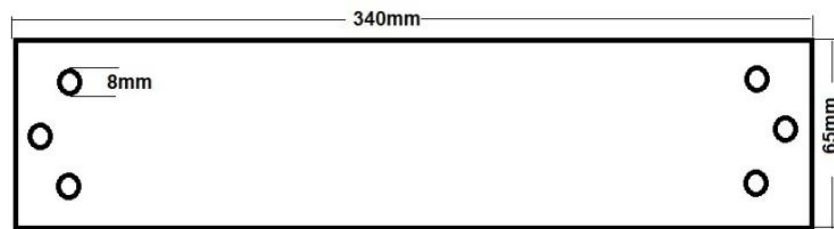


Figure 6.2 Schematic of the sample dimensions and loading hole positions

6.5 Tension setup

The LAFFAS system is built around a Hounsfield type W tensometer. Loading is done manually by rotating the loading lever and a screw mechanism displaces the movable jaw away from the fixed one thus applying load on the sample. Modifications were made to the tensometer jaw that is designed for Epstein size samples to accommodate the wider samples as shown in figure 6.2. The new jaw designed and built in-house from 316 grade stainless steel. The comparison between the standard and new designed jaw are shown in Figure 6.3. Several designs with varying hole dimensions and distance between them were tried and the current design was found to be the best using FEM modelling.

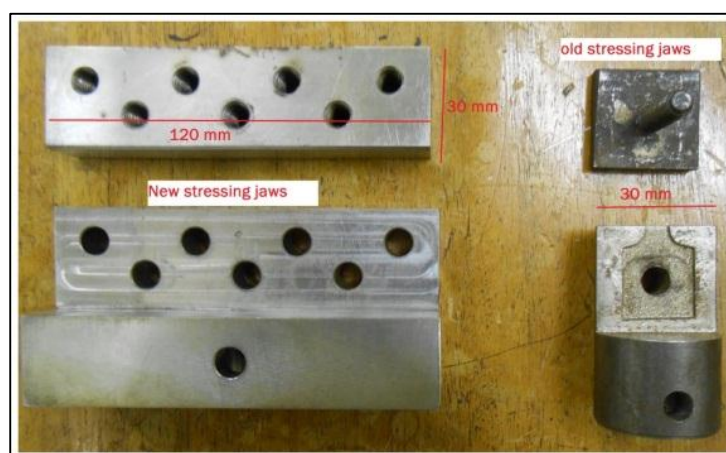


Figure 6.3 Comparison of the standard (old) and new jaws

6.6 Strain uniformity test

The uniformity of the stress applied by the new set of jaws on the sample was tested using four strain gauges. Four linear strain gauges of length 10mm with a gauge factor of 2.12 and a resistance of 350 Ω . The strain gauges are attached to LABVIEW Visual Interface (VI) capable of reading data from eight strain gauges at a time through a National Instruments NI9237 data acquisition card. The VI used to read the data from the strain gauges is shown in Figure 6.4. The sample with the strain gauges and their position is shown in Figure 6.5.

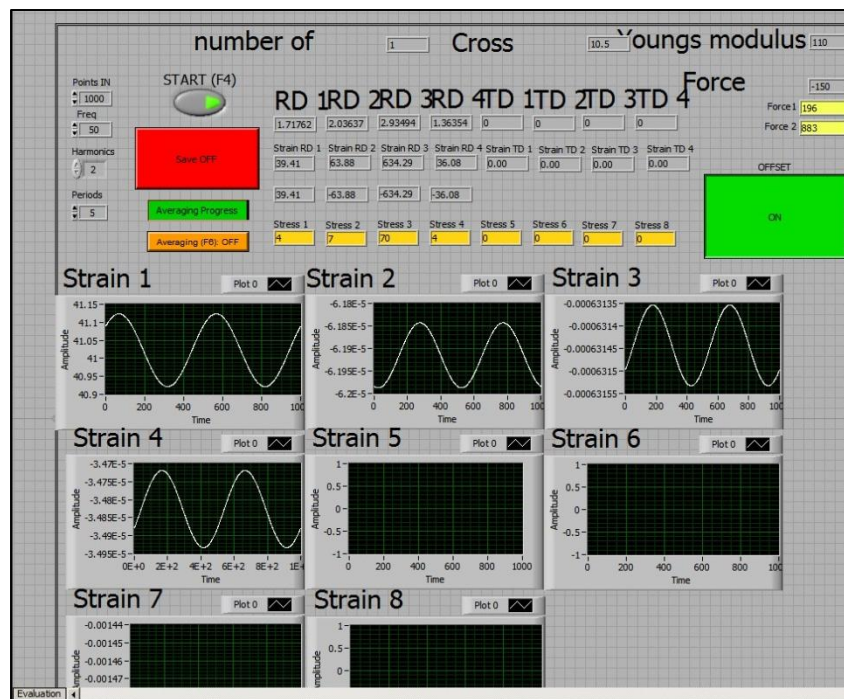


Figure 6.4 LabVIEW VI used to read data from the strain gauges (Acknowledgement: Mr. P Klimczyk, Wolfson centre for magnetics for the VI)

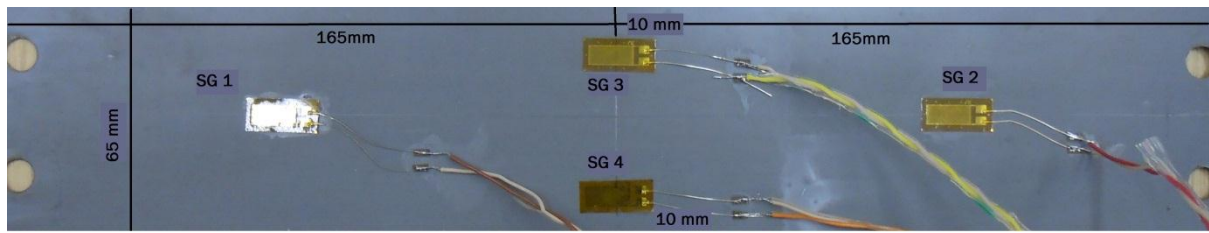
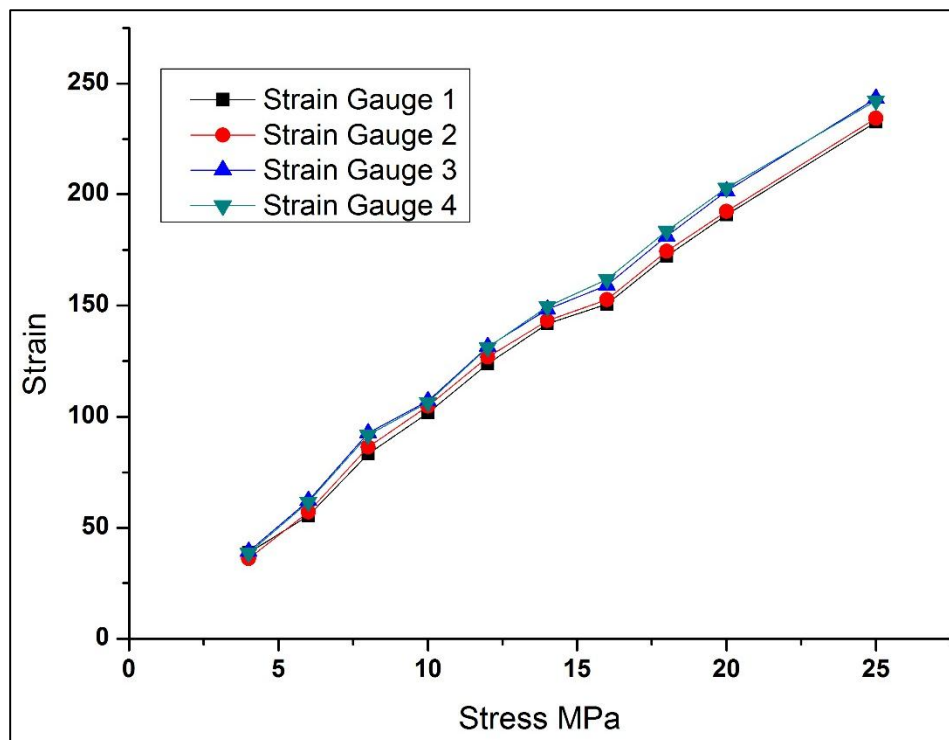


Figure 6.5 Strain gauges attached to the sample

The results of the strain gauge testing in Figure 6.6 shows the strain increases in the sample from the centre to the edges. The results showed the inability to make two Epstein width samples from one large sample of 65mm width. Only the 30mm wide sample at the middle of the 65mm original width can be used for further study owing to the non-uniformity of stress at the edges. Possibilities of wider samples and more holes to apply stress were not explored in this study.

Figure 6.6 Strain values at different stresses from four different strain gauges



SG – Strain gauge

6.7 Load cell and indicator – Calibration

The load cell type used in this tensometer is a Sensotec type 41 tension/compression load cell and an E525 type load indicator. The load cell is of the bonded foil strain gauge type and has a range of up to 2268 kg (5000 lb). The load cell is fitted onto the tensometer assembly. It is connected to the E525 type load indicator through a 12 way screw terminal and the indicator calibrates and reads the load data from the cell. The load cell and indicator assembly is shown in Figure 6.7.



Figure 6.7 Load cell and load indicator used in the LAFFAS system

Load cell calibration was performed using a standard load dial and the load indicator as specified in the instruction manual [2] and the results are shown in the table 6.3 below. Data from table 6.3 shows that a multiplication factor of 7 is to be used with the load indicator readings to obtain the value of load applied.

Table 6.3 Load cell calibration table

S.No	Load applied (N)	Load indicator reading (N)
1	100	14±0
2	200	28±0
3	300	42±1
4	400	56±0
5	500	72±0
6	600	86±1
7	700	100±0

6.8 Experiment atmosphere

Application of tension at high temperature is carried out in an inert atmosphere of nitrogen to prevent oxidation of the sample surface, which was a major disadvantage of the CASIM2 system. A welded mild steel box with bolted lid on top is used to contain the nitrogen atmosphere. Provisions for gas inlet and outlet, electrical cables for heating and opening to fit the thermocouple are built into the system. Openings for the shaft of the tensometer are also provided. All the openings were sealed with rubber 'O'-rings. Rubber 'O'-rings are sufficient since they are heated only by radiation for a very short span of time of the order of 80-100 seconds. The lid of the box is sealed with copper gasket bolted along with the lid. The atmosphere used here is 100% O₂ free nitrogen as opposed to 3%H₂-N₂ in the plant continuous annealing process. The welded and sealed box setup to contain the nitrogen atmosphere is shown in the Figure 6.8.

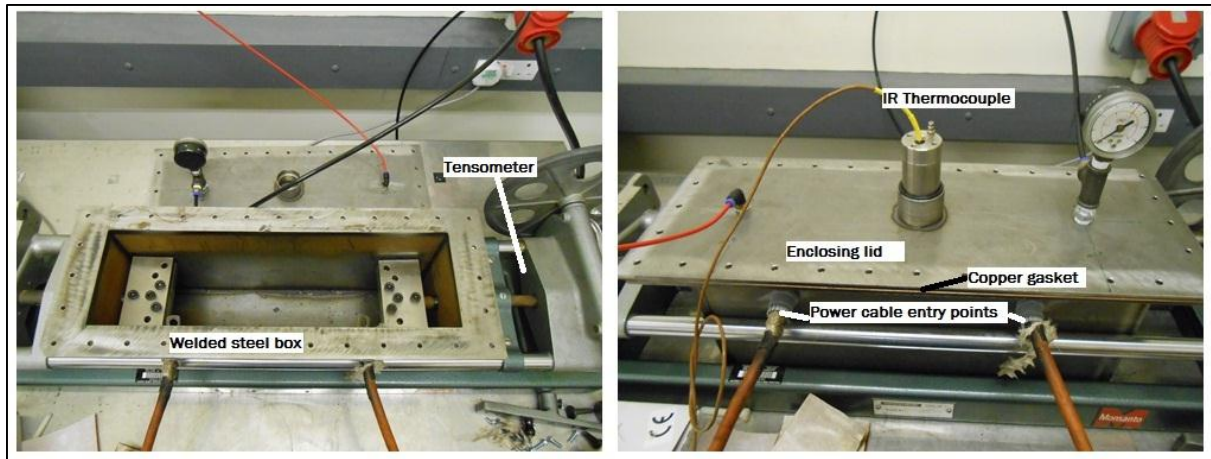


Figure 6.8 Bolted mild steel box for containing the nitrogen atmosphere sealed using copper gasket

6.9 Heating and temperature measurement

The heating setup in LAFFAS works on the resistance heating principle. The power required for resistance heating is supplied by a high current low voltage supply. Resistive heating method was used to obtain heating rates closer to that of the actual thermal flattening anneal line process. The temperature measurement was performed by an optical contactless infrared (IR) thermocouple. The IR thermocouple was chosen to avoid spot welding of contact thermocouples to every sample that is annealed in LAFFAS.

The heating and temperature measurement section of the LAFFAS setup consists of the following parts

1. High current low voltage power supply
2. External control system with a temperature controller and solid state relay
3. Infrared thermocouple for temperature measurement

A schematic of the electrical system is shown in the figure 6.9 below.

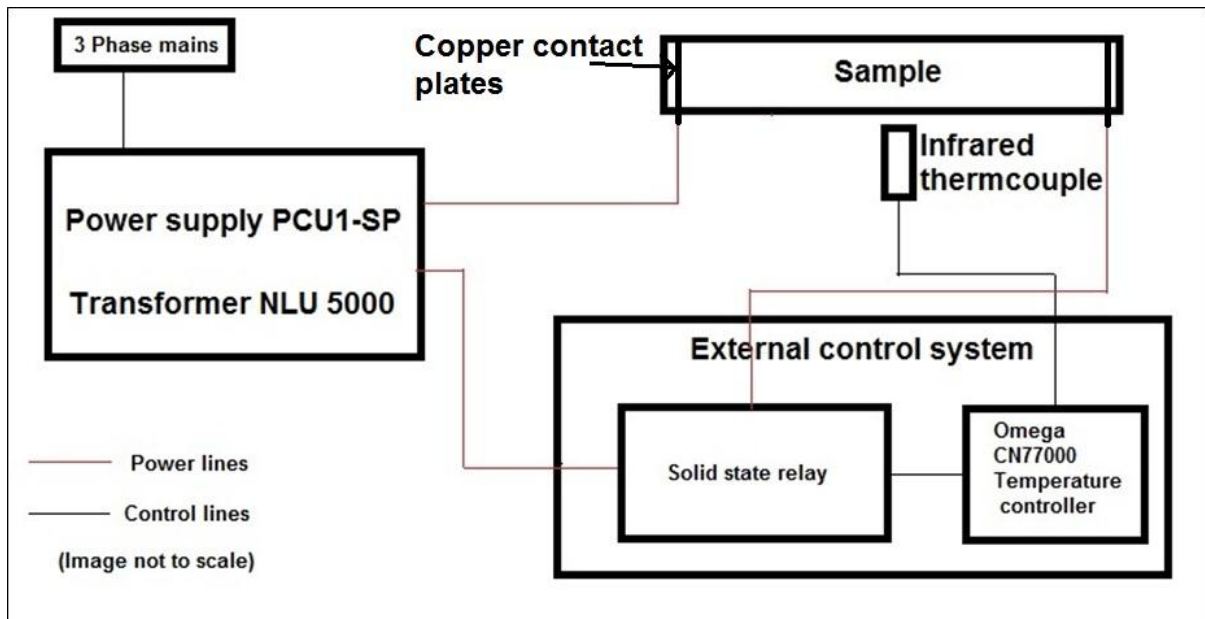


Figure 6.9 Schematic diagram of the power supply and feedback control system

6.9.1 Power source

The power source used is PCU1-SP [3] high current low voltage power supply from T&R test equipment with a NLU5000 transformer capable of output currents upto 5000A at varied voltage of 2-13.5V. The power source with the transformer module is shown in the Figure 6.10.



Figure 6.10 PCU1-SP high current low voltage power supply unit used in LAFFAS

6.9.2 Electrode design for supplying power

The current required for heating the sample to the required temperature of upto 850°C is calculated by finite element method simulations. Three types of electrode design were considered and type 2 was found to have the most uniform temperature distribution. The design and results are shown in figure 6.11.

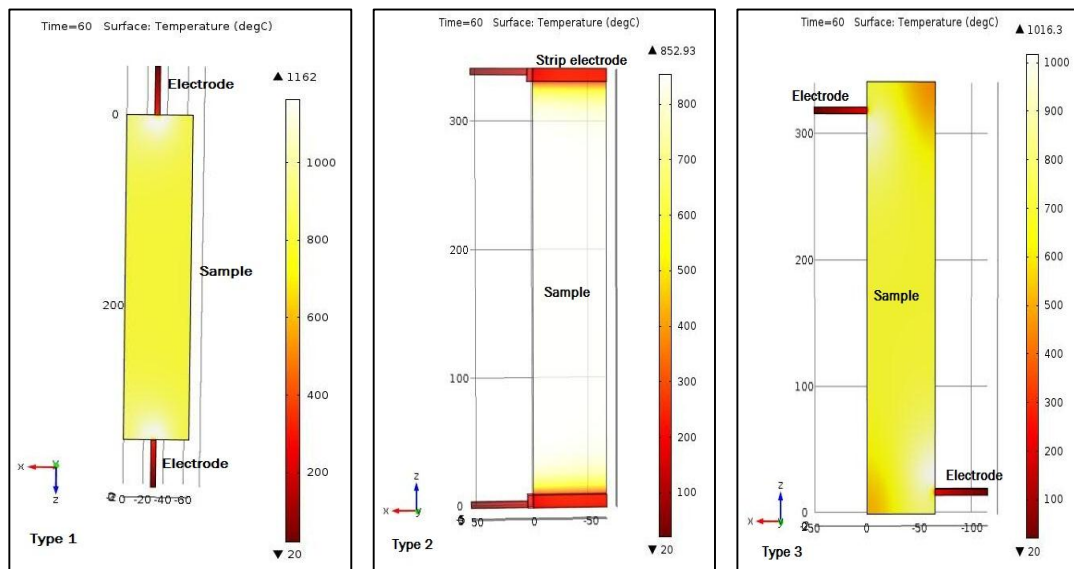


Figure 6.11 Simulation of current-temperature relationship for heating the sample to 850°C in 60 seconds with three types of electrode design

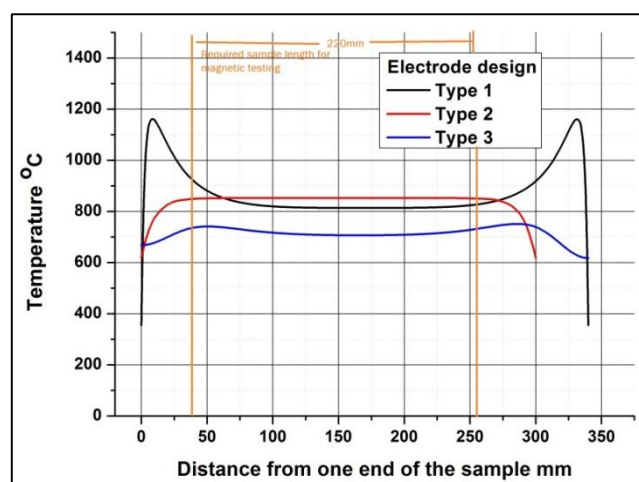


Figure 6.12 Comparison of temperature profile along the length of the sample for three different electrode designs (Temperature comparison made after 60 seconds)

The temperature profile across the length and width of the intended sample of 220mm x 30mm from the initial 330mm x 65mm sample should be uniform. Analysis of several electrode designs in Figure 6.11 shows that the type 2 design where the contact area of the electrode is along the full width of the sample gives the required uniformity. The uniformity along the length of the required sample (220mmx30mm) is shown in figure 6.12.

6.9.3 Temperature measurement – Infrared thermocouple

Temperature measurement is the first step to control the annealing process in the system. One of the drawbacks of the CASIM2 system is the difficulty in spot welding contact thermocouples to the samples without knowledge of the extent of heat damage to the sample. Hence a non-contact OS36-10 K type infrared thermocouple is used in this study. The field of view of the thermocouple is a 20mm diameter circle on the sample from which the average temperature is recorded. The thermocouple is placed such as the field of view is at the midpoint of the sample in both length and width direction. The temperature measurement range of the thermocouple is -45 to 1370°C. The thermocouple is fitted with an air cooling sleeve to protect the electronics from the high temperatures in the process. In the current LAFFAS system, the cooling system is unused due to the positioning of the thermocouple electronics at about 10 cm (distance between the sample and thermocouple of 7 cm + the electronics are situated at about 3 cm deep from the viewer of the thermocouple) away from the sample partly aided by the short time span of the experiment in the order of 80-100 seconds. Calibration of the thermocouple is done using data from a NEC infrared thermal imaging camera as standard heat source. Position of the thermocouple from the sample is illustrated in figure 6.13. The current-temperature data obtained from the thermal imaging camera used as the standard is shown in table 6.4 and figure 6.14.

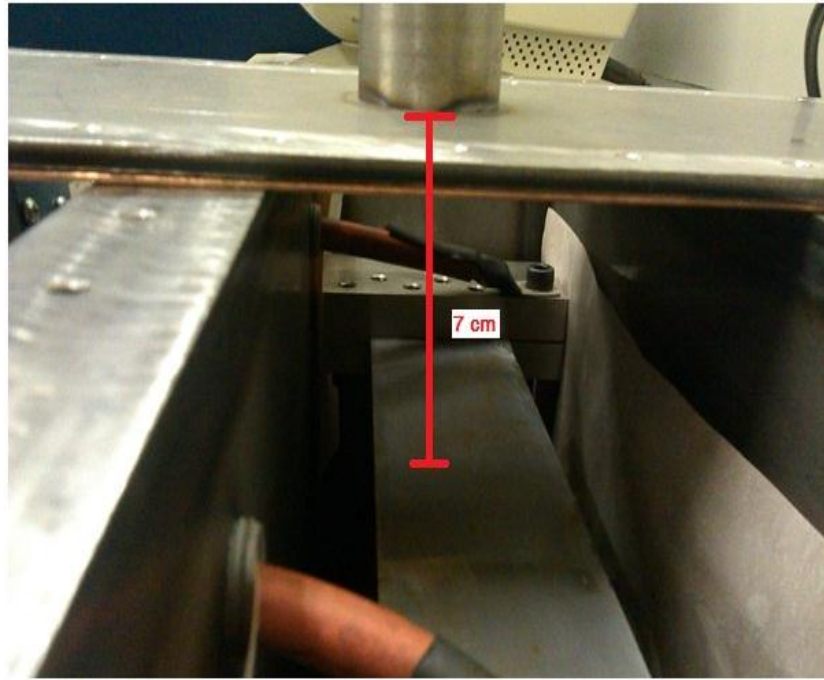
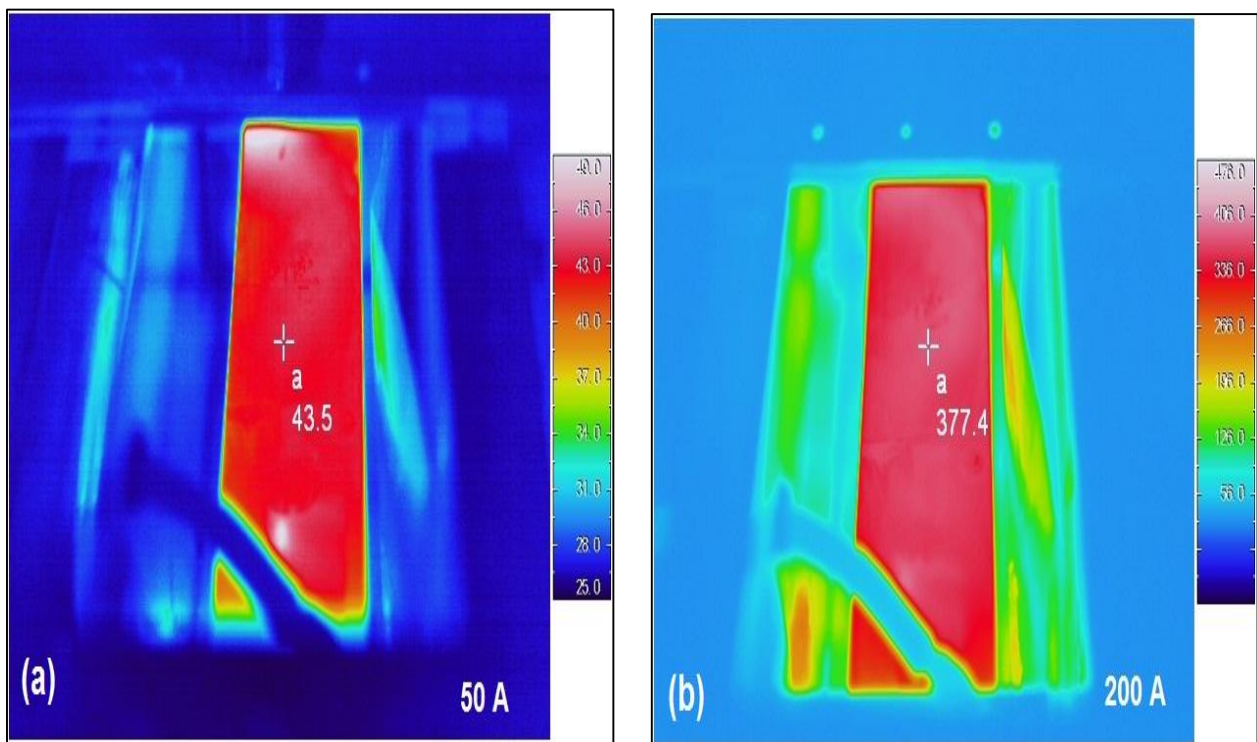


Figure 6.13 Distance of the thermocouple to the sample is illustrated (Lid of the nitrogen atmosphere box is kept open to show viewing area of the thermocouple on the interior)



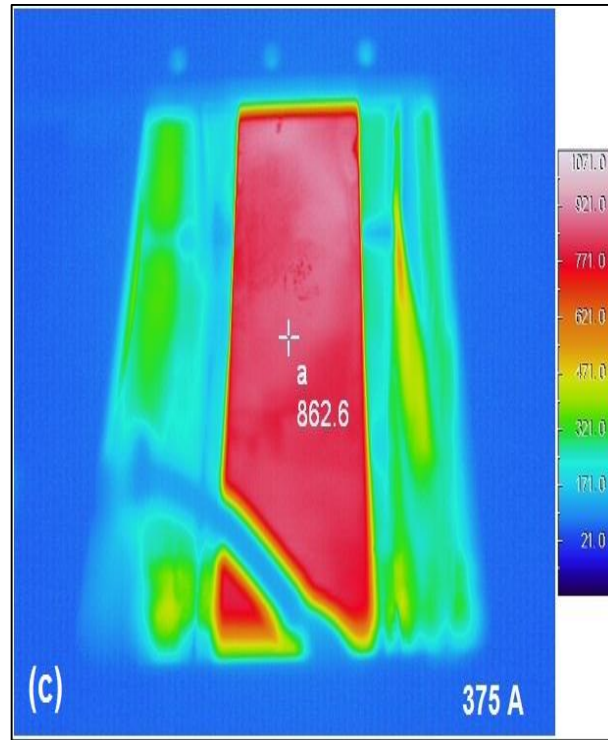


Figure 6.14 Thermal image of the sample with bounding box from the infrared thermal camera for an applied current of (a) 50 A (b) 200 A (c) 375 A

Table 6.4 Calibration table of applied current vs. temperature of the strip obtained by the thermal imaging camera (<1% uncertainty from the measured values in the calibrated range of -40 to 1200°C)

No.	Current (A)	Strip temperature (°C)
1	0	20.3
2	50	43.5
3	100	85.6
4	125	149.5
5	150	224.1
6	175	284.2
7	200	377.4
8	225	458.7
9	250	577.8
10	275	677.4
11	300	761.9
12	325	862.6

6.9.4 Control circuit

The control system of the PCU1-SP system is replaced with an external control system with a temperature controller and solid state relay that switches the power supply according to the temperature set points and the actual temperature. The solid state relay was used since the output from the temperature controller was 5V and insufficient to switch the power supply. Hence a solid state relay to switch upto 70A current at 230V is used inbetween the controller and power supply. The solid state relay is also attached with a heat sink for protection against heating due to high currents involved. The relay switches a 50A primary current input to the NLU5000 transformer. The control unit is shown in figure 6.15.

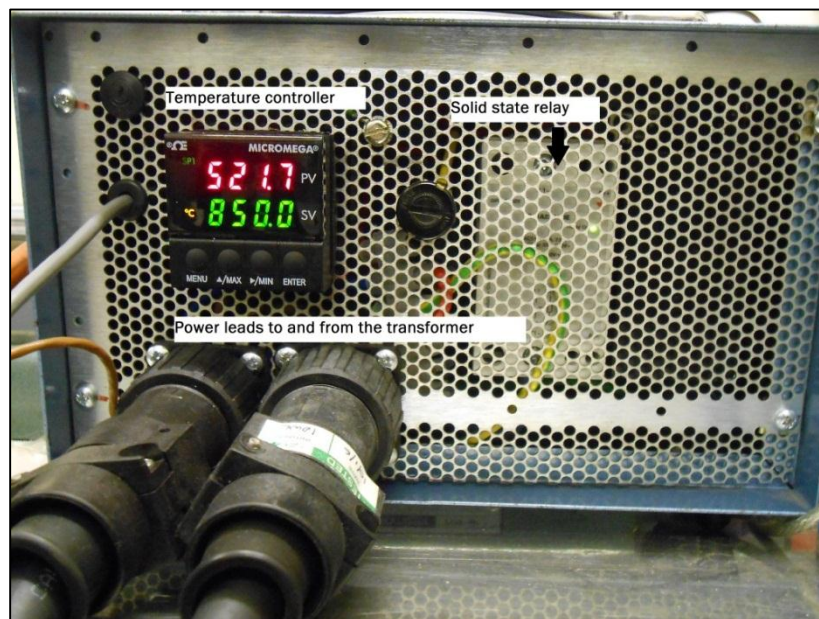


Figure 6.15 Control unit with temperature controller and solid state relay for controlling the power source

6.10 Summary

1. LAFFAS was designed to overcome the drawbacks of CASIM2 system for simulating the continuous thermal flattening anneal process.

2. A non-contact infrared thermocouple is used for temperature measurement to eliminate the need for spot welding thermocouples to each sample simulated in LAFFAS.
3. The simulation anneal takes place in a nitrogen atmosphere to prevent oxidation of the sample surface.
4. New jaws were designed to anneal samples upto 120mm in width compared to 30mm wide samples in CASIM2 system.
5. Stress uniformity test was performed on the sample with the new jaw design and the variation between the stress at four distinct points were within 2% showing the uniformity in stress application.
6. A small increase (approximately 5%) in stress at the edges of the sample was observed.
7. Electrical contact is made through the stressing jaws, hence coating is removed only at the ends of the sample.
8. No concave bend along the rolling direction has been observed after annealing in LAFFAS.

6.11 References

1. A Green, 'Report into the Feasibility of using the CASIM 2 furnace to simulate Thermal Flattening Line at Orb', Development and market research report number 23, Orb electrical steels, Newport, 2009.
2. Instruction manual – Hounsfield type-W tensometer, RDE equipments, UK, 1996.
3. Operating and maintenance manual – PCU1SP, T&R test equipments, UK, 2006.

Chapter 7

Experiments in LAFFAS (Lab Annealing Furnace for Flattening Anneal Simulation) and Magnetics-Microstructure correlation

7.1 Introduction

The purpose of LAFFAS is to study the continuous flattening anneal process line and produce samples at lab scale under different conditions of stress and temperature. The continuous flattening anneal line furnace is dynamic in terms of the temperature maintained and the strip speed. Simulation of varying strip speed and temperature variations was necessary to understand the change in dislocation structures and their corresponding effect on power losses. Power loss testing of the samples prepared under different simulated combinations of temperature and stress were performed. The microstructure of the samples was studied to understand the variation in dislocation structure with varying temperature and stress. All the experiments in this chapter were performed with the CGO+ material with average grain sizes of $10\pm 3\mu\text{m}$ and a mis-orientation tolerance of 7° from Goss texture.

7.2 Objectives of LAFFAS experiments

The objectives of this work are as follows:

1. To understand the mechanism of dislocation formation during continuous annealing process for CGO+
2. To understand the effect of varying stress on the steel strip which happens with varying line speeds in the process line
3. To understand the effect of varying strip peak temperatures to understand the dislocation dynamics during the process
4. To understand the effect of dislocations formed during the various combinations of temperature and stress on the magnetic properties of GOES
5. To understand the effect of further stress relief anneal on the dislocation structure and magnetic properties

7.3 Experimental procedure

In the continuous thermal flattening anneal line, the steel strip is elongated to a small strain of approximately 0.1% at a temperature of 850°C in a $N_2 + 3\% H_2$ atmosphere. The experimental procedure is designed to study the effect of the continuous flattening anneal line on the dislocation structure and its effect on magnetic properties of GOES at conditions similar to that of continuous flattening anneal line. A lab scale sample with dimensions 65 x 340 x 0.3 mm was prepared from material exiting the high temperature coil anneal process. A step-by-step experimental procedure is discussed in the subsequent sections.

7.3.1 Sample preparation for annealing

The sample dimensions required for simulating continuous flattening anneal is shown in section 6.4. The samples were attached to the jaws by bolts fastened through 8mm diameter holes punched in the strip at both ends. The cut and punched samples were brushed in running water to remove any excess magnesium oxide left over from the HTCA process. Cleaned samples were manually coated with a lab scale phosphate coating mix to simulate the phosphate coating applied at the beginning of the continuous flattening anneal process. The procedure for the preparation of 800 ml of the coating mix was as follows:-

- 1) 266ml of aluminium orthophosphate was added to a beaker with a magnetic stirrer
- 2) Add 470ml colloidal silica (30%)
- 3) The mixture was stirred for 30 seconds and 64ml of tap water was added
- 4) The mixture was left for 20 minutes before use

- 5) The coating mixture was maintained at less than 40°C to avoid thickening of the solution.

After coating the samples were cured for 30 seconds in a furnace pre-heated to 800°C. This procedure was to dry the coating without any significant change in the microstructure of the GOES.

7.3.2 Annealing in LAFFAS

Electrical contact between the sample and the jaws were made by removal of the insulating coating for 30mm length on both ends of the sample. In this work emery paper was used to remove the coating due to the inconsistency in coating removal depth by hydrochloric acid.

The sample was then fixed into the jaws and bolted at 3 points on each side. Power cables were attached to the jaws and the lid of the nitrogen gas enclosure was bolted along with copper gaskets. Nitrogen was purged through the enclosure for approximately 5 minutes at slightly above 1 bar pressure to remove any residual air and avoid oxidation of the sample.

Annealing was performed in stress-temperature combinations calculated from the variation in strip speed, zone temperature and the gauge of the material. The variation in stress according to the gauge of the material and line speed is shown in Appendix 5.2.

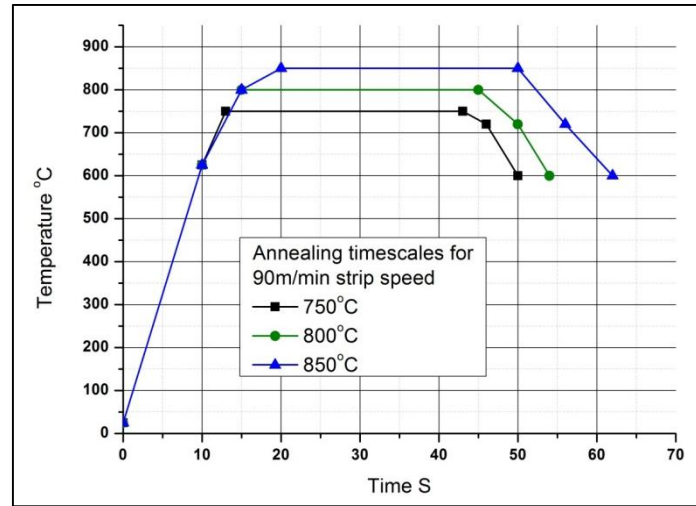


Figure 7.1 LAFFAS annealing cycle to simulate continuous flattening anneal

7.3.3 Measurement of elongation

Permanent elongation of the samples after annealing in LAFFAS was measured by variation in the distance between a pair of cross-hairs marked on the sample. The distance was measured by a travelling microscope with a resolution of 20µm. Care was taken by clamping the sample down during measurement to reduce errors introduced by small sample curvatures. Each sample was marked with two gauge lengths and elongation was measured as the average of the two elongation values obtained from each of these gauge length markings. Percentage elongation was calculated by equation 7.1 below.

$$\%E = \left(\frac{L_f - L_i}{L_i} \right) \times 100 \quad (7.1)$$

Where E is the elongation, L_f is the final gauge length after annealing and L_i is the initial gauge length before annealing.

The marking to measure the gauge length to calculate the percentage of elongation after annealing is shown in figure 7.2.

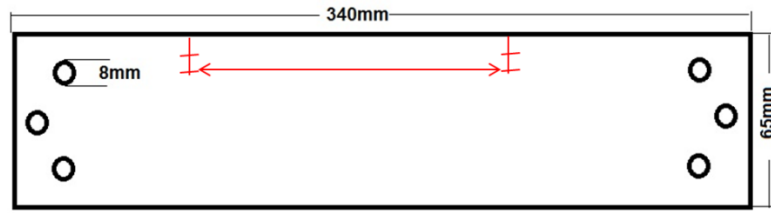


Figure 7.2 Schematic of a samples and gauge length marking

7.3.4 Calculation of dislocation density

Dislocation density was calculated using ImageJ, an open source image analysis software [1]. The steps used in processing an image to calculate the dislocation density were as follows:-

1. The image from the optical microscope is opened using ImageJ software.
2. Grey level threshold was set to highlight the dislocations from the image background
3. Particle analyser was used to set the size range for particles to be counted into the dislocation count
4. Dislocation density was counted per square centimetre from the dislocation count in the image

The accuracy of the software in counting the dislocation density relies on the ability to set particle size range to be counted. Stains from etching reagents and inclusions present in the image can be separated from dislocation decorations by careful selection of grey level and size variables respectively. Thus the particle count is accurate taking into account a small human error factor.

The following Figure 7.3 shows the steps in ImageJ.

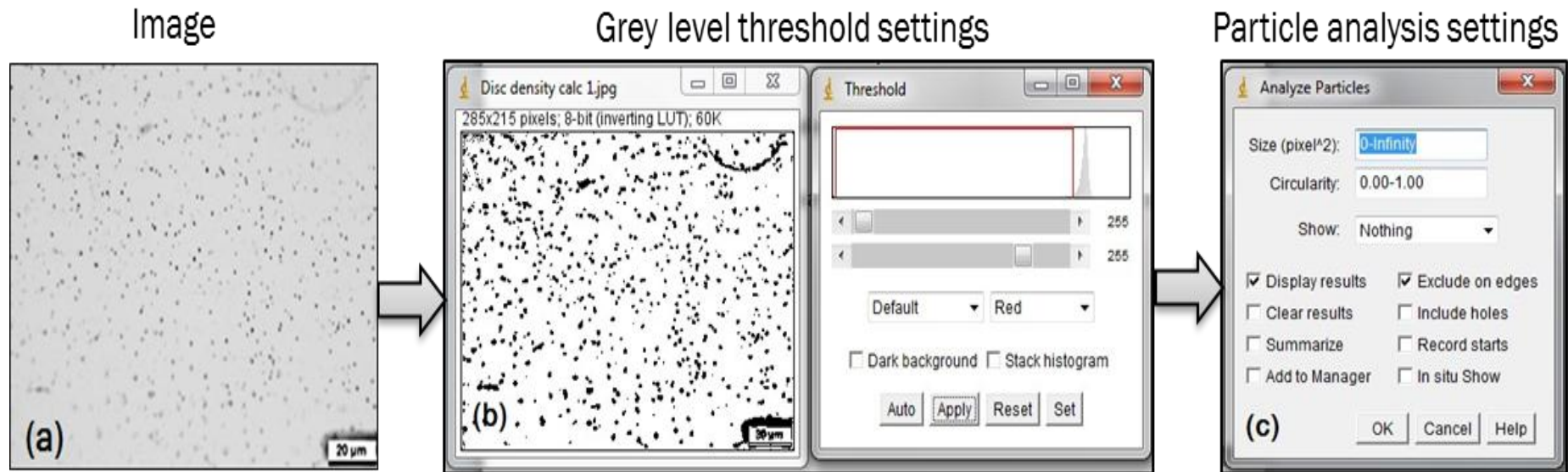


Figure 7.3 (a) Image for dislocation density calculation (b) Applying grey level threshold to separate dislocations from background
(c) Setting dislocation count parameters to separate noise in the image

7.4 Design of experiments

To design the experiments that simulate the continuous flattening anneal line, variation of temperature and stress needed to be understood. A combination of temperature and stress were used to determine the stress to be applied on the sample in LAFFAS experiments. The load in continuous flattening anneal is dependent on the speed and gauge thickness of the strip. In the simulator, load was varied on samples of the same thickness (0.3mm) to take into account the variation of stress on samples of different thicknesses. All the experiments were performed using 0.3mm gauge thick samples and the change in stress applied on different gauges in the process is simulated by varying loads applied in the simulator.

To simulate the effect of different stresses applied on the steel strip, the effect of stresses from 4-9 MPa at 850°C was studied. The peak strip temperature was maintained at 850°C which is the temperature maintained in continuous flattening anneal line. The temperature and rate of heating were obtained from the heat transfer model in Chapter 4.

To study the effect of variation in temperature and stress during annealing in 0.3mm gauge thickness samples, the heating rate followed was in agreement with 90m/min strip speed and is shown in Figure 7.1. This was to study the change in dislocation structure through the 750-850°C temperature range which is the region of interest due to changes in deformation mechanism from diffusion to dislocation climb as shown by the deformation mechanism maps in Chapter 5.

7.5 Material data

The material used in this study is known as CGO+. Studies could not be carried out on CGO and HiB electrical steels since these products were discontinued from their product list by Cogent Power Ltd. CGO+ has a grain size very close to HiB steel, but with an

increased manganese content of up to 0.2% compared to 0.06% in HiB. The following microstructures and deformation mechanisms in this chapter can thus be compared only to HiB deformation mechanism maps because of the similarity in grain size. However, the author acknowledges that there might be small variations from the HiB deformation mechanism maps because of changes in material constants caused by a change in the chemistry of the material. This approximation is being made since obtaining vast mechanical testing data and material constants for the new material is out of scope of this work due to the enormity of experimentation required to calculate all the thermodynamic and kinetic parameters as a function of temperature.

7.6 Results

7.6.1 Chemical testing

Chemical analysis on the samples annealed in LAFFAS was performed by X-ray diffraction (XRD) to check the effectiveness of the nitrogen atmosphere in preventing oxidation of sample surface. Samples annealed in air showed considerable oxidation as shown in Figure 7.4 by the iron oxide peaks. It also shows the similarity in composition between the sample annealed in nitrogen atmosphere and a sample cut from continuous flattening anneal line (M-line as designated in Figure 7.4). From this test, the importance and effectiveness of the protective nitrogen atmosphere is evident and all further tests were performed in a nitrogen atmosphere.

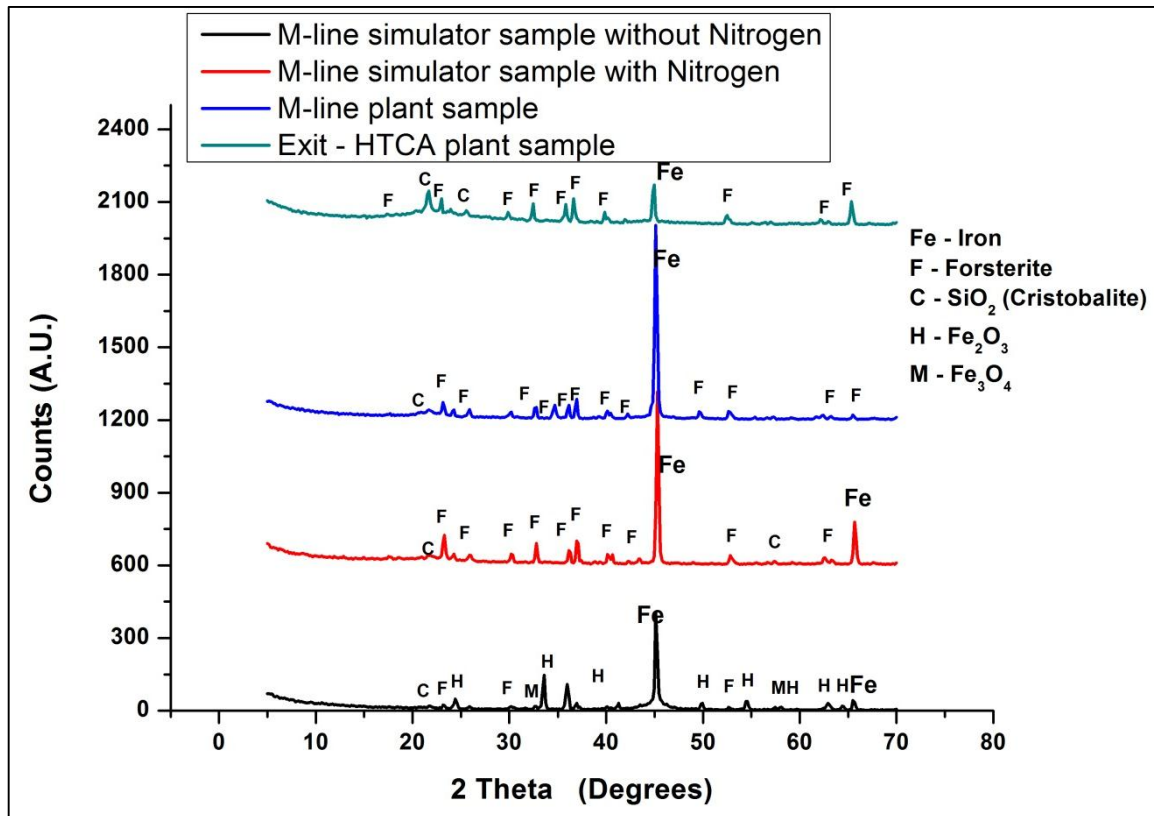


Figure 7.4 X-ray diffraction plots showing oxide formation in samples annealed in air and a good correlation between M-line (Continuous flattening anneal) and simulator samples

7.6.2 Effect of increase in stress on dislocation structures at 850°C

The load applied on the CGO+ strip in the continuous flattening anneal line varies according to the strip thickness and speed. To normalise the effect of the strip gauge thickness, in this study the stress was varied from 4-9 MPa on the 0.3mm thick samples. This covers the range of stress determined by the process parameters plotted over the deformation mechanism maps in Figures 5.16 to 5.20. The objective of this study was to understand the variation of dislocation structure with stress at 850°C which is the set temperature in the continuous flattening anneal line and the temperature achieved by the steel strip from the heat transfer model shown in Chapter 4. The resulting changes in dislocation structure are shown in Figures 7.5 to 7.10. The change in individual dislocation density with increasing stress is shown in Figure 7.11.

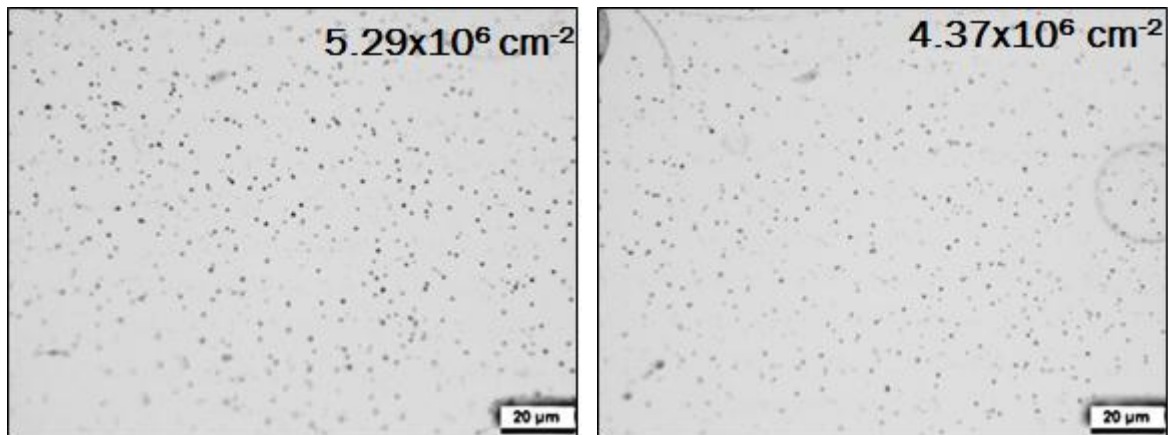


Figure 7.5 The dislocation structure resulting from annealing in LAFFAS at 4 MPa and 850°C in 0.3mm CGO+ steel

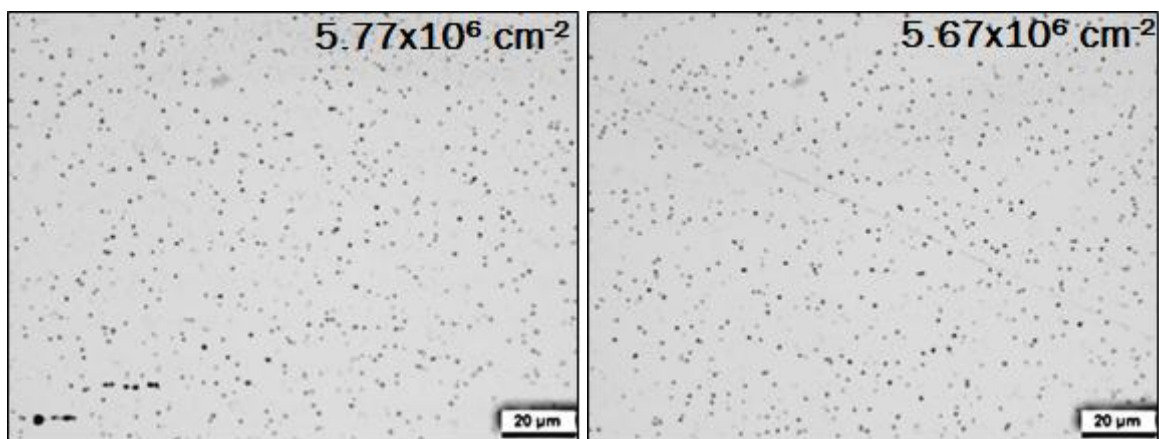


Figure 7.6 The dislocation structure resulting from annealing in LAFFAS at 5 MPa and 850°C in 0.3mm CGO+ steel

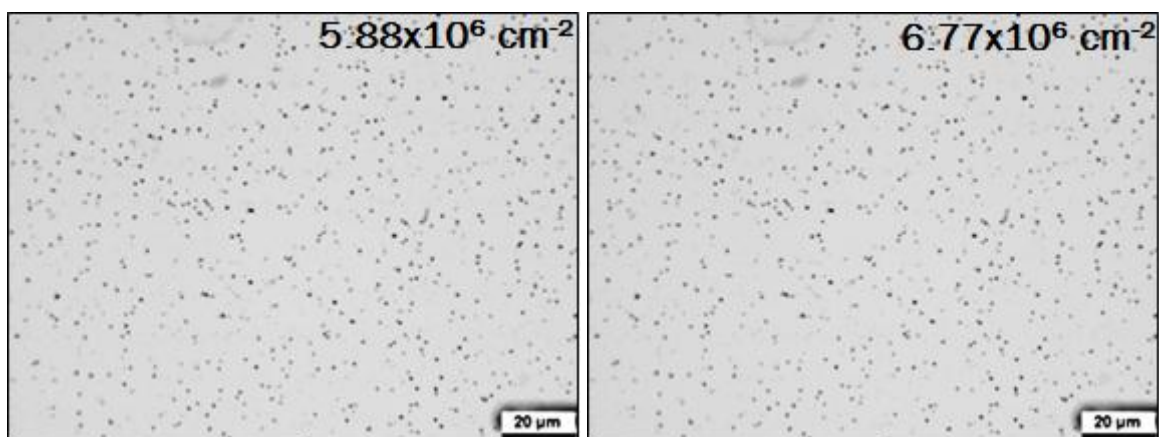


Figure 7.7 The dislocation structure resulting from annealing in LAFFAS at 6 MPa and 850°C in 0.3mm CGO+ steel

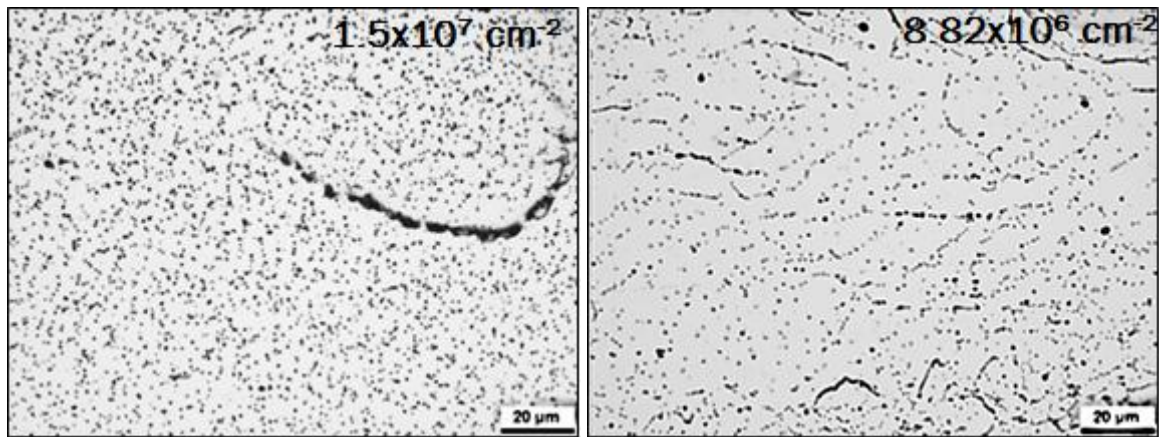


Figure 7.8 The dislocation structure resulting from annealing in LAFFAS at 7 MPa and 850°C in 0.3mm CGO+ steel

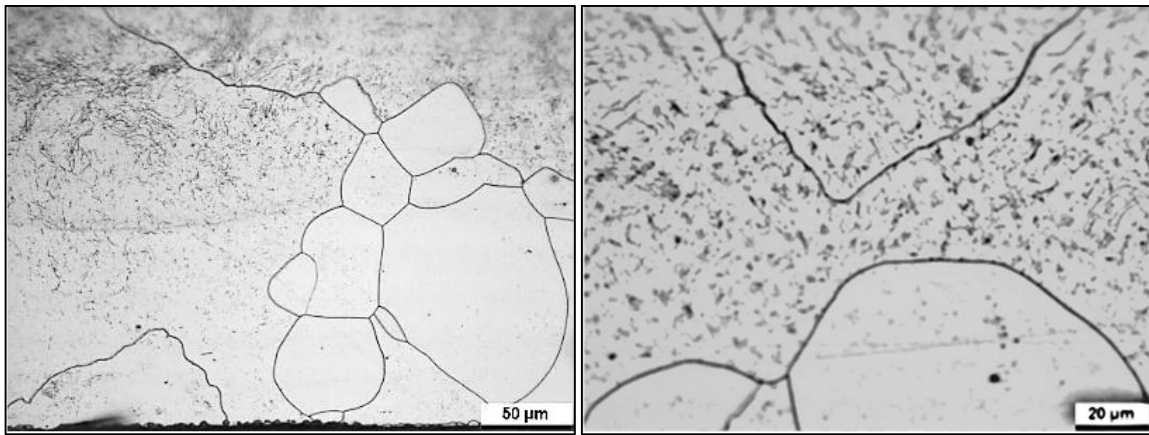


Figure 7.9 The dislocation structure resulting in partially recrystallised grain structure from annealing in LAFFAS at 8 MPa and 850°C in 0.3mm CGO+ steel

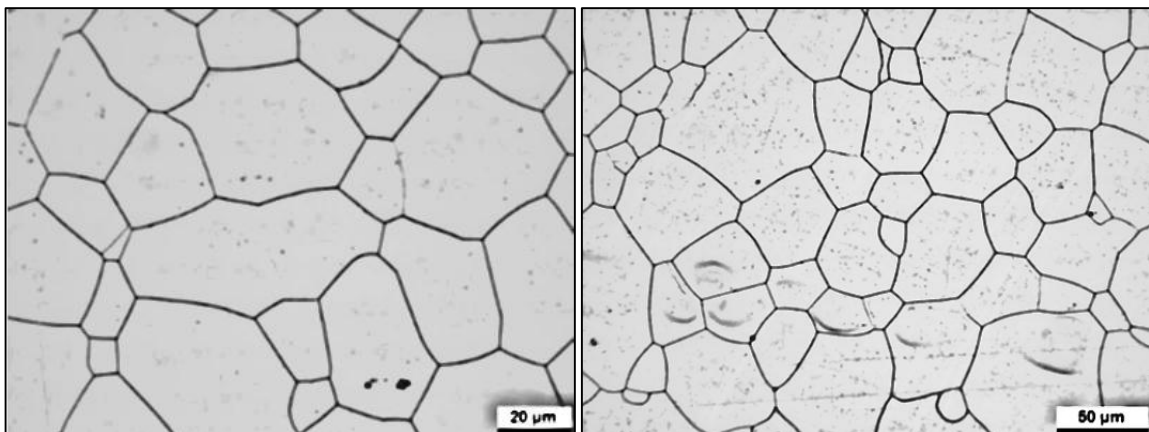


Figure 7.10 The dislocation structure resulting in completely recrystallised grain structure from annealing in LAFFAS at 9 MPa and 850°C in 0.3mm CGO+ steel

The increase in dislocation density with increasing stress is shown in figure 7.11 and the corresponding effect on specific total loss at 1.7T and 50Hz is shown. The specific total loss increases along with an increase in dislocation density.

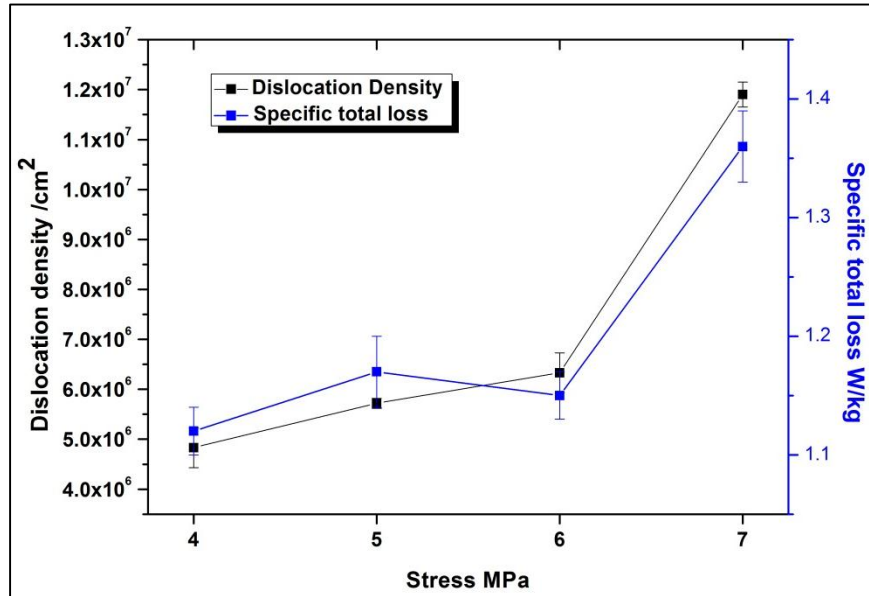


Figure 7.11 Increasing individual dislocation density from 4-7 MPa and the effect on specific total loss at 1.7T and 50Hz

The dislocation density and specific total loss correlation data shown in figure 7.11 omitted the data for samples annealed under 8 and 9 MPa stress because of the formation of grain boundaries and stress free grains due to dynamic recrystallisation.

7.6.3 Load-elongation study for CGO+

The effect of different stress-temperature combinations on the percentage of elongation, dislocation structure and their corresponding effect on specific total loss is studied in this section. Samples of CGO+ material were heat treated by LAFFAS at two different stresses of 4, 6 MPa and at three different temperatures of 750, 800 and 850°C according to the annealing cycle shown in figure 7.1. The results of the average percentage elongation at different combinations of temperature and stress are shown in figure 7.12.

The results show a comparison between the data for HiB from the literature [3] and CGO+ materials.

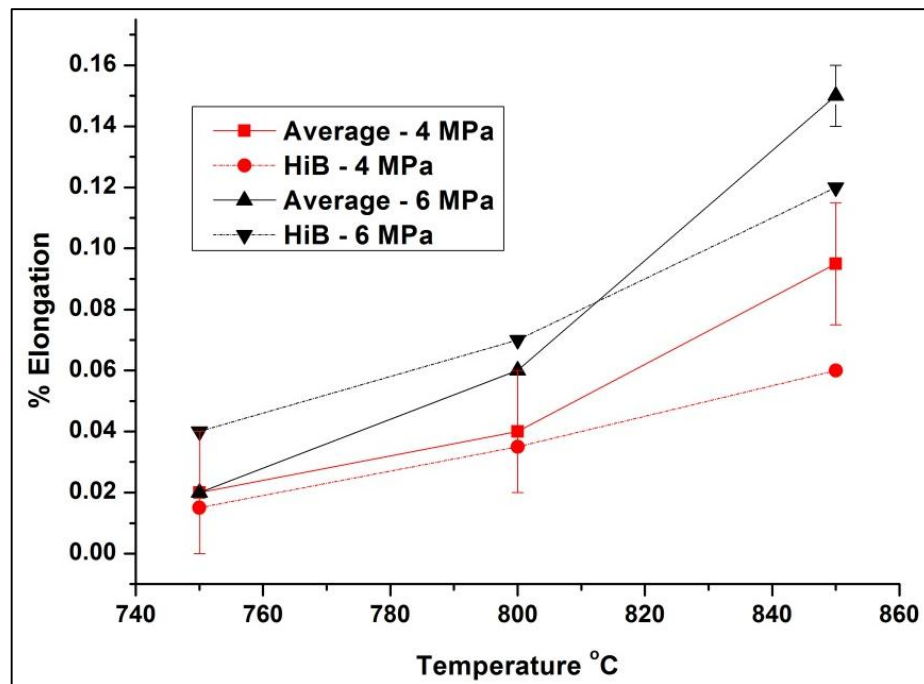
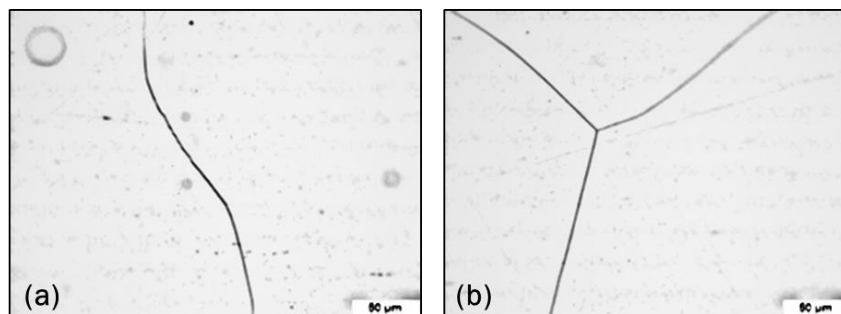


Figure 7.12 Comparison of average percentage elongation of three sets of CGO+ annealed at 6MPa and four sets of CGO+ annealed at 4 MPa with HiB material [3]

The following figures 7.13-7.14 show the variation in dislocation structures for different stress-temperature combinations. The correlation between dislocation structures formed in these combinations is essential to understand the trend in elongation vs. loss.



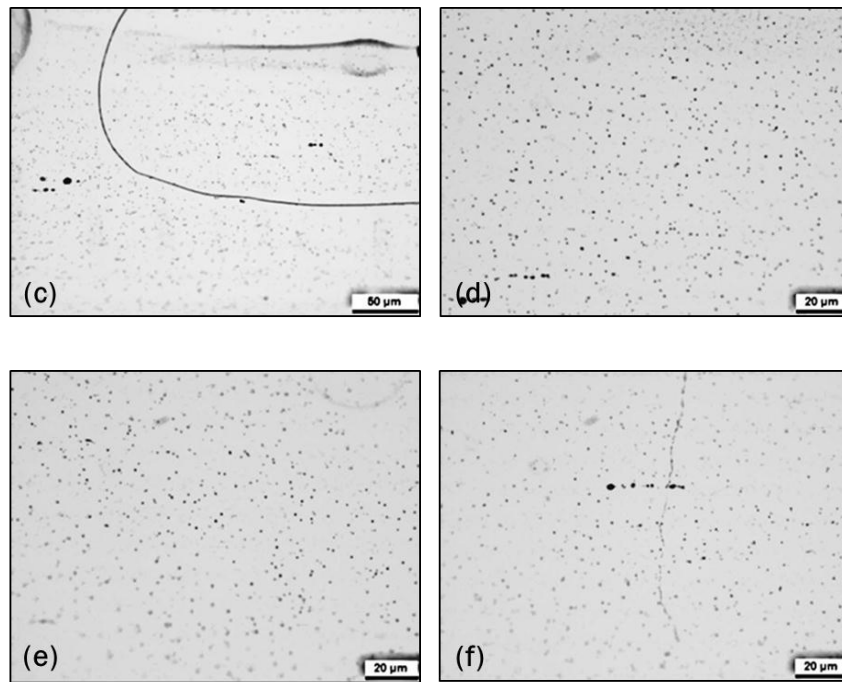
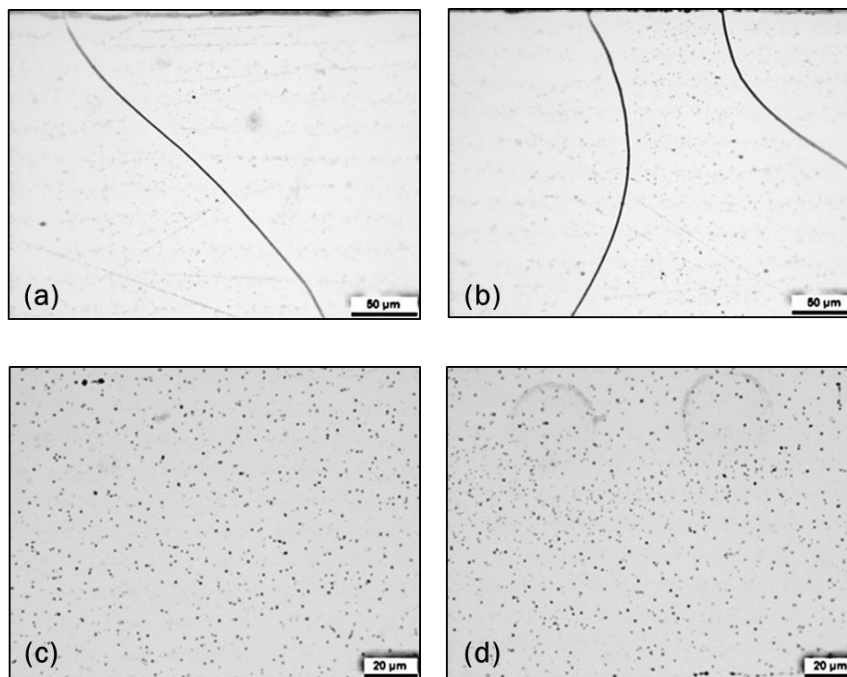


Figure 7.13 Dislocation structure of the edge section along the rolling direction in CGO+ after annealing at (a,b) 750 and 4 MPa (c,d) 800 and 4 MPa (e,f) 850 and 4 MPa



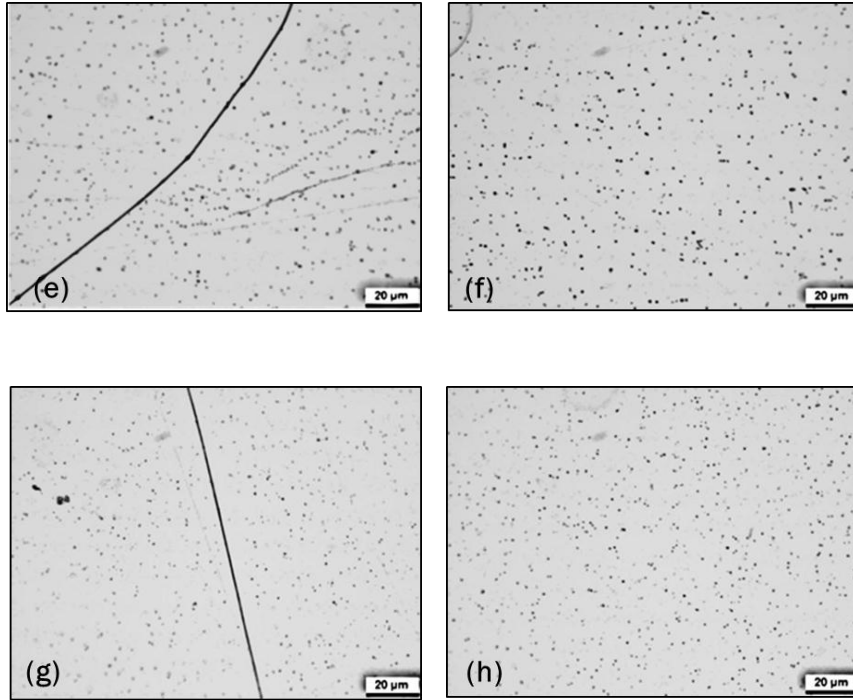


Figure 7.14 Dislocation structure of the edge section along the rolling direction in CGO+ after annealing at (a,b) 750 and 6 MPa (c,d) 800 and 6 MPa (e,f) 820 and 6 MPa (g,h) 850 and 6 MPa

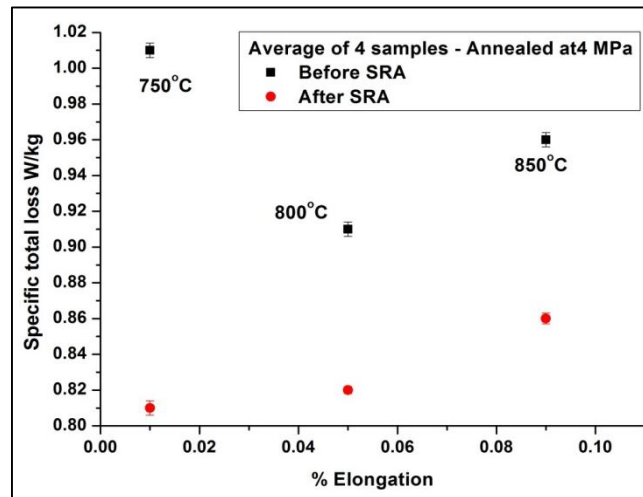


Figure 7.15 Comparison of specific total loss (1.5T and 50 Hz) with varying annealing temperatures and respective elongations after annealing at 4MPa

The relationship between the percentage elongation and dislocation structure to the specific total loss is shown in figures 7.15 - 7.17. The error bars indicate the variation

in the specific total loss in four samples annealed under the same stress-temperature combination. The samples were also tested for specific total loss after stress relief annealing in vacuum at 800°C for 1 hour to remove the cutting stresses.

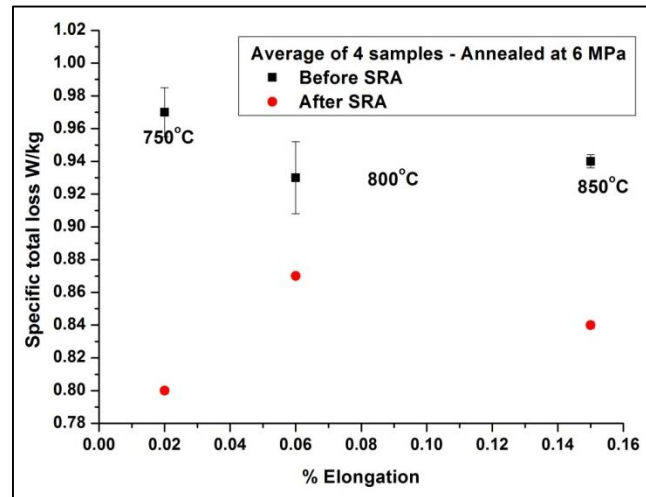


Figure 7.16 Comparison of specific total loss (1.5T and 50 Hz) with varying annealing temperatures and respective elongations after annealing at 6MPa

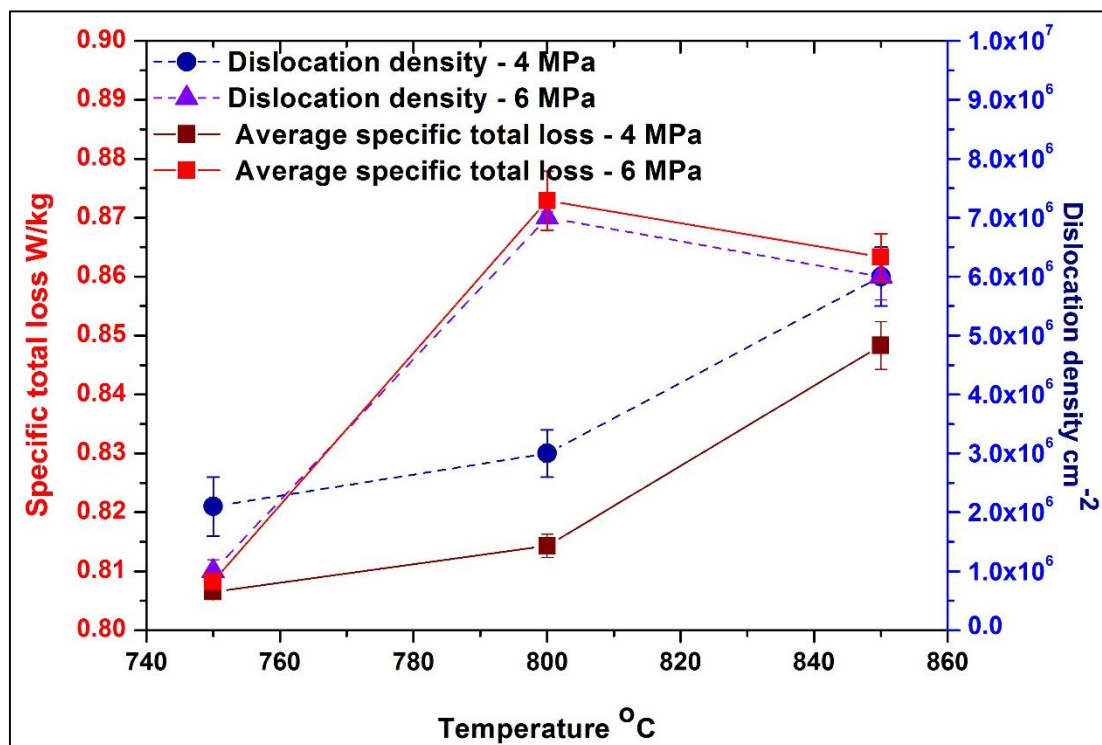


Figure 7.17 Variation in dislocation density with simulator annealing temperature at different temperatures and corresponding effect on specific total loss

7.6.4 Effect of stress relief annealing on specific total loss above threshold

dislocation density

The effect of stress relief anneal at 800°C for 1 hour on the dislocation structure of the sample which has a dislocation density higher than $1 \times 10^7 \text{ cm}^{-2}$ is discussed in this section. The $1 \times 10^7 \text{ cm}^{-2}$ is the point at which the specific total loss increases after stress relief annealing and hence this is considered to be the threshold dislocation density in this section. The results in figure 7.18 show an increase in specific total loss in five samples after the stress relief annealing in samples with dislocation density above $1 \times 10^7 \text{ cm}^{-2}$. The errors bars takes into account the measurement errors and repeatability of the data after three measurements.

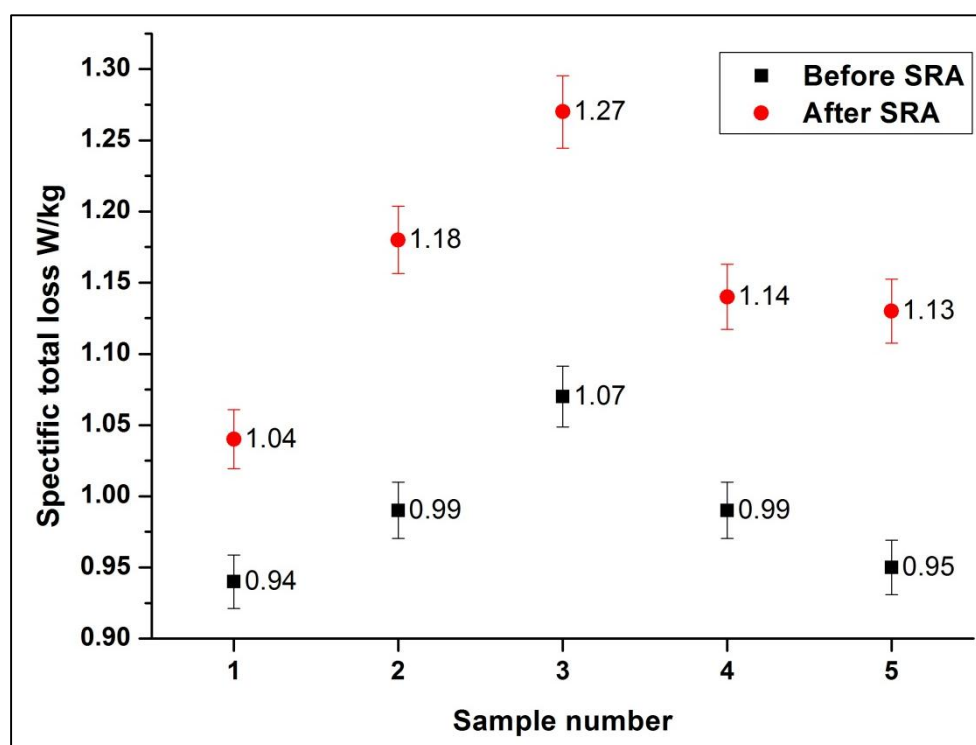


Figure 7.18 Comparison of specific total losses before and after stress relief annealing at 1.5T and 50Hz for samples with dislocation density above 10^7 cm^{-2}

The rearrangement of dislocations into small angle boundaries after stress relief annealing resulted in the increase in specific total loss. This is illustrated in figure 7.19

with dislocation structures before and after stress relief annealing and the corresponding specific total losses.

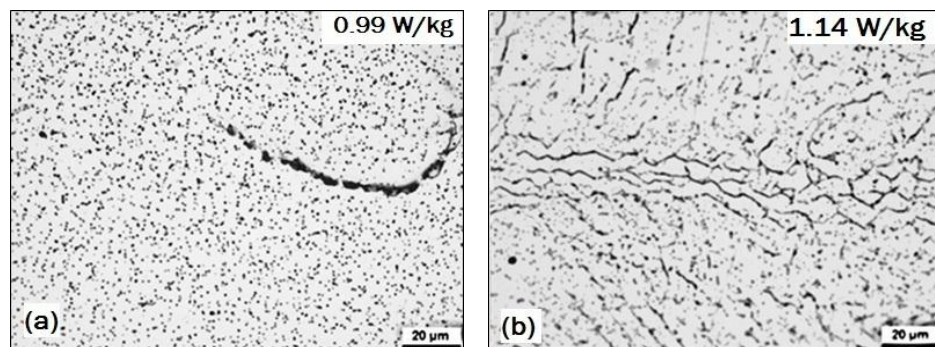


Figure 7.19 Edge section along the rolling direction showing dislocation images with specific total loss at 1.5T and 50 Hz for (a) Sample annealed in simulator at 7 MPa (b)

Same sample after stress relief anneal at 800°C for 1 hour after simulator anneal

7.7 Discussion

7.7.1 Effect of applied stress on dislocation density and power losses at 850°C in CGO+

An increase in stress from 4-7 MPa resulted in an increase in the dislocation density as shown in Figure 7.11. However, the deformation mode remained in the diffusion region as shown by the presence of only individual dislocations and the absence of any rearrangement of dislocations. Above 7 MPa, as shown in Figures 7.9 and 7.10, the dislocations rearranged themselves into small angle grain boundaries and dynamic recrystallisation took place forming new strain free grains. This re-arrangement and annihilation requires climb of dislocations and hence the deformation mechanism at this stress changes from diffusion creep to dislocation creep. In comparison with HiB material as shown in the deformation mechanism in Figure 5.6, where the deformation mechanism transforms from diffusion to dislocation climb mode at 5MPa stress whereas the CGO+

material withstood higher stress before the deformation mode changed from diffusion to creep mode at higher stress of above 6MPa.

Specific total loss at 1.5T flux density and 50Hz frequency increases with increasing dislocation density as shown in figure 7.11 which can be explained by the domain wall pinning effect by dislocations during magnetization. When the dislocation density exceeded the critical threshold of 10^7 cm^{-2} , stress relief annealing resulted in an increased specific total loss as shown in Figure 7.18. The stress relief anneal is used to relieve elastic stresses imparted into the sample during cutting. When the dislocation density was above the threshold, the stress relief anneal rearranged dislocations by forming small angle grain boundaries as well as relieving elastic stresses. This resulted in an increased specific total loss of 1.14W/kg after stress relief anneal in GOES compared to 0.99 W/kg at 1.5T and 50Hz, before stress relief anneal with a higher individual dislocation density.

The effect of re-arranged or altered dislocation structures to form small boundaries in the grains on the B-H characteristics of the material is shown in Figure 7.20. The rearranged dislocations in the form of small grain boundaries showed a profound effect on the coercivity of the material as shown in figure 7.20 and table 7.1 below. Sokolov et al. [2] reported similar trends with up to 10% increase in losses originating from the small angle grain boundaries rather than individual dislocations. The increase in coercivity of the material confirms this trend of rearrangement of dislocations after stress relief anneal as shown in Figure 7.20.

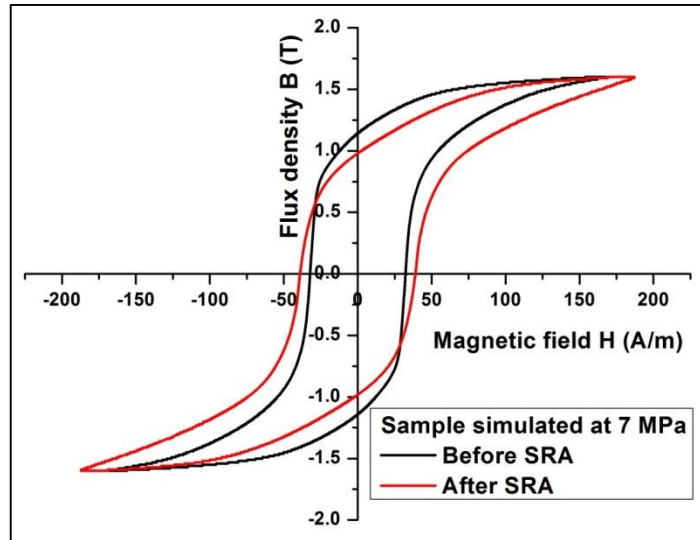


Figure 7.20 Increase in coercivity after stress relief annealing due to the formation of small angle grain boundaries (1.5T, 50Hz, Single strip test)

Table 7.1 Coercivity of samples LAFFAS annealed at 7MPa, before and after stress relief annealing (SRA) at 800°C for 1 hour

Sample number	Coercivity A/m	
	Before SRA	After SRA
1	30	30.5
2	28.1	34.5
3	30.9	37.5
4	28.3	33.8
5	27.4	32.7

The reduction in permeability in the low induction region of the B-H curve shown in figure 7.20, where the magnetization mechanism is by domain wall motion showed the increased pinning effect of small angled grain boundaries on magnetic domain wall movement.

7.7.2 Load – Temperature – Elongation in CGO+

Mechanical behaviour of CGO and HiB materials at high temperatures have been widely studied whereas the effect of high temperatures on CGO+ is not very well understood. The study to calculate percentage elongation of CGO+ at 750-850°C is important due to varying deformation mechanisms in operation in this range of temperatures as shown by the deformation mechanism map calculations in chapter 5. Five samples each were annealed at 750, 800 and 850°C at 4 MPa and 6 MPa stress. The trend of elongation against temperature that emerged for CGO+ was compared with traditional HiB material [3]. This comparison of their high temperature mechanical properties showed a marked difference in the response of CGO+ compared to HiB at both 4 MPa and 6 MPa. At 750°C, the elongation was lower than that of HiB material whereas at 850°C the elongation was 20% higher than that of HiB at 0.15% compared to that of 0.12% in HiB. This is an important understanding about the mechanical behaviour of CGO+ material since the process conditions at which HiB is manufactured are not suitable for CGO+ because of the higher sensitivity to stress at continuous flattening anneal peak temperatures. The mechanism behind this behaviour needs to be studied in detail and is outside the scope of this work. The effect of this variation in mechanical behaviour on the specific total loss is an important phenomenon to understand.

7.7.3 Effect of varying temperature and stress on power loss

The effect of different stress-temperature combination on the specific total loss of CGO+ is explained in this section. The average specific total loss of the CGO+ material followed the increasing trend of dislocation density with an increase in temperature and stress.

In the experiments where 4 MPa stress was applied, the dislocation density increased with increasing temperature from 750-850°C. The average specific total loss increased from 0.81 to 0.87 W/kg at 1.5T and 50 Hz as shown in figure 7.17. The error bars show the range of specific total losses of four sets of samples at each stress-temperature combination. In experiments where 6 MPa stress was applied, average dislocation density increased until 800°C and at 850°C the density of dislocations reduced from 6×10^6 to 4.5×10^6 /cm² as shown in figure 7.17. The specific total loss followed the dislocation density trend and hence a reduction from 0.88 to 0.86 W/kg was observed between samples annealed at 800 and 850°C.

The relationship between specific total loss and dislocation density showed the pinning effect of dislocations on domain wall motion and hence an increase in the specific total losses. However a fivefold increase in dislocation density from 1×10^6 cm⁻² to 5×10^6 cm⁻² resulted in very small increase in specific total loss from 0.81 to 0.87 W/kg at 1.5T and 50 Hz. This trend denotes the limited effect of individual dislocations on the movement of domain walls and hence the specific total losses.

The possible reason for decrease in dislocation density when the sample was LAFFAS annealed at 6 MPa and 850°C compared to 800°C could be that the assistance of higher stress (6MPa compared to 4MPa in the previous case) in dislocation movement and annihilation of the unlike dislocations by increased dislocation glide.

7.7.4 Comparison of B-H characteristics

The comparison of B-H characteristics of the samples annealed at different peak temperatures and 4, 6 MPa stresses are shown in figures 7.21 and 7.22 below. A few important points to be noted from the B-H curves are

1. The reduction in permeability in the high induction region for the samples annealed at lower peak temperature of 750°C. The change in the slope of the curve in the high induction region is the effect of elastic tensile stress applied by the weight of the magnetic testing yoke and not the effect of dislocations. This shows that annealing at 750°C was not sufficient to achieve the objective of strip flattening by continuous flattening anneal process.
2. There was no appreciable difference in coercivity (25 A/m approximately for all the samples) between samples annealed at 800 and 850°C peak temperatures considering the doubling in dislocation density from $3 \times 10^6/\text{cm}^2$ to $6 \times 10^6/\text{cm}^2$. This indicates the absence of a significant effect on the coercivity of the material by an increase in individual dislocations. Perryman et.al, [4] suggested that the major change in coercivity is from inclusions and lattice defects and not from local elastic stress variations. Hence a negligible change in coercivity shows the small effect of individual dislocations on coercivity.

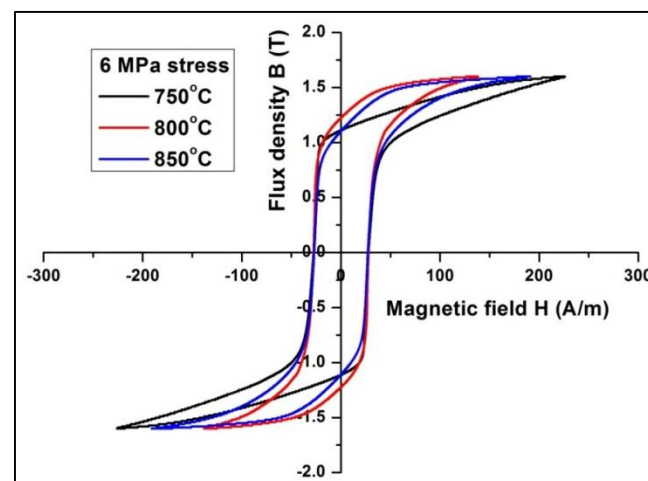


Figure 7.21 Comparison of B-H curves for CGO+ samples annealed at different temperatures and 6 MPa stress (1.5T, 50Hz, Single Epstein test)

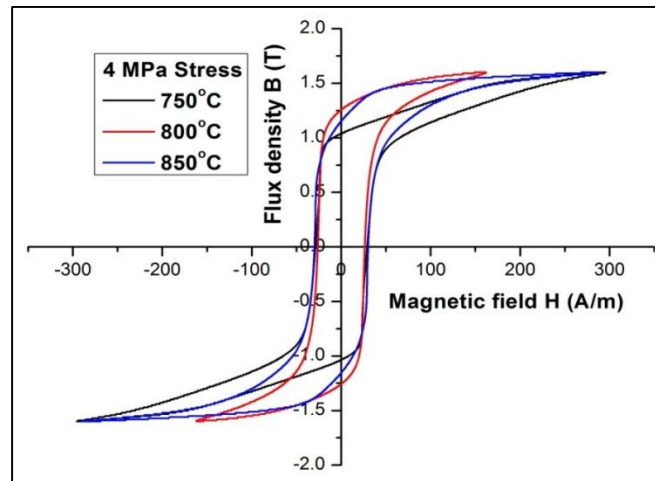


Figure 7.22 Comparison of B-H curves for CGO+ samples annealed at different temperatures and 4MPa stress (1.5T, 50Hz, Single Epstein test)

7.7.5 Relationship between the size of the pinning site and pinning effect

A comparison of size of domain pinning sites and the domain walls is necessary to understand the effect of individual dislocations. The effect of inclusion size on the pinning effect of domain walls in Iron crystals was studied by Dijkstra and Wert [4]. They reported the minimum size of inclusions is 120nm to have a pinning effect on domain walls in Iron crystal which are typically 180nm. They also concluded that the net effect on coercivity by inclusions which are of similar dimensions as the domain wall width is the highest whereas the effect of smaller inclusions (compared to domain wall width) is negligible.

Turner et.al [5] reported the pinning effect of inclusions in Fe-Si alloy and concluded that the pinning effect increases above 10 μ m inclusion size and a 26% increase in Barkhausen noise at 100 μ m inclusion size.

Dijkstra and Wert [4] showed that there are two components of energy involved in determining the pinning effect of inclusions which are described below

1. surface tension effect – depending on the decrease in magnetic domain wall volume when it encloses an inclusion
2. magnetic dipole effect – the magnetic dipole energy of the inclusion

Vicena [6] extended the theory proposed by Dijkstra et.al [4], about the size of inclusions on the pinning effect on domains to lattice defects. He derived an energy balance between the change in elastic field around the dislocation and the energy required to move a domain wall over the dislocation. He also concluded the effect of dislocations on domain pinning is much greater than the effect of inclusions. However the exact size of dislocation array required for pinning an 180nm wide domain wall is still unknown.

From section 7.4.4, it is hence clear that the increase in individual dislocation density did not result in domain wall pinning whereas a rearrangement in small grain boundaries as shown in 7.6.7 and 7.7.1, results in an increase in the pinning effect and hence the coercivity. This effect is discussed in greater detail in 8.6.10 with Barkhausen noise measurements.

7.8 Conclusions

1. LAFFAS was successful in simulating the continuous flattening line by producing samples at different stress and temperature combinations by producing samples for microstructure and magnetic testing at a lab scale.
2. A nitrogen protective atmosphere was essential to prevent sample oxidation during simulation of continuous flattening annealing.
3. Individual dislocation density increases when CGO+ samples were annealed at 850°C and increasing stresses from 4-7 MPa at 850°C above which dynamic recrystallisation took place resulting in a strain free fine grain structure.

4. Above a threshold dislocation density around $1 \times 10^7 \text{ cm}^{-2}$, stress relief annealing rearranged dislocations into small angle boundaries that had a detrimental effect on power loss more than individual dislocations as shown by the increase in loss to 1.14 W/kg from 0.99 W/kg at 1.5T and 50Hz, even though the number of individual dislocations reduced.
5. Measurement of percentage elongation at 4, 6 MPa and 750-850°C temperature combinations in CGO+ material showed the difference in response to stress at high temperature of CGO+ compared to HiB.
6. The CGO+ material elongated 20% more compared to that of conventional HiB materials with similar grain size at the continuous flattening anneal temperature of 850°C and 6MPa stress.
7. Process parameters set for HiB continuous flattening anneal process are not suitable for CGO+ due to the higher stress sensitivity of the material at 850°C and hence they resulted in specific total losses that were approximately 10% higher than a typical HiB material of the same thickness.
8. The dislocation count decreased at 6MPa and peak temperature of 850°C compared to the sample annealed at 800°C possibly because of the influence of increased temperature on the mobility and annihilation of dislocations.
9. The average specific total loss of 1.18 W/kg at 1.7T and 50Hz, for samples annealed at 850°C and 6 MPa shows the sensitivity of CGO+ at the continuous flattening anneal conditions compared to HiB with average losses of 1.05-1.1 W/kg at 1.7T and 50Hz.
10. LAFFAS experiments have revealed important understanding to improve the continuous flattening anneal process of CGO+.

7.9 References

1. C A Schneider, W S Rasband, K W Eliceiri, *NIH Image to ImageJ: 25 years of image analysis*, Nat Methods, 2012;9:671.
2. B K Sokolov, Y N Dragoshanski, V S Matveeva, M B Tsyrlin, F V Mineev, R B Puzhevich, *Inhomogeneity of magnetic properties of an anisotropic electrical steel and specific features of dislocation structures*, Russ J Nondestruct+, 2004; 40:11.
3. K W Jenkins, D Summerhill, A Coombs, Preparatory technical data on O.E.S products, Technical note – Cogent Power Ltd., 1994.
4. R Perryman, *Effects of tensile and compressive stress on 3% grain-oriented silicon iron*, J Phys D: Appl Phys., 1975; 8:1901.
5. L J Dijkstra, C Wert, *Effect of Inclusions on Coercive Force of Iron*, Phys Rev., 1950; 79(6):959.
6. S Turner, A J Moses, J P Hall, K Jenkins, *The effect of precipitate size on magnetic domain behavior in grainoriented electrical steels*, J Appl Phys., 2010:107.
7. F Vicena, *On the influence of dislocations on the coercivity of ferromagnetics*, Czechosl Journ Phys., 1955; 5:499.

Chapter 8

Factors affecting polygonization of dislocations and their effects on magnetic properties of Fe-3.25% Si steel

8.1 Introduction

Mobility of dislocations and the factors affecting the mobility have been widely studied but their effects on magnetic properties have not been studied. This chapter aims at studying the effect of individual dislocations and also energetically favourable rearrangement of dislocations on the magnetic properties of GOES. Effect of temperature, soaking time during heat treatment and initial orientation of the grains before deformation and heat treatment are studied.

8.2 Polygonization - mechanism

Polygonization is the processes of rearrangement of dislocations with the same signs by slip and climb mechanisms [1]. A typical polygonized grain structure in grain oriented electrical steel is shown in Figure 8.1.



Figure 8.1 Edge section of HiB GOES polygonized at 950°C showing a typical polygonized structure

Dislocations are created when crystalline solids are deformed plastically for ex., by bending. These dislocations can be re-arranged by increasing the mobility of dislocations at high temperatures. This process takes place in two steps.

1. Some of the dislocations created during the bending process annihilate with the oppositely signed dislocations.
2. The dislocations that were not annihilated slip and climb assisted by temperature (to cross the activation energy barrier to climb) to form low energy boundaries with every dislocation stress field cancelling out the stress field at the opposite end of the dislocation in the plane above or below it. [1].

During polygonization, strain energy in the deformed crystalline lattice can be lowered by the rearrangement of dislocations. A simple case of polygonization is shown in Figure 8.2. Plastic deformation by bending a metal, assuming the slip planes are aligned in the direction of stress and parallel to the surfaces, produces a large number of positively signed edge dislocations as shown in Figure 8.2. There are also negatively signed edge dislocations present in the lattice, the sign depending on the direction in which the half plane of atoms is arranged in a lattice. This simple case takes into account only edge dislocations without considering the interaction between edge and screw dislocations. Interaction between dislocations can have two driving forces – stress and temperature. Stress is the rate controlling variable for the movement of dislocations in their respective lattice planes and temperature is the rate controlling variable for movement perpendicular to the lattice plane in which the dislocations are present[1].

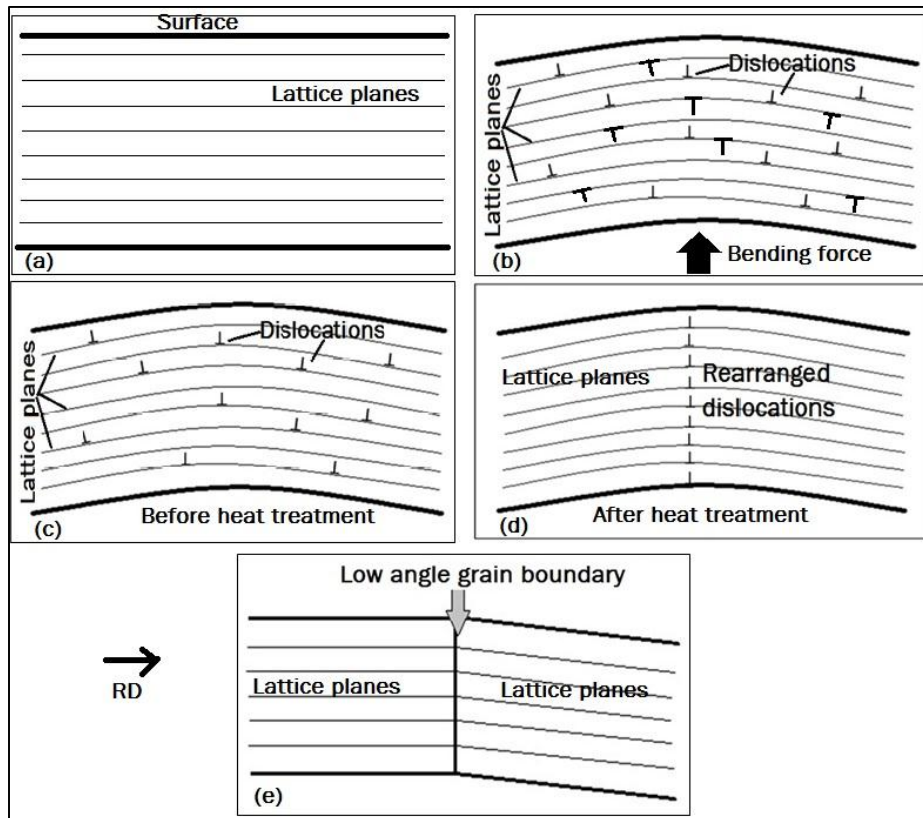


Figure 8.2 Schematic of the edge section of a crystalline material (a) Lattice planes in a crystalline material (b) Positive and negative edge dislocations in the as bent configuration (c) Annihilation of oppositely charged dislocations (d) Re-arranged dislocations after heat treatment (e) Formation of a polygonized low angle grain boundary

Step-by-step description of the polygonization phenomenon is shown in figure 8.2. A simple lattice structure showing lattice planes of atoms is shown in figure 8.2(a). Application of a plastic bending stress leads to the creation of both positive and negative dislocations as shown in figure 8.2(b). Unlike dislocations move in their respective planes and annihilation takes place leaving only the excess like signed dislocations as shown in figure 8.2(c). High temperature aids in the mobility of dislocations perpendicular to their respective lattice planes. This mobility results in the rearrangement of dislocations into energetically favourable structures as shown in figure 8.2(d) and 8.2(e) resulting a small

mis-orientation created between the two grains on either side of the boundary because of the arrangement of dislocations.

8.3 Driving forces for Polygonization

8.3.1 Temperature

Polygonization occurs by glide and climb of dislocations [1]. Glide, which is the movement of dislocations parallel to the slip plane, is facilitated by stress and occurs at temperatures $< 0.3T_m$ where T_m is the melting point of the metal. As the temperature increases, another mechanism of dislocation motion called climb, which is the movement of dislocations perpendicular to the slip plane in which it is present. Climb is dependent on vacancy diffusion towards or away from the end of a dislocation and thus thermally activated [1]. Climb usually happens at elevated temperatures above $0.3T_m$.

8.3.2 Reduction of force field between dislocations

Figure 8.3 shows the repulsive force between two like-signed dislocations in adjacent planes. The blue ellipse denoted the area of the tension field and the red one shows the area of the compressive field on the ends of dislocations as shown in figure 8.4 [2]. For the two dislocations D1 and D2 located as shown in the figure, the force between them are given by equations 1 and 2.

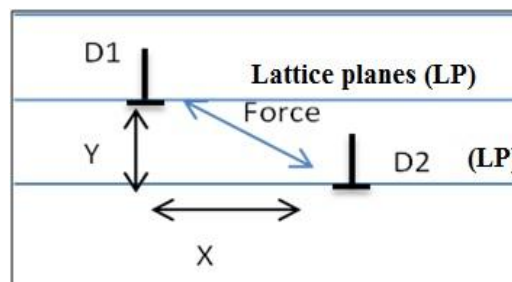


Figure 8.3 Force between two like dislocations on adjacent slip planes

Force field given by Equations (1) and (2) as derived by Dieter [2],

$$F_x = \frac{Gb^2}{2\pi(1-\nu)} \cdot \frac{x(x^2-y^2)}{(x^2+y^2)^2} \quad 1$$

$$F_y = \frac{Gb^2}{2\pi(1-\nu)} \cdot \frac{y(3x^2+y^2)}{(x^2+y^2)^2} \quad 2$$

Where G – shear modulus, b – Burger's vector, ν – Poisson's ratio

From Equations 1 and 2 the force between the two dislocations is minimal when they are arranged 45° or 90° with each other. At 45° separation between the two dislocations, force field in the x-direction becomes zero whereas at 90°, force field in y-direction becomes zero.

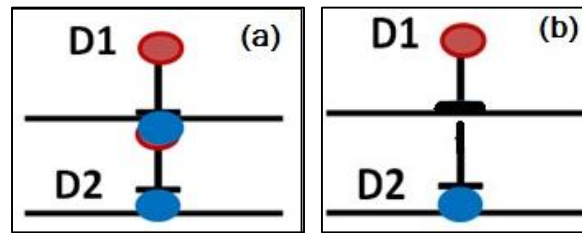


Figure 8.4 Schematic representation of force fields between two dislocations

(a) Coloured circles showing the tension and compression fields at ends of the dislocations (b) Cancellation of overlapping stress fields of D1 and D2 resulting in reduced overall stress field

Figure 8.4 shows the reduction in overall stress field by cancellation of the tension stress field of D1 and compression stress field of D2 in the adjacent plane. Thus a long vertical stack of dislocations has a much reduced total stress field because of the cancellation of tension field of one dislocation by the compressive field of the dislocation in the plane below as shown in Figure 8.2(d). Figure 8.2(e) shows the schematic result of polygonization of like signed dislocations to form a low angle grain boundary [2]. This

results in a small mis-orientation of less than 5° between the grain on the left and the right. Thus there are two driving forces for polygonization – temperature and reduced overall stress field.

8.4 Literature review on polygonization

8.4.1 Introduction to Polygonization

Polygonization has been widely studied in a variety of single crystals with various crystal structures. The factors affecting polygonization in single crystals is described in this section, because of the reduced complexity of the process in a single crystal without the influence of surrounding grains.

Effect of orientation of a slip plane to the stress axis in silicon single crystals with diamond cubic structure was studied by Vogel et al [3]. When the closely packed slip plane is aligned with the loading direction, dislocations are created in only one slip system assisting in easy climb and glide at a higher temperature. When the easy slip planes are aligned away from the loading direction, dislocations are created in several slip systems leading to Lomer-Cottrell [2] barriers for climb resulting in partial or no polygonization.

Kaun et al., reported the effect of temperature on dislocations created in molybdenum single crystals [4]. They studied the mobility of dislocations in a temperature range from 20-250°C. The resultant difference in mobility between two sets of dislocations revealed the increase in the mobility of edge dislocation with increasing temperature compared to screw dislocations [5].

Spitzig et al [5], reported the activation of different slip systems at various temperatures in iron single crystals. They also studied the variation in critical resolved shear stress with the degree of packing in the slip planes. The study revealed that the {110} planes are active at room temperatures with the {100} planes becoming increasingly

active at lower temperatures below 77K. This study showed there is a change in active slip systems according to the temperature.

It can be concluded from the above two studies that the effect of temperature, time of annealing and the orientation of slip planes to the stress axis are the factors affecting polygonization in a single crystal.

8.4.2 Polygonization in Fe-Si single crystals

Polygonization of dislocations in Fe-Si single crystals has been studied extensively and the temperature at which the dislocations polygonized to form small angle grain boundaries at fixed spacing is identified by Hibbard et al [6]. They reported the change in dislocation structure, especially the annihilation of unlike dislocations and re-arrangement of like dislocations into favourable low energy polygonized boundaries. Polygonization in Fe-Si single crystals is studied in detail at a range of temperatures. In single crystal Fe-3% Si alloy, complete polygonization takes place between 1020°C and 1060°C. Polygonized low angled grain boundaries are formed with a spacing of 20µm. Any increase in the soaking time at the above-mentioned temperature range did not alter the polygonized line spacing in case of single crystals [6]. This phenomenon in polycrystalline body centered cubic (BCC) materials is not understood.

8.4.3 Effect of microstructure and texture on magnetic properties of Fe-Si steel

Polygonization in polycrystalline Fe-3% Si alloy is an important phenomenon because of the dependence of magnetic properties on microstructure and texture of the material as explained by Gomes et al [7]. A model to understand the effect of mean grain size, texture factor (cumulative mis-orientation between Goss orientation and magnetization direction in an infinitesimal space) and Si content of the steel on magnetic induction at any given field was developed. This model showed a good correlation with

experiments in predicting the dependence of magnetic induction on the above mentioned three parameters up to a field of 300 A/m in commercial electrical steels with different composition and processing. At a higher applied field, magnetic anisotropy becomes the defining factor whereas at lower fields grain size and texture are found to be the decisive factors of magnetic induction at any given field. This is due to the dependence of magnetic induction on crystallographic texture because of the magnetization phenomenon by domain wall motion at low induction regions of the hysteresis curve. A quantitative dependence of the magnetic properties on texture, grain size and chemical composition is developed and hence showed the importance of understanding manufacturing processes of electrical steels to predict the final magnetic properties.

Sokolov et al [8], studied the effect of production processes on the resultant dislocation structures and specific total losses. The study addressed the inhomogeneity in specific total loss in electrical steel from the same process by studying the relationship between dislocation structures and specific total losses. The study concluded that the effect of grain boundary substructure is higher compared to individual dislocations. This is evident from the increase in specific total loss of samples with grain boundary substructure to 1.16 W/kg (1.7T and 50Hz) from 1.1 W/kg (1.7T and 50Hz) for samples with same individual dislocation density as the former but no grain boundary substructure. The formation of these grain boundary substructure in the material were linked to the creep mechanisms of deformation during continuous thermal flattening anneal process (at 850°C) [8].

Notoji et al [9], studied the effect of elastic and plastic strain on the mechanism of magnetization in electrical steel. A monotonous decrease in magnetization of the material at a constant field of 120A/m was observed up to 300 MPa (elastic up to 320 MPa) applied stress was reported. In the region of plastic stress (320 MPa and above) the magnetization

trend at a constant field of 120A/m was not decreasing monotonously. An initial increase in magnetization was observed upto 40 MPa and then the magnetization decreased. This trend was also observed during the magnetization reversal at 40 MPa stress. This is due to formation of lancet domains when the sample was deformed plastically [10]. The disappearance of lancet domains at 40 MPa stress was shown to be the reason for increased magnetization [9].

This objective of this study was to understand the rearrangement of dislocations and formation of small angled grain boundaries by polygonization of dislocations. It is important to understand the effect of polygonization on the magnetic properties of electrical steel. This part of the work studies the factors affecting the formation of polygonized low angle boundaries and their effect on domain size and the effect on power losses.

8.5 Experimental methods to study polygonized dislocations and its effects

Two types of Grain Oriented Electrical Steel (GOES) M120-27S (CGO) and M103-27P (HiB) are used in this study to understand the effect of polygonization on the power losses. High permeability grain oriented (HiB) and Conventional grain oriented (CGO) electrical steel were cut to Epstein size [11] (305x30mm) from the finished coil after continuous high temperature flattening anneal process.

Samples are cut from the product rolls by guillotine. The coating is then removed by immersion of the samples in 1N hydrochloric acid for 15 minutes. The samples are then washed with water and then acetone and dried immediately to avoid any rusting because of residual water. The samples are given a stress relief anneal at 810°C for 1 hour in a vacuum furnace to relieve cutting stresses.

The Epstein samples were bent to a radius of curvature of 50mm and held in place by fastener as shown in Figure 8.5.



Figure 8.5 (a) Schematic of the bend configuration of the Epstein length sample (b) Image of the bent Epstein fastened to maintain the curvature during annealing

These samples are then annealed in vacuum tube furnace at temperature and time combinations as shown in the Figures 8.6 and 8.7. Polygonization takes place by annealing under bending stress at higher temperatures as explained in section 8.2.

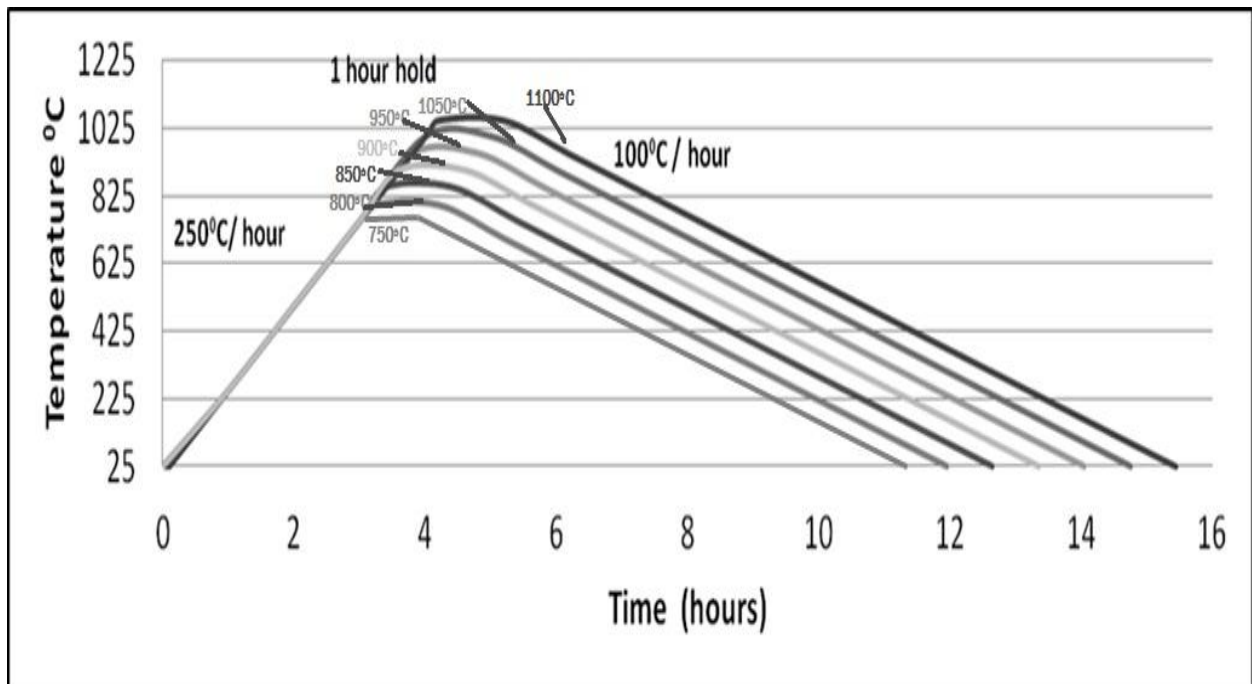


Figure 8.6 Heating rate, holding time and cooling rate for annealing at different temperatures

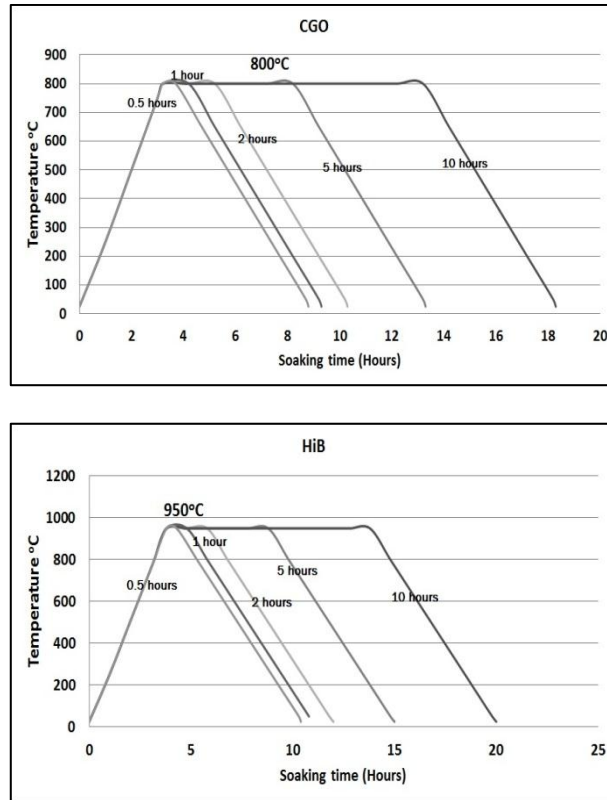


Figure 8.7 Annealing cycles for experiments at varying holding times of 30 minutes, 1,2,5 and 10 hours (a) for CGO (b) for HiB

The samples that were annealed under bend were then flattened and annealed at 810°C for one hour and furnace cooled at 150°C/hour to straighten them. Specific total loss is measured using the AC power loss measuring system [11].

All the samples were domain imaged before and after annealing for comparison of the domains before and after polygonization. Magnetic domains were imaged using Bitter technique with fine ferromagnetic powder dispersed using a surfactant in distilled water. An external vertically oriented magnetic field of 2.2 kA/m [12] aids the arrangement of the ferromagnetic powder along the stray fields that escape the sample perpendicular to the surface. Effects of edge stresses on domain images were avoided by the use of 100mm wide samples for domain imaging.

AC power loss measurements [11] were performed at 1.5 and 1.7T at 50 Hz and frequencies from 10-1000Hz in a single Epstein tester [11]. Five measurements were made in each sample. DC hysteresis loss measurement [13] was performed to separate the frequency dependent and independent components of losses to understand the effect of polygonized dislocations.

Localized power loss measurements were performed to provide useful insight into the effect of local variations in the orientation and microstructure of grains and their effect on magnetic properties. Localized magnetic flux density and magnetizing field were measured using a Hall probe and Needle sensor respectively [14]. Localized power loss testing was performed on samples with different degrees of polygonization to understand the grain to grain variation of polygonization and the power loss in any particular grain.

Barkhausen noise amplitude was measured before and after the polygonization heat treatment using an in-house Barkhausen noise measurement setup [15]. The system has a 100 turn primary magnetizing coil and a 500 turn secondary coil for detection of the induced e.m.f. A digital band pass filter was used to filter components in 25-75 KHz range to separate Barkhausen noise events from the faraday e.m.f [15]. The 25-75 KHz range is chosen because of the presence of highest Barkhausen noise peaks in this bandwidth range. The background noise was reduced by using a high resolution data acquisition card NI4461 capable of sampling at 200 KHz [15]. Epstein samples were tested in an acoustically shielded chamber to measure the Barkhausen noise peak and r.m.s amplitude at 1.5T and 50Hz for the samples before and after heat treatment.

The samples after annealing at different conditions and magnetic testing were cut by wire erosion and mounted in resin with the edge section along the rolling direction on the mount face for analysis. Usual metallographic sample preparation was followed to polish the surface of the edge section down to 1 μ m roughness and electrolytically etched

with Chrome-acetic etch for 3-5 minutes at 8V to decorate dislocations as reported by Morris et al [16]. The etched samples were then imaged at 500-1000x magnification using optical microscope to study the dislocation arrangement and the sub-structures in grain.

Orientation of the grains was studied by an Electron Back-Scattered Diffraction (EBSD) technique using field emission gun scanning electron microscope (FEGSEM) equipped with an EBSD detector. The grain size of GOES is relatively large compared with conventional metallurgical specimens which caused challenges due to the large areas that need to be scanned to obtain a reliable texture study. To mitigate this problem the edge section along the rolling direction was studied so that approximately 200 grains were taken into account for EBSD measurement and also the scan area was limited as shown in Figure 8.8. Twenty samples of 20x10x0.3 mm dimensions were cut by wire erosion method and stacked together to give a representative sample of the texture. This method was suggested to give representative results of the texture of large grained materials by Frommert et al [17]. Step size for the EBSD scan was 15 μ m and scan area was 25 mm x 6 mm.

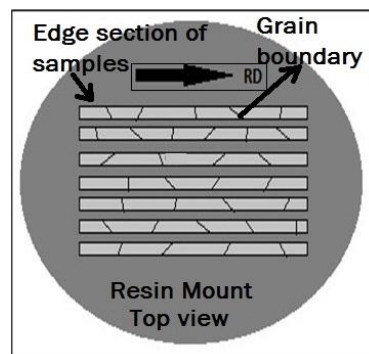


Figure 8.8 Schematic illustration of sample mounting arrangement to cover a large number of grains in electrical steel with average grain size of 3mm

8.6 Results

8.6.1 Effect of temperature on polygonization in CGO

The mechanism of polygonization shows dislocation glide and climb are the two predominant mechanisms. Hence temperature becomes a defining factor on the degree of polygonization. This is illustrated in Figure 8.9. An increase in temperature shows a progressive increase in the degree of polygonization in CGO up to 800°C above which the polygonized structures are annihilated.

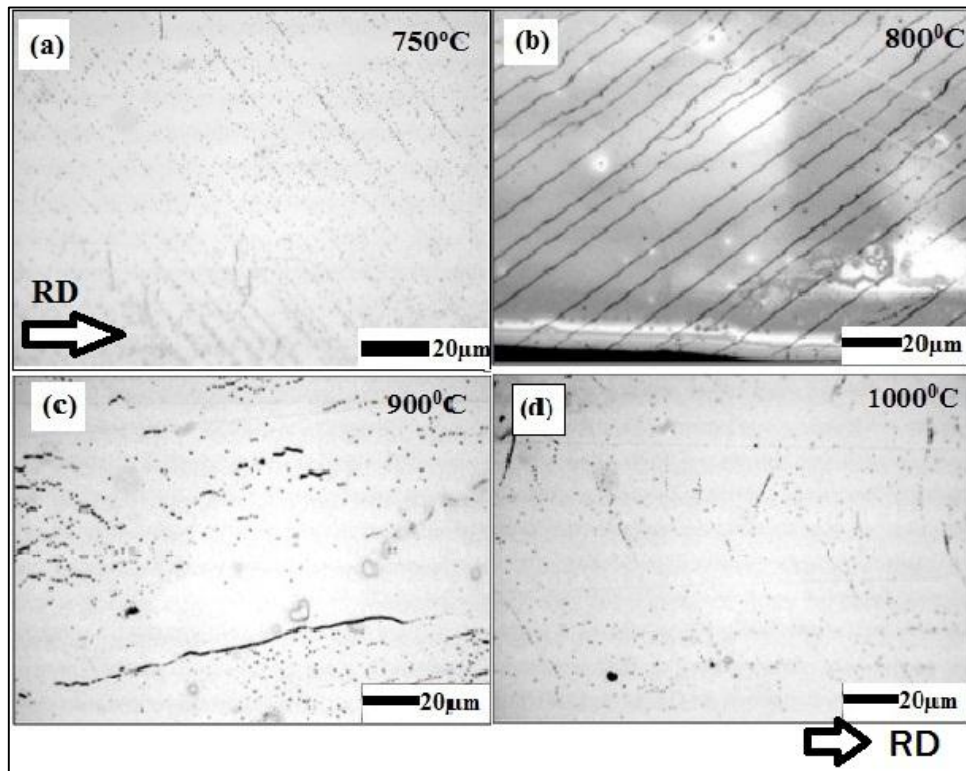


Figure 8.9 Effect of temperature on polygonization of dislocations in four samples of CGO at (a) 750°C (b) 800°C (c) 900°C (d) 1000°C for 1 hour in each case

8.6.2 Effect of temperature on polygonization in HiB

Temperature has identical effects on CGO and HiB except for the fact that polygonization is complete at a much higher temperature of 950°C compared to 800°C in CGO. At temperatures below 950°C polygonization is incomplete with a large number of

individual dislocations evident from Figure 8.10. As the temperature increases above 950°C the polygonized dislocations slowly annihilate into higher angle grain boundaries that do not possess any fixed orientation like the polygonized boundaries.

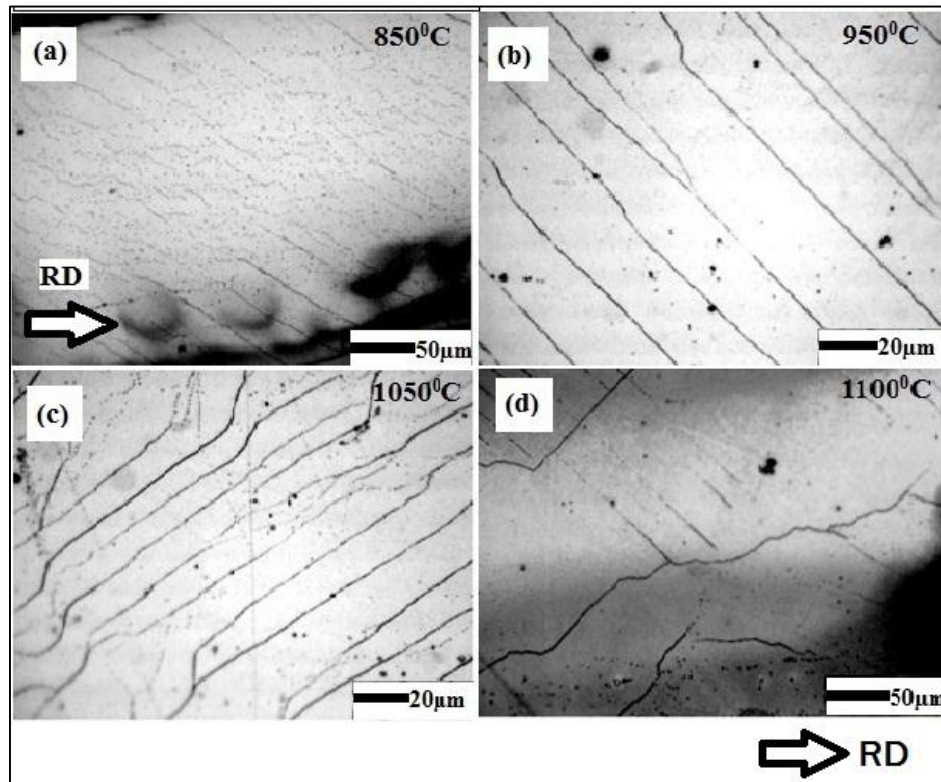


Figure 8.10 Effect of temperature on polygonization of dislocations in four samples of HiB at (a) 850°C (b) 950°C (c) 1050°C (d) 1100°C for 1 hour in each case [Direction of polygonized lines may be different due to difference in sample mounting and not metallurgical processes]

8.6.3 Effect of soaking time on degree of polygonization

To study the effect of varying soaking times, 5 samples each of CGO and HiB were soaked at 800 and 950°C as these are the optimized temperature for polygonization for CGO and HiB respectively for 30 minutes, 1, 2, 5 and 10 hours. Soaking time variation and its effects on CGO and HiB are illustrated in Figures 8.11 and 8.12 below.

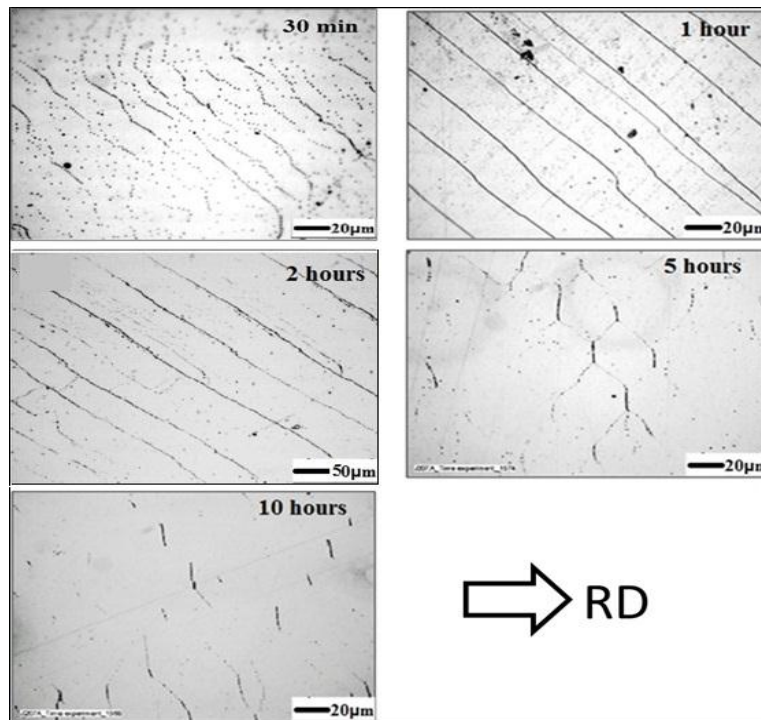


Figure 8.11 Effect of holding time at heat treating temperature on polygonization in HiB material at 950°C

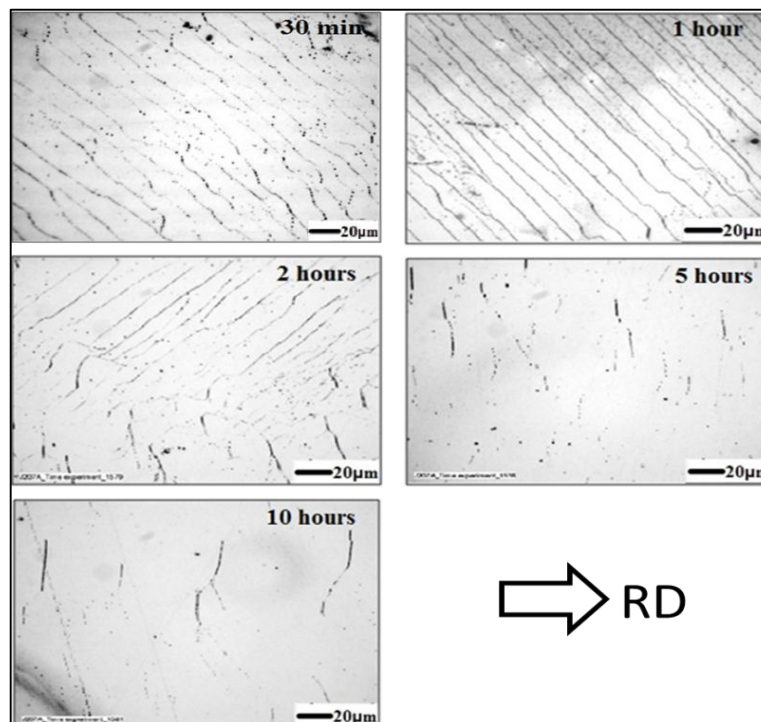


Figure 8.12 Effect of holding time at heat treating temperature on polygonization in CGO material at 800°C

Soaking at the requisite temperatures for 1 hour was found to be optimal for the completion of polygonized grain boundaries. Soaking times longer than 1 hour led to the polygonized boundaries being annihilated into fewer high angle grain boundaries as illustrated in Figures 8.11 and 8.12.

8.6.4 Dependence of polygonization on relative orientation of grains to direction of curvature

In any polycrystalline material, the orientation of each grain to the direction of application of load determines the deformation mechanism because of anisotropic behavior of different lattice planes to loading. Even in case of highly textured electrical steel, there exists a small mis-orientation between different grains and also away from the required Goss texture. The effect of this mis-orientation of grains in a polycrystalline material on polygonization has not been studied in detail.

A correlation of EBSD orientation data for different grains and the corresponding polygonized dislocation structures is shown in this section to understand the effect of individual grain orientation on degree of polygonization. Grains with a range of mis-orientation between their $\{110\}$ $\langle 100 \rangle$ system and loading direction from $2-20^\circ$ were selected from the EBSD texture plot shown in Figure 8.13. Polygonized dislocation structure of these grains were imaged and compared in Figure 8.14.

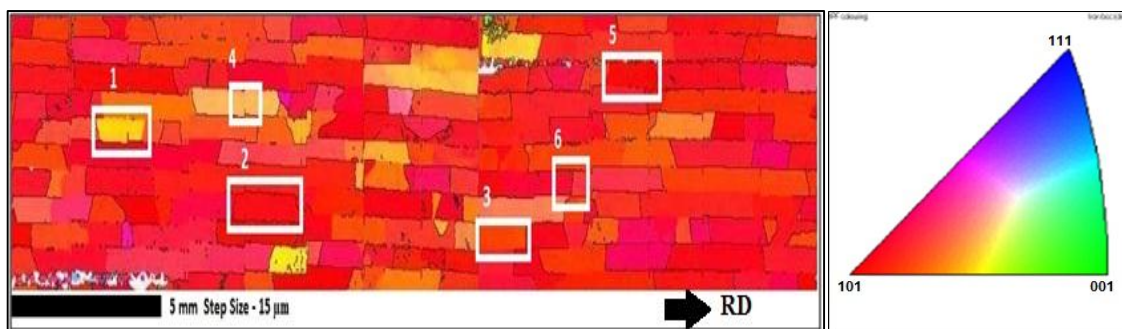


Figure 8.13 EBSD map of the edge section of a stack of samples cut from one Epstein with their relative orientations to Goss texture shown in the scale

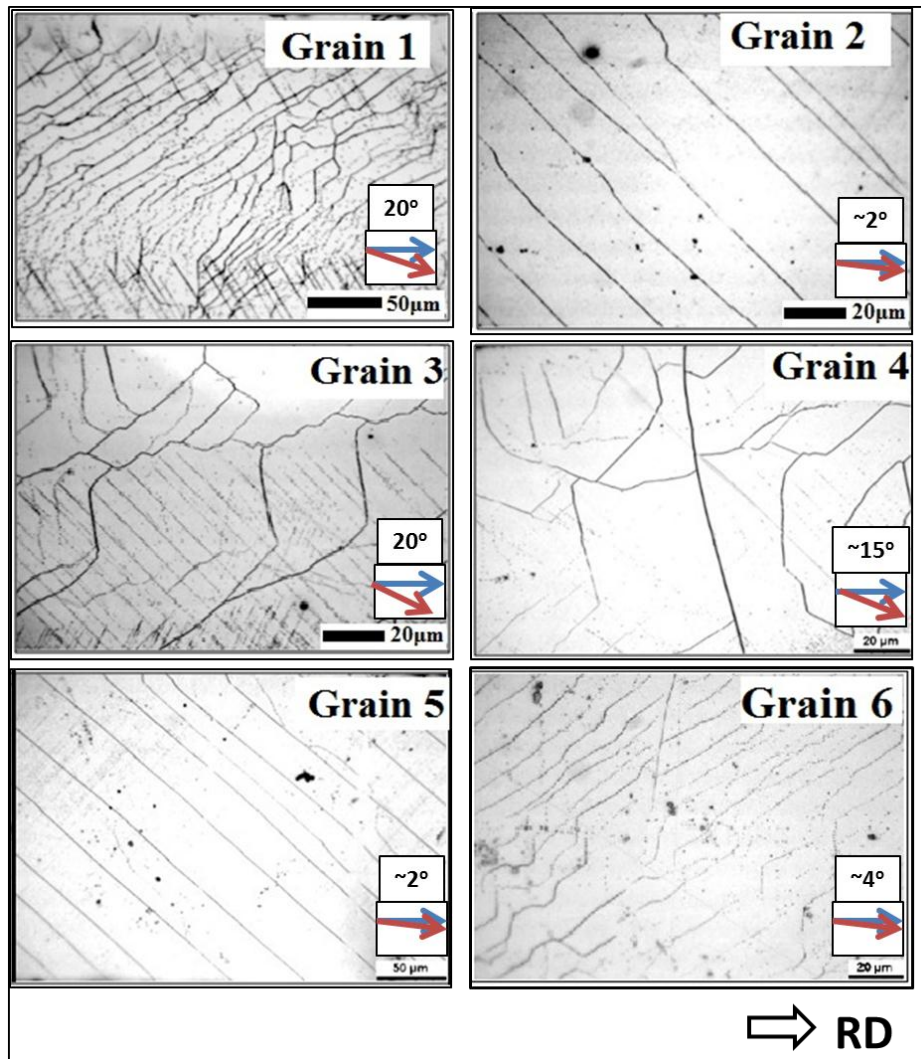


Figure 8.14 Difference in degree of polygonization depending on relative orientation of easy slip planes to the direction of curvature shown by the arrows (blue arrow showing the direction of curvature and red arrow showing the orientation of the grain) in the figure

8.6.5 Effect of degree of polygonization on magnetic domain structures

This section shows the effect of polygonized dislocations on magnetic domains. Comparison of magnetic domains before and after polygonization was performed to understand the effect of polygonized dislocations.

Change in domain widths was observed in some grains and no appreciable change in another set of grains in the same sample and hence the annealing conditions of the grains

are exactly the same. The difference is illustrated in figure 8.15. The value of average domain widths before and after polygonization, given in table 8.1, shows the grain-to-grain variation in change of domain widths.

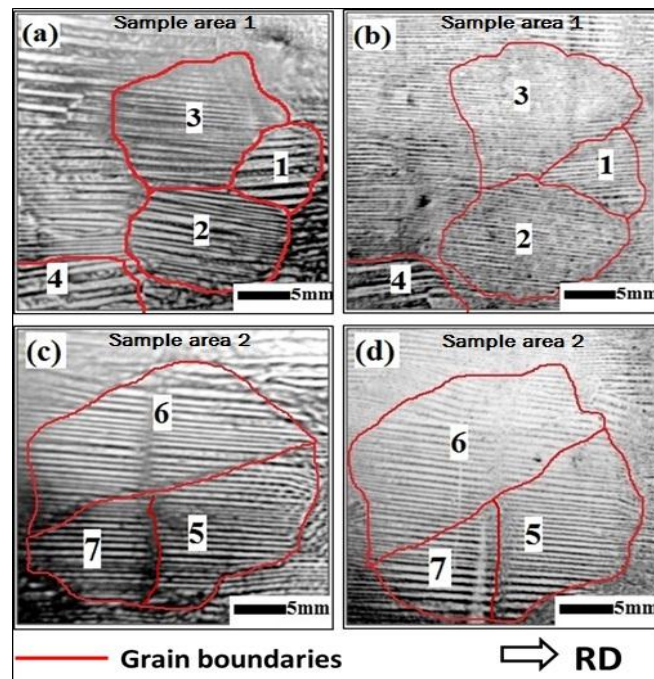


Figure 8.15 (a) and (c) are two sets of grains before polygonization, (b) and (d) are the same respective set of grains after polygonization. (a) and (b) - Magnetic domains in grains 1,2,3 refined from (a) to (b) whereas in Grain 4 domain width remains unchanged.

(c) and (d) - Magnetic domain size in grains 5-7 remain same before and after polygonization treatment (The boundaries are approximate due to the manual errors involved in identifying the boundary from a domain image)

Table 8.1 Average domain widths in the six grains studied in Figure 8.15

Sample area in Figure 8.15	Grain No.	Average domain width (mm)	
		Before polygonization	After polygonization
1	1	1.8	0.4
	2	0.7	0.4
	3	0.7	0.3
	4	1.4	1.3
2	5	0.8	0.8
	6	0.9	0.8
	7	0.9	0.9

The differences in change of magnetic domain widths in different grains of the same sample led to microstructural investigation of these two varieties of grains:

1. Grains where the magnetic domains are refined
2. Grains where the magnetic domains are unaltered

Table 8.1 shows the reduction in domain widths by a factor of 2-4 in grains 1-3 and no reduction in domain widths in grains 4-7. This is also illustrated in figure 8.15. Dislocation structure of these grains are shown in Figure 8.16.

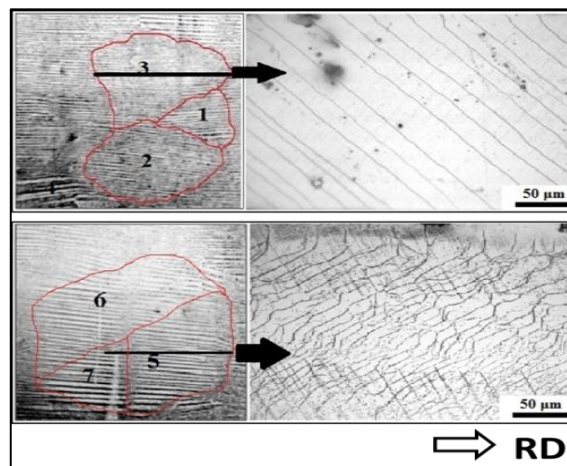


Figure 8.16 Micrograph showing the dislocation structure in the edge section of the grains with varied degree of change in domain width (Black lines show the location of the edge section)

8.6.6 Effect of polygonized line spacing on magnetic domain width

This section shows the effect of soaking time during anneal and the effect of line spacing on the change in magnetic domain width. Three samples of HiB were heat treated at 950°C for 1, 2 and 5 hours to study the domain structures by modified Bitter technique [15]. The average change in domain widths was analyzed before and after polygonization. Brailsford [18] reported a ratio between the width and length of domains in α -Fe at which both the magnetic domain wall and magnetostatic energy components are minimum. When

the values of domain width and length are given in centimeters, the ratio is given by Equation 3

$$W / \sqrt{L} = 0.07 \quad 3$$

Where W – Width of the domain in cm and L – Length of the domain in cm

The ratio between width and length of the domains were also analyzed and illustrated in Table 8.2. The variation in domain width in samples soaked for different times of 1,2 and 5 hours are illustrated in Figure 8.17.

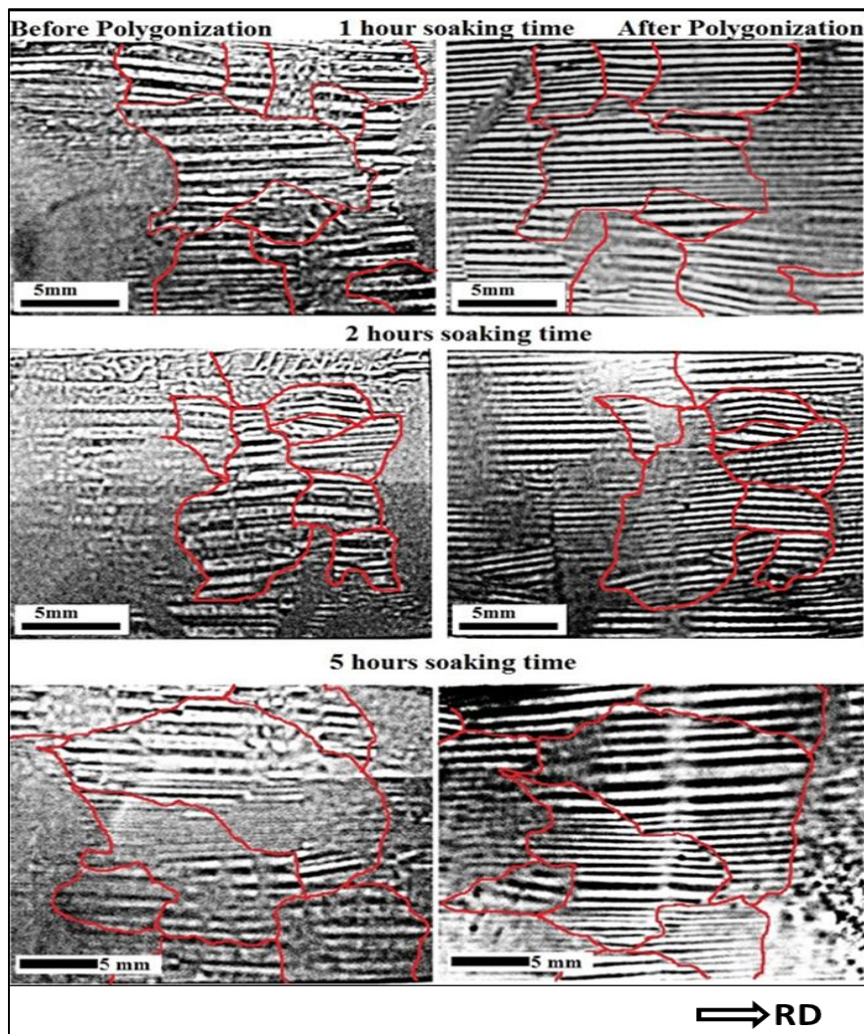


Figure 8.17 Effect of soaking time at 950°C on magnetic domain width – Width of the domains in samples soaked for 1 and 2 hours are reduced by a factor of 2-4 and samples soaked for 5 hours show no reduction in domain width

Table 8.2 Comparison of polygonized line spacing and average ratio between domain widths before and after polygonization in HGO material

Soaking time at 950°C (In hours)	Polygonized Line spacing (in μm)	Average ratio between domain widths before and after polygonization
1	20	4
2	50	4
5	Hexagonal wall spacing (20 μm)	1.3

Table 8.3 Length-to-width ratios after polygonization in HiB samples heat treated for 1 and 2 hours

Soaking time	Domain Length (cm)	Domain Width (cm)	Width $/\sqrt{\text{Length}}$
1 hour	0.518	0.049	0.068
	0.728	0.054	0.063
	0.46	0.042	0.062
	0.411	0.048	0.075
2 hours	0.628	0.061	0.077
	0.575	0.049	0.065
	1.532	0.061	0.049
	0.636	0.055	0.069

8.6.7 Effect of degree of polygonization on localized power losses

The effect of polygonization of dislocations on power loss was studied. Since polygonization is dependent on grain-to-grain orientation differences, localized power loss measurements were performed and compared to the orientation data of the grains. This is to correlate the polygonization of dislocations and change in power losses. Figure 8.18 shows the mis-orientation of each grain in the area studied to the Goss texture in the direction of applied stress. Localized power loss measurements before and after polygonization and their difference are shown in Figures 8.19.

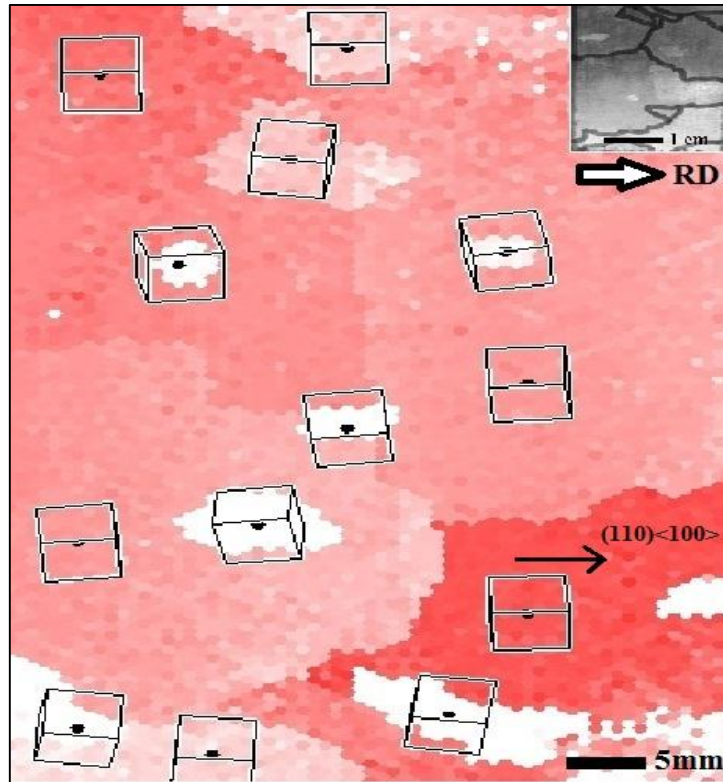


Figure 8.18 EBSD plot showing orientation data for each grain with respect to Goss texture along the rolling direction

From the results in section 6.5.4, it can be ascertained that the polygonization is complete in the grains with initial orientation within 2° of Goss texture. Localized power loss was measured before and after heat treatment to understand the effect of complete and incomplete polygonization on power loss. Hence in Figure 8.18, polygonization is complete in the grain at the lower right corner (bright red) of the EBSD plot whereas the polygonization is incomplete in all the other grains.

The above result when combined with the localized power loss measurement can give significant insight into the effect of degree of polygonization on specific total loss. The variation in grain-to-grain loss values are illustrated in Figure 8.19.

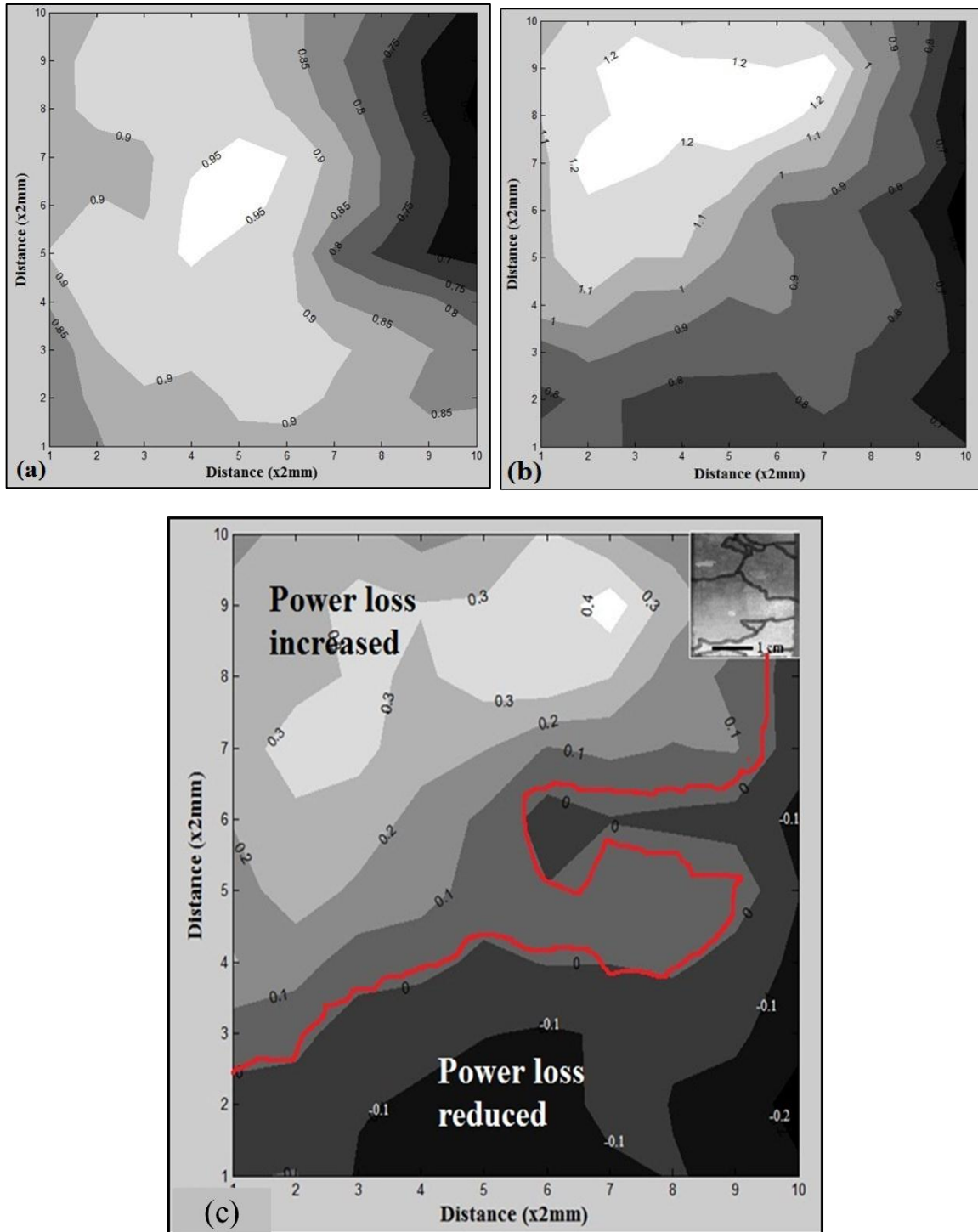


Figure 8.19 Localized power loss (W/kg) on a 20 x 20 mm sample a) before polygonization b) after polygonization c) Difference in power loss after annealing

The example shown in Figure 8.20 illustrates the relationship between change in domain structures and localized power loss variations. A HiB sample was annealed under a bend at 950°C for 1 hour. The domain structures and the resultant localized power loss

are shown in the figure. The difference between Goss orientation and the loading direction are shown on the respective grains in the domain image in Figure 8.20(b). The correlation with the localized power loss variation before and after polygonization anneal shows a reduction in localized power loss in grains 1-4 with Goss orientation with a small mis-orientation of approximately 2° and an increase in the power loss in grain 5 with larger mis-orientation. This is illustrated in Figure 8.20.

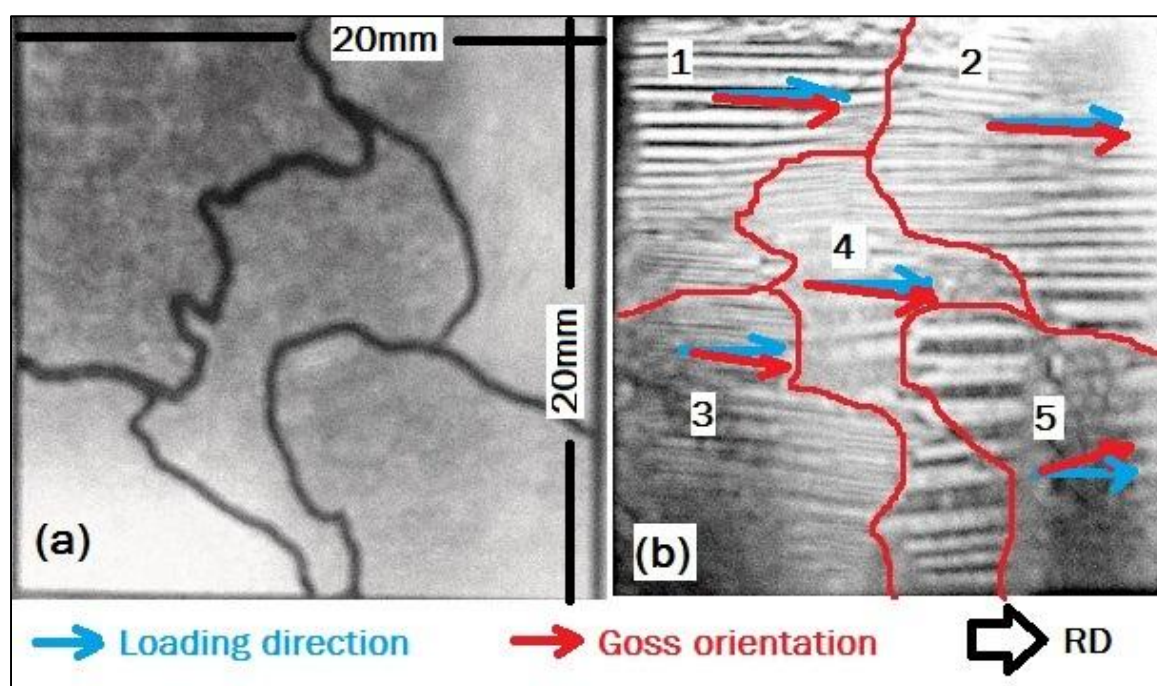


Figure 8.20 (a) A 20 x 20mm HiB sample with grains marked (b) Domain image of the sample after polygonization annealing

The localised loss measurement data before and after polygonization anneal is shown in Figure 8.21 for the samples shown above. The difference in localised losses before and after polygonization anneal show an increase in loss in grain 5 which is misoriented from Goss orientation.

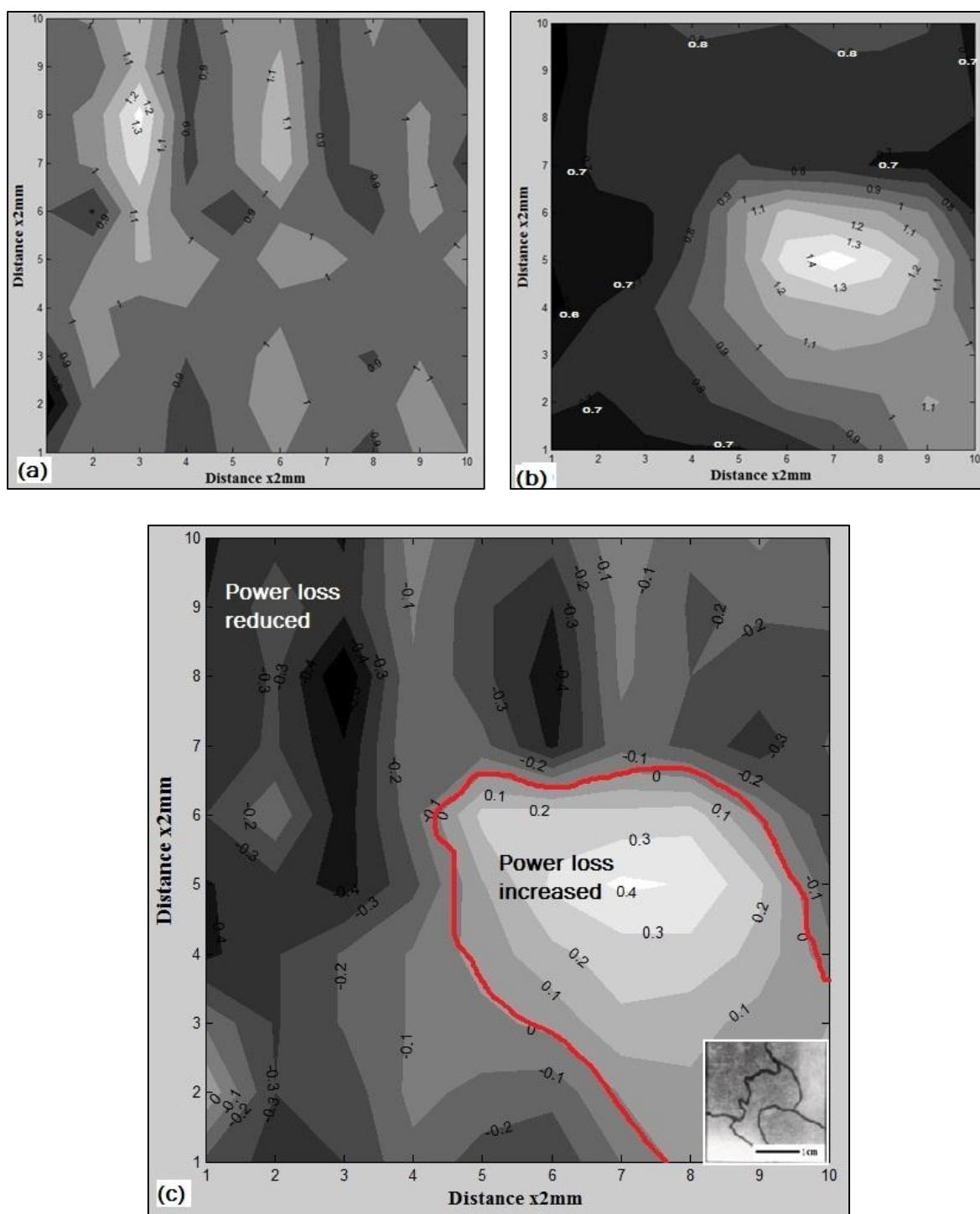


Figure 8.21 Localised power loss of sample described in figure 8.20 (a) Before polygonization anneal (b) After polygonization anneal (c) Difference plot of before and after polygonization anneal

8.6.8 Effect of polygonized dislocation on power losses in CGO

The effect of polygonized dislocations on power losses in CGO is studied by AC power loss single strip tests. To separate the influence of hysteresis loss and frequency dependent components which are eddy current and anomalous losses, DC magnetic testing was performed to measure only the hysteresis component of loss in the material. The hysteresis components shown in the following graphs are all measured by DC magnetic testing. The eddy current losses and the anomalous losses are separated from specific total loss as shown in appendix 8.1. Considering the resistivity of the material is unchanged before and after polygonization, the eddy current losses remain unaltered. Hence the increase in losses is due to the hysteresis and anomalous components. The change in each of the three loss components – hysteresis, eddy currents and anomalous before and after polygonization anneal in CGO are shown in Figures 8.22-8.24.

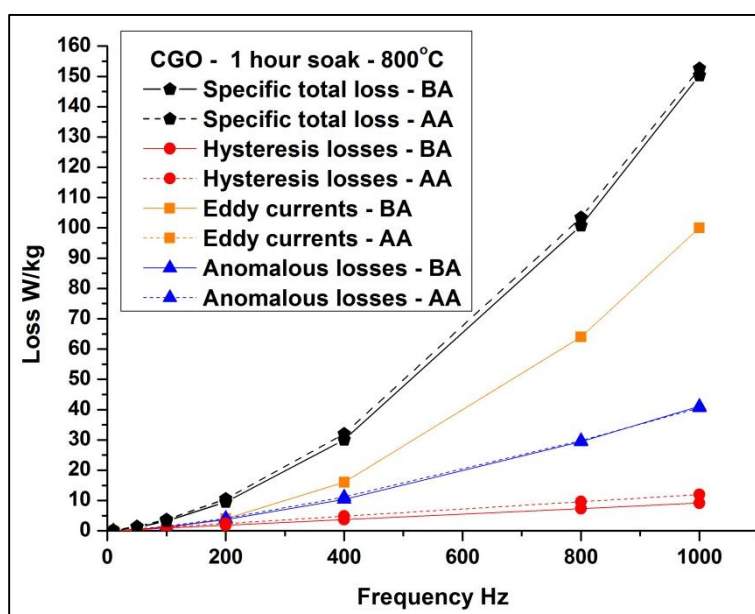


Figure 8.22 Comparison of losses before and after annealing in CGO sample soaked for 1 hour at 800°C (BA – Before annealing, AA – After annealing)

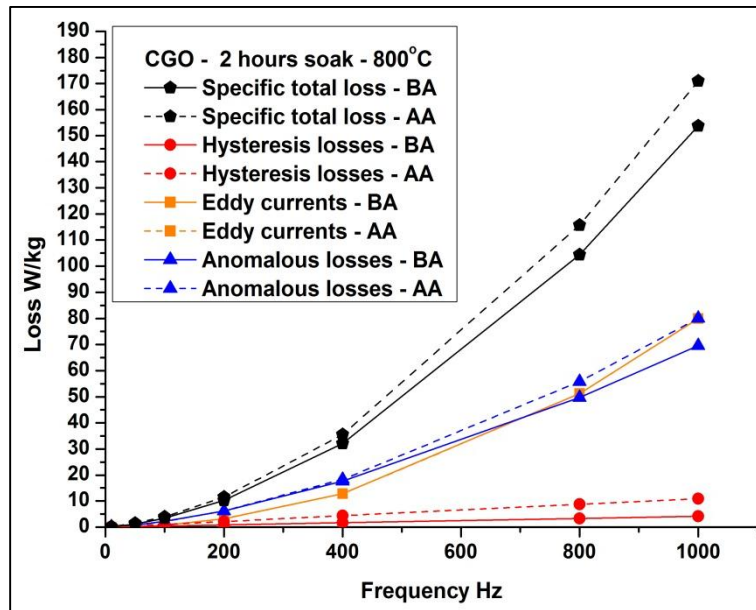


Figure 8.23 Comparison of losses before and after annealing in CGO sample soaked for 2 hours at 800°C (BA – Before annealing, AA – After annealing)

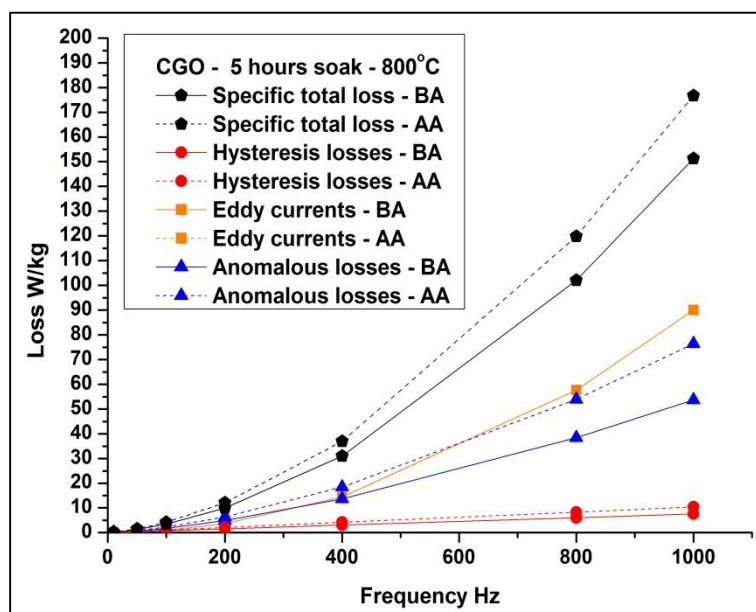


Figure 8.24 Comparison of losses before and after annealing in CGO sample soaked for 5 hours at 800°C (BA – Before annealing, AA – After annealing)

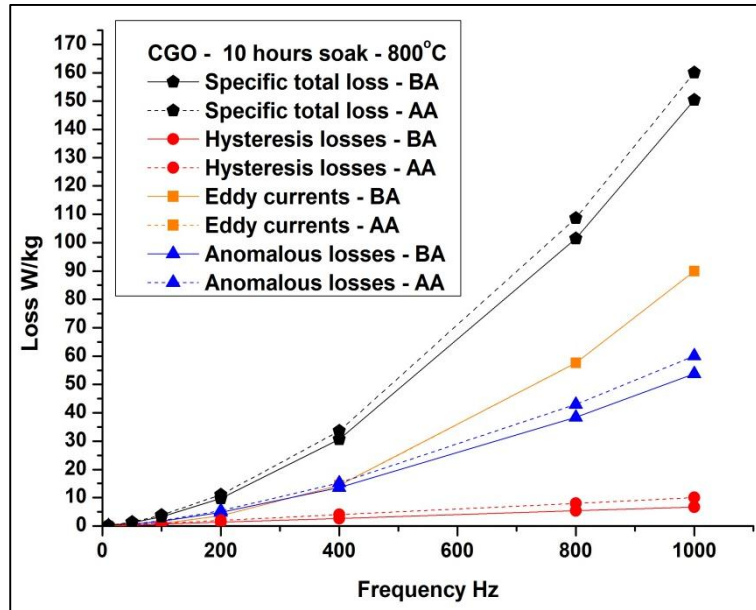


Figure 8.25 Comparison of losses before and after annealing in CGO sample soaked for 10 hours at 800°C (BA – Before annealing, AA – After annealing)

The percentage change in anomalous loss components is shown in Figure 8.26. It shows a reduction in anomalous loss components in samples annealed at 1 and 2 hours in a range of frequency from 10-200 Hz. This change is offset by the increase in hysteresis loss in these samples resulting in an overall increase in the specific total losses.

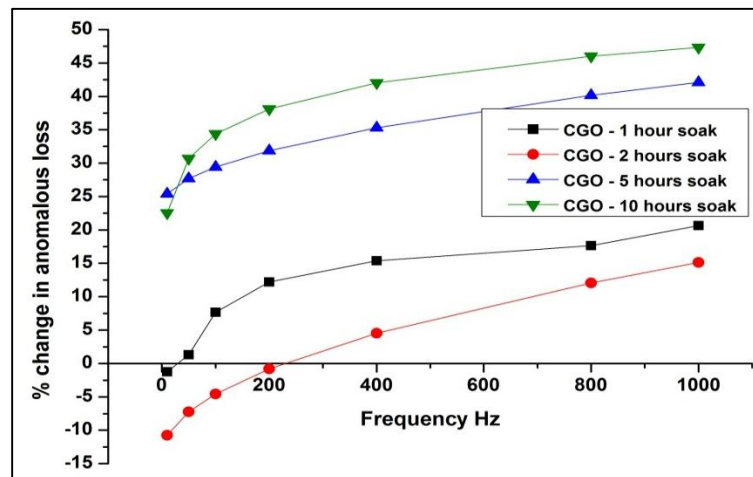


Figure 8.26 Change in percentage of Anomalous losses in CGO samples soaked at 800°C for different times

The change in hysteresis loss before and after polygonization anneal in CGO samples soaked at 800°C for different time durations is shown in Figure 8.27. The hysteresis components increased with increasing number of pinning sites in the grains as shown in the comparison of change in hysteresis and the microstructures shown in Figure 8.27.

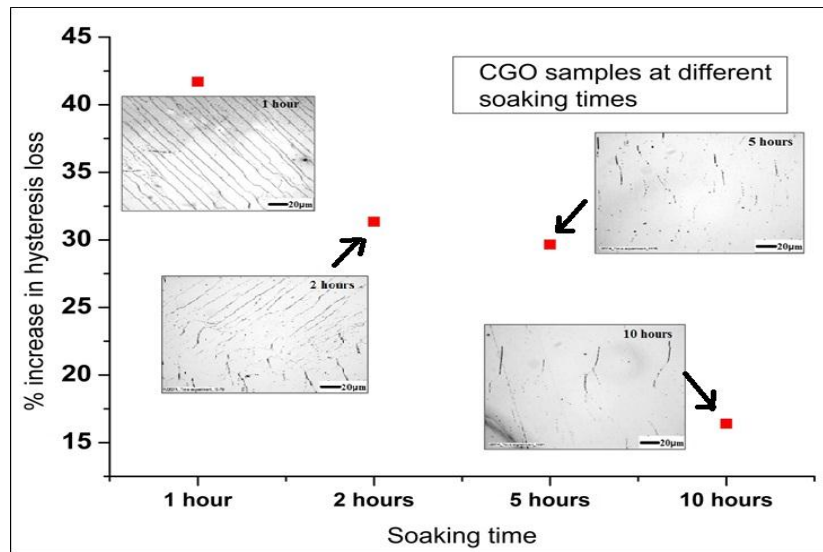


Figure 8.27 Percentage change in hysteresis loss in CGO with different dislocation structures after soaking at 800°C for varying soaking times

The change in B_{800} of the CGO samples before and after polygonization anneal is tabulated in table 8.4. The results show no appreciable difference of polygonization anneal on B_{800} .

Table 8.4 Permeability (B_{800}) change in CGO samples soaked at 800°C for different times

Soaking time	Permeability B_{800} (T)	
	Before polygonization	After polygonization
1 hour	1.83	1.83
2 hours	1.84	1.83
5 hours	1.84	1.83
10 hours	1.83	1.83

Specific total losses of 15 CGO samples at 50Hz show an increase in the specific total loss after polygonization anneal at 1 hour soaking time. A similar trend was prevalent at higher frequency of up to 800Hz. The specific total losses of the samples at 50Hz, 800HZ and 1.7T are shown in Figures 8.28 and 8.29 respectively.

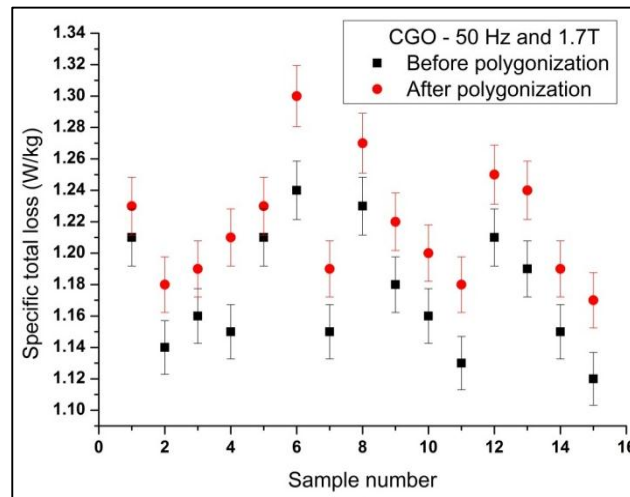


Figure 8.28 Comparison of specific total losses in CGO after 1 hour soaking at 800°C at 50Hz and 1.7T

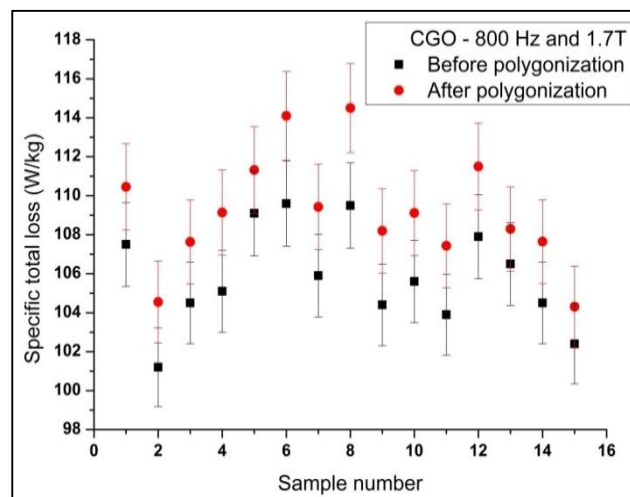


Figure 8.29 Comparison of specific total losses in CGO after 1 hour soaking at 800°C at 800Hz and 1.7T

8.6.9 Effect of polygonized dislocation on power losses in HiB

The effect of polygonized dislocations on specific total losses in HiB after annealing at various soaking times is shown in Figures 8.30-8.33.

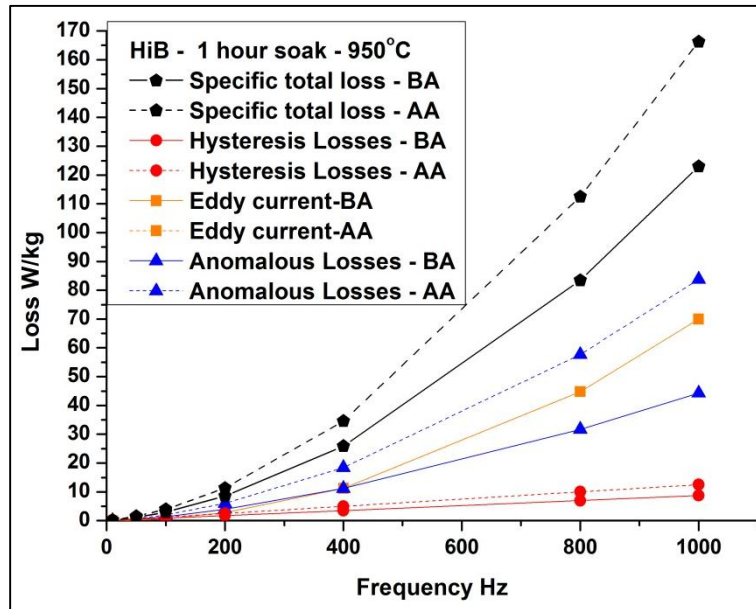


Figure 8.30 Comparison of losses before and after annealing in HiB sample soaked for 1 hour at 950°C (BA – Before annealing, AA – After annealing)

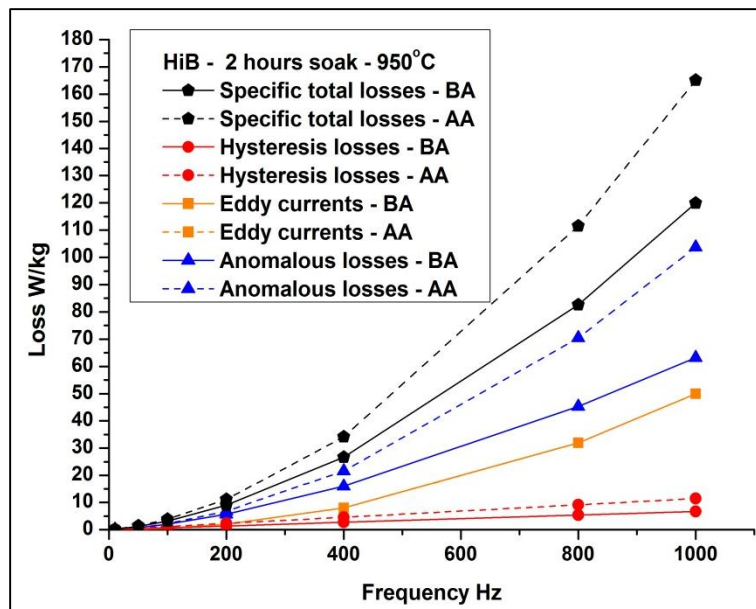


Figure 8.31 Comparison of losses before and after annealing in HiB sample soaked for 2 hours at 950°C (BA – Before annealing, AA – After annealing)

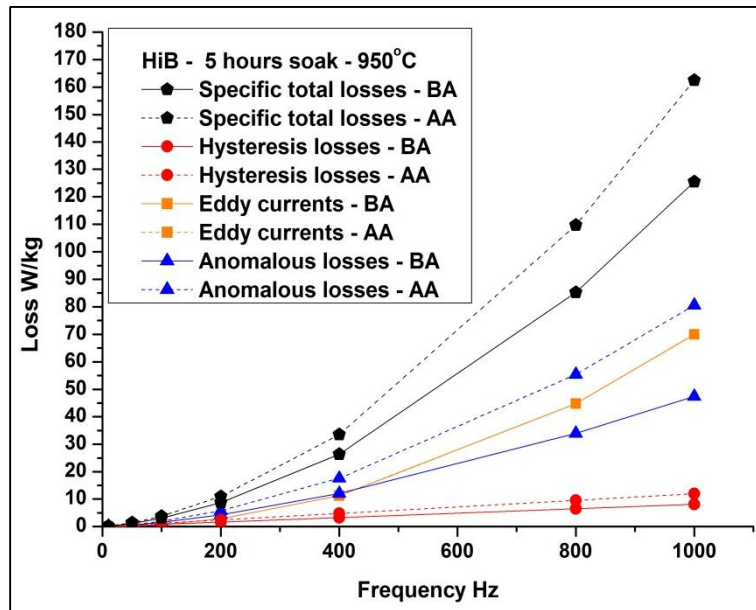


Figure 8.32 Comparison of losses before and after annealing in HiB sample soaked for 5 hours at 950°C (BA – Before annealing, AA – After annealing)

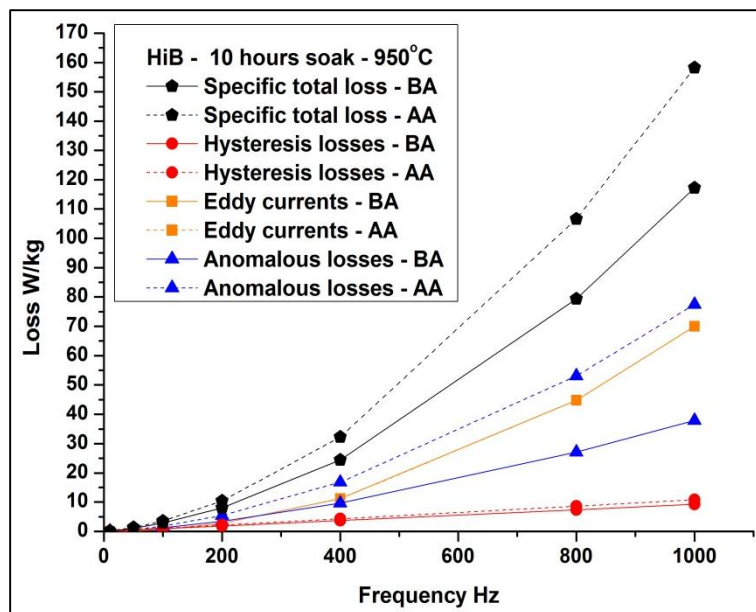


Figure 8.33 Comparison of losses before and after annealing in HiB sample soaked for 10 hours at 950°C (BA – Before annealing, AA – After annealing)

The percentage change in anomalous loss components in HiB is shown in Figure 8.34. It shows a reduction in anomalous loss components in samples annealed for 2 hours and tested at a frequency of 10 Hz. This change is offset by the increase in hysteresis loss in these samples resulting in an overall increase in the specific total losses.

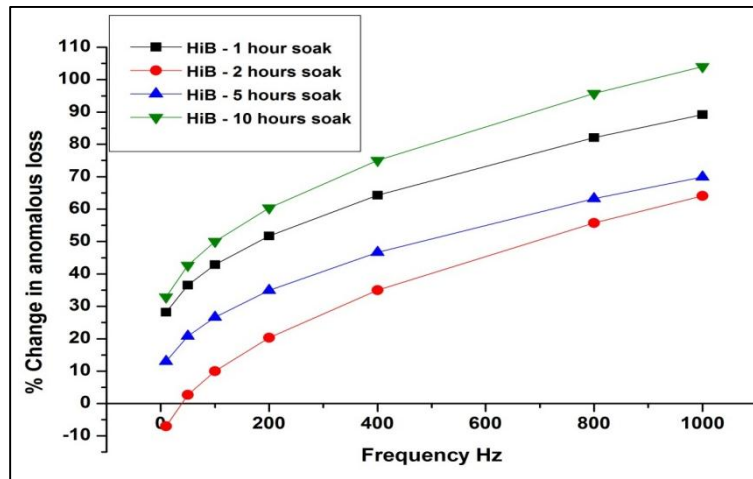


Figure 8.34 Change in percentage of Anomalous losses in HiB samples soaked at 950°C for different times

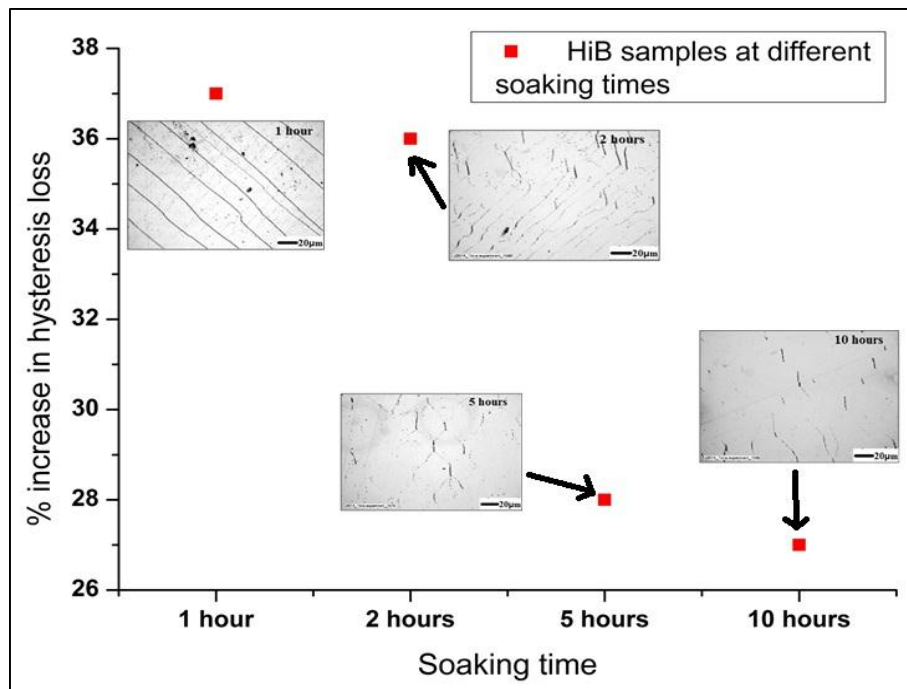


Figure 8.35 Percentage change in hysteresis loss in HiB with different dislocation structures after soaking at 950°C for varying soaking times

The change in hysteresis loss before and after polygonization anneal in HiB samples soaked at 950°C for different time durations is shown in Figure 8.35. The hysteresis components increased with increasing number of pinning sites in the grains as shown in the comparison of change in hysteresis and the microstructures shown in Figure 8.35.

The change in B_{800} of the HiB samples before and after polygonization anneal is tabulated in table 8.5. The results show no appreciable difference of polygonization anneal on B_{800} .

Table 8.5 Permeability (B_{800}) change in HiB samples soaked at 950°C for different times

Soaking time	Permeability B_{800} (T)	
	Before polygonization	After polygonization
1 hour	1.93	1.91
2 hours	1.92	1.89
5 hours	1.93	1.90
10 hours	1.93	1.90

Specific total losses of 15 HiB samples at 50Hz show an increase in the specific total loss after polygonization anneal at 1 hour soaking time. A similar trend was prevalent at higher frequency of up to 800Hz. The specific total losses of the samples at 50Hz, 800Hz and 1.7T are shown in Figures 8.36 and 8.37 respectively.

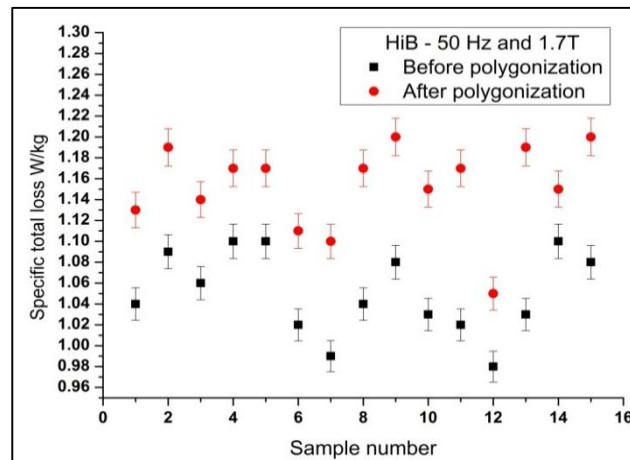


Figure 8.36 Comparison of specific total losses in HiB after 1 hour soaking at 950°C at 50Hz and 1.7T

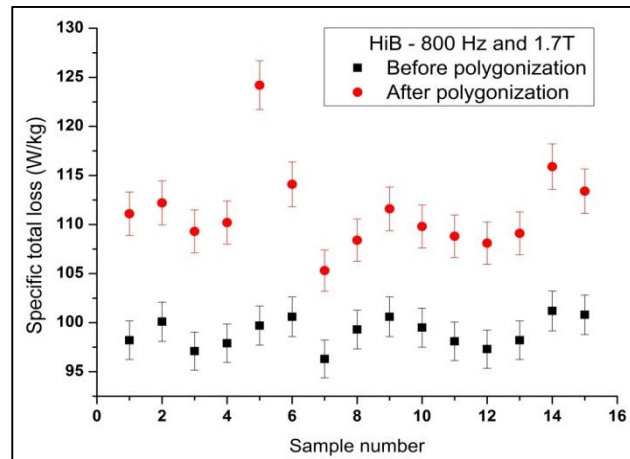


Figure 8.37 Comparison of specific total losses in HiB after 1 hour soaking at 800°C at 800Hz and 1.7T

8.6.10 Comparison of domain pinning effect in CGO and HiB

Barkhausen noise measurement was performed to understand the effect of polygonization anneal on domain wall pinning. Fewer high amplitude Barkhausen noise peaks are a sign of lower number of pinning sites, whereas a large number of low amplitude Barkhausen peaks show the presence of a large number of pinning sites.

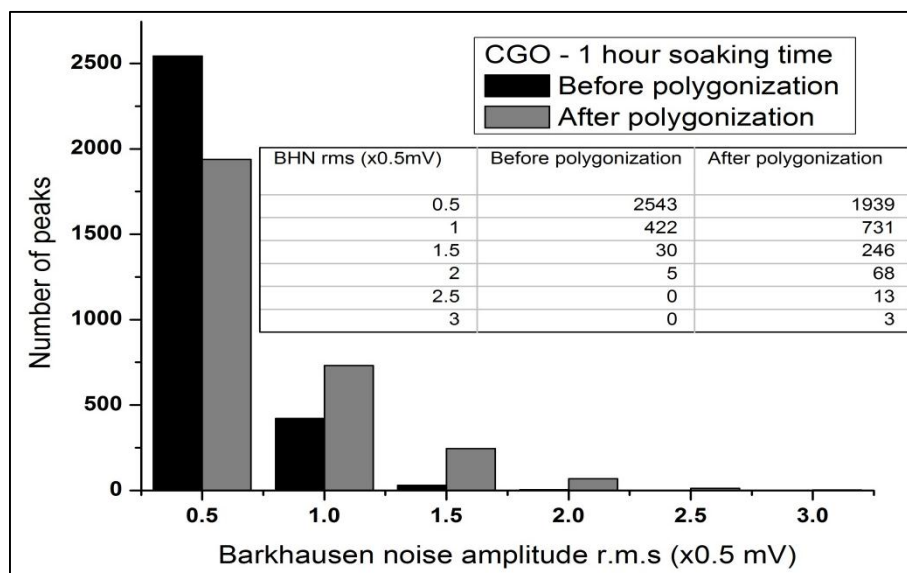


Figure 8.38 Comparison of number of Barkhausen noise peaks at different r.m.s amplitude before and after polygonization in CGO heat treated at 800°C for 1 hour with table inset showing the values

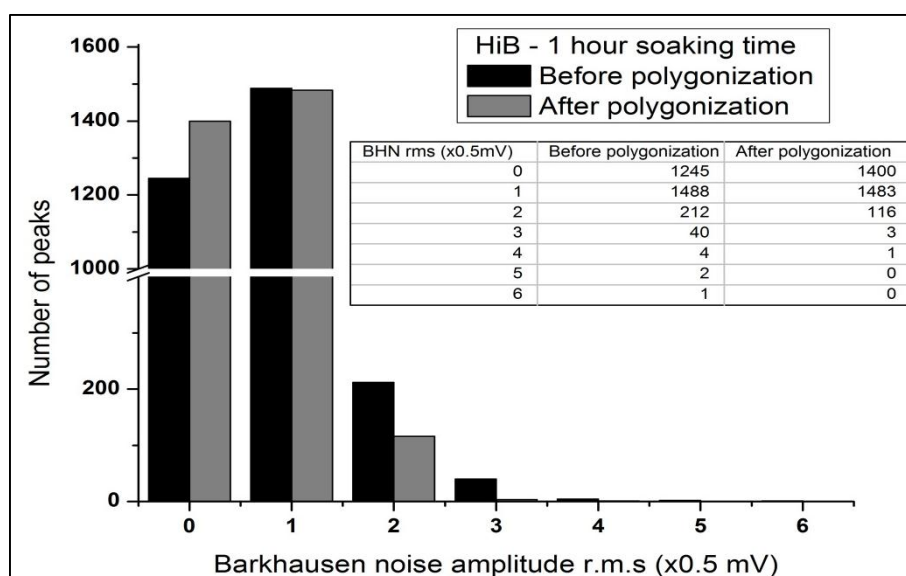


Figure 8.39 Comparison of number of Barkhausen noise peaks at different r.m.s amplitude before and after polygonization in HiB heat treated at 950°C for 1 hour with table inset showing the values

8.7 Discussion

8.7.1 Phase change and possibility of grain growth after heat treatment

To isolate the effect of polygonized dislocations on magnetic properties heat treatment temperatures were selected not to cause any metallurgical phase change in the material. Examination of the iron rich side of Fe-Si phase diagram shown in Figure 5.2 as illustrated by Bozorth [22] shows no phase change in Fe-Si system at 3.25% Si content (shown by the red line) upto temperatures close to the melting point. This confirms the absence of any change in metallurgical phases during the polygonization process.

Grain size was measured before and after heat treatment to study the change in grain size in a number of grains in HiB samples. The results in Figure 8.38 show no considerable change in the grain size after heat treatment. The data from the phase diagram and Figure 8.38 show that the change in magnetic properties are isolated effect

of only polygonized dislocations and not of other metallurgical parameters like grain size or phase change.

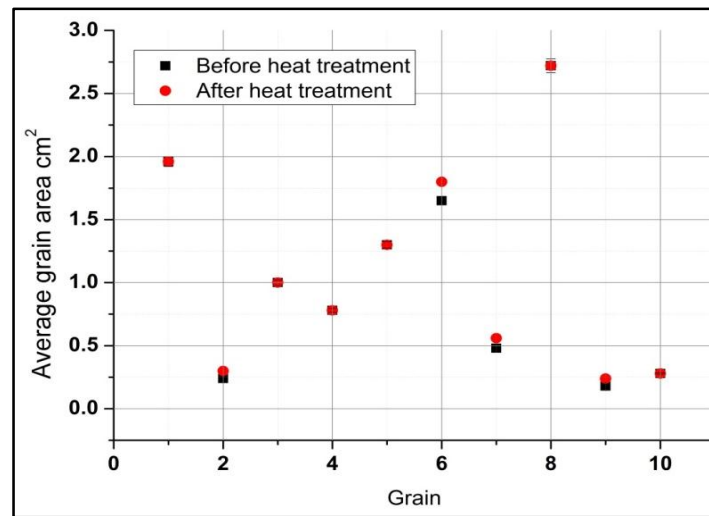


Figure 8.40 Grain size comparisons before and after heat treatment at 950°C for 1 hour in a HiB sample

8.7.2 Effect of temperature on polygonization

Polygonization of dislocations was completed in CGO and HiB by heat treating at different temperatures of 800°C and 950°C respectively. CGO, with an average grain size of about 3mm, possesses nine times more grain boundary area compared to HiB. Different temperature requirements for complete polygonization can be explained by the grain boundary area parameter.

1. The general trend of increase in the degree of polygonization with increase in temperature is because of the dependence of the polygonization on climb which is a process dependent on vacancy diffusion.
2. Annihilation of dislocations in CGO takes place at a comparatively lower temperature of 800°C because of the higher grain boundary area acting as dislocation sources [1]. When the dislocations produced are larger in number, annihilation and rearrangement

becomes easier compared to HiB which has nine times larger grains than CGO on average. This is also supported by the line spacing in CGO which was found to be 10 μ m compared to 25 μ m in HiB. Thus the temperature at which polygonization is complete is 800°C in CGO and 950°C in HiB. This theory is also supported by single crystal experiments by Hibbard et al [6] in which polygonization is complete only at 1060°C because of the absence of any grain boundaries.

3. The reason for the annihilation of polygonized structure in CGO above 800°C can also be explained by the presence of larger grain boundary areas. Annihilation of dislocations into already existing grain boundaries is more energetically favorable than the formation of low angle polygonized grain boundaries. Hence, the larger grain boundary area can also act as dislocation sinks annihilating dislocations and reducing the overall strain energy of the lattice.

8.7.3 Effect of soaking time at heat treatment temperature

In the previous section, the optimum temperature for the polygonization to complete was determined. Soaking time in the optimal temperature is an important process parameter as discussed by Hibbard et al [6]., where they reported an increase in the polygonized line spacing in Fe-Si single crystals with increase in time until about 10 hours after which the line spacing remains unaltered. In this study, results in section 8.6.2 shows that the polygonization process is complete between 1 and 2 hours in CGO whereas in HiB it is completed at 1 hour and the line spacing begins to widen after 1 hour. It is to be noted that the heat treatments for CGO and HiB are performed at 800 and 950°C respectively. In CGO, completely polygonized low angle boundaries are formed 10 μ m apart and remain unchanged until about 2 hours of soaking at 800°C. After two hours, the lines annihilate into fewer large angle boundaries at 5 hours before the structure disintegrates leaving grain boundaries that were present initially.

In case of HiB, polygonization is complete at 1 hour with 20 μ m spacing between the low angle boundaries. This spacing continually increases to 50 μ m in a sample soaked for 2 hours. After 2 hours, the polygonized line transforms into hexagonal cell structures before annihilating into grain boundaries. This is illustrated in figures 8.11 and 8.12.

The increase in polygonized line spacing and disappearance of the low angle grain boundaries in polycrystalline materials can be associated with the grain boundary area which can be effective sinks for dislocations by which strain energy of the lattice can be reduced. The resolved tensile stress near the boundaries creates an increased vacancy concentration and hence CGO with higher grain boundary area aids climb assisted by higher vacancy flux as suggested by Beere and Greenwood [23].

The increasing ease with which annihilation takes place in CGO, HiB and single crystal supports the above concept. It can also be suggested that the directionality of shear modulus of the material (G) is also responsible for the rearrangement of dislocations into further low angle hexagonal cell structures. The strain energy of a dislocation depends on shear modulus (G) and Burger's vector (B) [2]. Fe-3% Si being an anisotropic material can possess different strain energies for dislocations in different planes [24]. This factor also assists in the rearrangements of dislocations from the initial $\langle 111 \rangle$ polygonized direction to a more stable $\langle 001 \rangle$ direction as shown in Figure 8.39, when the soaking time was long enough for the dislocation mobility to take place. In CGO, the polygonized dislocations at longer soaking times annihilated into grain boundaries that were present initially to reduce the strain energy of the system.

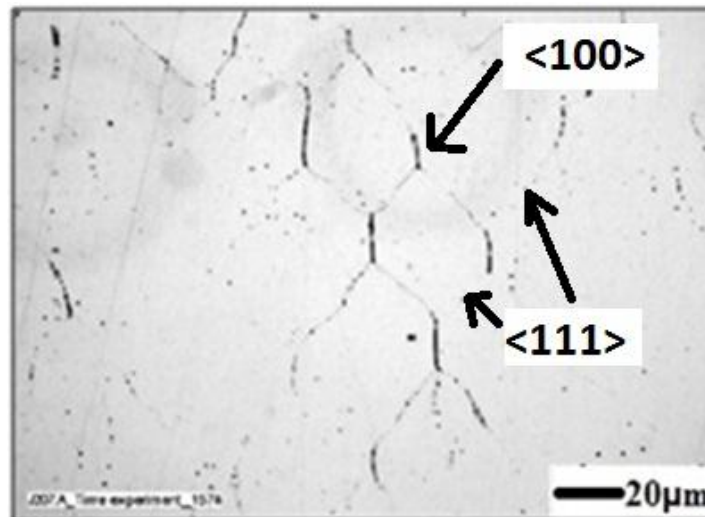


Figure 8.41 Dislocations rearranging from $\langle 111 \rangle$ to $\langle 100 \rangle$ after soaking for 5 hours

8.7.4 Polygonization dependence on orientation

A strong dependence was found of the degree of polygonization on initial orientation of the grains to the loading direction along the Goss texture. In grains that have the easy slip systems mis-oriented by approximately 2° from the loading direction, polygonization is complete whereas in grains with higher mis-orientations, polygonization is incomplete. Grains 2 and 5 in Figure 8.14 show a similar trend with complete polygonization. Grain 6 in Figure 8.14 shows the sensitivity of polygonization by showing the variation in the degree of polygonization between two grains that are mis-oriented by $3\text{--}4^\circ$.

The dependence of polygonization on orientation is due to the activation of different slip systems as described by Vogel et al [3]. The comparison of grain orientation data for a CGO Epstein sample to the grain-to-grain variation in degree of polygonization showed in Figures 8.13 and 8.14 shows a similar trend as explained by Vogel et al [3]. This trend can be explained by the combination of the following two mechanisms

- Activation of different slip systems with varying orientation of the grains and Ashby model
- Lomer-Cottrell Barriers

In grains with a large mis-orientation between their easy slip planes and the loading direction, more than one slip system is activated. For example in grains 1 and 4 from Figures 8.13 and 8.14, the slip systems are mis-oriented by 20° from the loading direction, two slip planes $\{110\}$ and $\{-110\}$ are activated (in which dislocations are mobile). Only $\{110\}$ plane is activated in grains 2 and 5 in Figures 8.13 and 8.14, that are oriented with their slip planes along the loading direction. This activation of different slip planes can be explained by Ashby model [2] that shows the creation of dislocations in other slip planes to compensate the voids caused by deformation.

An increase in the number of slip planes by this mechanism increases the barriers for mobility of these dislocations during polygonization. This intersection of dislocations in two different planes can possibly form a dislocation in a non-closely packed plane creating sessile (immobile) dislocations [2]. These formations of dislocations in non-closely packed planes are Lomer-Cottrell barriers resulting in incomplete polygonization as shown in Figure 8.40. This mechanism combines two mobile dislocations from $\{110\}$ and $\{-110\}$ to form a sessile dislocation in $\{100\}$ planes as shown in Figure 42 below.

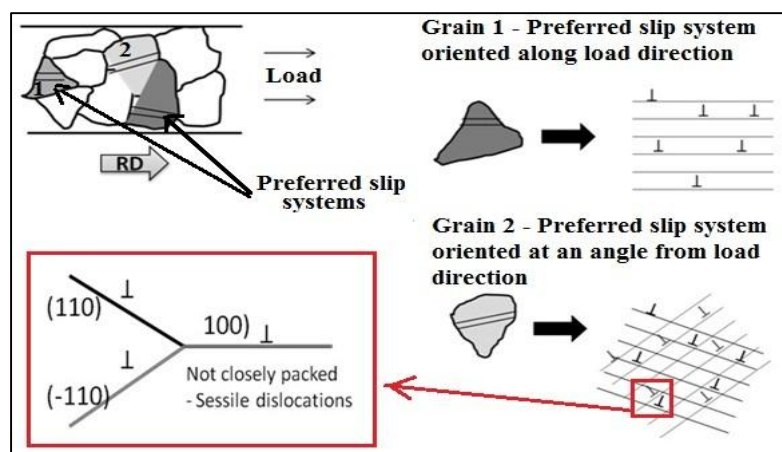


Figure 8.42 Mechanism of Lomer-Cottrell barrier formation in grains with different orientations from bend/load direction

8.7.5 Effect of polygonization on domain structure

Polygonized dislocations in the grain structure alter the strain energy of the lattice. Domain structure changes are a result of free energy minimization by reducing magnetostatic energy to compensate the strain energy by the polygonized boundaries. A decrease in domain widths results in increasing domain boundary energy. Hence any change in domain structure is an optimization of the above two factors.

The average domain width in grains where polygonization is complete is reduced by a factor of 2-4 as described by the change in energy components above. The effect of polygonized line spacing on magnetic domains shows an increase in polygonized line spacing from 20 to 50 μm did not result in alteration of domain widths. Analysis of the average domain width in HiB samples soaked for 1 and 2 hours at 950°C show very similar reduction in domain widths proving the change in domain width remains constant above 20 μm line separation distance. The ratio of domain widths is tabulated in Table 8.2.

Similar analyses on the domain width to length ratio for HiB samples soaked at 950°C for 1 and 2 hours is shown in Table 8.3. The resultant W/\sqrt{L} ratio suggests that the optimal ratio of 0.07 was attained at a polygonized line spacing of 20 μm above which any change in line spacing did not alter the dimensions of the magnetic domains.

8.7.6 Effect of polygonized dislocations on localized power losses

The variation in the degree of polygonization and the change in domain structures are both needed to understand the resultant change in power loss by polygonization as discussed in this section.

The localized power loss measurement of a 20x20 mm HiB sample before and after polygonization showed some grains with increased power loss and some with decreased

power loss as shown in Figures 8.19 and 8.21. The EBSD analysis of the same sample revealed the crystallographic orientation of the grains. Comparison between the orientation map and difference in localized power loss revealed a reduction in power loss in regions with near Goss texture. For orientations that are away from Goss texture in the magnetization direction, there was an overall increase in the losses. This can be understood by the difference in degree of polygonization with respect to orientation explained in the earlier sections. Complete polygonization is beneficial in reducing losses compared to incomplete polygonization that occurred in grains that were not favourably orientated (easy slip planes in load direction) in the magnetization direction.

8.7.7 Effect of polygonization on specific total loss

The relationship between specific total loss and polygonization is explained in this section. The loss components were split into Hysteresis component and frequency dependent (Eddy current + anomalous loss) components by performing DC magnetic testing with which hysteresis loss can be measured. The separation of Eddy current and anomalous loss components are shown in appendix 8.1. Figure 8.22-8.29 and Figures 8.30-8.37 show the change in losses in CGO and HiB Epstein strips respectively, heat treated at different soaking times of 1, 2, 5 and 10 hours. Hysteresis components increase due to the increase in the number of pinning sites in the grains. This is illustrated in Figures 8.27 and 8.35.

The flux density at 800 A/m magnetizing field (B_{800}), shows no appreciable difference between the sample before and after polygonization annealing whereas the analysis of B-H loop shows the difference in magnetizing field required to reach a flux density of 1.7T. This difference in magnetizing field is shown in Figure 8.43. In HiB, the initial permeability is higher than the original Epstein sample but the permeability in high

induction region above the 'knee' of the B-H curve reduced significantly as shown in Figure 8.43. In CGO, the initial permeability is close to that of the sample which was not bent and heat treated and reduces further in the high induction region of the B-H curve.

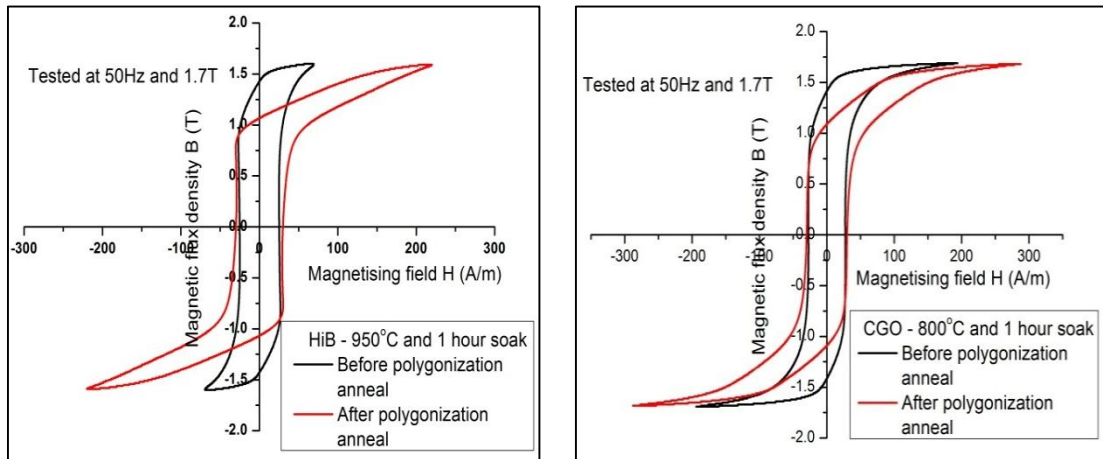


Figure 8.43 Comparison of B-H loop before and after polygonization anneal, of a HiB sample at 950°C and 1 hour and a CGO sample annealed at 800°C for 1 hour, tested at 50Hz and 1.7T

At low induction region, the mechanism of magnetization is by domain wall movement and in high induction regions the mechanism is by domain rotation under the influence of large magnetizing fields. The change in initial permeability in HiB indicates pinning effect by the small angled polygonized boundaries whereas in CGO, the initial permeability is largely unaltered from that of the initial sample indicating the absence of domain pinning effect.

This is also illustrated by the number of Barkhausen noise (BHN) peaks in the different amplitude voltages before and after polygonization in both these materials as shown in figures 8.38 and 8.39. BHN peaks showed an increase in the number of high amplitude peaks and a decrease in the lower amplitude peaks in CGO and vice versa in HiB. This shows an increase in pinning activity in HiB whereas lower domain pinning activity

in CGO. This denotes the ability of the boundaries to pin domain wall motion. In case of CGO, with a significantly higher number of small angle grain boundaries indicated by the smaller line spacing, the mis-orientation angle on either side of the boundaries is small and not significant enough to cause domain pinning effect.

Anomalous losses decrease in HiB samples annealed at 1 hour when tested at a frequency of 10Hz. In all other cases the anomalous losses increased after polygonization anneal. The specific total loss increased after polygonization anneal for all soaking times from 1-10 hours and test frequencies of 10-1000 Hz. In the case of CGO, samples soaked at the annealing temperature for 1 hour showed reduced anomalous losses up to 50Hz. The samples that are soaked for 2 hours showed reduced anomalous losses after polygonization anneal up to 200Hz. But increase in anomalous losses in CGO is lower than the increase in HiB. This can be attributed to the sensitivity of polygonization to the variation in the orientation of grains in a polycrystalline sample from Goss texture which is very difficult to control accurately during manufacturing processes.

8.8 Conclusions

The following conclusions can be drawn from the above experiments and their comparison with the magnetic domain images.

1. Polygonization is the re-arrangement of dislocations into low angle grain boundaries to reduce the free energy of the system and is aided by elevated temperature.
2. Polygonization in Fe-3.25% Si depends on heat treatment temperature, soaking time during heat treatment and the initial orientation of the grains to the direction of application of load.
3. In CGO, polygonization is complete when the bent sample is annealed at 800°C for 1 hour and the polygonized line spacing is approximately 10µm.

4. In HiB, polygonization is complete when the bent sample is annealed at 950°C for 1 hour and the polygonized line spacing is approximately 20µm.
5. An increase in soaking time to 2 hours increases the polygonized line spacing in HiB up to about 50µm above which the dislocations gets annihilated to form a strain free lattice or higher angle grain boundaries. The increase in line spacing is due to annihilation of more dislocations into grain boundaries.
6. No change in line spacing is observed in CGO between 1 and 2 hours soaking time and after 2 hours the polygonized boundaries annihilates to form a strain free lattice or higher angle grain boundaries.
7. Grain orientation with their easy slip system aligned to direction of curvature is optimum for complete polygonization. Mis-orientations greater than 2° created dislocations in intersecting lattice planes thus forming Lomer-Cottrell barriers and resulted in incomplete polygonization.
8. Formation of polygonized structures results in a change in domain widths. Domain width reduces by a factor of 2-4 with the introduction of completely polygonized grain boundaries. The degree of polygonization was shown to be an important parameter affecting the change in domain width.
9. As the polygonized line spacing increases above 20µm, the domain widths remained unaltered. This is due to the domain widths remaining unaltered after the ratio of width and length (W/\sqrt{L}) of the domains reaches 0.07 in Fe-3.25% Si, because of minimization of magnetostatic energy and magnetic domain wall energy at this ratio.
10. A decrease in localized losses was observed in grains where the domain Width/ $\sqrt{\text{Length}}$ ratio is at 0.07. Only grains with complete polygonization resulted in refined domains.

11. Specific total loss increased by 10-35% with increasing frequency after this process of polygonization because of the increase in both hysteresis and anomalous losses.
12. Samples where anomalous loss reduced at frequencies less than 200Hz after polygonization were offset by the increase in hysteresis loss and hence the specific total loss is higher after polygonization anneal.
13. Specific total loss increase is also due to the sensitivity of polygonization to initial orientation of the grains to the direction of loading resulting in incomplete polygonization in a high percentage of grains.

8.9 References

- 1) R E Reed-Hill, *Physical Metallurgy Principles*, Second edition, New york, Litton Educational Publishers, (1973).
- 2) G E Dieter, *Mechanical Metallurgy*, Third Edition, Newyork, McGraw Hill Publications,(1986).
- 3) F L Vogel Jr., *On the orientation effect in the polygonization of bent silicon crystals*, Acta Mater, 6-8 (1958) 532-534.
- 4) L Kaun, A Luft, J Richter, D Schulze , *Slip Line Pattern and Active Slip Systems of Tungsten and Molybdenum Single Crystals Weakly Deformed in Tension at Room Temperature*, J Phys B Solid State , 26(1968) 485-489.
- 5) W A Spitzig, A S Keh, *Orientation and Temperature Dependence of Slip in. Iron Single crystals*, Metall Trans, 1(1970)2751-2757.
- 6) W R Hibbard Jr., C G Dunn, *A study of (112) edge dislocations in bent silicon-iron single crystals*, Acta Mater, 4 (1956) 306-315.
- 7) E Gomes, J Schneider, K Verbeken, J Barros, Y Houbaert, *Correlation Between Microstructure, Texture, and Magnetic Induction in Nonoriented Electrical Steels*, IEEE T Magn, 46 (2010) 310-313.
- 8) B K Sokolov, Y N Dragoshanski, V S Matveeva, M B Tsyrlin, F V Mineev, R B Puzhevich, *Inhomogeneity of magnetic properties of anisotropic electrical steel and specific features of dislocation structures*, Russ J Nondestruct+, 2004; 40:11.
- 9) A Notoji, M Hayakawa, A Saito, *Strain-magnetization properties and domain structure change of silicon steel sheets due to plastic stress*, IEEE T Magn, 36-5 (2000) 3074-3077.

- 10) A Saito, K Yamamoto, K Yamane, *Decrease of magnetization in positive magnetostrictive material due to tensile stress*, J Magn Magn Mater., 112 (1982) 17.
- 11) BS EN 60404-3 ED 1.0/A2, *Magnetic materials: Methods of measurement of the magnetic properties of magnetic sheet and strip by means of a single sheet tester*, British Standards Institution, London.
- 12) X Xu, A J Moses, J P Hall, P I Williams, K Jenkins, *A Comparison of Magnetic Domain Images Using a Modified Bitter Pattern Technique and the Kerr Method on Grain-Oriented Electrical Steel*, IEEE T Magn, 47 (2011) 3531-3534.
- 13) P I Anderson, *Universal DC characterisation system for hard and soft magnetic materials*, Journal of Magnetism and Magnetic Materials 320 (2008), 589-593
- 14) A J Mohaddam, A J Moses, *Localised power loss measurement using remote sensors*, IEEE Trans Mag, 29-6 (1993) 2998.
- 15) N Chukwuchekwa, *PhD Thesis–Investigation of magnetic properties and Barkhausen noise in electrical steel*, Cardiff University, (2012) 54.
- 16) C E Morris, *Electropolishing of steel in Chrome-Acetic acid electrolyte*, Met Prog, 56(1949) 696-701.
- 17) M Frommert , C Zobrist , L Lahn, A Bottcher, D Raabe, S Zaefferer, *Texture measurement of grain-oriented electrical steels after secondary recrystallization*, J Magn Magn Mater., 320-20(2008) e657-e660.
- 18) F Brailsford, *Physical Principles of Magnetism*, First edition, London, Van Nostrand Company Ltd., (1966)168-169.
- 19) R M Bozorth, *Ferromagnetism*, New-Jersey, Wiley-Blackwell publishers (1993)
- 20) W B Beere, G W Greenwood, *The Effect of Hydrostatic Pressure on the Shrinkage of Cavities in Metals*, Met.Sci., 1971;5(1):107.

- 21) J Turley, G Sines, The anisotropy of Young's modulus, shear modulus and Poisson's ratio in cubic materials, J. Phys. D: Appl. Phys., 4(1971)264-271.

Chapter 9

Conclusions and future work

9.1 Conclusions

This study investigated the creation of dislocations in the continuous flattening anneal process and their corresponding effect on magnetic properties of grain oriented electrical steel.

A heat transfer FEM model of continuous flattening anneal line was developed to study the temperature distribution of the steel strip at different line speeds and at different time scales during the process. The model data was compared to pyrometer measurements from three points in the furnace and the agreement was within 20°C strip temperature. Heating of the strip close to 850°C takes place at zones 4-6, whereas zones 7-9 are homogenization zones where the temperature of the strip is homogenized. The peak temperature of the strip was 850-852°C irrespective of line speeds from 60-90 m/min. This is due to the temperature homogenization in zones 7-9.

The temperature profile data of the strip was used to understand the predominant deformation mechanisms in GOES during the continuous flattening anneal process. A deformation mechanism map was developed for CGO and HiB materials that showed the temperature-stress-strain rate combinations in which the diffusion and dislocation climb modes of deformation are active. Superimposing the temperature data from the heat transfer model and the stress applied on the strip in the process, the change in deformation mechanisms with varying gauge thickness, grain size and line speed were studied. The change in deformation mechanism is attributed to increasing stress at continuous anneal temperatures rather than the line speed because of the absence of significant changes in peak strip temperature according to line speeds.

LAFFAS was built for lab scale simulations of continuous flattening anneal process and produce samples for dislocation and magnetic properties testing. The system

overcame the drawbacks of the previous attempt by CASIM2 furnace by preventing oxidation of the sample, absence of a contact thermocouple and produced samples with Epstein width and 250mm length for magnetic testing. The objective is to validate the deformation mechanism model and to study the effect of continuous flattening process parameters on magnetic properties.

LAFFAS was successful in simulating the continuous flattening line by producing samples at different stress and temperature combinations by producing samples for microstructure and magnetic testing at a lab scale. Above a threshold dislocation density around $1 \times 10^7 \text{ cm}^{-2}$, stress relief annealing rearranged dislocations into small angle boundaries that had a detrimental effect on power loss.

Mechanical behaviour of CGO+ materials was different from that of conventional HiB materials with similar grain size as they underwent 20% more elongation at a continuous flattening anneal temperature of 850°C. Process parameters set for HiB continuous flattening anneal process are not suitable for CGO+ and the average specific total loss of 1.18 W/kg at 1.7T and 50Hz, for samples annealed at 850°C and 6 MPa shows the sensitivity of CGO+ at the continuous flattening anneal conditions compared to HiB with average losses of 1.05-1.1 W/kg under similar test conditions. LAFFAS experiments have revealed important understanding to improve the continuous flattening anneal process of CGO+.

The rearrangement of dislocations into energetically favourable structures (polygonization) under different annealing conditions and the factors affecting this process were studied. Polygonization in Fe-3.25% Si depends on heat treatment temperature, soaking time during heat treatment and the initial orientation of the grains to the direction of application of load were studied. Polygonization in polycrystalline materials depend on

initial orientation of each grain to the loading direction as well as the temperature and soaking time during heat treatment.

Formation of polygonized structures results in a change in domain widths. Domain width reduces by a factor of 2-4 with the introduction of completely polygonized grain boundaries. The degree of polygonization was shown to be an important parameter affecting the change in domain width. The change in domain widths remaining unaltered after the ratio of width and length (W/\sqrt{L}) of the domains reaches 0.07 in Fe-3.25% Si, because of minimization of magnetostatic energy and magnetic domain wall energy at this ratio. A localised decrease in specific total loss was observed at 1.5T and 50Hz in grains where polygonization was complete. Specific total loss increase from 10-35% in bulk polycrystalline material was due to the sensitivity of polygonization to initial orientation of the grains to the direction of loading resulting in incomplete polygonization in a high percentage of grains.

Overall, in this work the cause and effect of dislocation creation during continuous flattening anneal process, factors affecting their re-arrangement and the effects on magnetic properties of GOES was ascertained. The continuous flattening annealing process from heat distribution in the furnace, deformation mechanism of the steel and their respective effects on magnetic properties were elaborated.

9.2 Future work

The study on dislocation structure-magnetics correlation in the continuous flattening anneal process revealed the necessity of further study in the following areas

1. Developing mechanical property database for the new CGO+ material as a function of temperature by experimentation.

2. Improve the deformation mechanism model with experimental data for mechanical properties rather than data from literature to make sure that the experimental conditions are identical.
3. Use the code used in this study to construct a deformation mechanism map for CGO+.
4. Study of the dislocation structures and magnetic domain correlation using high resolution dynamic domain imaging to understand domain wall dynamics.
5. Automate the LAFFAS system and hence removing the need to two people operation and incorporate the ability to vary strain rate during loading.
6. Validate the effect of gauge thickness of CGO+ material on the deformation mechanism and magnetic properties.
7. In situ TEM investigation of dislocation dynamics during high temperature treatment.

Appendix 5.1

'C' - Computer program to calculate the predominant deformation mechanism

```
/* Table of constant values */

static integer c__9 = 9;
static integer c__1 = 1;
static integer c__5 = 5;
static integer c__3 = 3;
static doublereal c_b43 = 2.;
static doublereal c_b51 = 0.;
static doublereal c_b99 = 1.5;
static doublereal c_b100 = .5;
static doublereal c_b102 = .33;
static doublereal c_b107 = 3.;
static doublereal c_b110 = .75;
static doublereal c_b111 = 1.334;

/* Main program */ int MAIN__(void)
{
    /* Format strings */
    static char fmt_4[] = "(4x,\002T/Tm\002,12x,\002THRESHOLD\002,9x,\002BOR"
        "DER-FIELD\002,5x,\002PLASTICITY-FIELD\002,/)";
    static char fmt_441[] = "(5x,\002T/Tm\002,6x,\002Creep Mecahnism\002,3x"
        ",\002Sub-mecahnism\002,2x,\002Glide Mechanism\002,4x,\002Diffusi"
        "onal\002)";
    static char fmt_88[] = "(1x,\002Strain Rate=\002,e14.7,/ ,4x,\002Normaliz"
        "ed Stress\002,4x,\002Homologous Temperature\002)";
    static char fmt_888[] = "(2(6x,e14.7))";
    static char fmt_444[] = "(e14.7,2x,a16,4x,a10,3x,a16,3x,a8)";
    static char fmt_44[] = "(10(e14.7,5x))";
    static char fmt_2[] = "(10x,i4,\002%\002)";
    static char fmt_22[] = "(10x,\002Here we go!\002)";

    /* Local variables */
    integer i__1;
    doublereal d__1;
    olist o__1;

    /* Builtin functions */
    integer s_wsle(cilist *), do_lio(integer *, integer *, char *, ftnlen),
        e_wsle(void), f_open(olist *), s_rsle(cilist *), e_rsle(void),
        s_wsfe(cilist *), e_wsfe(void), do_fio(integer *, char *, ftnlen);
    double pow_dd(doublereal *, doublereal *), sqrt(doublereal), log(
        doublereal);
    /* Subroutine */ int s_copy(char *, char *, ftnlen, ftnlen), s_stop(char *
        , ftnlen);

    /* Local variables */
}
```



```

static doublereal trakiso1[100], trakiso2[100], sorowan1, sorowan2,
    critical[100];
static integer i__;
static doublereal ec;
static integer pb, ij, ii, il;
static doublereal kk, pi;
static integer ip;
static doublereal vf;
static integer it;
static doublereal tm, sr, st;
static integer ii2, i2l, i3l;
static doublereal gar;
static integer iji, ill;
static doublereal pbs[100], qes;
static integer way;
static doublereal pwt;
extern /* Subroutine */ int diff_(doublereal *, doublereal *,
    doublereal *, doublereal *, doublereal *, integer *, doublereal *,
    doublereal *, doublereal *, integer *);
static doublereal ddif, avac, incl_rad, perc, rgas, shear_mod1, bug_vec, rmin, smin,
rmax, smax;
static integer gway;
static doublereal trat[100], vnet[10000], srok;
static integer iout;
static doublereal siso1[100], siso2[100], vnet2[10000];
static char mecha[30], mechb[30], mechc[30], mechd[8];
static doublereal lamda;
extern /* Subroutine */ int glide_(doublereal *, doublereal *, doublereal
    *, doublereal *, doublereal *, integer *, doublereal *,
    doublereal *, doublereal *, doublereal *, doublereal *);
static doublereal ashpb[100], disc_dens, gsrec, mat_dens, ctemp[100], obsta,
    incl_dens, peirl, disc_glide[10000], str_rate, thres_temp[100], grain_size,
ashts[100],
    tratk[100], shear_mod1t[100];
extern /* Subroutine */ int power_(doublereal *, doublereal *, doublereal
    *, doublereal *, doublereal *, doublereal *,
    integer *, doublereal *, doublereal *);
static doublereal pwlow[10000], ashcri[100];
static integer difway;
static doublereal def_plastic[10000], stress[10000], diffflow[10000], shear_mod,
    sorowan, poisson, tstress;

/* I/O blocks */
static cilist io__1 = { 0, 6, 0, 0, 0 };
static cilist io__2 = { 0, 1, 0, 0, 0 };
static cilist io__4 = { 0, 1, 0, 0, 0 };
static cilist io__6 = { 0, 1, 0, 0, 0 };
static cilist io__8 = { 0, 1, 0, 0, 0 };
static cilist io__10 = { 0, 1, 0, 0, 0 };
static cilist io__12 = { 0, 1, 0, 0, 0 };
static cilist io__14 = { 0, 1, 0, 0, 0 };

```

```

static cilist io___16 = { 0, 1, 0, 0, 0 };
static cilist io___18 = { 0, 1, 0, 0, 0 };
static cilist io___20 = { 0, 1, 0, 0, 0 };
static cilist io___22 = { 0, 1, 0, 0, 0 };
static cilist io___24 = { 0, 1, 0, 0, 0 };
static cilist io___26 = { 0, 1, 0, 0, 0 };
static cilist io___28 = { 0, 1, 0, 0, 0 };
static cilist io___30 = { 0, 10, 0, fmt_4, 0 };
static cilist io___31 = { 0, 12, 0, fmt_441, 0 };
static cilist io___32 = { 0, 8, 0, fmt_88, 0 };
static cilist io___90 = { 0, 8, 0, fmt_888, 0 };
static cilist io___91 = { 0, 8, 0, fmt_888, 0 };
static cilist io___98 = { 0, 12, 0, fmt_444, 0 };
static cilist io___99 = { 0, 10, 0, fmt_44, 0 };
static cilist io___101 = { 0, 6, 0, fmt_2, 0 };
static cilist io___102 = { 0, 6, 0, fmt_22, 0 };

```

```

/*    PARAMETER(PI=3.1416590D+00) */

```

```

s_wsle(&io___1);
do_lio(&c___9, &c___1, "Wait! Processing...", (ftnlen)19);
e_wsle();

```

```

/* Units */

```

```

o__1.oerr = 0;
o__1.ounit = 1;
o__1.ofnmlen = 8;
o__1.ofnm = "DEFMECH-MAP.in";
o__1.orl = 0;
o__1.osta = 0;
o__1.oacc = 0;
o__1.ofm = 0;
o__1.oblnk = 0;
f_open(&o__1);
o__1.oerr = 0;
o__1.ounit = 10;
o__1.ofnmlen = 13;
o__1.ofnm = "DEFMECH-MAP_bor";
o__1.orl = 0;
o__1.osta = 0;
o__1.oacc = 0;
o__1.ofm = 0;
o__1.oblnk = 0;
f_open(&o__1);
o__1.oerr = 0;
o__1.ounit = 12;
o__1.ofnmlen = 16;
o__1.ofnm = "DEFMECH-MAP_mech";
o__1.orl = 0;

```

```

o__1.osta = 0;
o__1.oacc = 0;
o__1.ofm = 0;
o__1.oblnk = 0;
f_open(&o__1);
o__1.oerr = 0;
o__1.ounit = 8;
o__1.ofnmlen = 15;
o__1.ofnm = "DEFMECH-MAP_strainplot";
o__1.orl = 0;
o__1.osta = 0;
o__1.oacc = 0;
o__1.ofm = 0;
o__1.oblnk = 0;
f_open(&o__1);
/*      open(14,file='pruebas') */

/* This reads data from MAP.DAT */

s_rsle(&io__2);
do_lfo(&c__5, &c__1, (char *)&incl_rad, (ftnlen)sizeof(doublereal));
e_rsle();
s_rsle(&io__4);
do_lfo(&c__5, &c__1, (char *)&grain_size, (ftnlen)sizeof(doublereal));
e_rsle();
s_rsle(&io__6);
do_lfo(&c__5, &c__1, (char *)&disc_dens, (ftnlen)sizeof(doublereal));
e_rsle();
s_rsle(&io__8);
do_lfo(&c__5, &c__1, (char *)&ddif, (ftnlen)sizeof(doublereal));
e_rsle();
s_rsle(&io__10);
do_lfo(&c__5, &c__1, (char *)&qes, (ftnlen)sizeof(doublereal));
e_rsle();
s_rsle(&io__12);
do_lfo(&c__5, &c__1, (char *)&shear_mod1, (ftnlen)sizeof(doublereal));
e_rsle();
s_rsle(&io__14);
do_lfo(&c__5, &c__1, (char *)&bug_vec, (ftnlen)sizeof(doublereal));
e_rsle();
s_rsle(&io__16);
do_lfo(&c__5, &c__1, (char *)&mat_dens, (ftnlen)sizeof(doublereal));
e_rsle();
s_rsle(&io__18);
do_lfo(&c__5, &c__1, (char *)&incl_dens, (ftnlen)sizeof(doublereal));
e_rsle();
s_rsle(&io__20);
do_lfo(&c__5, &c__1, (char *)&pwt, (ftnlen)sizeof(doublereal));
e_rsle();
s_rsle(&io__22);
do_lfo(&c__5, &c__1, (char *)&str_rate, (ftnlen)sizeof(doublereal));

```

```

e_rsle();
s_rsle(&io__24);
do_lfo(&c__5, &c__1, (char *)&gsrec, (ftnlen)sizeof(doublereal));
e_rsle();
s_rsle(&io__26);
do_lfo(&c__5, &c__1, (char *)&gar, (ftnlen)sizeof(doublereal));
e_rsle();
s_rsle(&io__28);
do_lfo(&c__3, &c__1, (char *)&it, (ftnlen)sizeof(integer));
e_rsle();

/* Headers */

s_wsfe(&io__30);
e_wsfe();
s_wsfe(&io__31);
e_wsfe();
s_wsfe(&io__32);
do_fio(&c__1, (char *)&str_rate, (ftnlen)sizeof(doublereal));
e_wsfe();

/* Constants: */

pi = 3.141659;
kk = 1.381e-23;
rgas = 8.31451;
poisson = .33;
tm = 1751.;
shear_mod = 83.6648;
sr = str_rate;

/* Vacancy area calculation */

d__1 = bug_vec / 2.;
avac = pi * pow_dd(&d__1, &c_b43);

i__ = 1;
ii = 1;
for (iji = 4; iji <= 100; iji += 3) {
    thres_temp[i__ - 1] = tm / 100.0 * iji;
    ctemp[i__ - 1] = thres_temp[i__ - 1] - 273.15f;

/*Shear mod vs Temp */

    if (thres_temp[i__ - 1] <= 1173.)
    {
        shear_mod1t[i__ - 1] = thres_temp[i__ - 1] * -.00568182 + shear_mod;
    }
    else if (thres_temp[i__ - 1] > 1173.)
    {
        shear_mod1t[i__ - 1] = thres_temp[i__ - 1] * -.036 + 119.228;
    }
}

```

```

    }
    shear_mod1t[i__ - 1] *= 1e3;

/* Threshold stress */

    rmax = incl_rad * 2.;
    rmin = bug_vec * 2.;
    vf = pwt * mat_dens / incl_dens;
    lamda = incl_rad * 1.25 * sqrt(pi * 2. / (vf * 3.));
    sorowan1 = bug_vec / lamda * log(rmax / rmin);
    sorowan2 = shear_mod1t[i__ - 1] * .83 / (pi * 2. * sqrt(1. - poisson));
    sorowan = sorowan1 * sorowan2;
    tstress = sorowan * .33;

/* Reset Counters */

    il = 1;
    ip = 0;
    iout = 0;

/* Elastic Collapse for BCC */

    ec = .1;
    smax = ec * shear_mod1t[i__ - 1];
    smin = shear_mod1t[i__ - 1] * .001;

    d__1 = smax;
    for (st = tstress; st <= d__1; st += 1.) {
        stress[il - 1] = st;

/* Diff flow */

        diff_(&thres_temp[i__ - 1], &diffflow[il - 1], &rgas, &st, &
            shear_mod1t[i__ - 1], &difway, &gsrec, &lamda, &gar, &it);

/* Glide */

        glide_(&thres_temp[i__ - 1], &shear_mod1t[i__ - 1], &st, &bug_vec,
&disc_glide[il -
            1], &gway, &lamda, &incl_rad, &shear_mod, &obsta, &peirl);
        if (obsta >= peirl) {
            srok = obsta;
        } else {
            srok = peirl;
        }

/* Power-Law creep */

        power_(&thres_temp[i__ - 1], &def_plastic[il - 1], &rgas, &shear_mod1t[i__ - 1],
&
            shear_mod, &st, &bug_vec, &way, &tstress, &pwlow[il - 1]);

```

```

        ++il;
/* L11: */
}

ij = 0;
pb = 0;
i__1 = il - 1;
for (ii2 = 1; ii2 <= i__1; ++ii2)
{

/* Plastic deformation limit */

    if (def_plastic[0] < disc_glide[0]) {
        if (def_plastic[ii2 - 2] < disc_glide[ii2 - 2] && def_plastic[ii2] > disc_glide[
            ii2]) {
            ++pb;
        }
    }
    if (def_plastic[0] > disc_glide[0]) {
        if (def_plastic[ii2 - 2] > disc_glide[ii2] && def_plastic[ii2] < disc_glide[ii2])
        {
            ++pb;
        }
    }
    if (def_plastic[ii2 - 1] == disc_glide[ii2 - 1]) {
        ++pb;
    }
    if (pb == 1) {
        pbs[i__ - 1] = stress[ii2 - 1];
    }

/* Borders */

    if (pwlow[0] < diffflow[0]) {
        if (pwlow[ii2 - 2] < diffflow[ii2 - 2] && pwlow[ii2] > diffflow[
            ii2]) {
            ++ij;
        }
    }
    if (pwlow[0] > diffflow[0]) {
        if (pwlow[ii2 - 2] > diffflow[ii2 - 2] && pwlow[ii2] < diffflow[
            ii2]) {
            ++ij;
        }
    }
    if (pwlow[ii2 - 1] == diffflow[ii2 - 1]) {
        ++ij;
    }
    if (ij == 1) {
        critical[i__ - 1] = stress[ii2 - 1];
    }
}

```

```

/* L111: */
    }

    i2l = 1;
    i3l = 1;
    i__1 = il - 2;
    for (ill = 2; ill <= i__1; ++ill) {

/* Strain rate curves*/

        if (stress[ill - 1] >= stress[0] && stress[ill - 1] < pbs[i__ - 1]
            ) {
            vnet2[i2l - 1] = pwlow[ill - 1] + diffflow[ill - 1];
            if (vnet2[i2l - 1] > str_rate * .25 && vnet2[i2l - 1] < str_rate *
                1.25) {
                siso2[i__ - 1] = stress[ill - 1] / (sqrt(3.) * shear_mod1t[i__
                    - 1]);
                trakiso2[i__ - 1] = thres_temp[i__ - 1] / tm;
            }
            ++i2l;
        }

/* Strain rates in plastic flow */

        if (stress[ill - 1] >= pbs[i__ - 1] && stress[ill - 1] < stress[
            il - 3]) {
            if (disc_glide[ill - 1] > def_plastic[ill - 1]) {
                vnet[i3l - 1] = disc_glide[ill - 1];
            } else {
                vnet[i3l - 1] = def_plastic[ill - 1];
            }
            if (vnet[i3l - 1] > str_rate * .25 && vnet[i3l - 1] < str_rate *
                1.25) {
                siso1[i__ - 1] = stress[ill - 1] / (sqrt(3.) * shear_mod1t[i__
                    - 1]);
                trakiso1[i__ - 1] = thres_temp[i__ - 1] / tm;
            }
            ++i3l;
        }
    }
/* L1111: */
}

/* Checking system */

/* write(14,4444) */
/* WRITE(14,*)(thres_temp(i)/tm) */
/* write(14,44)(stress(1)/shear_mod1t(i)),def_plastic(1),pwlow(1),diffflow(1), */
/* & disc_glide(1),vnet(1),vnet2(1) */
/* write(14,44)(stress(il-1)/shear_mod1t(i)),def_plastic(il-1),pwlow(il-1), */
/* & diffflow(il-1),disc_glide(il-1),vnet(i3L-1),vnet2(i2L-1) */

```

```

/* ----- RESULTS ----- */

/* Threshold Stress */

    ashts[i__ - 1] = tstress / (sqrt(3.) * shear_mod1t[i__ - 1]);

/* Boundaries */

    ashcri[i__ - 1] = critical[i__ - 1] / (sqrt(3.) * shear_mod1t[i__ - 1]);
    if (ashcri[i__ - 1] <= ashts[i__ - 1]) {
        iout = 1;
    }
    if (iout == 1) {
        ashcri[i__ - 1] = ashts[i__ - 1];
    }
    ashpb[i__ - 1] = pbs[i__ - 1] / (sqrt(3.) * shear_mod1t[i__ - 1]);

/* Strain rate curves */

    srok /= sqrt(3.) * shear_mod1t[0] * 1e6;
    if (i__ == 1) {
        s_wsfe(&io__90);
        do_fio(&c__1, (char *)&srok, (ftnlen)sizeof(doublereal));
        do_fio(&c__1, (char *)&c_b51, (ftnlen)sizeof(doublereal));
        e_wsfe();
    }
    if (siso2[i__ - 1] == 0.) {
        goto L12;
    }
    s_wsfe(&io__91);
    do_fio(&c__1, (char *)&siso2[i__ - 1], (ftnlen)sizeof(doublereal));
    do_fio(&c__1, (char *)&trakiso2[i__ - 1], (ftnlen)sizeof(doublereal));
    e_wsfe();

/* Melting temperature Tm=1.2Tr, where Tr is recrystallisation T(=1510 C) */

L12:
    trat[i__ - 1] = ctemp[i__ - 1] / 1478.;
    tratk[i__ - 1] = thres_temp[i__ - 1] / tm;

/* Dislocation motion mechanism */

    if (ij == 0) {
        s_copy(mecha, "Diff Flow", (ftnlen)30, (ftnlen)16);
        if (difway == 1) {
            s_copy(mechb, "Lattice", (ftnlen)30, (ftnlen)7);
        } else if (difway == 0) {
            s_copy(mechb, "Boundary", (ftnlen)30, (ftnlen)8);
        }
    } else if (ij != 0) {

```



```

        s_copy(mecha, "Power-Law", (ftnlen)30, (ftnlen)9);
        if (way == 1) {
            s_copy(mechb, "Lattice", (ftnlen)30, (ftnlen)7);
        } else if (way == 0) {
            s_copy(mechb, "Core", (ftnlen)30, (ftnlen)4);
        }
    }

/* Mechanism of Glide motion */

    if (gway == 1) {
        s_copy(mechc, "Peierls force", (ftnlen)30, (ftnlen)13);
    } else if (gway == 0) {
        s_copy(mechc, "Discrete Obstacles", (ftnlen)30, (ftnlen)18);
    }

/* Mechanism of Diff Flow */

    if (difway == 1) {
        s_copy(mechd, "Lattice", (ftnlen)8, (ftnlen)7);
    } else if (difway == 0) {
        s_copy(mechd, "Boundary", (ftnlen)8, (ftnlen)8);
    }

/* Output MPa */

    s_wsfe(&io___98);
    do_fio(&c__1, (char *)&tratk[i__ - 1], (ftnlen)sizeof(doublereal));
    do_fio(&c__1, mecha, (ftnlen)30);
    do_fio(&c__1, mechb, (ftnlen)30);
    do_fio(&c__1, mechc, (ftnlen)30);
    do_fio(&c__1, mechd, (ftnlen)8);
    e_wsfe();
    s_wsfe(&io___99);
    do_fio(&c__1, (char *)&tratk[i__ - 1], (ftnlen)sizeof(doublereal));
    do_fio(&c__1, (char *)&ashts[i__ - 1], (ftnlen)sizeof(doublereal));
    do_fio(&c__1, (char *)&ashcri[i__ - 1], (ftnlen)sizeof(doublereal));
    do_fio(&c__1, (char *)&ashpb[i__ - 1], (ftnlen)sizeof(doublereal));
    e_wsfe();
    ++i__;

/* Output data */

    perc = i__ / 35. * 100.;
    perc = (doublereal) ((integer) perc);
    if (perc >= (doublereal) (ii * 25)) {
        s_wsfe(&io___101);
        i__1 = ii * 25;
        do_fio(&c__1, (char *)&i__1, (ftnlen)sizeof(integer));
        e_wsfe();
        ++ii;
    }

```

```

        }
        if (perc >= 95.) {
            s_wsfe(&io____102);
            e_wsfe();
        }
/* L1: */
}

/* -----  FORMAT STATEMENTS  ----- */

/* L112: */
/* L442: */
/* L4444: */
/* L10: */

    s_stop("", (ftnlen)0);
    return 0;
} /* MAIN__ */

/*
*****
***** */

/* Subroutine */ int diff_(double real *temp, double real *df,
    double real *r__, double real *s, double real *smo, integer *is,
    double real *gs, double real *l, double real *gar, integer *it)
{
    /* Builtin functions */
    double exp(double real), pow_dd(double real *, double real *);

    /* Local variables */
    static double real m, t, bb, db, qb, kk, pi, dv, ss, qv, db0, dv0, st1,
        st2, deff, rhob, cons, smok, coble, omega;

/* Constants: */

    *is = 0;
    pi = 3.1416;
    dv0 = 5e-5;
    qv = 2.51e5;
    qb = 1.75e5;
    omega = 1.18e-29;
    db0 = 1.1e-12;
    kk = 1.381e-23;
    t = *temp;
    smok = *smo * 1e6;
    bb = 1e-10;

```

```

/* Coble creep */

st1 = bb * *smo / *gs;

/* Threshold stress */

st2 = bb * .1 * *smo / (*l * 3.);

/* Output */

if (st1 + st2 > *s) {
    *s = st1 + st2;
}

ss = (*s - st1 - st2) / *smo;
db = db0 * exp(-qb / (*r__ * t));
dv = dv0 * exp(-qv / (*r__ * t));
if (*it == 1) {
    goto L1;
}
if (*it == 2) {
    goto L2;
}
if (*it == 3) {
    goto L3;
}

/* Equiaxed (h = w) */

L3:
deff = dv + pi * db / *gs;
*df = omega * 42. * smok * deff * ss / (t * kk * (*gs * *gs));
goto L4;

/* Elongated grain (h ~ w) */

L2:
deff = dv / pow_dd(gar, &c_b43) + pi * db / (*gs * pow_dd(gar, &c_b99));
*df = omega * 42. * smok * deff * ss / (t * kk * (*gs * *gs));
goto L4;

/* Elongated (h >> w) */

L1:
deff = dv / *gar + pi * db / (*gs * pow_dd(gar, &c_b100));
*df = omega * 16. * smok * deff * ss / (t * kk * (*gs * *gs));

/* Coble creep calc */

L4:
rhob = ss / bb * .9;

```

```

m = rhob * db * pow_dd(&bb, &c_b43) * pow_dd(&omega, &c_b102) / (kk * t);
cons = deff * 21. * omega / (kk * t * *gs * m);
*df /= cons + 1;

coble = pi * db / *gs;
if (dv > coble) {
    *is = 1;
}
return 0;
} /* diff_ */

/*
*****
***** */

/* Subroutine */ int power_(double real *te, double real *pwlaw, double real *
    r__, double real *smo, double real *sok, double real *stress, double real
    *burgv, integer *i__, double real *smin, double real *pwg)
{
    /* System generated locals */
    double real d__1, d__2;

    /* Builtin functions */
    double sqrt(double real), pow_dd(double real *, double real *), exp(
        double real);

    /* Local variables */
    static double real n, t, a2, dc, qc, kk, ax, dv, pi, bx, tm, ss, qv, st,
        dc0, dv0, deff, core, sinh__, smok, powf, ssth, smot, alpha,
        sinhb;

    t = *te;

    /* Constants: */

    pi = 3.141659;
    *i__ = 0;
    tm = 1751.;

    /* Creep exponent */

    if (t / tm <= .6f) {
        n = 7.7;
    }
    if (t / tm > .6f && t / tm <= .8f) {
        n = t / tm * -18.8 + 18.5f;
    }
    if (t / tm > .8f) {
        n = 4.;
    }
}

```

```

d__1 = sqrt(3.);
d__2 = n + 1.;
a2 = pow_dd(&d__1, &d__2) * 100.;
dv0 = 5e-5;
qv = 2.51e5;
qc = 1.74e5;
dc0 = 1e-23;
kk = 1.381e-23;
smok = *sok * 1e9;
smot = *smo * 1e6;
st = *smin;

dv = dv0 * exp(-qv / (*r__ * t));
dc = dc0 * exp(-qc / (*r__ * t));
ss = *stress / *smo;
deff = dv + dc * 10. * ss * ss / (*burgv * *burgv);

/* Power-law breakdown*/

powf = a2 * deff * smot * *burgv / (kk * t);
alpha = smok * 700. / smot;
ax = alpha * ss;
sinh__ = (exp(ax) - exp(-ax)) / 2.;
d__1 = sinh__ / alpha;
*pwlaw = powf * pow_dd(&d__1, &n);

/* Low stress */

ssth = (*stress - st) / *smo;
bx = alpha * ssth;
sinhb = (exp(bx) - exp(-bx)) / 2.;
d__1 = sinhb / alpha;
*pwg = powf * pow_dd(&d__1, &n);

/* Output */

if (*pwlaw >= 1e308) {
    *pwlaw = 1e308;
}
if (*pwg >= 1e308) {
    *pwg = 1e308;
}

core = dc * .01 * ss * ss / (*burgv * *burgv);
if (dv > core) {
    *i__ = 1;
}
/* L1: */
return 0;

```

```

} /* power_ */

/*
*****
***** */

/* Subroutine */ int glide_(double real *temp, double real *sm, double real *
    stress, double real *burgv, double real *gf, integer *i__, double real *
    l, double real *r__, double real *smokg, double real *gl1, double real *
    gl2)
{
    /* System generated locals */
    double real d__1;

    /* Builtin functions */
    double exp(double real), pow_dd(double real *, double real *);

    /* Local variables */
    static double real t, g1, kk, gp, ss, smo, exp1, exp2, smok, thao1, thao2,
        energy1, energy2, strain1, strain2;

    /* Constants: */

    *i__ = 0;
    g1 = 1e6;
    gp = 1e14;
    kk = 1.381e-23;
    smok = *smokg * 1e9;

    t = *temp;
    smo = *sm;
    ss = *stress;

    /* Strain due to discrete obstacles */

    energy1 = smok * .001 * *burgv * *burgv * *r__;
    thao1 = smok * *burgv / *l * 3.;
    exp1 = 1. - ss * 1e6 / thao1;
    if (ss * 1e6 > thao1) {
        strain1 = g1;
        goto L11;
    }
    strain1 = g1 * exp(-energy1 * exp1 / (kk * t));

    /* Strain due to lattice resistance */

L11:
    energy2 = smok * .1 * pow_dd(burgv, &c_b107);

```

```

thao2 = smok * .06;
if (ss * 1e6 > thao2) {
    d__1 = ss / smo;
    strain2 = gp * pow_dd(&d__1, &c_b43);
    goto L22;
}
d__1 = ss * 1e6 / thao2;
exp2 = 1. - pow_dd(&d__1, &c_b110);
exp2 = pow_dd(&exp2, &c_b111);
d__1 = ss / smo;
strain2 = gp * pow_dd(&d__1, &c_b43) * exp(-energy2 * exp2 / (kk * t));

/* Pierls force */

L22:
    if (strain2 <= strain1) {
        *gf = strain2;
    } else {
        *gf = strain1;
    }

    if (strain2 < strain1) {
        *i__ = 1;
    }

    *gl1 = thao1;
    *gl2 = thao2;
    return 0;
} /* glide_ */

/* Main program alias */ int ashby_map__ () { MAIN__ (); return 0; }

```

Appendix 5.2 - Calculation of stress on the strip from thickness and line speed

Furnace process parameters in the continuous annealing process are calculating the stress applied on the strip depending on the strip material and drive speed.

Furnace tension is calculated by adding a furnace tension trim to the standard tension of 190kg load applied on to the strip by the drive rolls at the end of the furnace.

Furnace trim is calculated by the equation below

$$\text{Furnace trim} = \frac{(\text{Stress factor} \times \text{width of the strip} \times \text{Gauge of the strip}) \times (\text{Tension trim} + 100)}{1000}$$

A 5.2.1 Calculations for HiB

Table A2.1 Calculation of stress applied as a function of line speed for 0.23mm strip

Sheet thickness in mm	Line speed m/s	Load kg	Force N	Cross section area m ²	Stress MPa
0.23	10	190	1863.9	0.00023	8.10
	20	190	1863.9	0.00023	8.10
	30	190	1863.9	0.00023	8.10
	40	190	1863.9	0.00023	8.10
	50	211	2069.91	0.00023	9.00
	60	214.41	2103.362	0.00023	9.15
	70	217.53	2133.969	0.00023	9.28
	80	217.53	2133.969	0.00023	9.28
	90	217.53	2133.969	0.00023	9.28

Table A2.2 Calculation of stress applied as a function of line speed for 0.27mm strip

Sheet thickness in mm	Line speed m/s	Load Kg	Force N	Cross section area m ²	Stress MPa
0.27	10	190.00	1863.90	0.00027	6.90
	20	190.00	1863.90	0.00027	6.90
	30	190.00	1863.90	0.00027	6.90
	40	190.00	1863.90	0.00027	6.90
	50	215.21	2111.20	0.00027	7.82
	60	218.66	2145.02	0.00027	7.94
	70	222.32	2180.95	0.00027	8.08
	80	222.32	2180.95	0.00027	8.08
	90	222.32	2180.95	0.00027	8.08

Table A2.3 Calculation of stress applied as a function of line speed for 0.3mm strip

Strip thickness in mm	Line speed m/s	Load Kg	Force N	Area m ²	Stress MPa
0.3	10	190.00	1863.90	0.0003	6.21
	20	190.00	1863.90	0.0003	6.21
	30	190.00	1863.90	0.0003	6.21
	40	190.00	1863.90	0.0003	6.21
	50	218.01	2138.68	0.0003	7.13
	60	221.84	2176.25	0.0003	7.25
	70	225.91	2216.18	0.0003	7.39
	80	225.91	2216.18	0.0003	7.39
	90	225.91	2216.18	0.0003	7.39

Calculations for CGO

Table A2.4 Calculation of stress applied as a function of line speed for 0.23mm strip

Sheet thickness in mm	Line speed m/s	Load	Force N	Area m ²	Stress MPa
0.23	10	164.30	1611.83	0.00023	7.01
	20	164.30	1611.83	0.00023	7.01
	30	164.76	1616.33	0.00023	7.03
	40	167.06	1638.83	0.00023	7.13
	50	169.35	1661.34	0.00023	7.22
	60	190.00	1863.90	0.00023	8.10
	70	210.65	2066.46	0.00023	8.98
	80	212.94	2088.97	0.00023	9.08
	90	215.24	2111.47	0.00023	9.18
	100	217.53	2133.98	0.00023	9.28

Table A2.5 Calculation of stress applied as a function of line speed for 0.27mm strip

Strip thickness in mm	Line speed m/s	Load Kg	Force N	Area m ²	Stress MPa
0.27	10	159.84	1567.99	0.00027	5.81
	20	159.84	1567.99	0.00027	5.81
	30	160.37	1573.27	0.00027	5.83
	40	163.07	1599.69	0.00027	5.92
	50	165.76	1626.11	0.00027	6.02
	60	190.00	1863.90	0.00027	6.90
	70	214.24	2101.69	0.00027	7.78
	80	216.93	2128.11	0.00027	7.88
	90	219.63	2154.53	0.00027	7.98
	100	222.32	2180.95	0.00027	8.08

Table A2.6 Calculation of stress applied as a function of line speed for 0.3 mm strip

Strip thickness in mm	Line speed m/s	Load Kg	Force N	Area m ²	Stress MPa
0.3	10	156.48	1535.11	0.0003	5.12
	20	156.48	1535.11	0.0003	5.12
	30	157.08	1540.98	0.0003	5.14
	40	160.08	1570.34	0.0003	5.23
	50	163.07	1599.69	0.0003	5.33
	60	190.00	1863.90	0.0003	6.21
	70	216.93	2128.11	0.0003	7.09
	80	219.93	2157.46	0.0003	7.19
	90	222.92	2186.82	0.0003	7.29
	100	225.91	2216.18	0.0003	7.39

Table A2.7 Calculation of stress applied as a function of line speed for 0.35mm strip

Strip thickness in mm	Line speed m/s	Load Kg	Force N	Area m ²	Stress MPa
0.35	10	150.90	1480.31	0.00035	4.23
	20	150.90	1480.31	0.00035	4.23
	30	151.60	1487.16	0.00035	4.25
	40	155.09	1521.41	0.00035	4.35
	50	158.58	1555.66	0.00035	4.44
	60	190.00	1863.90	0.00035	5.33
	70	221.42	2172.14	0.00035	6.21
	80	224.91	2206.39	0.00035	6.30
	90	228.40	2240.64	0.00035	6.40
	100	231.90	2274.89	0.00035	6.50

The value of temperature is obtained from the heat transfer model in chapter 4 and in combination with the stress values calculated from the furnace values are plotted onto the deformation mechanism maps. This shows the change in deformation mechanism of the strip in continuous annealing line.

Appendix 8.1

Method used in separation of loss components from specific total loss

1. Measure the specific total loss at different frequencies of 10, 50, 100, 200, 400, 800 Hz and 1 KHz.
2. Calculate the loss per cycle from the specific total loss and the corresponding frequency.
3. Calculate the square root of frequency.
4. Plot the square root of frequency vs. loss per cycle in the x and y axis respectively.
5. Fit a polynomial

$$P = AX + BX^2 + CX^D$$

Where P – Specific total loss, A – Hysteresis loss components, B – Eddy current component, C – Anomalous loss component, D – 1.5 to 1.6 for GOES , X – frequency. An example calculation and corresponding polynomial fit is shown in the example below.

Table A8.1 Calculation of loss per cycle and square root of frequency

Frequency f (Hz)	Specific total loss P (W/kg)	Loss per cycle P/f (W/kg/Hz)	Sqrt (f)
10	0.1501	0.01501	3.16227766
50	1.076	0.02152	7.071067812
100	2.978	0.02978	10
200	8.733	0.043665	14.14213562
400	27.23	0.068075	20
800	86.92	0.10865	28.28427125
1000	127.6	0.1276	31.6227766

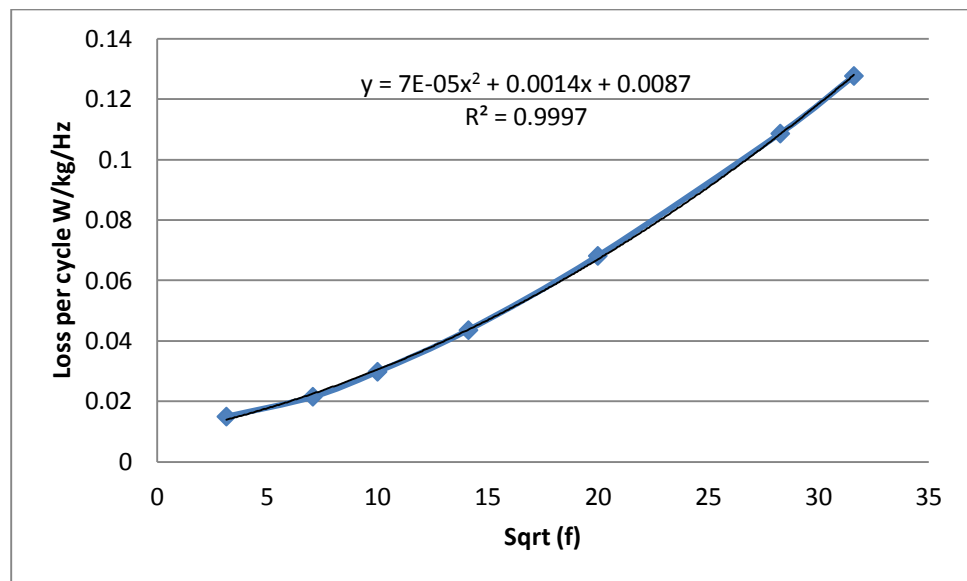


Figure A 8.1 Polynomial fitting the data shown in Table 8.1A